Contents

1 Introduction

Pattern formation, i.e. the spontaneous emergence of spatial order, is a widespread phenomenon in nature, and also in laboratory experiments. Examples can be given from almost every field of science, some of them very familiar, such as fingerprints, the stripes on the skin of a tiger or zebra, the spots on the skin of a leopard, the dunes in a desert, and some others less evident, such as the convection cells in a fluid layer heated from below, and the ripples formed in a vertically oscillated plate covered with sand [1].

All these patterns have something in common: they arise in spatially extended, dissipative systems which are driven far from equilibrium by some external stress. "Spatially extended" means that the size of the system is, at least in one direction, much larger than the characteristic scale of the pattern, determined by its wavelength. The dissipative nature of the system implies that spatial inhomogeneities disappear when the external stress is weak, and the uniform state of the system is stable. As the stress is increased, the uniform state becomes unstable with respect to spatial perturbations of a given wavelength. In this way, the system overcomes dissipation and the state of the system changes abruptly and qualitatively at a critical value of the stress parameter. The very onset of the instability is, however, a linear process. The role of nonlinearity is to select a concrete pattern from a large number of possible patterns.

These ingredients of pattern-forming systems can be also found in many optical systems (the most paradigmatic example is the laser), and, consequently, formation of patterns of light can also be expected. In optics, the mechanism responsible for pattern formation is the interplay between diffraction, off-resonance excitation and nonlinearity. Diffraction is responsible for spatial coupling, which is necessary for the existence of nonhomogeneous distributions of light.

Some patterns found in systems of very different nature (hydrodynamic, chemical, biological or other) look very similar, while other patterns show features that are specific to particular systems. The following question then naturally arises: which peculiarities of the patterns are typical of optics only, and which peculiarities are generic? At the root of any universal behavior of pattern-forming systems lies a common theoretical description, which is independent of the system considered. This common behavior becomes evident

after the particular microscopic models have been reduced to simpler models, called order parameter equations (OPEs). There is a very limited number of universal equations which describe the behavior of a system in the vicinity of an instability; these allow understanding of the patterns in different systems from a unified point of view.

The subject of this book is transverse light patterns in nonlinear optical resonators, such as broad-aperture lasers, photorefractive oscillators and optical parametric oscillators. This topic has already been reviewed in a number of works [2, 3, 4, 5, 6, 7, 8, 9, 10]. We treat the problem here by means of a description of the optical resonators by order parameter equations, reflecting the universal properties of optical pattern formation.

1.1 Historical Survey

The topic of optical pattern formation became a subject of interest in the late 1980s and early 1990s. However, some hints of spontaneous pattern formation in broad-aperture lasers can be dated to two decades before, when the first relations between laser physics and fluids/superfluids were recognized [11]. The laser–fluid connection was estalished by reducing the laser equations for the class A case (i.e. a laser in which the material variables relax fast compared with the field in the optical resonator) to the complex Ginzburg–Landau (CGL) equation, used to describe superconductors and superfluids. In view of this common theoretical description, it could then be expected that the dynamics of light in lasers and the dynamics of superconductors and superfluids would show identical features.

In spite of this insight, the study of optical patterns in nonlinear resonators was abandoned for a decade, and the interest of the optical community turned to spatial effects in the unidirectional mirrorless propagation of intense light beams in nonlinear materials. In the simplest cases, the spatial evolution of the fields is just a filamentation of the light in a focusing medium; in more complex cases, this evolution leads to the formation of bright spatial solitons [12]. The interest in spatial patterns in lasers was later revived by a series of works. In [13, 14], some nontrivial stationary and dynamic transverse mode formations in laser beams were demonstrated. It was also recognized [15] that the laser Maxwell–Bloch equations admit vortex solutions. The transverse mode formations in [13, 14], and the optical vortices in [15] were related to one another, and the relation was confirmed experimentally (Fig. 1.1) [16, 17]. The optical vortices found in lasers are very similar to the phase defects in speckle fields reported earlier [18, 19].

The above pioneering works were followed by an increasing number of investigations. Efforts were devoted to deriving an order parameter equation for lasers and other nonlinear resonators; this would be a simple equation capturing, in the lowest order of approximation, the main spatio-temporal properties of the laser radiation. The Ginzburg–Landau equation, as derived
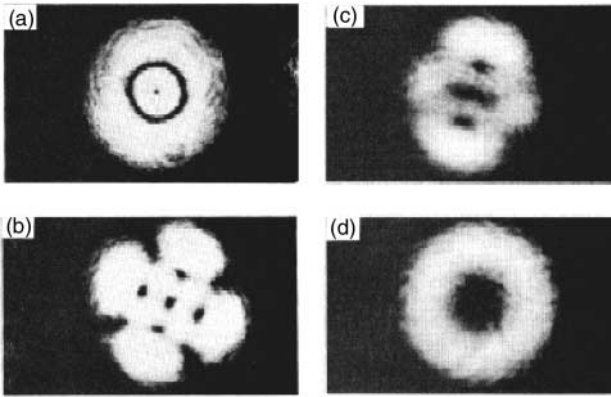
Fig. 1.1. The simplest patterns generated by a laser, which can be interpreted as locked transverse modes of a resonator with curved mirrors. From [17], ©1991 American Physical Society

in [11], is just a very simple model equation for lasers with spatial degrees of freedom. Next, attempts were made to derive a more precise order parameter equation for a laser [15, 20], which led to an equation valid for the red detuning limit. Red detuning means that the frequency of the atomic resonance is less than the frequency of the nearest longitudinal mode of the resonator. This equation, however, has a limited validity, since it is not able to predict spontaneous pattern formation: the laser patterns usually appear when the cavity is blue-detuned. Depending on the cavity aperture, higher-order transverse modes [17] or tilted waves [21] can be excited in the blue-detuned resonator.

The problem of the derivation of an order parameter equation for lasers was finally solved in [22, 23], where the complex Swift–Hohenberg (CSH) equation was derived. Compared with the Ginzburg–Landau equation, the CSH equation contains additional nonlocal terms responsible for spatial mode selection, thus inducing a pattern formation instability. Later, the CSH equation for lasers was derived again using a multiscale expansion [24]. The CSH equation describes the spatio-temporal evolution of the field amplitude. Also, an order parameter equation for the laser phase was obtained, in the form of the Kuramoto–Sivashinsky equation [25]. It is noteworthy that both the Swift–Hohenberg and the Kuramoto–Sivashinsky equations appear frequently in the description of hydrodynamic and chemical problems, respectively.

The derivation of an order parameter equation for lasers means a significant advance, since it allows one not only to understand the pattern formation mechanisms in this particular system, but also to consider the broad-aperture laser in the more general context of pattern-forming systems in nature [1].

The success in understanding laser patterns initiated a search for spontaneous pattern formation in other nonlinear resonators. One of the most extensively studied systems has been photorefractive oscillators, where the theoretical backgrounds were laid [26], complicated structures experimentally observed [27, 28] and order parameter equations derived [29]. Intensive studies of pattern formation in passive, driven, nonlinear Kerr resonators were also performed [30, 31, 32, 33]. Also, the patterns in optical parametric oscillators received a lot of attention. The basic patterns were predicted [34, 35], and order parameter equations were derived in the degenerate [36, 37] and nondegenerate [38] regimes. The connection between the patterns formed in planar- and curved-mirror resonators was treated in [39], where an order parameter equation description of weakly curved (quasi-plane) nonlinear optical resonators was given.

These are just a few examples. In the next section, the general characteristics of nonlinear resonators, and the state of the art are reviewed.

1.2 Patterns in Nonlinear Optical Resonators

The patterns discussed in the main body of the book are those appearing in nonlinear optical resonators only. This particular configuration is characterized by (1) strong feedback and (2) a mode structure, both due to the cavity. The latter also implies temporal coherence of the radiation. Thanks to the feedback, the system does not just perform a nonlinear transformation of the field distribution, where the fields at the output can be expressed as some nonlinear function of the fields at the input and of the boundary conditions. Owing to the feedback, the system can be considered as a nonlinear dynamical system with an ability to evolve, to self-organize, to break spontaneously the spatial translational symmetry, and in general, to show its "own" distributions not present in the initial or boundary conditions.

Nonlinear optical resonators can be classified in different ways: by the resonator geometry (planar or curved), by the damping rates of the fields (class A, B or C lasers), by the field–matter interaction process (active and passive systems) and in other ways. After order parameter equations were derived for various systems, a new type of classification became possible. One can distinguish several large groups of nonlinear resonators, each of which can be described by a common order parameter equation:

1. Laser-like nonlinear resonators, such as lasers of classes A and C, photorefractive oscillators, and nondegenerate optical parametric oscillators. They are described by the complex Swift–Hohenberg equation,

$$\frac{\partial A}{\partial t} = (D_0 - 1) A - A |A|^2 + \mathrm{i} \left(a\nabla^2 - \omega\right) A - \left(a\nabla^2 - \omega\right)^2 A \,,$$

   and show optical vortices as the basic localized structures, and tilted waves and square vortex lattices as the basic extended patterns.

2. Resonators with squeezed phase, such as degenerate optical parametric oscillators and degenerate four-wave mixers. They are described, in the most simplified way, by the real Swift–Hohenberg equation,

$$\frac{\partial A}{\partial t} = (D_0 - 1)\, A - A^3 + \left(a\nabla^2 - \omega\right)^2 A \, ,$$

and show phase domains and phase solitons as the basic localized structures, and stripes and hexagons as the basic extended patterns.
3. Lasers with a slow population inversion D (class B lasers). They cannot be described by a single order parameter equation, but can be described by two coupled equations,

$$\frac{\partial A}{\partial t} = (D - 1)\, A + \mathrm{i}\left(a\nabla^2 - \omega\right) A - \left(a\nabla^2 - \omega\right)^2 A \, ,$$
$$\frac{\partial D}{\partial t} = -\gamma \left(D - D_0 + |A|^2\right) ,$$

and their basic feature is self-sustained dynamics, in particular the "restless vortex".
4. Subcritical nonlinear resonators, such as lasers with intracavity saturable absorbers or optical parametric oscillators with a detuned pump. The effects responsible for the subcriticality give rise to additional terms in the order parameter equation, which in general has the form of a modified Swift–Hohenberg equation,

$$\frac{\partial A}{\partial t} = F\left(D_0, A, |A|^n, \nabla^2\right) + \mathrm{i}\left(a\nabla^2 - \omega\right) A - \left(a\nabla^2 - \omega\right)^2 A \, ,$$

where F represents a nonlinear, nonlocal function of the fields. Its solutions can show bistability and, as consequence, such systems can support bistable bright spatial solitons.

This classification is used throughout this book as the starting point for studies of pattern formation in nonlinear optical resonators. The main advantage of this choice is that one can investigate dynamical phenomena not necessarily for a particular nonlinear resonator, but for a given class of systems characterized by a common order parameter equation, and consequently by a common manifold of phenomena.

In this sense, the patterns in nonlinear optics can be considered as related to other patterns observed in nature and technology, such as in Rayleigh–Bénard convection [40], Taylor–Couette flows [41], and in chemical [42] and biological [43] systems. The study of patterns in nonlinear resonators has been strongly influenced and profited from the general ideas of Haken's synergetics [44] and Prigogine's dissipative structures [45, 46]. On the other hand, the knowledge achieved about patterns in nonlinear resonators provides feedback to the general understanding of pattern formation and evolution in nature.

Next we review the basic transverse patterns observable in a large variety of optical resonators. It is convenient to distinguish between two kinds of patterns: localized structures, and extended patterns in the form of spatially periodic structures.

1.2.1 Localized Structures: Vortices and Solitons

A transverse structure which enjoys great popularity and on which numerous studies have been performed, is the optical vortex, a localized structure with topological character, which is a zero of the field amplitude and a singularity of the field phase.

Although optical vortices have been mainly studied in systems where free propagation occurs in a nonlinear material (see Sect. 1.3), some works have treated the problem of vortex formation in resonators. As mentioned above, the early studies of these fascinating objects [15, 16, 17, 18, 19] strongly stimulated interest in studies of pattern formation in general. The existence of vortices indicates indirectly the analogy between optics and hydrodynamics [22, 47, 48, 49]. It has been shown that the presence of vortices may initiate or stimulate the onset of (defect-mediated) turbulence [27, 50, 51, 52, 53]. Vortices may exist as stationary isolated structures [54, 55] or be arranged in regular vortex lattices [17, 23, 28]. Also, nonstationary dynamics of vortices have been reported, both of single vortices [56, 57] and of vortex lattice structures [58]. Recently, optical vortex lattices have been experimentally observed in microchip lasers [59].

Another type of localized structure is spatial solitons, which are non-topological structures. Although such structures do not appear exclusively in optical systems [60, 61, 62], they are now receiving tremendous interest in the field of optics owing to possible technological applications. A spatial soliton in a dissipative system, being bistable, can carry a bit of information, and thus such solitons are very promising for applications in parallel storage and parallel information processing.

Spatial solitons excited in optical resonators are usually known as cavity solitons. Cavity solitons can be classified into two main categories: amplitude (bright and dark) solitons, and phase (dark-ring) solitons. Investigations of the formation of bright localized structures began with early work on bistable lasers containing a saturable absorber [63, 64] and on passive nonlinear resonators [65].

Amplitude solitons can be excited in subcritical systems under bistability conditions, and can be considered as homoclinic connections between the lower (unexcited) and upper (excited) states. They have been reported for a great variety of passive nonlinear optical resonators, such as degenerate [66, 67, 68] and nondegenerate [69, 70] optical parametric oscillators, and for second-harmonic generation [71, 72, 73] (Fig. 1.2), where the bistability was related to the existence of a nonlinear resonance [37]. In some systems, the interaction of solitons and their dynamical behavior have been studied [73,
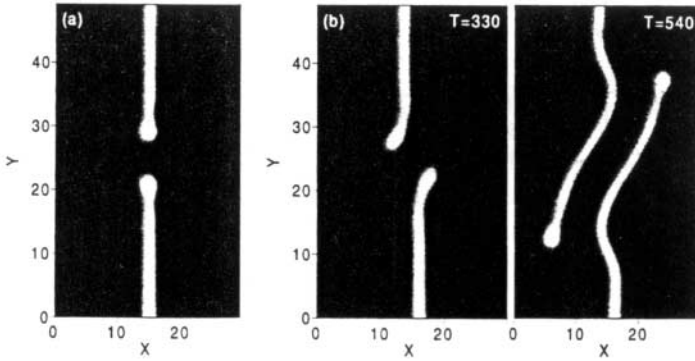
Fig. 1.2. Interaction of two moving amplitude solitons in vectorial intracavity second-harmonic generation: (**a**) central collision, (**b**) noncentral collision. From [73], ©1998 American Physical Society

74, 75]. Resonators containing Kerr media also support amplitude solitons, as a result of either Kerr [76] or polarization (vectorial) [77] instabilities.

In active systems, bright solitons have been demonstrated in photorefractive oscillators [78, 79, 80] and in lasers containing saturable absorbers [81, 82] or an intracavity Kerr lens [83]. A promising system for practical applications is the vertical cavity surface emission laser (VCSEL), which forms a microresonator with a semiconductor as a nonlinear material. The theoretically predicted patterns for this system [84, 85, 86, 87, 88, 89] were recently experimentally confirmed in [90].

The required subcriticality condition is usually achieved by introducing an intracavity absorbing element. However, recently, stable solitons in the absence of an additional medium have been reported in cascade lasers [91].

Besides the amplitude solitons in subcritical nonlinear resonators, a different type of bistable soliton exists in supercritical resonators. Such systems are characterized by a broken phase symmetry of the order parameter, and solutions with only two possible phase values are allowed. In this case the solitons connect two homogeneous solutions of the same amplitude but of opposite phase. Such phase solitons, which are round, stable phase domains of minimum size, appear as a dark ring on a bright background. This novel type of optical soliton is now receiving a lot of interest, since the solitons are seemingly much easier to realize experimentally than their bright counterparts in subcritical systems.

One of the systems most investigated has been the degenerate optical parametric oscillator (DOPO), either in the one-dimensional case [92, 93] or in the more realistic case of two transverse dimensions [94, 95, 96, 97]. Also, the soliton formation process [98, 99, 100] and its dynamical behavior [101, 102] have been analyzed. Optical bistability in a passive cavity driven by a coherent external field is another example of a system supporting such phase
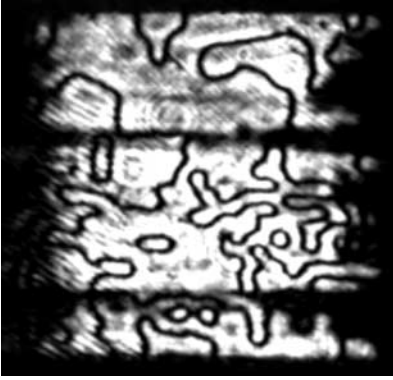
Fig. 1.3. Phase domains and phase (dark-ring) solitons in a cavity four-wave-mixing experiment. From [115], ©1999 Optical Society of America
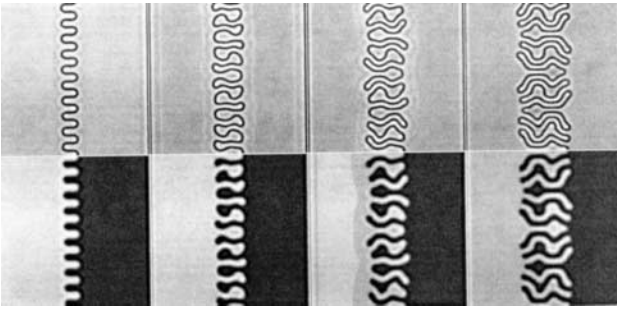
Fig. 1.4. Modulational instability of a straight domain boundary and formation of a finger pattern, in a type II degenerate optical parametric oscillator. The *upper row* shows the intensity, and the *lower row* the phase pattern. From [102], ©2001 American Physical Society

solitons [103, 104, 105, 106, 107]. Both the DOPO and systems showing optical bistability are systems described by a common order parameter equation, the real Swift–Hohenberg equation [108]. Systems with a higher order of nonlinearity, such as vectorial Kerr resonators, have also been shown to support phase solitons [109, 110, 111].

Phase solitons can form bound states, resulting in soliton aggregates or clusters [94, 112].

Phase solitons in a cavity are seemingly much easier to excite than their counterparts in subcritical systems. In fact, such phase solitons have already been experimentally demonstrated in degenerate four-wave mixers [113, 114, 115] (Figs. 1.3 and 1.4).

1.2.2 Extended Patterns

Besides the localized patterns, vortices and solitons, to which the book is mainly devoted, extended patterns in optical resonators have been also extensively studied. In optical resonators, two main categories of patterns can

be distinguished. One class of patterns appears in low-aperture systems, characterized by a small Fresnel number, such as a laser with curved mirrors. Since this is the most typical configuration of an optical cavity, this phenomenon was observed in the very first experimental realizations, although a systematic study was postponed to a later time [16]. The patterns of this kind are induced by the boundary conditions, and can be interpreted as a weakly nonlinear superposition of a small number of cavity modes of Gauss–Hermite or Gauss–Laguerre type.

Theoretical predictions based on modal expansions of the field [14, 116, 117] have been confirmed by a large number of experiments, some of them reported in [118, 119, 120, 121, 122]. Owing to the particular geometry of the cavity, this kind of pattern is almost exclusively optical. If the aperture is increased, the number of cavity modes excited can grow, and so the spatial complexity of the pattern grows[123].

The other class of extended optical patterns is typical of large-aperture resonators, formed by plane mirrors in a ring or a Fabry–Pérot configuration. The transverse boundary conditions have a weak influence on the system dynamics, in contrast to what happens in small-aperture systems. Consequently, the patterns found in these systems are essentially nonlinear, and the system dynamics can be reduced to the evolution of a single field, called the order parameter.

The simplest patterns in these systems consist of a single tilted or traveling wave (TW), which is the basic transverse solution in a laser [21], although more complex solutions formed by several TWs have been found [125, 124]. The predicted laser TW patterns have been observed in experiments with large-Fresnel-number cavities [126, 127, 128]. The TW solutions are also found in passive resonators described by the same order parameter equation, such as nondegenerate optical parametric oscillators (OPOs) [35, 129]. The effect of an externally injected signal in a laser has been also studied [130, 131], showing the formation of more complex patterns, such as rolls or hexagons.

Roll, or stripe, patterns are commonplace for a large variety of nonlinear passive cavities, such as degenerate OPOs [34], four-wave mixers [37], systems showing optical bistability [31, 132] and cavities containing Kerr media [133]. Patterns with hexagonal symmetry are also frequently found in such resonators [134, 135]. Both types of pattern are familiar in hydrodynamic systems, such as systems showing Rayleigh–Bénard convection.

Another kind of traveling solution existing in optical resonators corresponds to spiral patterns, such as those found in lasers [136, 137] and in OPOs [138, 139], which are typical structures in chemical reaction–diffusion systems.

When more complex models, including additional effects, are considered, a larger variety of patterns, sometimes of exotic appearance, is found. Some such models generalize the above cited models by considering the existence

of competition between different parametric processes [140, 141] or between scalar and vectorial instabilities [142], the walk-off effect due to birefringence in the medium [143, 144, 145], or external temporal variation of the cavity parameters [146].

Some systems allow the simultaneous excitation of patterns with different wavenumbers. These systems form patterns with different periodicities that have been called quasicrystals [147, 148] and daisy patterns [149] (Fig. 1.5).

The experimental conditions for large-aspect-ratio resonators are not easy to achieve. Most of the experiments performed have studied multimode regimes involving high-order transverse modes. The formation of the patterns described above was reported in lasers [126, 127, 128] and OPOs [151, 152]. The observed patterns correspond well to the numerical solutions of large-aspect-ratio models. Conditions for boundary-free, essentially nonlinear patterns were obtained in [78, 153] with the use of self-imaging resonators, which allowed the experimenters to obtain Fresnel numbers of arbitrarily high value.

All the patterns reviewed above are two-dimensional, the light being distributed in the transverse space perpendicular to the resonator axis, and evolving in time. Recently, the possibility of three-dimensional patterns was demonstrated for OPOs [154], nonlinear resonators with Kerr media [155, 156], optical bistability [157] and second-harmonic generation [158].

Finally, the problem of the effect of noise on the pattern formation properties of a nonlinear resonator has also been treated. One can expect that
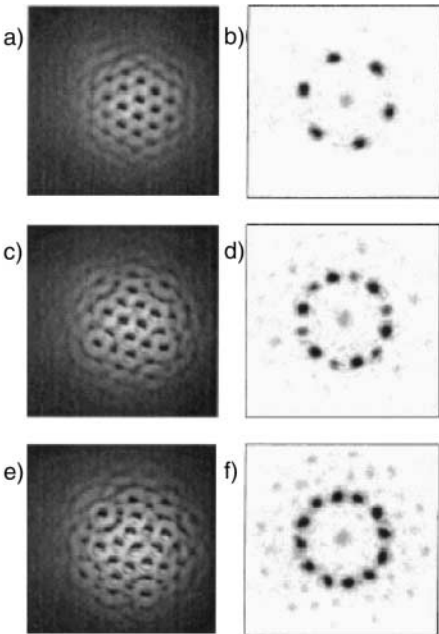
Fig. 1.5. Experimentally observed hexagonal patterns with sixfold and twelvefold symmetry (quasipatterns), in a nonlinear optical system with continuous rotational symmetry. From [150], ©1999 American Physical Society

noise, which is present in every system, will bring about new features in the spatio-temporal dynamics of the system. First, noise can modify (shift) the threshold of pattern formation [159]. Second, owing to noise, the precursors of patterns can be seen below the pattern formation threshold [160, 161, 162]. While a noiseless pattern-forming system below the pattern formation threshold shows no pattern at all, since all perturbations decay, one observes in the presence of noise a particular form of spatially filtered noise, which in the field of nonlinear optics has been called "quantum patterns" when the noise is of quantum origin [163, 164, 165]. Above the pattern formation threshold, noise can also result in defects (dislocations or disclinations) of the patterns [166, 167].

1.3 Optical Patterns in Other Configurations

In parallel with the studies on nonlinear resonators, pattern formation problems have been considered in other optical configurations. These configurations can be divided into the following categories, according to their geometry and complexity.

1.3.1 Mirrorless Configuration

When an intense light beam propagates in a nonlinear medium, it can experience filamentation effects, leading to periodic spatial distributions [168], or develop into self-trapped states of light, or solitons. The self-focusing action of the nonlinearity compensated by diffraction results in self-sustained bright spatial solitons [12], which can exist as isolated states or form complex ensembles, sometimes interacting in a particle-like fashion [169, 170, 171, 172, 173, 174, 175]. Also, dark solitons [176, 177, 178, 179, 180, 181, 182, 183, 184] and optical vortices [185, 186, 187, 188, 189, 190, 191, 192, 193, 194, 195, 196] have been described and experimentally observed. In such a mirrorless configuration feedback is absent, and one obtains not a spontaneous pattern formation, but just a nonlinear transformation of the input distribution. This nonlinear transformation can be very complicated, and can be described by complicated integro-differential equations. However, every transformation remains a transformation, and without feedback it does not lead to spontaneous pattern formation. Some other mirrorless schemes, where optical pattern formation has been predicted, are based on the interaction of two counterpropagating pumping waves in a nonlinear medium. It has been shown that the waves that appear through nonlinear mixing processes have their lowest threshold at certain angles with respect to the pumping waves, and may result in a wide variety of patterns, either extended, such as rolls or hexagons [197, 198, 199, 200, 201, 202, 203, 204](Fig. 1.6), or localized [205]. Experimental confirmation has been obtained using various nonlinear media, such as atomic vapors and photorefractive crystals.
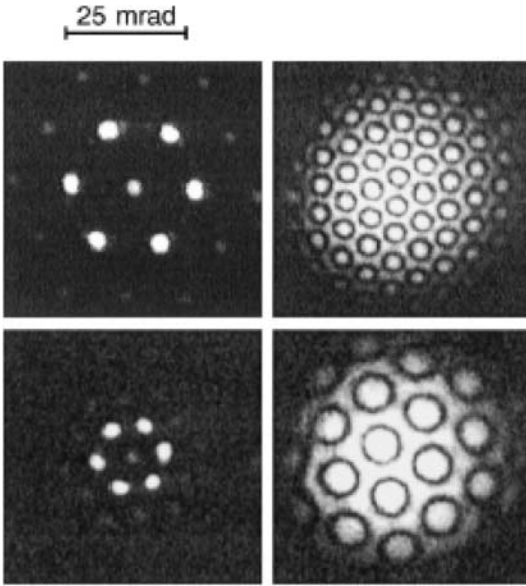
Fig. 1.6. Hexagonal patterns with different spatial scales observed in a photorefractive crystal with a single pump wave. From [203], ©1991 Optical Society of America

1.3.2 Single-Feedback-Mirror Configuration

The presence of a mirror introduces feedback into the system. Unlike the case in the previous schemes, here nonlinearity and diffraction act at different spatial locations. The most typical configuration is formed by a thin slice of a Kerr medium and a mirror at some distance. Theoretical studies have predicted structures mainly with hexagonal symmetry [206, 207, 208, 209] (Fig. 1.7), although more complex solutions have been found [210, 214]. From the experimental side, various nonlinear media, such as atomic vapors [211, 212], and Kerr [213] and photorefractive [214] media have been used successfully. Also, this configuration led to the first realization of localized structures in nonlinear optics [215]. The dynamics and interaction of these localized structures have been extensively investigated [216, 217, 218, 219] (Fig. 1.8).

1.3.3 Optical Feedback Loops

Another configuration, somewhat between the single feedback mirror and the nonlinear resonator, is the feedback loop. In such a configuration, one has the possibility of acting on the field distribution on every round trip through the loop, continuously transforming the pattern distribution. Some typical two-dimensional transformations are the rotation, translation, scaling and filtering of the pattern. The first work obtained pattern formation by controlling the spatial scale and the topology of the transverse interaction of
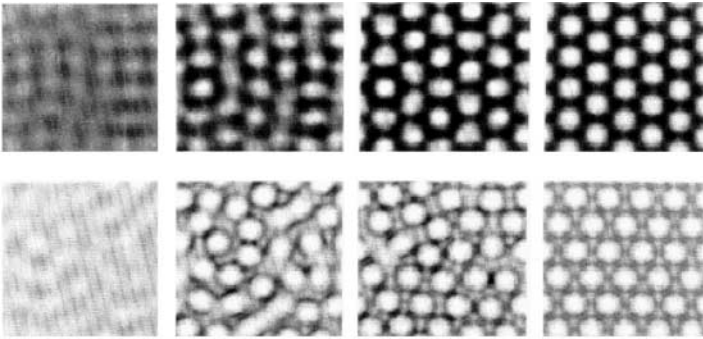
Fig. 1.7. Hexagon formation in a single-feedback-mirror configuration. Numerical results from [207], ©1991 American Physical Society
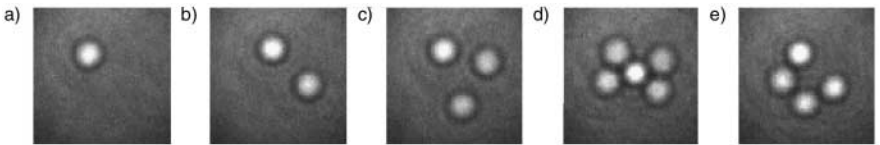
Fig. 1.8. Dissipative solitons observed experimentally in sodium vapor with a single feedback mirror. From [219], ©2000 American Physical Society
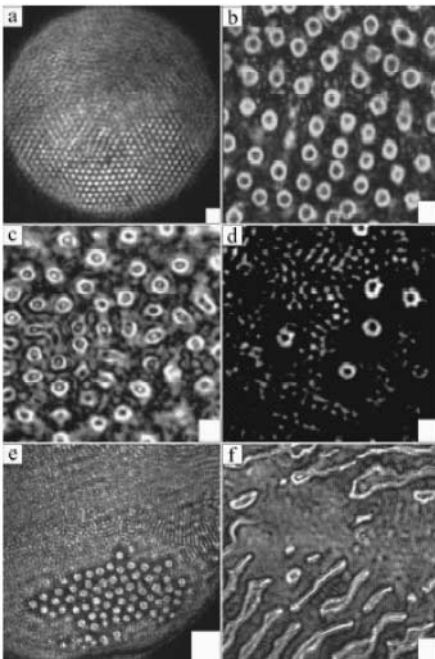
Fig. 1.9. Experimental patterns in an optical system with two-dimensional feedback. (**a**) Hexagonal array, (**b**)–(**d**) "black-eye" patterns, (**e**) island of bright localized structures, (**f**) optical squirms. From [224], ©1998 American Physical Society
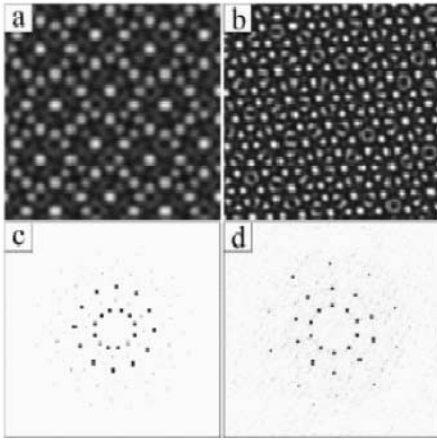
Fig. 1.10. Quasicrystal patterns with dodecagonal symmetry, with different spatial scales, together with the corresponding spatial spectra. From [224], ©1998 American Physical Society

the light field in a medium with cubic nonlinearity [220, 221, 222], by controlling the phase of the field with a spatial Fourier filter [223, 224] (Figs. 1.9 and 1.10), and by introducing a medium with a binary-type refractive nonlinear response [225].

A very versatile system is a feedback loop with a liquid-crystal light valve acting as a phase modulator with a Kerr-type nonlinearity. The conversion from a phase to an intensity distribution, required to close the feedback loop, can be performed by two means: by free propagation (diffractional feedback) [226, 227] or by interference with reflected waves (interferential feedback), as shown in Fig. 1.11 [228, 229, 230]. In both cases, a great variety of kaleidoscope-like patterns have been obtained theoretically and experimentally. The patterns can also be controlled by means of nonlocal interactions, via rotation [231, 232, 233] (Fig. 1.12) or translation [234, 235] of the signal in the feedback loop, giving rise to more exotic solutions such as quasicrys-
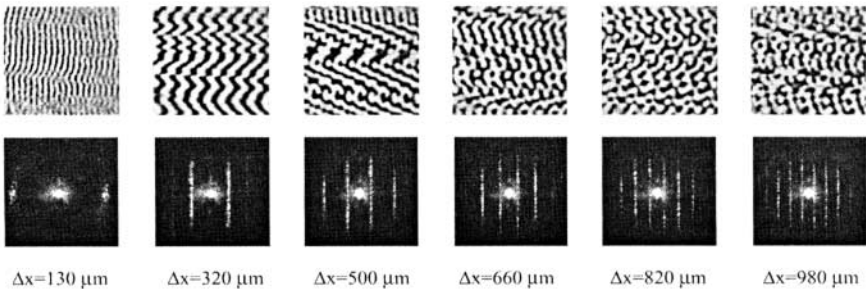
Fig. 1.11. Patterns in a liquid-crystal light valve in the interferential feedback configuration, for increasing translational nonlocality Δx. The near field (*top row*) is shown together with the corresponding spectrum (*bottom row*). From [230], ©1998 American Physical Society
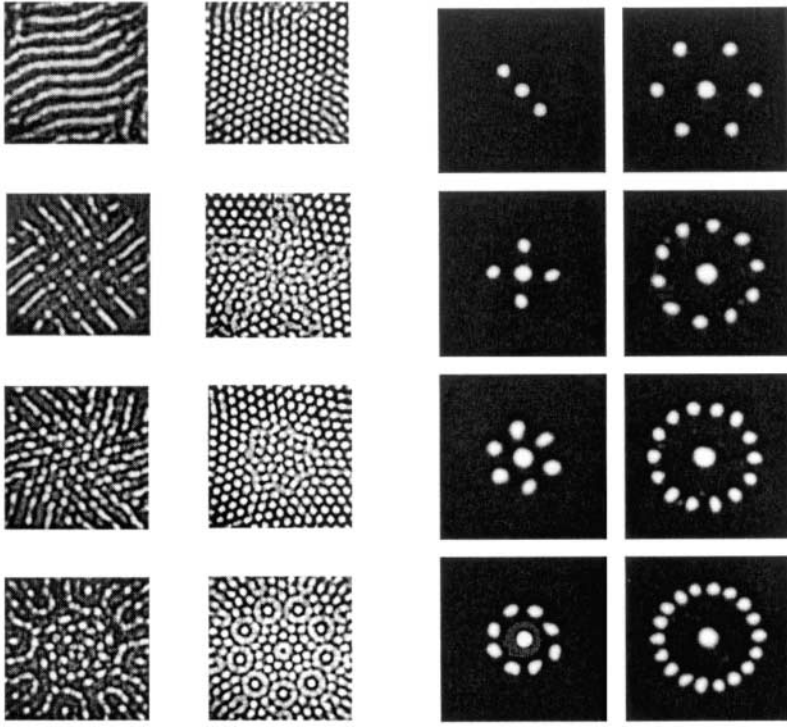
Fig. 1.12. Crystal and quasicrystal patterns obtained experimentally by rotation of the signal in a liquid-crystal light valve feedback loop. The *first* and *second columns* show the near-field distributions, and the *third* and *fourth columns* the corresponding far fields. From [231], ©1995 American Physical Society
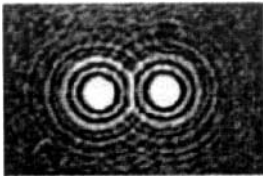
Fig. 1.13. Bound state of spatial solitons in a liquid-crystal light valve interferometer. From [236], ©2002 American Physical Society

tals and drifting patterns. The existence of spatial solitons and the formation of bound states of solitons have also been reported experimentally in the liquid-crystal light valve system [236], as shown in Fig. 1.13.

1.4 The Contents of this Book

In Chaps. 2 and 3, the order parameter equations for broad-aperture lasers and for other nonlinear resonators are obtained. These chapters are relatively mathematical; however, the OPEs derived here pave the way for the

subsequent chapters of the book. The derivation of the OPEs for class A and class C lasers is given in Chap. 2. For completeness, two techniques of derivation are given: one based on the adiabatic elimination of the fast variables, and one based on multiscale expansion techniques. Both procedures lead to the complex Swift–Hohenberg equation as the OPE for lasers. The CSH equation describes the spatio-temporal dynamics of the complex-valued order parameter, which is proportional to the envelope of the optical field. In Chap. 3, the OPEs for optical parametric oscillators and photorefractive oscillators (PROs) are derived. In the degenerate case, the resulting equation is shown to be the real Swift–Hohenberg equation, first obtained in a hydrodynamic context. For large pump detuning values, a generalized model including nonlinear resonance effects is obtained. In the case of PROs, the adiabatic elimination technique is used to derive the CSH equation. The order parameter equations derived in Chaps. 2 and 3 divide nonlinear optical resonators into distinct classes, and thus allow one to study pattern formation phenomena without necessarily considering every nonlinear optical system separately; instead, one can consider classes of the systems.

Chapters 2 and 3 are devoted to the patterns of the first class of systems, that described by the CSH equation, i.e. lasers, photorefractive oscillators and nondegenerate OPOs. The localized patterns in this class of systems are optical vortices: these are zeros of the amplitude of the optical field, and are simultaneously singularities of the field phase. Optical vortices dominate the dynamics of the system in near-resonant cases (when the detuning is close to zero). The CGL equation in this near-resonant limit can be rewritten in a hydrodynamic form. Owing to this analogy between laser and hydrodynamics, the dynamics of the transverse distribution of the laser radiation are very similar to the dynamics of a superfluid. It is shown that optical vortices of the same topological charge rotate around one another; a pair of vortices of the same charge translate in parallel through the aperture of the laser or annihilate, depending on the parameters.

In Chap. 5, the limit of large or moderate detuning is considered. The CSH equation cannot be rewritten in a hydrodynamic form, but the dynamics of the fields can still be well interpreted by hydrodynamic means. For large detuning, tilted waves are excited. In hydrodynamic terms, flows with a velocity of fixed magnitude but arbitrary direction are favored. This results, in particular, in counterpropagating flows separated by vortex sheets. This also leads to optical vortices advected by the mean flow, and similar phenomena. Such phenomena are analyzed theoretically and demonstrated numerically. A pattern of square symmetry, called a square vortex lattice, consisting of four counterpropagating flows in the form of a cross, is also described and discussed.

In Chap. 6, the effects of the curvature of the mirrors of the resonator are analyzed. The majority of theoretical investigations of pattern formation in nonlinear optics, including those in the largest part of this book, have been

performed by assuming a plane-mirror cavity model. However, in experiments resonators with curved mirrors are often used. Therefore a model of a laser with curved mirrors is introduced. The presence of curved mirrors results in an additional term in the order parameter equation, proportional to the total curvature of the mirrors in the resonator. This term produces a coordinate-dependent (parabolic) phase shift of the order parameter during propagation in the resonator. The presence of the parabolic potential allows one to expand the field of the resonator in terms of the eigenfunctions (transverse modes) of the potential. Although this mode expansion is strictly valid for linear resonators only, the nonlinearity in the resonator results in a weakly nonlinear coupling of the complex amplitudes of the modes. As a result, an infinite set of coupled ordinary differential equations for complex-valued mode amplitudes is derived. This gives an alternative way of investigating the transverse dynamics of a laser, by solving the equations for the mode amplitudes instead of solving the partial differential equations. The technique of mode expansion is shown to be extremely useful when one is dealing with a small number of transverse modes. In particular, the transverse dynamics of class A lasers and photorefractive oscillators are considered; the phenomena of transverse mode pulling and locking are observed. Chapter 6 also deals with degenerate resonators, such as self-imaging and confocal resonators. In such resonators, the longitudinal mode separation is an integer multiple of the transverse mode separation. It is shown, by analysis of the corresponding $ABCD$ matrices, that self-imaging resonators are equivalent to planar resonators of zero length. This insight opened up new possibilities for experimenting with transverse patterns in nonlinear optical systems, and allowed the first experimental realization of a number of phenomena predicted theoretically for nonlinear resonators.

Chapter 7 deals with patterns in class B lasers. Class B lasers are not describable by the CSH equation. Owing to the slowness of the population inversion, the order parameter equation in this case is not a single equation belonging to one of the classes defined above, but a system of two coupled equations, resembling those derived for excitatory or oscillatory chemical systems, where the (slow) population inversion plays the role of the recovery variable, and the fast optical field plays the role of the excitable variable. An analysis of such self-sustained spatio-temporal dynamics in a class B laser is performed. The vortices, which are stationary in a class A laser, perform self-sustained meandering in a class B laser, a phenomenon known as the "restless vortex". Also, vortex lattices experience self-sustained oscillatory dynamics. Either the vortices in the lattice oscillate in such a way that neighboring vortices rotate in antiphase, thus resulting in an "optical" mode of vortex lattice oscillation, or the vortex lattice drifts spontaneously with a well-defined velocity, thus resulting in an "acoustic" oscillation mode.

The following chapters, Chaps. 8 to 11, are devoted to amplitude and phase domains, as well as amplitude and phase solitons in bistable nonlinear

optical systems. The general theory of subcritical spatially extended systems is developed in Chap. 8, where two mechanisms of creation of subcriticality in optical resonators are described: one due to the presence of a saturable absorber, and one due to the presence of a nonlinear resonance. A discussion in terms of order parameter equations is given.

In Chap. 9, a theoretical description and experimental evidence of domain dynamics and spatial solitons in lasers containing a saturable absorber are presented. Two different resonator configurations are used: a self-imaging resonator where both nonlinearities (due to the gain and to saturable absorption) are placed at the same location on the optical axis of the resonator, and a self-imaging resonator where the two nonlinearities are placed at Fourier-conjugated locations. For spatially coincident nonlinearities, the evolution of domains is demonstrated numerically and experimentally, with the eventual appearance of spatial solitons. For nonlinearities placed in conjugate locations in the resonator, the competition, mutual interaction and drift of solitons are investigated, also both theoretically and experimentally.

In Chap. 10, a subcriticality mechanism different from saturable absorption is studied, in this case related to the existence of a nonlinear resonance due to nonresonant pumping. As an example, the order parameter equation obtained in Chap. 3 for a degenerate OPO with a detuned pump is considered. The nonlinear resonance implies that the pattern wavenumber depends on the intensity of the radiation. With approriate values of the detuning, the nonlinear resonance can lead to bistability, and thus allow the excitation of amplitude domains and spatial solitons. Numerical results from the DOPO mean-field model are given for comparison.

In Chap. 11, the dynamics of phase domains in supercritical real-valued order parameter systems, such as the degenerate OPO, are analized. These systems should properly be described by the real Swift–Hohenberg equation. It is demonstrated that the domain boundaries, the lines of zero intensity separating domains of opposite phase, may contract or expand depending on the value of the resonator detuning. In this way, the domain boundaries behave as elastic ribbons, with the elasticity coefficient depending on the detuning. Contracting domains, observed for small values of the detuning, eventually disappear. Expanding domains are found for large values of the detuning, and their evolution results in labyrinthine structures. For intermediate values of the detuning, the contracting domain boundaries stop contracting at a particular radius. The latter scenario results in stable rings of domain boundaries, which are phase solitons. The experimental confirmation of the predicted phenomena is described.

In Chap. 12, the Turing pattern formation mechanism, typical of chemical reaction–diffusion systems, is shown to exist also in nonlinear optics. The pattern formation mechanism described in most of the chapters of the book is based on an off-resonance excitation. The Turing mechanism, however, is based on the interplay between the diffusion and/or diffraction of interacting

components. In particular, the emergence of Turing-like patterns is predicted to occur in active and passive systems, concrete examples being lasers with a strongly diffusing population inversion, and degenerate OPOs with a strongly diffracting pump wave. In both cases, one field plays the role of activator, and the other the role of inhibitor. It is also shown that the effect of diffusion and/or diffraction contributes to the stabilization of spatial solitons and allows the existence of complex states resembling molecules of light.

In Chap. 13, we describe the three-dimensional structures of light predicted to occur in resonators described by the three-dimensional Swift–Hohenberg equation. This order parameter equation describes a class of nonlinear optical resonators including the synchronously pumped OPO. Various structures embedded in the envelopes of spatio-temporal light pulses are discussed, in the form of extended patterns (lamellae and tetrahedral patterns), light bubbles (the analogue of the phase solitons in two dimensions) and vortex rings. These structures exist when the OPO resonator length is matched to the length of the pump (mode-locked) laser, which emits a continuous or finite train of picosecond pulses. A three-dimensional modulation can develop on the subharmonic pulses generated, depending on several parameters such as the detuning from the resonance of the OPO cavity, and the mismatch of the resonator lengths for the pump and OPO lasers.

The final chapter, Chap. 14, deals with the influence of noise on spatial structures in nonlinear optics. Noise, which is not considered in the rest of the book, is always present in a real experiment, in the form of vacuum noise (always inevitable) or noise due to technological limitations. It is shown that the noise affects the pattern formation in several ways. Above the modulation instability threshold, where extended patterns are expected, the noise destroys the long-range order in the pattern. Rolls and other extended structures still exist in the presence of noise, but they may display defects (such as dislocations and disclinations) with a density proportional to the intensity of the noise. Also, below the modulation instability threshold, where no patterns are expected in the ideal (noiseless) case, the noise is amplified and can result in (noisy) patterns. The symmetry of a pattern may show itself even below the pattern formation threshold, thanks to the presence of noise. This can be compared with a single-transverse-mode laser, where the coherence in the radiation develops continuously, and where the spectrum of the luminescence narrows continuously when the generation threshold is approached from below.

References

1. M.C. Cross and P.C. Hohenberg, Pattern formation outside of equilibrium, Rev. Mod. Phys. **65**, 851 (1993). 1, 3
2. L.A. Lugiato, Spatio-temporal structures part I, Phys. Rep. **219**, 293 (1992). 2

3. C.O. Weiss, Spatio-temporal structures part II, Phys. Rep. **219**, 311 (1992). 2

4. L.A. Lugiato, Transverse nonlinear optics: introduction and review, Chaos, Solitons Fractals **4**, 1251 (1994). 2

5. L.A. Lugiato, M. Brambilla and A. Gatti, Optical pattern formation, Adv. At. Mol. Opt. Phys. **40**, 229 (1998). 2

6. F.T. Arecchi, S. Boccaletti and P.L. Ramazza, Pattern formation and competition in nonlinear optics, Phys. Rep. **318**, 83 (1999). 2

7. K. Staliunas, *Optical Vortices*, Horizons in World Physics, vol. 228, ed. by M. Vasnetsov and K. Staliunas (Nova Science, New York, 1999). 2

8. Y.S. Kivshar, Spatial optical solitons, in *Nonlinear Science at the Dawn of the 21st Century*, Lecture Notes in Physics, vol. 542, ed. by P.L. Christiansen, M.P. Sørensen and A.C. Scott (Springer, Berlin, Heidelberg, 2000), p.173. 2

9. R. Neubecker and T. Tschudi, Pattern formation in nonlinear optical systems, Chaos Solitons Fractals **10**, 615 (1999). 2

10. M.A. Vorontsov and W.B. Miller, Self-organization in nonlinear optics – kaleidoscope of patterns, in *Self-Organization in Optical Systems and Applications in Information Technology*, ed. by M.A. Vorontsov and W.B. Miller (Springer, Berlin, Heidelberg, 1995) pp. 1-25. 2

11. R. Graham and H. Haken, Laserlight – first example of a second order phase transition far from thermal equilibrium, Z. Phys. **237**, 31 (1970). 2, 3

12. S.A. Akhmanov, R.V. Khoklov and A.P. Sukhorukov, in *Laser Handbook*, ed. by F.T. Arechi and E.O. Schultz-DuBois (North-Holland, Amsterdam, 1972). 2, 11

13. L.A. Lugiato, C. Oldano and L.M. Narducci, Cooperative frequency locking and stationary spatial structures in a laser, J. Opt. Soc. Am. B **5**, 879 (1988). 2

14. L.A. Lugiato, G.L. Oppo, J.R. Tredicce, L.M. Narducci and M.A. Pernigo, Instabilities and spatial complexity in a laser, J. Opt. Soc. Am B **7**, 1019 (1990). 2, 9

15. P. Coullet, L. Gil and F. Rocca, Optical vortices, Opt. Commun. **73**, 403 (1989). 2, 3, 6

16. C.H. Tamm, Frequency locking of two transverse optical modes of a laser, Phys. Rev. A **38**, 5960 (1988). 2, 6, 9

17. M. Brambilla, F. Battipede, L.A. Lugiato, V. Penna, F. Prati, C. Tamm, and C.O. Weiss, Transverse laser patterns I: Phase singularity crystals, Phys. Rev. A **43**, 5090 (1991). 2, 3, 6

18. M.V. Berry, J.F. Nye and F.P. Wright, The elliptic umbilic diffraction catastrophe, Phil. Trans. R. Soc. London **291**, 453 (1979). 2, 6

19. N.B. Baranova, B.Ya. Zel'dovich, A.V. Mamaev, N.F. Pilipetskii and V.V. Shkunov, Sov. Phys. JETP Lett. **33**, 196 (1981). 2, 6

20. G.-L. Oppo, G.P. D'Alessandro and W.J. Firth, Spatio-temporal instabilities of lasers in models reduced via center manifold techniques, Phys. Rev. A **44**, 4712 (1991). 3

21. P.K. Jakobsen, J.V. Moloney, A.C. Newell, R. Indik, Space–time dynamics of wide-gain section lasers, Phys. Rev. A **45**, 8129 (1992). 3, 9

22. K. Staliunas, Laser Ginzburg–Landau equation and laser hydrodynamics, Phys. Rev. A **48**, 1573 (1993). 3, 6

23. K. Staliunas and C.O. Weiss, Tilted and standing waves and vortex lattices in class-A lasers, Physica D 81, **79** (1995). 3, 6

24. J. Lega, J.V. Moloney and A.C. Newell, Universal description of laser dynamics near threshold, Physica D **83**, 478 (1995). 3
25. K. Wang, N.B. Abraham and L.A. Lugiato, Leading role of optical phase instabilities in the formation of certain laser transverse patterns, Phys. Rev. A **47**, 1263 (1993). 3
26. G. D'Alessandro, Spatio-temporal dynamics of a unidirectional ring oscillator with photorefractive gain, Phys. Rev. A **46**, 2791 (1992). 4
27. F.T. Arecchi, G. Giacomelli, P.L. Ramazza and S. Residori, Vortices and defect statistics in two dimensional optical chaos, Phys. Rev. Lett. **67**, 3749 (1991). 4, 6
28. D. Hennequin, L. Dambly, D. Dangoise and P. Glorieux, Basic transverse dynamics of a photorefractive oscillator, J. Opt. Soc. Am. B **11**, 676 (1994). 4, 6
29. K. Staliunas, M.F.H. Tarroja, G. Slekys, C.O. Weiss and L. Dambly, Analogy between photorefractive oscillators and class-A lasers, Phys. Rev. A **51**, 4140 (1995). 4
30. P. Mandel, M. Georgiou and T. Erneux, Transverse effects in coherently driven nonlinear cavities, Phys. Rev. A **47**, 4277 (1993). 4
31. M. Tlidi, M. Georgiou and P. Mandel, Transverse patterns in nascent optical bistability, Phys. Rev. A **48**, 4605 (1993). 4, 9
32. L.A. Lugiato and R. Lefever, Spatial dissipative structures in passive optical systems, Phys. Rev. Lett. **58**, 2209 (1987). 4
33. L.A. Lugiato and C. Oldano, Stationary spatial patterns in passive optical systems: two-level atoms, Phys. Rev. A **37**, 3896 (1988). 4
34. G.L. Oppo, M. Brambilla and L.A. Lugiato, Formation and evolution of roll patterns in optical parametric oscillators, Phys. Rev. A 49, 2028 (1994). 4, 9
35. S. Longhi, Traveling-wave states and secondary instabilities in optical parametric oscillators, Phys. Rev. A **53**, 4488 (1996). 4, 9
36. K. Staliunas, Transverse pattern formation in optical parametric oscillators, J. Mod. Opt. **42**, 1261 (1995). 4
37. G.J. de Valcárcel, K. Staliunas, E. Roldán and V.J. Sánchez-Morcillo, Transverse patterns in degenerate optical parametric oscillation and degenerate four-wave mixing, Phys. Rev. A **54**, 1609 (1996). 4, 6, 9
38. S. Longhi and A. Geraci, Swift–Hohenberg equation for optical parametric oscillators, Phys. Rev. A **54**, 4581 (1996). 4
39. G.J. de Valcárcel, Order-parameter equations for transverse pattern formation in nonlinear optical systems with nonplanar resonators, Phys. Rev. A **56**, 1542 (1997). 4
40. Lord Rayleigh, On the dynamics of revolving fluids, Proc. R. Soc. London Ser. A **93**, 148 (1916). 5
41. R.C. DiPrima and H.L. Swinney, in *Hydrodynamical Instabilities and the Transition to Turbulence*, ed. by H.L. Swinney and J.P. Gollub (Springer, New York, 1981). 5
42. A.M. Turing, *The Chemical Basis of Morphogenesis*, Phil. Trans. R. Soc. London B **237**, 37 (1952). 5
43. H. Meinhardt, *Models of Biological Pattern Formation* (Academic Press, London, 1982). 5
44. H. Haken, *Synergetics, an Introduction* (Springer, Berlin, 1977). 5
45. I. Prigogine and R. Lefever, Symmetry breaking instabilities in dissipative systems, J. Chem. Phys. **48**, 1695 (1968). 5

46. G. Nicolis and I. Prigogine, *Self-Organization in Nonequilibrium Systems* (Willey, New York, 1977). 5

47. M. Brambilla, L.A. Lugiato, V. Penna, F. Prati, C. Tamm and C.O.Weiss, Transverse laser patterns II: variational principle for pattern selection, spatial multistability, and laser hydrodynamics, Phys. Rev. A **43**, 5114 (1991). 6

48. K. Staliunas, Dynamics of optical vortices in a laser beam, Opt. Commun. **90**, 123 (1992). 6

49. F.T. Arecchi, Space–time complexity in nonlinear optics, Physica D **51**, 450 (1991). 6

50. P. Coullet, L. Gil and J. Lega, Defect-mediated turbulence, Phys. Rev. Lett. **62**, 1619 (1989). 6

51. L. Gil, K. Emilsson and G.L. Oppo, Dynamics of spiral waves in a spatially inhomogeneous Hopf bifurcation, Phys. Rev. A **45**, R567 (1992). 6

52. G. Huyet, M.C. Martinoni, J.R. Tredicce and S. Rica, Spatiotemporal dynamics of lasers with large Fresnel number, Phys. Rev. Lett. **75**, 4027 (1995). 6

53. G. Indebetow and S.R. Liu, Defect-mediated spatial complexity and chaos in a phase-conjugate resonator, Opt. Commun. **91**, 321 (1992). 6

54. R. Neubecker, M. Kreuzer and T. Tschudi, Phase defects in a nonlinear Fabry–Perot resonator, Opt. Commun. **96**, 117 (1993). 6

55. G.L. Lippi, T. Ackemann, L.M. Hoffer, A. Gahl and W. Lange, Interplay of linear and nonlinear effects in the formation of optical vortices in a nonlinear resonator, Phys. Rev. A **48**, R4043 (1993). 6

56. G. Balzer, C. Denz, O. Knaup and T. Tschudi, Circling vortices and pattern dynamics in a unidirectional photorefractive ring oscillator, Chaos, Solitons Fractals **10**, 725 (1998). 6

57. C.O. Weiss, H.R. Telle, K. Staliunas and M. Brambilla, Restless optical vortices, Phys. Rev. A **47**, R1616 (1993). 6

58. K. Staliunas and C.O. Weiss, Nonstationary vortex lattices in large aperture class-B lasers, J. Opt. Soc. Am. B **12**, 1142 (1995). 6

59. Y.F. Chen and Y.P. Lan, Transverse pattern formation of optical vortices in a microchip laser with a large Fresnel number, Phys. Rev. A **65**, 013802 (2002). 6

60. K.A. Gorshkov, L.N. Korzinov, M.I. Rabinowich and L.S. Tsimring, Random pinning of localized states at the birth of deterministic disorder within gradient models, J. Stat. Phys. **74**, 1033 (1994). 6

61. L.S. Tsimring and I. Aranson, Cellular and localized structures in a vibrated granular layer, Phys. Rev. Lett. 79, 213 (1997). 6

62. J. Dewel, P. Borkmans, A. De Wit, B. Rudovics, J.J. Perraud, E. Dulos, J. Boissonade and P. De Kepper, Pattern selection and localized structures in reaction–diffusion systems, Physica A **213**, 181 (1995). 6

63. N.N. Rosanov, Diffractive autosolitons in nonlinear interferometers, J. Opt. Soc. Am. B **7**, 1057 (1990). 6

64. N.N. Rosanov, *Transverse Patterns in Wide-Aperture Nonlinear Optical Systems*, Progress in Optics, vol. 35, ed. by E. Wolf (North-Holland, Amsterdam, 1996). 6

65. S. Fauve and O. Thual, Solitary waves generated by subcritical instabilities in dissipative systems, Phys. Rev. Lett. **64**, 282 (1990). 6

66. K. Staliunas and V.J. Sánchez-Morcillo, Localized structures in degenerate optical parametric oscillators, Opt. Commun. **139**, 306 (1997). 6

67. S. Longhi, Localized structures in degenerate optical parametric oscillators, Phys. Scr. **56**, 611 (1997). 6

68. S. Trillo and M. Haelterman, Excitation and bistability of self-trapped signal beams in optical parametric oscillators, Opt. Lett. **23**, 1514 (1998). 6

69. S. Longhi, Spatial solitary waves in nondegenerate optical parametric oscillators near an inverted bifurcation, Opt. Commun. **149**, 335 (1998). 6

70. G.J. de Valcárcel, E. Roldán and K. Staliunas, Cavity solitons in nondegenerate optical parametric oscillators, Opt. Commun. **181**, 207 (2000). 6

71. C. Etrich, U. Peschel and F. Lederer, Solitary waves in quadratically nonlinear resonators, Phys. Rev. Lett. **79**, 2454 (1997). 6

72. S. Longhi, Spatial solitary waves and patterns in type II second-harmonic generation, Opt. Lett. **23**, 346 (1998). 6

73. U. Peschel, D. Michaelis, C. Etrich and F. Lederer, Formation, motion, and decay of vectorial cavity solitons, Phys. Rev. E **58**, 2745 (1998). 6, 7

74. D.V. Skryabin and W.J. Firth, Interaction of cavity solitons in degenerate optical parametric oscillators, Opt. Lett. **24**, 1056 (1999). 7

75. D.V. Skryabin, Instabilities of cavity solitons in optical parametric oscillators, Phys. Rev. E **60**, R3508 (1999). 7

76. W.J. Firth and A. Lord, Two dimensional solitons in a Kerr cavity, J. Mod. Opt. **43**, 1071 (1996). 7

77. V.J. Sánchez-Morcillo, I. Pérez-Arjona, F. Silva, G.J. de Valcárcel and E. Roldán, Vectorial Kerr-cavity solitons, Opt. Lett. **25**, 957 (2000). 7

78. M. Saffman, D. Montgomery and D.Z. Anderson, Collapse of a transverse-mode continuum in a self-imaging photorefractively pumped ring resonator, Opt. Lett. **19**, 5180 (1994). 7, 10

79. G. Slekys, K. Staliunas and C.O. Weiss, Spatial solitons in optical photorefractive oscillators with saturable absorber, Opt. Commun. **149**, 113 (1998). 7

80. W. Królikowski, M. Saffman, B. Luther-Davies and C. Denz, Anomalous interaction of spatial solitons in photorefractive media, Phys. Rev. Lett. **80**, 3240 (1998). 7

81. V.B. Taranenko, K. Staliunas and C.O. Weiss, Spatial soliton laser: localized structures in a laser with a saturable absorber in a self-imaging resonator, Phys. Rev. A **56**, 1582 (1997). 7

82. K. Staliunas, V.B. Taranenko, G. Slekys, R. Viselga and C.O. Weiss, Dynamical spatial localized structures in lasers with intracavity saturable absorbers, Phys. Rev. A **57**, 599 (1998). 7

83. A.M. Dunlop, E.M. Wright and W.J. Firth, Spatial soliton laser, Opt. Commun. **147**, 393 (1998). 7

84. M. Brambilla, L.A. Lugiato, F. Prati, L. Spinelli and W.J. Firth, Spatial soliton pixels in semiconductor devices, Phys. Rev. Lett. **79**, 2042 (1997). 7

85. D. Michaelis, U. Peschel and F. Lederer, Multistable localized structures and superlattices in semiconductor optical resonators, Phys. Rev. A **56**, R3366 (1997). 7

86. L. Spinelli, G. Tissoni, M. Brambilla, F. Prati and L.A. Lugiato, Spatial solitons in semiconductor microcavities, Phys. Rev. A **58**, 2542 (1998). 7

87. G. Tissoni, L. Spinelli, M. Brambilla, T. Maggipinto, I. Perrini and L.A. Lugiato, Cavity solitons in passive bulk semiconductor microcavities. I. Microscopic model and modulational instabilities, J. Opt. Soc. Am. B **16**, 2083

(1999); G. Tissoni, L. Spinelli, M. Brambilla, T. Maggipinto, I. Perrini and L.A. Lugiato, Cavity solitons in passive bulk semiconductor microcavities. II. Dynamical properties and control, J. Opt. Soc. Am. B **16**, 2095 (1999).   7

88. T. Maggipinto, M. Brambilla, G. Harkness and W. J. Firth, Cavity solitons in semiconductor microresonators: existence, stability, and dynamical properties, Phys. Rev. E **62**, 8726 (2000).   7

89. L. Spinelli and M. Brambilla, Signal amplification by means of cavity solitons in semiconductor microcavities, Eur. Phys. J. D **6**, 523 (1999).   7

90. V.B. Taranenko, I. Ganne, R.J. Kuszelewicz and C.O. Weiss, Patterns and localized structures in bistable semiconductor resonators, Phys. Rev. A **61**, 0638818 (2000).   7

91. R. Vilaseca, M.C. Torrent, J. García-Ojalvo, M. Brambilla and M. San Miguel, Two-photon cavity solitons in active optical media, Phys. Rev. Lett. **87**, 083902 (2001).   7

92. S. Longhi, Dark solitons in degenerate optical parametric oscillators, Opt. Lett. **21**, 860 (1996).   7

93. S. Trillo, M. Haelterman and A.P. Sheppard, Stable topological spatial solitons in optical parametric oscillators, Opt. Lett. **22**, 970 (1997).   7

94. K. Staliunas and V.J. Sánchez-Morcillo, Spatial localized structures in degenerate optical parametric oscillators, Phys. Rev. A **57**, 1454 (1998).   7, 8

95. M. Le Berre, D. Leduc, E. Ressayre and A. Tallet, Striped and circular domain walls in the DOPO, J. Opt. B: Quantum Semiclass. Opt. **1**, 153 (1999).   7

96. G.L. Oppo, A.J. Scroggie and W.J. Firth, Stabilization of domain walls in optical parametric oscillators, J. Opt. B: Quantum Semiclass. Opt. **1**, 133 (1999).   7

97. M. Tlidi, M. Le Berre, E. Ressayre and A. Tallet, High-intensity localized structures in the degenerate optical parametric oscillator: comparison between the propagation and the mean-field models, Phys. Rev. A **61**, 043806 (2000).   7

98. M. Le Berre, E. Ressayre and A. Tallet, Kinetics of domain walls in the degenerate optical parametric oscillator, J. Opt. B: Quantum Semiclass. Opt. **2**, 347 (2000).   7

99. M. Tlidi, P. Mandel, M. LeBerre, E. Ressayre, A. Tallet and L. Di Menza, Phase-separation dynamics of circular domain walls in the degenerate optical parametric oscillator, Opt. Lett. **25**, 487 (2000).   7

100. G.-L. Oppo, A.J. Scroggie and W.J. Firth, Characterization, dynamics and stabilization of diffractive domain walls and dark ring cavity solitons in parametric oscillators, Phys. Rev. E **63**, 066209 (2001).   7

101. G. Izus, M. San Miguel and M. Santagiustina, Bloch domain walls in type-II optical parametric oscillators, Opt. Lett. **25**, 1454 (2000).   7

102. G. Izús, M. San Miguel and M. Santagiustina, Phase-locked spatial domains and Bloch domain walls in type-II optical parametric oscillators, Phys. Rev. E **64**, 056231 (2001).   7, 8

103. M. Tlidi, P. Mandel and R. Lefever, Localized structures and localized patterns in optical bistability, Phys. Rev. Lett. **73**, 640 (1994).   8

104. M. Tlidi and P. Mandel, Spatio-temporal patterns and localized structures in nonlinear optics, Phys. Rev. E **56**, 6524 (1997).   8

105. M. Tlidi and P. Mandel, Scaling laws for localized pattern formation in optical bistability, Europhys. Lett. **44**, 449 (1998).   8

106. M. Tlidi, P. Mandel and R. Lefever, Kinetics of localized pattern formation in optical systems, Phys. Rev. Lett. **81**, 979 (1998). 8

107. M. Tlidi and P. Mandel, Space–time localized structures in the degenerate optical parametric oscillator, Phys. Rev. A **59**, R2575 (1999). 8

108. K. Staliunas and V.J. Sánchez-Morcillo, Dynamics of domains in the Swift–Hohenberg equation, Phys. Lett. A **241**, 28 (1998). 8

109. R. Gallego, M. San Miguel and R. Toral, Selfsimilar domain growth, localized structures and labyrinthine patterns in vectorial Kerr resonators, Phys. Rev. E **61**, 2241 (2000). 8

110. E. Hernandez-Garcia, M. Hoyuelos, P. Colet and M. San Miguel, Dynamics of localized structures in vectorial waves, Phys. Rev. Lett. **85**, 744 (2000). 8

111. D. Gomila, P. Colet, G.-L. Oppo and M. San Miguel, Stable droplets and growth laws close to the modulational instability of a domain wall, Phys. Rev. Lett. **87**, 194101 (2001). 8

112. A.G. Vladimirov, J.M. McSloy, D.V. Skryabin and W.J. Firth, Two-dimensional clusters of solitary structures in driven optical cavities, Phys. Rev. E **65**, 046606 (2002). 8

113. V.B. Taranenko, K. Staliunas and C.O. Weiss, Pattern formation and localized structures in degenerate optical parametric mixing, Phys. Rev. Lett. **81**, 2236 (1998). 8

114. V.B. Taranenko, M. Zander, P. Wobben and C.O. Weiss, Stability of localized structures in degenerate wave mixing, Appl. Phys. B **69**, 337 (1999). 8

115. C.O. Weiss, M. Vaupel, K. Staliunas, G. Slekys and V.B. Taranenko, Solitons and vortices in lasers, Appl. Phys. B **68**, 151 (1999). 8

116. F. Prati, M. Brambilla and L.A. Lugiato, Pattern formation in lasers, Rivista Nuovo Cimento **17**, 1 (1994). 9

117. M. Brambilla, M. Cattaneo, L.A. Lugiato, R. Pirovano, F. Prati, A.J. Kent, G.-L. Oppo, A.B. Coates, C.O. Weiss, C. Green, E.J. D'Angelo and J.R. Tredicce, Dynamical transverse laser patterns I: theory, Phys. Rev. A **49**, 1427 (1994). 9

118. H. Lin and N.B. Abraham, Mode formation and beating in the transverse pattern dynamics in a laser, Opt. Commun. **79**, 476 (1990). 9

119. A.B. Coates, C.O. Weiss, C. Green, E.J. D'Angelo, J.R. Tredicce, M. Brambilla, M. Cattaneo, L.A. Lugiato, R. Pirovano, F. Prati, A.J. Kent and G.-L. Oppo, Dynamical transverse laser patterns II: experiments, Phys. Rev. A **49**, 1452 (1994). 9

120. H. Li, T.L. Lucas, J.G. McInerney and R.A. Morgan, Transverse modes and patterns of electrically pumped vertical-cavity surface-emitting semiconductor lasers, Chaos, Solitons Fractals **4**, 1619 (1994). 9

121. A. Barsella, P. Alcantara Jr., L. Guidoni and E. Arimondo, Dynamics of LSA transverse patterns for an infrared CO_2 laser with OsO_4 intracavity saturable absorber, Opt. Commun. **117**, 455 (1995). 9

122. E. Louvergneaux, D. Hennequin, D. Dangoisse and P. Glorieux, Transverse mode competition in a CO_2 laser, Phys. Rev A **53**, 4435 (1996). 9

123. Z. Chen, N.B. Abraham, S. Balle, E.J. D'Angelo and J.R. Tredicce, Space–time dynamics in the transverse patterns of a laser from a model not restricted a priori to a few modes, Chaos, Solitons Fractals **4**, 1489 (1994). 9

124. Q. Feng, J.V. Moloney, and A.C. Newell, Transverse patterns in lasers, Phys. Rev. A **50**, R3601 (1994). 9

125. G. Huyet, C. Mathis, H. Grassi, J.R. Tredicce and N.B. Abraham, Regarding standing vs. traveling waves in the transverse spatial patterns of homogeneously and inhomogeneously broadened lasers, Opt. Commun. **111**, 488 (1994). 9

126. F. Encinas-Sanz, J.M. Guerra and I. Pastor, Transverse pattern morphogenesis in a CO_2 laser, Opt. Lett. **21**, 1153 (1996). 9, 10

127. S.P. Hegarty, G. Huyet, J.G. McInerney and K.D. Choquette, Pattern formation in the transverse section of a laser with a large fresnel number, Phys. Rev. Lett. **82**, 1434 (1999). 9, 10

128. J. Houlihan, J.R. O'Callaghan, V. Voignier, G. Huyet, J.G. McInerney and B. Corbett, Experimental observation of traveling waves in the transverse section of a laser, Opt. Lett. **26** 1556 (2001). 9, 10

129. V.J. Sánchez-Morcillo, G.J. de Valcárcel, E. Roldán and K. Staliunas, Traveling wave–standing wave competition in a generalized Swift–Hohenberg equation, Phys. Rev. E **57**, R4731 (1998). 9

130. M. Georgiou and P. Mandel, Transverse effects in a laser with an injected signal, Chaos, Solitons Fractals **4**, 1657 (1994). 9

131. S. Longhi, Transverse patterns in a laser with an injected signal, Phys. Rev. A **56**, 2397 (1997). 9

132. J. Nalik, L.M. Hoffer, G.L. Lippi, C. Vorgerd and W. Lange, Transverse optical bistability and formation of transverse structures in a sodium-filled Fabry–Pérot resonator, Phys. Rev. A **48**, R4237 (1992). 9

133. J.B. Geddes, J.V. Moloney, E.M. Wright and W.J. Firth, Polarization patterns in a nonlinear cavity, Opt. Commun. **111**, 623 (1994). 9

134. W.J. Firth, A.J. Scroggie, G.S. McDonald and L.A. Lugiato, Hexagonal patterns in optical bistability, Phys. Rev. A **46**, R3609 (1992). 9

135. V.B. Taranenko, C.O. Weiss and B. Schäpers, From coherent to incoherent hexagonal patterns in semiconductor resonators, Phys. Rev. A **65**, 013812 (2002). 9

136. D. Yu, W. Lu and R.G. Harrison, Origin of spiral wave formation in excitable optical systems, Phys. Rev. Lett. **77**, 5051 (1996). 9

137. D. Yu, W. Lu and R.G. Harrison, Dynamic bistability and spiral waves in a laser, J. Opt. B: Quantum Semiclass. Opt. **1**, 25 (1999). 9

138. P. Lodahl, M. Bache and M. Saffman, Spiral intensity patterns in the internally pumped optical parametric oscillator, Phys. Rev. Lett. **85**, 4506 (2000). 9

139. S. Longhi, Spiral waves in a class of optical parametric oscillators, Phys. Rev. E **63**, 055202 (2001). 9

140. P. Lodahl and M. Saffman, Pattern formation in singly resonant second-harmonic generation with competing parametric oscillation, Phys. Rev. A **60**, 3251 (1999). 10

141. S. Longhi, Hexagonal patterns in multistep optical parametric processes, Opt. Lett. **26**, 713 (2001). 10

142. M. Hoyuelos, D. Walgraef, P. Colet and M. San Miguel, Patterns arising from the interaction between scalar and vectorial instabilities in two-photon resonant Kerr cavities, Phys. Rev. E **65**, 046620 (2002). 10

143. M. Santagiustina, P. Colet, M. San Miguel and D. Walgraef, Noise-sustained convective structures in nonlinear optics, Phys. Rev. Lett. **79**, 3633 (1997). 10

144. H. Ward, M.N. Ouarzazi, M. Taki and P. Glorieux, Transverse dynamics of optical parametric oscillators in presence of walk-off, Eur. Phys. J. D **33**, 275 (1998). 10

145. M. Santagiustina, P. Colet, M. San Miguel and D. Walgraef, Walk-off and pattern selection in optical parametric oscillators, Opt. Lett. **23**, 1167 (1998). 10

146. S. Longhi, Nonadiabatic pattern formation in optical parametric oscillators, Phys. Rev. Lett. **84**, 5756 (2000). 10

147. S. Longhi, Transverse patterns in nondegenerate intracavity second-harmonic generation, Phys. Rev. A **59**, 4021 (1999). 10

148. S. Longhi, Quasipatterns in second-harmonic generation, Phys. Rev. E 59, R24 (1999). 10

149. M. Le Berre, A.S. Patrascu, E. Ressayre and A. Tallet, Daisy patterns in the passive ring cavity with diffusion effects, Opt. Commun. **123**, 810 (1996). 10

150. R. Herrero, E. Große Westhoff, A. Aumann, T. Ackemann, Yu.A. Logvin and W. Lange, Twelvefold quasiperiodic patterns in a nonlinear optical system with continuous rotational symmetry, Phys. Rev. Lett. **82**, 4627 (1999). 10

151. M. Vaupel, A. Maitre and C. Fabre, Observation of pattern formation in optical parametric oscillators, Phys. Rev. Lett. **83**, 5278 (1999). 10

152. S. Ducci, N. Treps, A. Maître, and C. Fabre, Pattern formation in optical parametric oscillators, Phys. Rev. A **64**, 023803 (2001). 10

153. K. Staliunas, G. Slekys and C.O. Weiss, Nonlinear pattern formation in lasers: shocks, domains of tilted waves, and cross-roll patterns, Phys. Rev. Lett. **79**, 2658 (1997). 10

154. K. Staliunas, Three-dimensional Turing structures and spatial solitons in optical parametric oscillators, Phys. Rev. Lett. **81**, 81 (1998). 10

155. M. Tlidi, M. Haelterman and P. Mandel, Three-dimensional structures in diffractive and dispersive nonlinear cavities, Quantum Semiclass. Opt. **10**, 869 (1998). 10

156. M. Tlidi, Three-dimensional crystals and localized structures in diffractive and dispersive nonlinear ring cavities, J. Opt. B: Quantum Semiclass. Opt. **2**, 438 (2000). 10

157. M. Tlidi, M. Haelterman and P. Mandel, 3D patterns and pattern selection in optical bistability, Europhys. Lett. **42**, 505 (1998). 10

158. M. Tlidi and P. Mandel, Three-dimensional optical crystals and localized structures in cavity second harmonic generation, Phys. Rev. Lett. **83**, 4995 (1999). 10

159. J. Garcia-Ojalvo and J.M. Sancho, *Noise in Spatially Extended Systems* (Springer, New York, 1999). 11

160. R.J. Deissler, External noise and the origin and dynamics of structure in convectively unstable systems, J. Stat. Phys. **54**, 1459 (1989). 11

161. J. Garcia-Ojalvo, A. Hernandez-Machado and J.M. Sancho, Effects of external noise on the Swift–Hohenberg equation, Phys. Rev. Lett. **71**, 1542 (1993). 11

162. R. Mueller, K. Lippert, A. Kuehnel and U. Behn, First-order nonequilibrium phase transition in a spatially extended system, Phys. Rev. E **56**, 2658 (1997). 11

163. L.A. Lugiato and A. Gatti, Spatial structure of a squeezed vacuum, Phys. Rev. Lett. **70**, 3868 (1993). 11

164. A. Gatti, H. Wiedermann, L.A. Lugiato, I. Marzoli, G.L. Oppo and S.M. Barnett, Langevin treatment of quantum fluctuations and optical patterns in optical parametric oscillators below threshold, Phys. Rev. A **56**, 877 (1997). 11

165. R. Zambrini, M. Hoyuelos, A. Gatti, P. Colet, L. Lugiato and M. San Miguel, Quantum fluctuations in a continuous vectorial Kerr medium model, Phys. Rev. A **62**, 063801 (2000). 11

166. J. Viñals, E. Hernández-Garcia, M. San Miguel and R. Toral, Numerical study of the dynamical aspects of pattern selection in the stochastic Swift–Hohenberg equation in one dimension, Phys. Rev. A **44**, 1123 (1991). 11

167. K.R. Elder, J. Viñals and M. Grant, Ordering dynamics in the two-dimensional stochastic Swift-Hohenberg equation, Phys. Rev. Lett. **68**, 3024 (1992). 11

168. A.V. Mamaev, M. Saffman, D.Z. Anderson and A.A. Zozulya, Propagation of light beams in anisotropic nonlinear media: from symmetry breaking to spatial turbulence, Phys. Rev. A **54**, 870 (1996). 11

169. K. Hayata and M. Koshiba, Multidimensional solitons in quadratic nonlinear media, Phys. Rev. Lett. **71**, 3275 (1993). 11

170. W.E. Torruellas, Z. Wang, D.J. Hagan, E.W. VanStryland, G.I. Stegemann, L. Torner and C.R. Menyuk, Observation of two-dimensional spatial solitary waves in a quadratic medium, Phys. Rev. Lett. **74**, 5036 (1995). 11

171. D. Mihalache, D. Mazilu, L.C. Crasovan, L. Torner, B.A. Malomed and F. Lederer, Three-dimensional walking spatiotemporal solitons in quadratic media, Phys. Rev. E **62**, 7340 (2000). 11

172. J.J. García-Ripoll, V.M. Pérez-García, E. A. Ostrovskaya and Y. S. Kivshar, Dipole-mode vector solitons, Phys. Rev. Lett. **85**, 82 (2000). 11

173. D.V. Skryabin and W.J. Firth, Generation and stability of optical bullets in quadratic nonlinear media, Opt. Commun. **148**, 79 (1998). 11

174. M. Mitchell, M. Segev and D.N. Christodoulides, Observation of Multihump Multimode Solitons, Phys. Rev. Lett. **80**, 4657 (1998). 11

175. G.I. Stegemann and M. Segev, Optical spatial solitons and their interactions: universality and diversity, Science **286**, 1518 (1999). 11

176. Y.S. Kivshar and X. Yang, Dynamics of dark solitons, Chaos, Solitons Fractals **4**, 174 (1994). 11

177. M. Haelterman and A.P. Sheppard, Polarization domain walls in diffractive or dispersive Kerr media, Opt. Lett. **19**, 96 (1994). 11

178. M. Haelterman and A.P. Sheppard, Bifurcations of the dark soliton and polarization domain walls in Kerr media, Phys. Rev. E **49**, 4512 (1994). 11

179. A.P. Sheppard and M. Haelterman, Polarization-domain solitary waves of circular symmetry in Kerr media, Opt. Lett. **19**, 859 (1994). 11

180. M. Haelterman and Y. Louis, Optical domain walls in atomic vapors, J. Nonlin. Opt. Phys. Mat. **5**, 447 (1996). 11

181. A.V. Mamaev, M. Saffman and A.A. Zozulya, Propagation of dark stripe beams in nonlinear media: snake instability and creation of optical vortices, Phys. Rev. Lett. **76**, 2262 (1996). 11

182. D. Neshev, A. Dreischuh, V. Kamenov, I. Stefanov, S. Dinev, W. Fließer and L. Windholz, Generation and intrinsic dynamics of ring dark solitary waves, Appl. Phys. B **64**, 429 (1997). 11

183. A. Dreischuh, G.G. Paulus and F. Zacher, Quasi-two-dimensional dark spatial solitons and generation of mixed phase dislocations, Appl. Phys. B **69**, 107 (1999). 11

184. A. Dreischuh, S. Chervenkov, D. Neshev, G.G. Paulus and H. Walther, Generation of lattice structures of optical vortices, J. Opt. Soc. Am. B **19**, 550 (2002). 11

185. V. Basistiy, V.Yu. Bazhenov, N.S. Soskin and M.V. Vasnetsov, Optics of light beams with screw dislocations, Opt. Commun. **103**, 422 (1993). 11

186. G.A. Swartzlander and C.T. Law, Optical vortex solitons observed in Kerr nonlinear media, Phys. Rev. Lett. **69**, 2503 (1992). 11

187. G.A. Swartzlander and C.T. Law, The optical vortex soliton, Opt. Photon. News **4**, 10 (1993). 11

188. G.A. Swartzlander and C.T. Law, Polarized optical vortex solitons: Instabilities and dynamics in Kerr nonlinear media, Chaos, Solitons Fractals **4**, 1759 (1994). 11

189. K.T. Gahagan and G.A. Swartzlander, Optical vortex trapping of particles, Opt. Lett. **21**, 827 (1996). 11

190. G.A. Swartzlander, C.T Law and D. Rozas, Propagation dynamics of optical vortices, J. Opt. Soc. Am. B **14**, 3054 (1997). 11

191. G.A. Swartzlander, D. Rozas and Z.S. Sacks, Experimental observation of fluidlike motion of optical vortices, Phys. Rev. Lett. **79**, 3399 (1997). 11

192. G.A. Swartzlander, Z.S. Sacks and D. Rozas, Holographic formation of optical-vortex filaments, J. Opt. Soc. Am. B **15**, 2226 (1998). 11

193. G.A. Swartzlander, Nonlinear optical catastrophe from a smooth initial beam, Opt. Lett. **24**, 1224 (1999). 11

194. D. Rozas and G.A Swartzlander, Observed rotational enhancement of nonlinear optical vortices, Opt. Lett. **25**, 126 (2000). 11

195. Y.S. Kivshar and E.A. Ostrovskaya, Optical vortices, Opt. Photon. News **12**, 27 (2001). 11

196. B. Luther-Davies, J. Christou, V. Tikhonenko and Y.S. Kivshar, Optical vortex solitons: experiment versus theory, J. Opt. Soc. Am. B **14**, 3045 (1997). 11

197. W.J. Firth and C. Pare, Transverse modulational instabilities for counterpropagating beams in Kerr media, Opt. Lett. **13**, 1096 (1988). 11

198. G. Grynberg, E. Le Bihan, P. Verkerk, P. Simoneau, J.R.R. Leite, D. Bloch, S. Le Boiteaux and M. Ducloy, Observation of instabilities due to mirrorless four-wave mixing oscillation in sodium, Opt. Commun. **67**, 363 (1988). 11

199. G. Grynberg and J. Paye, Spatial instability for a standing wave in a nonlinear medium, Europhys. Lett. **8**, 29 (1989). 11

200. M. Haelterman, A.P. Sheppard and A.W. Snyder, Bimodal counterpropagating spatial solitary-waves, Opt. Commun. **103**, 145 (1993). 11

201. M. Saffman, A.A. Zozulya and D.Z. Anderson, Transverse instability of energy-exchanging counterpropagating waves in photorefractive media, J. Opt. Soc. Am. B **11**, 1409 (1994). 11

202. J.B. Geddes, R.A. Indik, J.V. Moloney and W.J. Firth, Hexagons and squares in a passive nonlinear optical system, Phys. Rev. A **50**, 3471 (1994). 11

203. P.M. Lushnikov and A.V. Mamaev, Spontaneous hexagon formation in photorefractive crystal with a single pump wave, Opt. Lett. **24**, 1511 (1999). 11, 12

204. M. Schwab, C. Denz and M. Saffman, Transverse modulational instability in counterpropagating two-wave mixing with frequency detuning of the pump beams, J. Opt. Soc. Am. B **18**, 628 (2001). 11

205. S. Pitois, G. Millot and S. Wabnitz, Polarization domain wall solitons with counterpropagating laser beams, Phys. Rev. Lett. **81**, 1409 (1998). 11

206. W.J. Firth, Spatial instabilities in a Kerr medium with a single feedback mirror, J. Mod. Opt. **37**, 151 (1991).   12
207. G.P. D'Alessandro and W.J. Firth, Spontaneous hexagon formation in a nonlinear optical medium with feedback mirror, Phys. Rev. Lett. **66**, 2597 (1991).   12, 13
208. G. D'Alessandro, E. Pampaloni, P.L. Ramazza, S. Residori and F.T. Arecchi, Amplitude equations and pattern formation in a liquid crystal light valve experiment, Phys. Rev. A **52**, 4176 (1995).   12
209. A.J. Scroggie and W.J. Firth, Pattern formation in an alkali-metal vapour with a feedback mirror, Phys. Rev. A **53**, 2752 (1996).   12
210. M.A. Vorontsov and A.Yu. Karpov, Pattern formation due to interballoon spatial mode coupling, J. Opt. Soc. Am. B **14**, 34 (1997).   12
211. G. Giusfredi, J.F. Valley, R. Pon, G. Khitrova and H.N. Gibbs, Optical instabilities in sodium vapor, J. Opt. Soc. Am. B **5**, 1181 (1988).   12
212. W. Lange, Yu.A. Logvin and T. Ackemann, Spontaneous optical patterns in an atomic vapor: observation and simulation, Physica D **96**, 230 (1996).   12
213. M.A. Vorontsov and A.Y. Karpov, Stimulated optical patterns in a Kerr slice-feedback mirror-type experiment, J. Mod. Opt. **44**, 439 (1997).   12
214. C. Denz, M. Schwab, M. Sedlatschek, T. Tschudi and T. Honda, Pattern dynamics and competition in a photorefractive feedback system, J. Opt. Soc. Am. B **15**, 2057 (1998).   12
215. M. Kreuzer, A. Schreiber and B. Thüring, Evolution and switching dynamics of solitary spots in nonlinear optical feedback system, Mol. Cryst. Liq. Cryst. **282**, 91 (1996).   12
216. A. Schreiber, B. Thuring, M. Kreuzer and T. Tschudi, Experimental investigation of solitary structures in a nonlinear optical feedback system, Opt. Commun. **136**, 415 (1997).   12
217. M. Kreuzer, B. Thüring and T. Tschudi, Creation, dynamics and stability of localized states in a nonlinear optical feedback system, Asian J. Phys. **7**, 678 (1998).   12
218. Yu.A. Logvin, B. Schäpers and T. Ackemann, Stationary and drifting localized structures near a multiple bifurcation point, Phys. Rev E **61**, 4622 (2000).   12
219. B. Schäpers, M. Feldmann, T. Ackemann and W. Lange, Interaction of localized structures in an optical pattern-forming system, Phys. Rev. Lett. **85**, 748 (2000).   12, 13
220. S.A. Akhmanov, M.A. Vorontsov, V.Yu. Ivanov, A.V. Larichev and N.I. Zheleznik, Controlling transverse wave interactions in nonlinear optics: generation and interaction of spatiotemporal structures, J. Opt. Soc. Am. B **9**, 78 (1992).   14
221. M.A. Vorontsov, N.G. Iroshnikov and R.L. Abernathy, Diffractive patterns in a nonlinear optical system with spatial interaction, Chaos, Solitons Fractals **4**, 1701 (1994).   14
222. N.I. Zheleznik, M. Le Berre, F. Ressayre and A. Tallet, Rotating spiral waves in a nonlinear optical system with spatial interaction, Chaos, Solitons Fractals **4**, 1717 (1994).   14
223. M.A. Vorontsov and W.J. Firth, Pattern formation and competition in nonlinear optical systems with two-dimensional feedback, Phys. Rev. A **49**, 2891 (1994).   14

224. M.A. Vorontsov and B.A. Samson, Nonlinear dynamics in an optical system with controlled two-dimensional feedback: black-eye patterns and related phenomena, Phys. Rev. A **57**, 3040 (1998).   13, 14

225. B.A. Samson and M.A. Vorontsov, Localized states in a nonlinear optical system with a binary-phase slice and a feedback mirror, Phys. Rev. A **56**, 1621 (1997).   14

226. E. Pampaloni, S. Residori and F.T. Arecchi, Roll–hexagon transition in a Kerr-like experiment, Europhys. Lett. **24**, 647 (1993).   14

227. E. Pampaloni, P.L. Ramazza, S. Residori and F.T. Arecchi, Experimental evidence of boundary-induced symmetries in an optical system with a Kerr-like nonlinearity, Europhys. Lett. **25**, 587 (1994).   14

228. F.T. Arecchi, A.V. Larichev, P.L. Ramazza, S. Residori, J.C. Ricklin and M.A. Vorontsov, Experimental observation of space–time chaos in a nonlinear optical system with 2D feedback, Opt. Commun. **117**, 492 (1995).   14

229. P.L. Ramazza, S. Residori, E. Pampaloni and A.V. Larichev, Transition to space–time chaos in a nonlinear optical system with two-dimensional feedback, Phys. Rev. A **53**, 400 (1996).   14

230. P.L. Ramazza, S. Ducci and F.T. Arecchi, Optical diffraction-free patterns induced by a discrete translational transport, Phys. Rev. Lett. **81**, 4128 (1998).   14

231. E. Pampaloni, P.L. Ramazza, S. Residori and F.T. Arecchi, Two-dimensional crystals and quasicrystals in nonlinear optics, Phys. Rev. Lett. **74**, 258 (1995).   14, 15

232. S. Residori, P.L. Ramazza, E. Pampaloni, S. Boccaletti and F.T. Arecchi, Domain coexistence in two dimensional optical patterns, Phys. Rev. Lett. **76**, 1063 (1996).   14

233. E. Pampaloni, S. Residori, S. Soria and F.T. Arecchi, Phase locking in nonlinear optical patterns, Phys. Rev. Lett. **78**, 1042 (1997).   14

234. P.L. Ramazza, S. Boccaletti, A. Giaquinta, E. Pampaloni, S. Soria and F.T. Arecchi, Optical pattern selection by lateral wavefront shift, Phys. Rev. A **54**, 3472 (1996).   14

235. P.L. Ramazza, S. Boccaletti and F.T. Arecchi, Transport induced patterns in an optical system with focussing nonlinearity, Opt. Commun. **136**, 267 (1997).   14

236. P.L. Ramazza, E. Benkler, U. Bortolozzo, S. Boccaletti, S. Ducci and F.T. Arecchi, Tailoring the profile and interactions of optical localized structures, Phys. Rev. E **65**, 066204 (2002).   15

2 Order Parameter Equations for Lasers

Order parameter equations are the simplest (minimal) equations that describe, in the leading order, the dynamics of the field in broad-aperture lasers and other nonlinear optical systems. This chapter is devoted to the derivation of OPEs for lasers.

The OPEs have a twofold significance in studying the formation and evolution of transverse patterns in nonlinear optics. First, they usually allow a simplification of the analytical and numerical treatment, since the OPEs are structurally simpler than the initial (microscopic) equations. The OPEs are often obtained in the form of the complex Ginzburg–Landau or the complex Swift–Hohenberg equation. These equations have been intensively studied in recent years outside optics, and their properties are well, although not completely, known. Thus, a reduction to these equations solves a part of the problem [1].

Second, the OPEs allow one to consider the patterns in a particular system (in our case, a laser) from a general point of view. As shown below, the reduced laser equations in some limits are similar to the hydrodynamic (Navier–Stokes) equation. In the other limit (a class B laser), the reduced equations are similar to those derived for oscillatory chemical and biological systems. Thus the derivation of OPEs allows one to demonstrate an analogy between nonlinear optics and hydrodynamics in one limit, and between nonlinear optics and oscillatory chemical systems in the other limit. A knowledge of the existence of vortices in superfluids allows one to predict vortices in nonlinear optics thanks to the optics–hydrodynamics analogy, and similarly a knowledge of "self-sustained meandering" of spiral waves in oscillatory or excitable systems provides a motivation to look for the "restless vortex" in class B lasers.

We start from a semiclassical model of a laser, the Maxwell–Bloch (MB) system of equations, which includes transverse degrees of freedom. We then reduce the MB system using two alternative methods: adiabatic elimination (Sect. 2.3.1) and the multiscale expansion technique (Sect. 2.3.2). We deal in this chapter with class A and class C lasers, since these cases lead to a single OPE in the form of the CGL or CSH equation. The study of a class B laser (a laser with relatively slow population inversion) is postponed to

Chap. 7, since this class of laser leads to more complicated OPEs, and to richer dynamics than those of class A and class C lasers.

2.1 Model of a Laser

Our starting point is the semiclassical Maxwell–Bloch (MB) equation system, which describes many types of lasers with transverse degrees of freedom:

$$\frac{\partial E}{\partial t} = \kappa \left[-(1 + \mathrm{i}\omega) E + P + \mathrm{i} d \nabla^2 E \right], \tag{2.1a}$$

$$\frac{\partial P}{\partial t} = -\gamma_\perp (P - ED), \tag{2.1b}$$

$$\frac{\partial D}{\partial t} = -\gamma_\parallel \left(D - D_0 + \frac{1}{2} (EP^* + E^* P) \right). \tag{2.1c}$$

The complex fields $E(\boldsymbol{r}, t)$ and $P(\boldsymbol{r}, t)$ are the envelopes of the electromagnetic (optical) field and of the polarization, and $D(\boldsymbol{r}, t)$ is the real valued field of the population inversion, which in the absence of stimulated radiation is equal to its unsaturated value $D_0(\boldsymbol{r})$. κ is the relaxation rate of the optical field in the resonator due to the (small) transmittivity of the mirrors and to linear losses in the resonator; $\gamma_\perp$ and $\gamma_\parallel$ are the decay rates of the polarization and population inversion, respectively. Finally, ω is the resonator detuning (the detuning of the resonance frequency of the corresponding longitudinal mode with respect to the center of gain line).

It is assumed that the optical field $E(\boldsymbol{r}, t)$ is linearly polarized, and the gain line is homogeneously broadened. It is also assumed that only one longitudinal mode family is excited. Otherwise, there would be a dependence on the longitudinal coordinate z, and not only a dependence on the time t and on the transverse coordinates $\boldsymbol{r} = (x, y)$ as in (2.1).

The system (2.1) describes a laser with multiple transverse modes but a single longitudinal mode. The evolution in time is assumed to occur on a timescale much slower than the round-trip time of the light in the cavity; otherwise, the assumption of a single longitudinal mode would be invalid.

The diffraction term is related to the spatial degrees of freedom. This term, being nonlocal, couples the field throughout the cross section of the laser, and is responsible for the collective behavior of the laser radiation.

The simplest limit of the Maxwell–Bloch system (2.1) is the class A laser, in which the polarization and population inversion are fast compared with the optical field in the resonator. In this limit, sometimes called the "good cavity limit", the fast material variables can be adiabatically eliminated, and a relatively simple order parameter equation can be obtained. A straightforward adiabatic elimination has been performed in this case in [2]. Although many pattern-forming properties of lasers are lost in this adiabatic elimination, let us start from this procedure.

It is assumed that the material variables decay fast, i.e. $\kappa/\gamma_\perp = \mathcal{O}(\varepsilon)$ and $\kappa/\gamma_\parallel = \mathcal{O}(\varepsilon)$, where ε is a smallness parameter, and that the temporal derivatives of all variables have finite values, i.e. $\partial E/\partial t \sim \partial P/\partial t \sim \partial D/\partial t = \mathcal{O}(1)$. Multiplying both sides of (2.1b) and (2.1c) by $\kappa/\gamma_\perp$ and $\kappa/\gamma_\parallel$, respectively, we obtain the result that the left-hand sides of both equations are of order $\mathcal{O}(\varepsilon)$. Keeping only the terms of zero order $\mathcal{O}(1)$, we can eliminate the material variables from (2.1b) and (2.1c), and obtain

$$D = \frac{D_0}{1 + |E|^2}, \quad P = \frac{D_0 E}{1 + |E|^2}. \tag{2.2}$$

The expressions (2.2) imply that the material variables P and D follow instantaneously, or adiabatically, the changes of the field variable E. Inserting (2.2) into (2.1a) we obtain a single equation for the field,

$$\frac{\partial E}{\partial \tau} = -E + \frac{D_0 E}{1 + |E|^2} + \mathrm{i}\left(a\nabla^2 - \omega\right)E, \tag{2.3}$$

where $\tau = \kappa t$ is a slow time. Close to the emission threshold $p = (D_0 - 1) \ll 1$, the emitted fields are relatively weak, $|E|^2 \ll 1$, which allows a cubic approximation for the nonlinear term in (2.3),

$$\frac{\partial E}{\partial t} = pE + \mathrm{i}\left(a\nabla^2 - \omega\right)E - E|E|^2; \tag{2.4}$$

this is the complex Ginzburg–Landau equation. In (2.4), p is the balance between the gain and loss of the laser, and is a criticality parameter of the CGL.

The CGL equation is a crude approximation for a laser. For instance, the selection of transverse wavenumber (transverse mode) is not accounted for by (2.4). A linear stability analysis of the zero (nonlasing) solution of (2.4) leads to equal growth exponents of all the components of the spatial spectrum, which can be easily checked by inserting a test solution in the form of a tilted wave, $E(\boldsymbol{r}, t) = e \exp(\mathrm{i}\boldsymbol{k} \cdot \boldsymbol{r} + \lambda t)$, with a small amplitude e, linearizing it with respect to e, and calculating the exponent λ. Here $\boldsymbol{k} = \boldsymbol{k}_\perp$ is the transverse wavenumber, or, in other words, the transverse component of the wavevector tilted with respect to the optical axis of the resonator. The value of λ is independent of the transverse wavenumber $k = |\boldsymbol{k}|$ and is equal to $\lambda = p = D_0 - 1$.

It is well known, however, that lasers emit particular transverse modes (transverse wavenumbers) that depend on the length of the resonator. When the maximum of the gain line coincides with a particular transverse mode family (Fig. 2.1), the corresponding transverse mode is favored, and grows the fastest. This tunability property of the laser is lost in the derivation of (2.4). It is not difficult to understand why spatial-frequency selection is absent in (2.4): the derivation assumes, among other things, the condition $\gamma_\perp/\kappa \to \infty$,
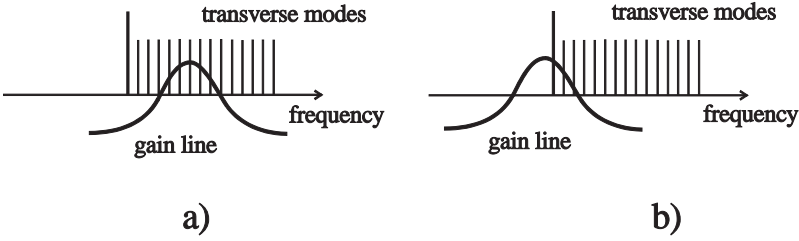
Fig. 2.1. Transverse modes of the resonator and the gain line of the amplifying medium of a laser. In the resonator length is varied, the transverse modes are shifted with respect to the gain line, which allows the tuning of the modes. By increasing the resonator length, one tunes to higher-order transverse mode families (**a**). This corresponds to a negative detuning parameter ω in (2.1). By decreasing the resonator length, one excites the lower-order transverse mode families (**b**). This corresponds to a positive detuning

which means that the gain line is infinitely broad. An infinitely broad gain line obviously cannot cause a transverse frequency selection. In order to account for the spatial-frequency selection a more sophisticated derivation of the laser OPE is required, which is the subject of the following sections.

To continue with the derivation of a more precise OPE a linear stability analysis of the laser equations is useful.

2.2 Linear Stability Analysis

A standard technique is applied here to investigate the stability of the non-lasing solution of (2.1), given by $E(\boldsymbol{r},t) = 0$, $P(\boldsymbol{r},t) = 0$, $D(\boldsymbol{r},t) = D_0$. By perturbing this trivial zero solution by $E(\boldsymbol{r},t) = e \exp(\mathrm{i}\boldsymbol{k} \cdot \boldsymbol{r} + \lambda t)$, $P(\boldsymbol{r},t) = p \exp(\mathrm{i}\boldsymbol{k} \cdot \boldsymbol{r} + \lambda t)$ and $D(\boldsymbol{r},t) = D_0 + d \exp(\mathrm{i}\boldsymbol{k} \cdot \boldsymbol{r} + \lambda t)$, inserting it into (2.1) and gathering the linear terms with respect to e, p and d, we obtain

$$\lambda e = -\mathrm{i}\kappa \left(\omega + ak^2\right) e - \kappa e + \kappa p \,, \tag{2.5a}$$

$$\lambda p = -\gamma_\perp p + \gamma_\perp e D_0 \,, \tag{2.5b}$$

$$\lambda d = -\gamma_\parallel d \,. \tag{2.5c}$$

The last equation in (2.5) is not coupled to the rest, and therefore the calculation of one λ-branch is trivial: $\lambda_3 = -\gamma_\parallel$. The solution of the secular equation (the solvability condition of (2.5) with respect to e and p) gives two other branches of the growth exponent:

$$\lambda_{1,2}\left(\Delta\omega\right) = -\frac{\kappa + \gamma_\perp + \mathrm{i}\kappa\,\Delta\omega}{2} \pm \frac{1}{2}\sqrt{\left(\kappa - \gamma_\perp + \mathrm{i}\kappa\,\Delta\omega\right)^2 + 4\gamma_\perp\kappa D_0}\,. \tag{2.6}$$
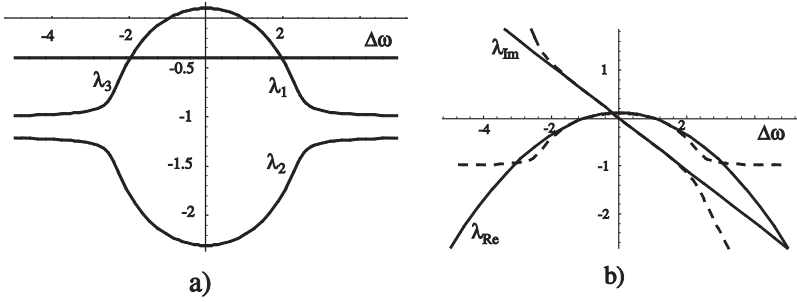
Fig. 2.2. The real parts of the three Lyapunov growth exponents depending on the transverse wavenumber for the MB equations (2.1) with $\kappa = 1$, $\gamma_\perp = 1.2$ and $\gamma_\parallel = 0.4$. The λ_3 branch is associated with the decay of the population inversion, and is the horizontal straight line. b) The real and imaginary part of the most relevant (upper) branch of the Lyapunov growth exponents (2.6) - dashed curves, and their Taylor expansions (2.8) - solid curves.

Here $\Delta\omega = \omega + ak^2$ is proportional to the deviation of the mode with transverse wavenumber k from its resonant value, $\omega_{\mathrm{res}} = -ak^2$. Figure 2.2 illustrates the dependence given by (2.6).

From (2.6), the threshold for the laser emission (which occurs when $\lambda = 0$) is

$$D_0 = 1 + \frac{\kappa^2}{\left(\kappa + \gamma_\perp\right)^2}\Delta\omega^2 . \tag{2.7}$$

A simplification of (2.1) is possible when only one λ-branch is relevant to the dynamics of the system. This occurs, in particular, for class A and class C lasers close to the emission threshold. In this case the other two branches (the eigenvalue given by (2.6) with the negative sign, and also the straight line $\lambda = -\gamma_\parallel$ associated with the relaxation of population inversion) lie deep below the zero axis, and the dynamics related to these branches are enslaved by the dynamics related to the upper branch. We can expand the upper λ-branch in a Taylor series around its maximum, which gives

$$\frac{\kappa + \gamma_\perp}{\kappa\gamma_\perp}\lambda(\Delta\omega) = p - \mathrm{i}\,\Delta\omega - \frac{\kappa^2}{\left(\kappa + \gamma_\perp\right)^2}\Delta\omega^2. \tag{2.8}$$

This is plotted in Fig. 2.2b as the solid curves.

The growth rate (2.8) is obtained by assuming that $\Delta\omega$ is of $\mathcal{O}(\varepsilon)$ and $p = (D_0 - 1)$ is of $\mathcal{O}(\varepsilon^2)$. In this case the truncation of the Taylor series at $\mathcal{O}(\varepsilon^3)$ leads to (2.8). It is also possible to perform the Taylor expansion under different smallness assumptions, which leads to slightly different expressions.

The linear stability analysis predicts the initial stage of evolution of the radiation from the initial (thermal or quantum) noise. To illustrate the dynamics predicted by (2.8), the Maxwell–Bloch system (2.1) was integrated

numerically, starting from a random field distribution in space. A series of
plots illustrating the evolution of the field in the linear stage is given in
Figs. 2.3 and 2.4. A discrimination against nonresonant components in the
spatial spectrum is clearly seen: either a central spot (Fig. 2.3) or a reso-
nant ring (Fig. 2.4) emerges from the initial broadband spatial spectrum,
depending on the detuning of the resonator. The radius of the resonant ring
is given by $k^2 = -\omega/a$, in accordance with the results of the linear stabil-
ity analysis (2.6). In the spatial domain, structures with a particular spatial
scale develop, which is related to the radius of the resonant ring; this scale is
$l = 2\pi/k = 2\pi/\sqrt{-a/\omega}$.

The linear stability analysis allows us to write down a model equation
that describes the linear stage of the field evolution. Recall that, in the linear
stability analysis, one substitutes the time evolution operator $\partial/\partial t$ by λ, and
the Laplace operator ∇^2 by $-k^2$. The opposite substitution (i.e. the substi-
tution in (2.8) of the algebraic variables by their corresponding operators)
leads to

$$\frac{\partial A}{\partial \tau} = pA + i\left(a\nabla^2 - \omega\right)A - \frac{\kappa^2}{\left(\kappa + \gamma_\perp\right)^2}\left(a\nabla^2 - \omega\right)^2 A\,, \qquad (2.9)$$

where $A(\boldsymbol{r}, \tau)$ is the order parameter related to the optical field in the laser
resonator (the relation between $A(\boldsymbol{r}, \tau)$ and $E(\boldsymbol{r}, t)$ is obtained in the next
section), and τ is a normalized time, $\tau = t\kappa\gamma_\perp/(\kappa + \gamma_\perp)$.

The last plots in Figs. 2.3 and 2.4 correspond to the nonlinear stage of the
evolution. Here the wavevectors from the resonant spot and from the reso-
nant ring, respectively, start to compete. Also, a nonlinear broadening of the
resonant ring (Fig. 2.4) or of the central spot (Fig. 2.3) occurs. The ring in
the spatial spectral domain (Fig. 2.4) can split into a few spots: one spot cor-
responds to a single tilted wave; two symmetrically placed spots correspond
to two counterpropagating tilted waves; several spots placed irregularly on
the ring correspond to domains of differently directed tilted waves; and four
spots correspond to a more fundamental pattern, the cross-roll, or square
vortex lattice pattern. The nonlinear patterns will be discussed in detail in
the following chapters. The linear theory can say nothing about the symme-
try of the nonlinear pattern: the last plots in Figs. 2.3 and 2.4 are beyond
the predictions of the linear order parameter equation (2.8). From the linear
theory (linear stability analysis), one can learn only that the most favored
modes (or wavenumbers) have a particular value that depends on the de-
tuning. The spatial spectral components grow to infinity, since there is no
mechanism to prevent their exponential growth in this linear theory. There
is no competition between wavevectors in the framework of the linear theory.
To retrieve the correct nonlinear picture of the evolution, one needs to close
the linear evolution equation (2.8) with some saturating nonlinear terms.

This closure is performed in the following sections in two different ways,
both using results from the linear stability analysis. One possibility is the
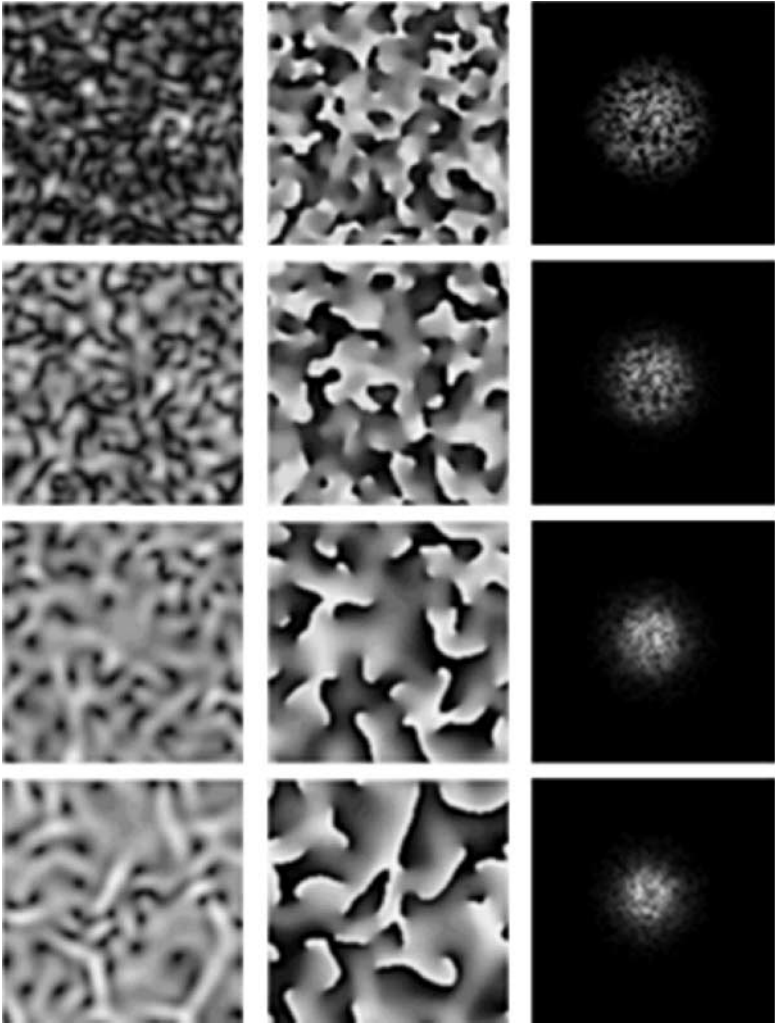
Fig. 2.3. Linear stage of spatial pattern formation for zero detuning. The intensity, the phase and the spatial Fourier spectra of the field are shown in the *left*, *center* and *right columns* respectively. The calculations start from a random distribution of the optical field (with a broadband spatial spectrum). The parameters used were $\omega = 0$, $\kappa = 1$, $\gamma_\perp = 2$, $\gamma_\parallel = 10$ and $a = 0.0005$. The integration was performed with periodic boundary conditions in a region of unit size. Time increases from *top* to *bottom row*. Plots are given at times $t = 0.5$, where there is essentially a speckle field of the laser radiation; $t = 2.5$, where the spot in the Fourier domain starts to narrow (filtering of the spatial spectrum occurs); $t = 7.5$, where the resonant spot continues narrowing, and regularization in the near field occurs (the vortex structure is more pronounced); and $t = 25$, where a nonlinear "vortex glass" structure develops. The spot in the far field does not narrow any further (its narrowing due to linear effects is compensated by nonlinear broadening)
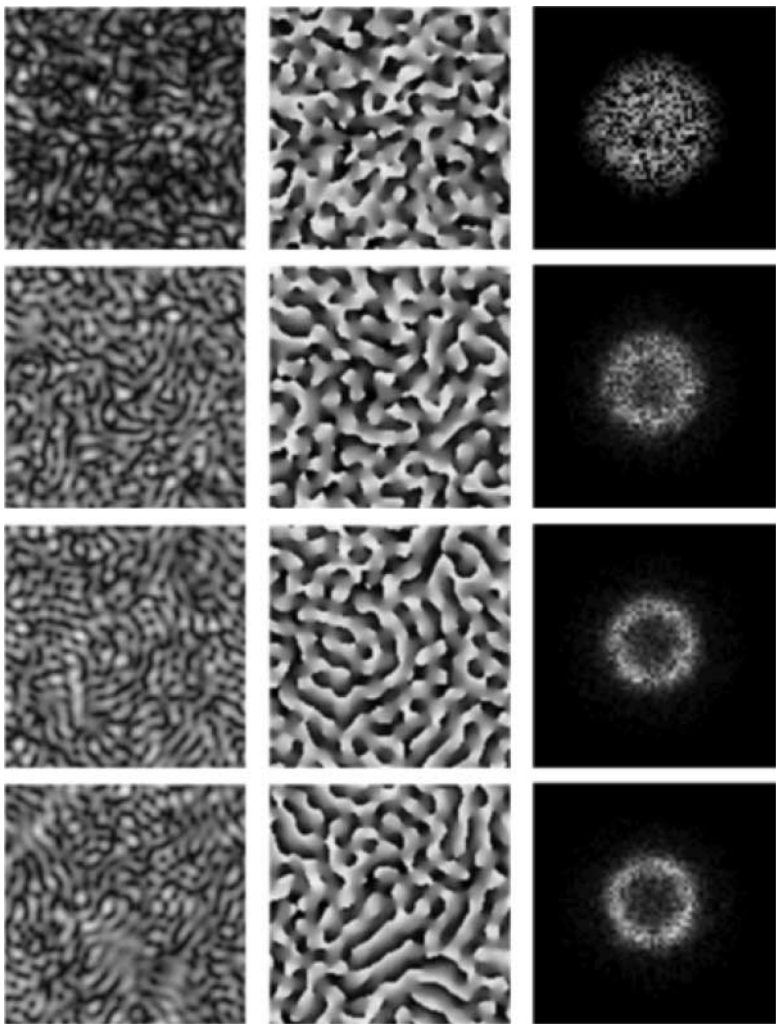
Fig. 2.4. Linear stage of spatial pattern formation for finite negative detuning. The parameters and initial conditions are as in Fig. 2.3 except for the detuning $\omega = -2$. Plots are given at times $t = 1$, where there is essentially a speckle field of the laser radiation; $t = 5$, where the resonant ring starts to emerge in the far field; $t = 15$, where the resonant ring narrows, and the field distribution in the near field seems to be more regular; and $t = 25$, where different components from the ring start to compete. In the near field the domains of tilted waves (the areas of relatively homogeneous distribution) start to emerge

adiabatic elimination technique [2, 3]. The other is the multiscale expansion technique, as developed in [4] for the laser.

2.3 Derivation of the Laser Order Parameter Equation

The order parameter equation for a laser is derived in this section. For completeness, two techniques of derivation are used, adiabatic elimination and the multiscale expansion, both leading to the same result. Physically, both derivations have the same purpose: to get rid of unnecessary degrees of freedom. This is illustrated in Fig. 2.5, where it is symbolically shown how the dynamics in the three-dimensional phase space can be reduced to dynamics in a two-dimensional space by a suitable transformation of the coordinate system. In general, the derivation of an order parameter equation is always related to a reduction of the dimension of the original problem: $R^n \rightarrow R^m$, with $m < n$.
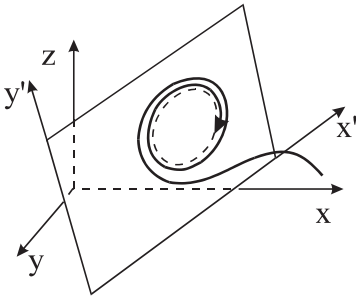
Fig. 2.5. A dimension reduction is achieved by a suitable transformation of the coordinate system

2.3.1 Adiabatic Elimination

The adiabatic-elimination (AE) technique consists of the following steps:

1. Linear stability analysis. In this stage, the eigenvalues are calculated and the corresponding eigenvectors are determined. The eigenvectors are mutually orthogonal with respect to the linear part of the equation system.
2. The initial nonlinear equation system is rewritten in the basis of the eigenvectors of the corresponding linearized problem. Owing to the nonlinear terms, the eigenvectors are mutually coupled.
3. The eigenvectors with negative eigenvalues are adiabatically eliminated from the corresponding equations. It is assumed that the eigenvectors with negative eigenvalues are dominated by the eigenvectors with positive eigenvalues.

This procedure leads to an order parameter equation. We illustrate how the adiabatic-elimination technique described above works for the special case of a class C laser, when the relaxation rates for the optical field and the polarization are equal, i.e. $\kappa = \gamma_\perp$. This simplifies the problem from an algebraic point of view, without losing generality.

The eigenvalues of the linearized problem (2.6), under the assumption $\kappa = \gamma_\perp$, simplify to

$$\lambda_{1,2}\left(\Delta\omega\right) = -\kappa\frac{2 + \mathrm{i}\,\Delta\omega \pm \sqrt{4D_0 - \Delta\omega^2}}{2}\,, \tag{2.10}$$

where $\Delta\omega = \omega - a\nabla^2$ is an operator, unlike the case for (2.6), where the Laplace operator ∇^2 was substituted by $-k^2$.

The linear stability analysis can be rewritten in a more convenient matrix form. In the matrix representation, the linearized equations (2.5a) and (2.5b) are expressed in the following way:

$$\frac{\partial \boldsymbol{e}}{\partial t} = \mathcal{L}\boldsymbol{e}\,, \tag{2.11}$$

where $\boldsymbol{e} = (e, p)^{\mathrm{T}}$ is the state vector of the system, and

$$\mathcal{L} = \kappa \begin{pmatrix} -1 - \mathrm{i}\,\Delta\omega & 1 \\ D_0 & -1 \end{pmatrix} \tag{2.12}$$

is the linear evolution matrix. The linear stability analysis is nothing but a procedure of diagonalization of the linear evolution matrix $\mathcal{L}$. Multiplying (2.11) from the left by the transformation matrix S (to be determined below), and inserting formally the unit matrix $I = S^{-1}S$ between $\mathcal{L}$ and $\boldsymbol{e}$ in the right-hand side of (2.11), we obtain

$$S\frac{\partial \boldsymbol{e}}{\partial t} = S\mathcal{L}S^{-1}S\boldsymbol{e}\,. \tag{2.13}$$

The matrix product $S\mathcal{L}S^{-1}$ then gives the diagonal matrix

$$\Lambda = \begin{pmatrix} \lambda_1 & 0 \\ 0 & \lambda_2 \end{pmatrix}, \tag{2.14}$$

consisting of the eigenvalues $\lambda_{1,2}$, if the transformation matrix is adjoint to the eigenvector matrix V, i.e. $S = \left(V^{-1}\right)^{\mathrm{T}}$. The eigenvector matrix V transforms the coordinate system to one with axes directed along the eigenvectors of the system; the coordinates in this new coordinate system $\boldsymbol{A} = (A, B)^{\mathrm{T}}$ are related to the old coordinates $\boldsymbol{e} = (e, p)^{\mathrm{T}}$ by $\boldsymbol{A} = S\boldsymbol{e}$, and, vice versa, $\boldsymbol{e} = S^{-1}\boldsymbol{A}$.

Specifically, the matrix of eigenvectors is

$$V = \begin{pmatrix} 1 & (1/2)\left(i\,\Delta\omega + \sqrt{4D_0 - \Delta\omega^2}\right) \\ 1 & (1/2)\left(i\,\Delta\omega - \sqrt{4D_0 - \Delta\omega^2}\right) \end{pmatrix}, \tag{2.15}$$

and its adjoint transformation matrix $S = (V^{-1})^{\mathrm{T}}$ is

$$S = \frac{1}{\sqrt{\kappa}\sqrt{4D_0 - \Delta\omega^2}} \begin{pmatrix} (1/2)\left(-i\,\Delta\omega + \sqrt{4D_0 - \Delta\omega^2}\right) & 1 \\ (1/2)\left(i\,\Delta\omega + \sqrt{4D_0 - \Delta\omega^2}\right) & 1 \end{pmatrix}. \tag{2.16}$$

In (2.16), the normalizing coefficient has been chosen in such a way, that the expressions given later for the nonlinear terms simplify maximally.

The full nonlinear equations (2.1) in the matrix representation are

$$\frac{\partial \boldsymbol{E}}{\partial t} = \mathcal{L}\boldsymbol{E} + N\boldsymbol{E}, \tag{2.17a}$$

$$\frac{\partial D}{\partial t} = -\gamma_{\parallel}\left(D - D_0 + \frac{1}{2}\left(EP^* + E^*P\right)\right), \tag{2.17b}$$

where $\boldsymbol{E} = (E, P)^{\mathrm{T}}$, and (2.17b) has been written in a scalar form. The nonlinear evolution matrix is

$$N = \begin{pmatrix} 0 & 0 \\ D - D_0 & 0 \end{pmatrix}. \tag{2.18}$$

Now we multiply (2.17a) by the transformation matrix (as in (2.14)) in order to change to the new variables A and B; also, we express the old field and polarization variables E and P in terms of the new ones in (2.17b). The nonlinear evolution matrix in the new basis is

$$SNS^{-1} = \frac{D - D_0}{\sqrt{4D_0 - \Delta\omega^2}} \begin{pmatrix} 1 & 1 \\ -1 & -1 \end{pmatrix}. \tag{2.19}$$

Taking into account the relations above, (2.17) converts to

$$\frac{\partial}{\partial t} \begin{pmatrix} A \\ B \end{pmatrix} = \begin{pmatrix} \lambda_1 & 0 \\ 0 & \lambda_2 \end{pmatrix} \begin{pmatrix} A \\ B \end{pmatrix} + \frac{D - D_0}{\sqrt{4D_0 - \Delta\omega^2}} \begin{pmatrix} 1 & 1 \\ -1 & -1 \end{pmatrix} \begin{pmatrix} A \\ B \end{pmatrix} \tag{2.20a}$$

$$\frac{\partial D}{\partial t} = -\gamma_{\parallel}\left(D - D_0 + \frac{\kappa}{2}\sqrt{4D_0 - \Delta\omega^2}(|A|^2 - |B|^2)\right). \tag{2.20b}$$

Adiabatic elimination can be performed if one λ-branch (namely the λ_1 branch) dominates, and the other two branches lie deep below the zero axis.

In this case, from (2.20b), the equation for the (enslaved) variable of the population inversion D is

$$D - D_0 = -\frac{\kappa}{2}\sqrt{4D_0 - \Delta\omega^2}\left(|A|^2 - |B|^2\right).\tag{2.21}$$

Inserting (2.21) into the equation for the enslaved variable B, we obtain

$$\frac{\partial B}{\partial t} = \lambda_2 B + \frac{\kappa}{2}\left(|A|^2 - |B|^2\right)(A + B).\tag{2.22}$$

Assuming a near-threshold condition, together with the "close-to-resonance" condition $\Delta\omega = \mathcal{O}(\varepsilon)$, we obtain $\lambda_2 = -2\kappa$ in the lowest order. The enslaved variable B is negligibly small compared with its master variable A, i.e. $|B| \ll |A|$, and can be eliminated adiabatically from (2.22) to obtain $B = (1/4)|A|^2 A$, which justifies the assumption about the smallness of B close to the threshold.

There now remains the equation for the order parameter A, which is associated with the unstable λ_1 branch. From (2.20), we obtain

$$\frac{\partial A}{\partial t} = \lambda_1 A - \frac{\kappa}{2}\left(|A|^2 - |B|^2\right)(A + B),\tag{2.23}$$

which, taking into account the smallness of B and using the expression (2.10) for λ_1, simplifies to

$$\frac{\partial A}{\partial t} = \frac{\kappa}{2}\left(-\mathrm{i}\,\Delta\omega + \sqrt{4D_0 - \Delta\omega^2} - 2\right)A - \frac{\kappa}{2}|A|^2 A.\tag{2.24}$$

Expanding the square root in a Taylor series (assuming the "near-threshold" and "close-to-resonance" conditions discussed above) we obtain

$$\frac{2}{\kappa}\frac{\partial A}{\partial t} = pA + \mathrm{i}\left(a\nabla^2 - \omega\right)A - \frac{1}{4}\left(a\nabla^2 - \omega\right)^2 A - |A|^2 A.\tag{2.25}$$

This is the final result, the order parameter equation, which captures the essential features of the nonlinear dynamics of the laser under the assumptions made here. For arbitrary values of κ and $\gamma_\perp$ (but assuming that both parameters are of $\mathcal{O}(1)$) we obtain the OPE for the general case of a class C laser,

$$\frac{\partial A}{\partial \tau} = pA + \mathrm{i}\left(a\nabla^2 - \omega\right)A - \frac{\kappa^2}{\left(\kappa + \gamma_\perp\right)^2}\left(a\nabla^2 - \omega\right)^2 A - |A|^2 A,\tag{2.26}$$

where $\tau = t\kappa\gamma_\perp/(\kappa + \gamma_\perp)$ is a normalized time.

Let us now repeat all assumptions used to derive (2.26):

- "near-threshold" condition: $p = D_0 - 1 = \mathcal{O}(\varepsilon^2)$. It follows from this condition that the field amplitude A is small: $A = \mathcal{O}(\varepsilon)$.

- "close-to-resonance" condition: $\Delta\omega = a\nabla^2 - \omega = \mathcal{O}(\varepsilon)$.
- Class C laser assumption: $\kappa, \gamma_\perp$ and $\gamma_\parallel = \mathcal{O}(1)$. If $\gamma_\parallel$ is small (the case of a class B laser), then the adiabatic elimination of the population inversion is impossible, and one ends up with a system of two equations and two order parameters. This case will be investigated in Chap. 7.

All the simplifications used here follow from the above assumptions. For instance, the enslaved parameter B was neglected because of its smallness. Indeed, from the expression $B = (1/4)|A|^2 A$, it follows that $B = \mathcal{O}(\varepsilon^3)$, and thus this neglect is justified.

The terms on the right-hand side of (2.26) are of the third order of smallness, except for the diffraction term, which is of the second order of smallness. Consequently, the evolution occurs on two timescales: the evolution due to diffraction (e.g. the beating of the transverse modes of the laser) occurs on a slow timescale $T_1 = \mathcal{O}(1/\varepsilon)$, and the dynamics related to the linear growth of the fields and nonlinear saturation (e.g. the buildup of the radiation in the laser) occur on an even slower temporal scale $T_2 = \mathcal{O}(1/\varepsilon^2)$.

The detuning term was considered as a scalar during the derivation of the OPE (2.26), although it is an operator. This detuning operator does not commute with the order parameter $A(\boldsymbol{r}, t)$, nor with the nonlinearities. If we take into account this noncommutativity, the nonlinear term in the OPE (2.25) becomes

$$N = -\frac{\kappa}{2\sqrt{4D_0 - \Delta\omega^2}} \tag{2.27}$$
$$\times \left(A\frac{-\mathrm{i}\,\Delta\omega + \sqrt{4D_0 - \Delta\omega^2}}{2}A^* + A^*\frac{\mathrm{i}\,\Delta\omega + \sqrt{4D_0 - \Delta\omega^2}}{2}A \right) A,$$

where the operators act on the variables to the right of them. Now, calculating the nonlinear term (2.27) and taking into account of the above smallness conditions (retaining the terms of $\mathcal{O}(\varepsilon^3)$), we obtain $N = -(\kappa/2)|A|^2 A$, which leads again to (2.25) and (2.26).

The OPE (2.25), and also (2.26), is called the complex Swift–Hohenberg equation, owing to its similarity to the usual real Swift–Hohenberg equation [5].

Equation (2.26) retains all the ingredients of spatial pattern formation in lasers. One important property of the radiation in lasers is its diffraction. The second term on the right-hand side accounts for that. The third term on the right-hand side describes the spatial-frequency selection, a phenomenon essential for the correct description of narrow-gain-line lasers. In many such lasers, selection of the spatial frequency (transverse mode) is possible by tuning the length of the resonator: particular transverse modes fall under the gain line and thus can be excited. Owing to the spatial-frequency selection term, the maximum amplification occurs at a nonzero transverse wavenumber $k^2 = -\omega/a$, which depends on the detuning ω. This means that a laser with

negative detuning emits waves at an angle to the optical axis of the resonator (conical emission). Such a detuning-caused pattern-forming instability of lasers was first predicted in [6].

The first and last terms on the right-hand side of (2.26) give the normal form of a supercritical Hopf bifurcation. When the control parameter $p = D_0 - 1$ goes through zero a bifurcation occurs, bringing the system from a stable point corresponding to the nonlasing solution $A = 0$ to a ring corresponding to the lasing solution $|A|^2 = p$, characterized by a fixed amplitude but arbitrary phase.

2.3.2 Multiple-Scale Expansion

Another method that allows one to derive the OPE is the multiple-scale expansion technique, widely used in nonlinear analysis. The starting point is again a linear stability analysis, but the evolution equation of the order parameter is found as a solvability condition.

This technique consists of the following steps:

1. The relevant variables and parameters of the system are expressed in terms of a smallness parameter ε. This allows one to write the fields as an asymptotic expansion,

$$\boldsymbol{v} = \sum_{n=1}^{\infty} \varepsilon^n \boldsymbol{v}_n \,. \tag{2.28}$$

2. The original equations are expanded, and the coefficients of powers of ε are gathered. At order n, the equation has the form $L\boldsymbol{v}_n = \boldsymbol{g}_n$, which is linear in $\boldsymbol{v}_n$, where $\boldsymbol{g}_n$ contains the nonlinear interactions and variations of the fields at lower orders, and L is a linear operator.
3. A solvability condition is applied at some order n, to require the existence of solutions. This is done by requiring that $\boldsymbol{g}_n$ be orthogonal to the solutions of the adjoint homogeneous problem, $L^*\boldsymbol{v}_n = 0$. This process is also known as the Fredholm alternative theorem.
4. Finally, at a given order, a closed equation is obtained for the evolution of one single variable, namely the order parameter.

In the following, we apply this method to the Maxwell–Bloch equations (2.1) [4].

First, we assume that the near-to-resonance condition holds, requiring that $\Delta\omega = \left(a\nabla^2 - \omega\right)$ be a small quantity:

$$\Delta\omega = \varepsilon\Theta \,. \tag{2.29}$$

In the original paper [4], ω and ∇^2 were both required to be small. This restricts seriously the validity of the order parameter equation. Here we note that requiring only $\Delta\omega$ to be small, leads to the same result, and this allows

us to consider cases where ω and ∇^2 are moderate or large, as long as their difference is small.

We make also the near-to-threshold assumption,

$$D_0 = 1 + p\,, \quad p = \mu\varepsilon^2\,. \tag{2.30}$$

With these assumptions, the laser variables depend on slow temporal and spatial scales, which can be determined by using the results of the linear stability analysis. The eigenvalue (2.8), which determines the temporal evolution in the linear stage, has terms of first and second order in ε. We can then define two temporal scales,

$$T_1 = \varepsilon t\,, \quad T_2 = \varepsilon^2 t\,, \tag{2.31}$$

which allows us to expand the temporal derivative as

$$\frac{\partial}{\partial t} = \varepsilon\frac{\partial}{\partial T_1} + \varepsilon^2\frac{\partial}{\partial T_2}\,. \tag{2.32}$$

Finally, we expand the fields around the trivial solution:

$$E = \sum_{n=1}^{\infty}\varepsilon^n e_n\,, \quad P = \sum_{n=1}^{\infty}\varepsilon^n p_n\,, \quad D = D_0 + \sum_{n=1}^{\infty}\varepsilon^n d_n\,. \tag{2.33}$$

All the definitions (2.29)–(2.33) are now introduced into the Maxwell–Bloch equations (2.1). Powers of ε are gathered, and the equations are solved recursively at each order.

At the first order,

$$e_1 = p\,, \quad d_1 = 0\,. \tag{2.34}$$

At the second order,

$$\frac{1}{\kappa}\frac{\partial e_1}{\partial T_1} = -e_2 + p_2 + \mathrm{i}\Theta e_1\,, \tag{2.35a}$$

$$\frac{1}{\gamma_\perp}\frac{\partial p_1}{\partial T_1} = e_2 - p_2\,, \tag{2.35b}$$

$$0 = d_2 - \frac{1}{2}\left(e_1^* p_1 + p_1^* e_1\right)\,. \tag{2.35c}$$

The compatibility of (2.35a) and (2.35b) requires that

$$\frac{\partial e_1}{\partial T_1} = \mathrm{i}\frac{\kappa\gamma_\perp}{\kappa + \gamma_\perp}\Theta e_1\,, \tag{2.36}$$

while the polarization is related to the field through

$$p_2 = e_2 - \mathrm{i}\frac{\kappa}{\kappa + \gamma_\perp}\Theta e_1\,. \tag{2.37}$$

Both of these relations will be useful later, at the next order. From (2.35c), we obtain

$$d_2 = - |e_1|^2 . \tag{2.38}$$

At the order $\mathcal{O}(\varepsilon^3)$, the equations read

$$\frac{1}{\kappa}\frac{\partial e_1}{\partial T_2} + \frac{1}{\kappa}\frac{\partial e_2}{\partial T_1} = -e_3 + p_3 + \mathrm{i}\Theta e_2 , \tag{2.39a}$$

$$\frac{1}{\gamma_\perp}\frac{\partial p_1}{\partial T_2} + \frac{1}{\gamma_\perp}\frac{\partial p_2}{\partial T_1} = e_3 - p_3 + \mu e_1 + d_2 e_1 . \tag{2.39b}$$

This system reduces, by applying a solvability condition that actually consists in eliminating the dependence on third-order contributions, to

$$\left(\frac{1}{\kappa} + \frac{1}{\gamma_\perp}\right)\left(\frac{\partial e_1}{\partial T_2} + \frac{\partial e_2}{\partial T_1}\right) = \mu e_1 - e_1 |e_1|^2 + \mathrm{i}\Theta e_2 - \frac{\kappa^2}{(\kappa + \gamma_\perp)^2}\Theta^2 e_1 , \tag{2.40}$$

where, in obtaining the last term, we have used

$$\frac{1}{\gamma_\perp}\frac{\partial p_2}{\partial T_1} = \frac{1}{\gamma_\perp}\frac{\partial e_2}{\partial T_1} - \frac{1}{\gamma_\perp}\frac{\kappa}{\kappa + \gamma_\perp}\mathrm{i}\Theta\frac{\partial e_1}{\partial T_1} = \frac{1}{\gamma_\perp}\frac{\partial e_2}{\partial T_1} + \frac{\kappa^2}{(\kappa + \gamma_\perp)^2}\Theta^2 e_1 . \tag{2.41}$$

Equation (2.40) depends now only on the field amplitude at different orders. Let us now define an order parameter $A = \varepsilon e_1 + \varepsilon^2 e_2$. The evolution of the order parameter with respect to the original time t is given by

$$\frac{\partial A}{\partial t} = \varepsilon^2\frac{\partial e_1}{\partial T_1} + \varepsilon^3\left(\frac{\partial e_2}{\partial T_1} + \frac{\partial e_1}{\partial T_2}\right) = \varepsilon^2\frac{\kappa\gamma_\perp}{\kappa + \gamma_\perp}\mathrm{i}\Theta e_1 + \varepsilon^3\left(\frac{\partial e_2}{\partial T_1} + \frac{\partial e_1}{\partial T_2}\right) . \tag{2.42}$$

Finally, (2.42), expressed in terms of the original variables, gives the evolution equation of the order parameter,

$$\left(\frac{1}{\kappa} + \frac{1}{\gamma_\perp}\right)\frac{\partial A}{\partial t} = (D_0 - 1) A - A |A|^2$$

$$+ \mathrm{i}\left(a\nabla^2 - \omega\right) A - \frac{\kappa^2}{(\kappa + \gamma_\perp)^2}\left(a\nabla^2 - \omega\right)^2 A , \tag{2.43}$$

which coincides with (2.26), obtained by using the adiabatic-elimination procedure.

References

1. M.C. Cross and P.C. Hohenberg, Pattern formation outside of equilibrium, Rev. Mod. Phys. **65**, 851 (1993). 33

2. R. Graham and H. Haken, Laserlight – first example of a second order phase transition far from thermal equilibrium, Z. Phys. **237**, 31 (1970). 34, 41

3. K. Staliunas, Laser Ginzburg–Landau equation and laser hydrodynamics, Phys. Rev. A **48**, 1573 (1993). 41

4. J. Lega, J.V. Moloney and A.C. Newell, Swift–Hohenberg equation for lasers, Phys. Rev. Lett. **73**, 2978 (1994). 41, 46

5. J.B. Swift and P.C. Hohenberg, Hydrodynamic fluctuations at the convective instability, Phys. Rev. A 15, 319 (1977). 45

6. L.A. Lugiato and R. Lefever, Spatial dissipative structures in passive optical systems, Phys. Rev. Lett. **58**, 2209 (1987). 46

3 Order Parameter Equations
for Other Nonlinear Resonators

3.1 Optical Parametric Oscillators

An optical parametric oscillator basically consists of a nonlinear $\chi^{(2)}$ medium inside a resonator driven by a coherent field of amplitude $\bar{E}$ and frequency ω_L, which propagates along the optical axis of the resonator, parallel to the z axis. The crystal converts the intracavity pump field of frequency ω_L and amplitude A_0 into two fields of frequency $f_1\omega_L$ and $f_2\omega_L$, and of amplitude A_1 and A_2, the signal and idler waves, respectively. Energy conservation requires that $f_1 + f_2 = 1$. Three longitudinal modes of the cavity with frequencies ω_m^c ($m = 0, 1, 2$) are assumed to be close to the frequencies $f_m\omega_L$ (where $f_0 = 1$). Under these conditions, and making some of the usual assumptions of nonlinear optics (the mean-field limit, the paraxial and single-longitudinal-mode approximations), the evolution equations for the pump, signal and idler fields can be written as [1]

$$\frac{\partial A_0}{\partial t} = \gamma_0 \left[-(1 + i\omega_0) A_0 + \bar{E} - A_1 A_2 + i a_0 \nabla^2 A_0 \right], \tag{3.1a}$$

$$\frac{\partial A_1}{\partial t} = \gamma_1 \left[-(1 + i\omega_1) A_1 + A_0 A_2^* + i a_1 \nabla^2 A_1 \right], \tag{3.1b}$$

$$\frac{\partial A_2}{\partial t} = \gamma_2 \left[-(1 + i\omega_2) A_2 + A_0 A_1^* + i a_2 \nabla^2 A_2 \right], \tag{3.1c}$$

where γ_m are the cavity decay rates, $\omega_m = \left(\omega_m^c - f_m\omega_L\right)/\gamma_m$ are the detunings and $a_m = c^2/2\gamma_m f_m \omega_L$ are the diffraction coefficients.

The signal and idler fields can have arbitrary frequencies, since f_1 and f_2 are free (within the restriction $f_1 + f_2 = 1$). In the particular case $f_1 = f_2 = 1/2$, both fields have the same frequency $\omega_L/2$, leading to degenerate oscillation (the DOPO). In this case, the model takes the form

$$\frac{\partial A_0}{\partial t} = \gamma_0 \left[-(1 + i\omega_0) A_0 + \bar{E} - A_1^2 + i a_0 \nabla^2 A_0 \right], \tag{3.2a}$$

$$\frac{\partial A_1}{\partial t} = \gamma_1 \left[-(1 + i\omega_1) A_1 + A_0 A_1^* + i a_1 \nabla^2 A_1 \right]. \tag{3.2b}$$

Note that the degenerate model follows from the condition $X_1 = X_2$, where X is any of the variables. One might think that, in principle, the results from the nondegenerate model would include also those corresponding to the

degenerate model. However, this is not true in general, owing to the complex character of the fields.

We start the analysis with the simpler, degenerate case.

3.2 The Real Swift–Hohenberg Equation for DOPOs

In order to simplify the analysis of this section, we make the following changes of variables in the model (3.2):

$$A_0 = E - (1 + i\omega_0)X \ , \tag{3.3a}$$

$$A_1 = \sqrt{1 + \omega_0^2}\,Y \ , \tag{3.3b}$$

$$\bar{E} = (1 + i\omega_0)E \ . \tag{3.3c}$$

The DOPO model now reads

$$\frac{\partial X}{\partial t} = -\gamma\,(1 + i\omega_0)\left(X + Y^2\right) + i\frac{1}{2}\nabla^2 X \ , \tag{3.4a}$$

$$\frac{\partial Y}{\partial t} = -\,(1 + i\omega_1)\,Y + \left[E + (1 - i\omega_0)X\right]Y^* + i\nabla^2 Y \ , \tag{3.4b}$$

where the time is normalized to γ_1, the space variables are to a_1, $\gamma = \gamma_0/\gamma_1$ and we have used $a_0 = a_1/2$.

In this new representation, the simplest stationary solution takes the form

$$X = Y = 0 \ , \tag{3.5}$$

which is actually the trivial (nonlasing) solution.

3.2.1 Linear Stability Analysis

Next a stability analysis of the trivial solution (3.5) is performed against space-dependent perturbations, with arbitrary wavenumber k. The linearization of the system leads to the following eigenvalues:

$$\lambda_0 = -\gamma\left[1 \pm i\left(\omega_0 + \frac{k^2}{2\gamma}\right)\right], \tag{3.6}$$

$$\lambda_1 = -1 \pm \sqrt{E^2 - (\omega_1 + k^2)^2} \ . \tag{3.7}$$

Clearly, λ_0 has a negative real part for any value of the perturbation wavenumber k. In contrast, one root of λ_1 becomes positive for a given pump value, indicating the presence of a bifurcation at

$$E_{\mathrm{B}}(k) = \sqrt{1 + (\omega_1 + k^2)^2} \ . \tag{3.8}$$

The emission threshold corresponds to the minimum value of $E_{\mathrm{B}}(k)$, which occurs at a critical wavenumber $k = k_{\mathrm{c}}$. Identically to the case of the laser, the bifurcation depends on the sign of the detuning:

1. For $\omega_1 > 0$, the instability occurs at $k_c = 0$, corresponding to homogeneous emission. Thus, a positive detuning implies that no patterns (no modes of the resonator) are excited.
2. For $\omega_1 < 0$, the instability occurs at $k_c = \sqrt{-\omega_1}$, corresponding to a pattern-forming instability (conical emission).

The pump threshold is different for different signs of the detuning. From (3.8) it follows that $E_0 = E_B(k_c) = \sqrt{1 + \omega_1^2}$ for a positive detuning, while $E_0 = 1$ for a negative detuning. The situation in this respect is identical to that in lasers.

3.2.2 Scales

We use the multiscale expansion technique described in Sect.2.3.2 to derive an order parameter equation for a DOPO. Obviously, adiabatic elimination is also possible and leads to the same result [2]. The first step consists in the determination of the proper scalings.

We make again the near-to-threshold assumption,

$$E = E_0 + \varepsilon^2 E_2 \ . \tag{3.9}$$

The near-to-resonance assumption,

$$a_1 \nabla^2 - \omega_1 = \varepsilon \Theta \ , \tag{3.10}$$

unlike the case for lasers, is not always valid. It is valid for self-imaging resonators (see Chaps. 5 and 11), which allows one to obtain independent values of the diffraction coefficients for both waves. However, for plane mirror resonators, strictly one should assume that both the detuning and the diffraction are small:

$$a_0 \nabla^2 \sim \mathcal{O}(\varepsilon), \quad \omega_1 \sim \mathcal{O}(\varepsilon) \ . \tag{3.11}$$

To find the characteristic scale of the temporal evolution, we investigate how the eigenvalue behaves under the above assumptions. Substitution of (3.9)–(3.11) in (3.7) and expanding into Taylor series leads to

$$\lambda_1 = \left((E - E_0) - \frac{1}{2} \left(\omega_1 + k^2 \right)^2 \right) + \mathcal{O}(\varepsilon^4) \ , \tag{3.12}$$

which is valid for both signs of the detuning. In particular, the largest eigenvalue is always $\lambda_1(k_c) = E - E_0 \sim \mathcal{O}(\varepsilon^2)$, which suggests the introduction of a slow timescale T, given by

$$T = \varepsilon^2 t \ . \tag{3.13}$$

The linear stability analysis does not predict any particular order of magnitude for the pump detuning. Therefore, the pump detuning can in principle

be chosen freely. However, we can use a property of the homogeneous solution of the DOPO model to obtain some useful information. As shown in [3], the homogeneous, nontrivial solution of the DOPO model shows bistable behavior for $\omega_0\omega_1 > 1$. As the order of magnitude of ω_1 is required in our analysis to be $\mathcal{O}(\varepsilon)$, we can consider two main cases:

1. $\omega_0 \sim \mathcal{O}(1)$, covering only a monostable situation, and
2. $\omega_0 \sim \mathcal{O}(\varepsilon^{-1})$, covering also bistable situations.

In the following, we treat these two cases separately.

3.2.3 Derivation of the OPE

Consider an expansion of the fields in the form

$$X = \sum_{n=1}^{\infty} \varepsilon^n x_n , \quad Y = \sum_{n=1}^{\infty} \varepsilon^n y_n , \tag{3.14}$$

together with the scalings (3.9), (3.10), (3.12) and (3.13), and either (a) moderate or (b) large pump detuning. Substitution in (3.4) leads to a system of equations to be solved at each order.

(a) Moderate Pump Detuning. At $\mathcal{O}(\varepsilon)$, we find the solution

$$x_1 = 0 , \tag{3.15}$$

together with the relation

$$y_1 = y_1^* , \tag{3.16}$$

i.e. the signal field is, in the lowest order, real-valued. At $\mathcal{O}(\varepsilon^2)$, the equations read

$$x_2 = -y_1^2 , \tag{3.17a}$$

$$y_2 - y_2^* = -\mathrm{i}\Theta y_1 . \tag{3.17b}$$

At $\mathcal{O}(\varepsilon^3)$, only the equation for the signal field is relevant, which reads

$$\frac{\partial y_1}{\partial T} = -y_3 + y_3^* + E_2 y_1 + (1 - \mathrm{i}\omega_0) x_2 y_1^* + \mathrm{i}\,\Theta y_2 . \tag{3.18}$$

The solvability of (3.18) can be checked by adding it to its complex conjugate, in order to eliminate the explicit third-order contributions. Then, taking into account (3.16) and (3.17), after some algebra, we find

$$\frac{\partial y_1}{\partial T} = E_2 y_1 - y_1^3 - \frac{1}{2}\Theta^2 y_1 , \tag{3.19}$$

which can be written in terms of the initial parameters. If we define the order parameter as $A = \varepsilon y_1$, (3.19) leads to

$$\frac{\partial A}{\partial t} = (E-1)A - A^3 - \frac{1}{2}\left(\omega_1 - \nabla^2\right)^2 A \;, \tag{3.20}$$

which is the real Swift–Hohenberg (RSH) equation for the order parameter A. The RSH equation was first derived in a hydrodynamic context [4], and was later used to describe several nonlinear optical systems, such as optical bistability and four-wave mixing [5].

(b) Large Pump Detuning. We repeat the derivation now, but using the scalings (3.9)–(3.11) together with $\omega_0 = \Omega_0/\varepsilon$. From the first and second order, we obtain (3.15) and (3.17a) again, and also

$$x_3 = -2y_1 y_2 \;, \tag{3.21a}$$
$$y_2 - y_2^* = -\mathrm{i}\left(\Theta + \Omega_0 y_1^2\right)y_1 \;. \tag{3.21b}$$

The third order results in

$$\frac{\partial y_1}{\partial T} = -y_3 + y_3^* + \mathrm{i}\Omega_0\left(2y_2 + y_2^*\right) + E_2 y_1 - y_1^3 + \mathrm{i}\Theta y_2 \;. \tag{3.22}$$

By adding (3.22) to its complex conjugate, and using (3.21) we finally obtain

$$\frac{\partial y_1}{\partial T} = E_2 y_1 - y_1^3 - \frac{1}{2}\left(\Theta + \Omega_0 y_1^2\right)^2 y_1 \;, \tag{3.23}$$

which, expressed in terms of the original parameters, results in the following order parameter equation:

$$\frac{\partial A}{\partial t} = (E-1)A - A^3 - \frac{1}{2}\left(\omega_1 - \nabla^2 - \omega_0 A^2\right)^2 A \;, \tag{3.24}$$

where A is the signal amplitude to leading order.

Note that (3.24) reduces to (3.20) when ω_0 is small. The term appearing at large ω_0 is responsible for the intensity-dependent wavenumber selection, corresponding to a spatial nonlinear resonance. Many important features of pattern formation are related to this effect, which will be discussed in Chap. 10.

3.3 The Complex Swift–Hohenberg Equation for OPOs

Again, it is convenient to make some changes in the model before starting the multiscale expansion procedure. The derivation is simplified if we apply to (3.1) the changes (3.3a) and (3.3c), together with

$$A_1 = \sqrt{1 + \omega_0^2} Y e^{i\Omega t}, \ A_2 = \sqrt{1 + \omega_0^2} Z e^{-i\Omega t}. \tag{3.25}$$

The changes now include a change in the reference frequency Ω, given by

$$\Omega = \frac{a_1\omega_2 - a_2\omega_1}{a} \ , \tag{3.26}$$

where $a = (a_1\gamma_1 + a_2\gamma_2) / (\gamma_1 + \gamma_2)$. This corresponds physically to the elimination of the frequency shift of the signal and idler waves at the generation threshold, which appears at a negative value of the effective detuning parameter, defined by

$$\omega = \frac{\omega_1\gamma_1 + \omega_2\gamma_2}{\gamma_1 + \gamma_2} \ . \tag{3.27}$$

With these changes, the equations (3.1) read

$$\frac{\partial X}{\partial t} = \gamma_0 \left[-(1 + i\omega_0)(X + YZ) + i\tilde{a}_0 \nabla^2 X \right], \tag{3.28a}$$

$$\frac{\partial Y}{\partial t} = \gamma_1 \left[-Y - i\tilde{a}_1 (\omega - \nabla^2) Y + EZ^* + i(1 + i\Delta_0) XZ^* \right], \tag{3.28b}$$

$$\frac{\partial Z}{\partial t} = \gamma_2 \left[-Z - i\tilde{a}_2 (\omega - \nabla^2) Z + EY^* + i(1 + i\Delta_0) XY^* \right], \tag{3.28c}$$

where X, Y and Z are the new pump, signal and idler fields, respectively, and $\tilde{a}_i = a_i/a$. For the new model (3.28), the trivial nonlasing solution again takes the simple form

$$X = Y = Z = 0 \ . \tag{3.29}$$

3.3.1 Linear Stability Analysis

The linearization of (3.28) around (3.29), with spatially dependent perturbations, leads to the following growth rates for the perturbations:

$$\lambda_0 = \gamma_0 \left[-1 + i\left(\Delta_0 + ak^2\right) \right] \ , \tag{3.30}$$

and

$$\lambda_1 = -\frac{1}{2}(\gamma_1 + \gamma_2) - i\frac{1}{2}(\tilde{a}_1\gamma_1 - \tilde{a}_2\gamma_2)(\omega + k^2)$$
$$\pm \frac{1}{2}\sqrt{\left[(\gamma_1 - \gamma_2) + i(\tilde{a}_1\gamma_1 + \tilde{a}_2\gamma_2)(\omega + k^2)\right]^2 + 4\gamma_1\gamma_2 E^2}. \tag{3.31}$$

An instability of (3.29) can be caused by the upper (plus sign) branch of (3.31). The threshold for this instability of (3.29) is

$$E_{\mathrm{B}}(k) = \sqrt{1 + (\omega + k^2)^2} \ . \tag{3.32}$$

Unlike the degenerate case, where the bifurcation is static (the eigenvalue is real), the bifurcation here is oscillatory (Hopf), since the perturbations grow with a frequency given by

$$\nu = -\frac{2\gamma_1\gamma_2}{\gamma_1 + \gamma_2}\left(\tilde{a}_1 - \tilde{a}_2\right)\left(\omega + k^2\right). \tag{3.33}$$

Note that in the degenerate case $\omega_1 = \omega_2$, $\gamma_1 = \gamma_2$ and $a_1 = a_2$ ($\nu = 0$), the eigenvalue (3.31) converts into (3.7), obtained in the analysis of the degenerate case, which is real. In fact, the expression (3.31) becomes identical to that obtained for the DOPO, (3.8), with ω_1 replaced by ω.

3.3.2 Scales

We assume again the near-to-threshold condition (3.9) and the close-to-resonance condition. The latter now takes the form

$$\nabla^2 - \omega = \varepsilon\Theta , \tag{3.34}$$

with the additional condition $\tilde{a}_0\nabla^2 \sim \mathcal{O}(\varepsilon)$, as discused in Sect. 3.2.2. Under these smallness assumptions, the eigenvalue (3.31) can be approximated by

$$\gamma^{-1}\lambda = -\mathrm{i}\frac{\tilde{a}_1 - \tilde{a}_2}{2}\left(\omega + k^2\right) + \left((E-1) - \frac{1}{2}\left(\omega + k^2\right)^2\right), \tag{3.35}$$

which is similar to (2.9) for the laser case.

The eigenvalue (3.35) is now complex. The imaginary part is $\mathcal{O}(\varepsilon)$, while the real part is $\mathcal{O}(\varepsilon^2)$. This suggests the introduction of two different temporal scales, $T_1 = \varepsilon t$ and $T_2 = \varepsilon^2 t$, and consequently the following expansion for the temporal derivative

$$\frac{\partial}{\partial t} = \varepsilon\frac{\partial}{\partial T_1} + \varepsilon^2\frac{\partial}{\partial T_2} . \tag{3.36}$$

Again, the order of magnitude of the pump detuning can be chosen freely. For simplicity, in the following we restrict the analysis to the case $\omega_0 \sim \mathcal{O}(1)$.

3.3.3 Derivation of the OPE

Consider the system (3.28), with the smallness conditions described above, together with a power expansion of the fields in the form

$$X = \sum_{n=1}^{\infty}\varepsilon^n x_n , \quad Y = \sum_{n=1}^{\infty}\varepsilon^n y_n , \quad Z = \sum_{n=1}^{\infty}\varepsilon^n z_n . \tag{3.37}$$

At the first order

$$x_1 = 0 \ , \tag{3.38a}$$

$$y_1 = z_1^* \ . \tag{3.38b}$$

At the second order

$$x_2 = -y_1 z_1 = - \left| y_1 \right|^2 \ . \tag{3.39}$$

The other fields evolve with respect to the slow time T_1:

$$\frac{\partial y_1}{\partial T_1} = \gamma_1 \left(z_2^* - y_2 - i\tilde{a}_1 \Theta y_1 \right) \ , \tag{3.40a}$$

$$\frac{\partial z_1^*}{\partial T_1} = \gamma_2 \left(-z_2^* + y_2 + i\tilde{a}_2 \Theta z_1^* \right) \ . \tag{3.40b}$$

Taking into account (3.38b), and adding (3.40a) to (3.40b), we obtain a closed equation for the evolution of the signal with respect to the slow time T_1,

$$\frac{\partial y_1}{\partial T_1} = -i \frac{\gamma_1 \gamma_2}{\gamma_1 + \gamma_2} \left(\tilde{a}_1 - \tilde{a}_2 \right) \Theta y_1 \ . \tag{3.41}$$

Subtracting (3.40a) from (3.40b) gives

$$z_2^* = y_2 + i\Theta y_1 \ , \tag{3.42}$$

where we have used the relation $\left(\gamma_1 \tilde{a}_1 + \gamma_2 \tilde{a}_2 \right) / \left(\gamma_1 + \gamma_2 \right) = 1$. At the third order, only the equations for the signal and idler fields are relevant:

$$\frac{1}{\gamma_1} \left(\frac{\partial y_2}{\partial T_1} + \frac{\partial y_1}{\partial T_2} \right) = \tag{3.43a}$$
$$z_3^* - y_3 - i\tilde{a}_1 \Theta y_2 + E_2 z_1^* + i \left(1 - i\omega_0 \right) x_2 z_1^* \ ,$$

$$\frac{1}{\gamma_2} \left(\frac{\partial z_2^*}{\partial T_1} + \frac{\partial z_1^*}{\partial T_2} \right) = \tag{3.43b}$$
$$-z_3^* + y_3 + i\tilde{a}_2 \Theta z_2^* + E_2 y_1 - i \left(1 + i\omega_0 \right) x_2^* y_1 \ .$$

The solvability condition is obtained by adding (3.43a) to (3.43b), resulting in

$$\frac{1}{\gamma_1} \left(\frac{\partial y_2}{\partial T_1} + \frac{\partial y_1}{\partial T_2} \right) + \frac{1}{\gamma_2} \left(\frac{\partial z_2^*}{\partial T_1} + \frac{\partial y_1}{\partial T_2} \right) \tag{3.44}$$
$$= -i\tilde{a}_1 \Theta y_2 + i\tilde{a}_2 \Theta z_2^* + 2E_2 y_1 - 2y_1 \left| y_1 \right|^2 \ .$$

The dependence of (3.44) on z_2^* can be eliminated by substitution of (3.42), leaving

$$\left(\frac{1}{\gamma_1} + \frac{1}{\gamma_2} \right) \left(\frac{\partial y_2}{\partial T_1} + \frac{\partial y_1}{\partial T_2} \right)$$
$$= 2E_2 y_1 - 2y_1 \left| y_1 \right|^2 - i \left(\tilde{a}_1 - \tilde{a}_2 \right) \Theta y_2 - \Theta^2 y_1. \tag{3.45}$$

We now define the order parameter A as $A = \varepsilon y_1 + \varepsilon^2 y_2$. We can express its evolution on the original timescale as

$$\frac{\partial A}{\partial t} = \varepsilon^2 \frac{\partial y_1}{\partial T_1} + \varepsilon^3 \left(\frac{\partial y_2}{\partial T_1} + \frac{\partial y_1}{\partial T_2} \right)$$

$$= \varepsilon^2 \left[-\mathrm{i} \frac{\gamma_1 \gamma_2}{\gamma_1 + \gamma_2} \left(\tilde{a}_1 - \tilde{a}_2 \right) \Theta y_1 \right] + \varepsilon^3 \left(\frac{\partial y_2}{\partial T_1} + \frac{\partial y_1}{\partial T_2} \right) . \qquad (3.46)$$

Finally, the evolution equation of the order parameter can be written in terms of the original parameters as

$$\frac{1}{\Gamma} \frac{\partial A}{\partial t} = (E - 1) A - A \left| A \right|^2 - \mathrm{i} d \left(\omega - \nabla^2 \right) A - \frac{1}{2} \left(\omega - \nabla^2 \right)^2 A , \qquad (3.47)$$

where $\Gamma = \gamma_1 \gamma_2 / (\gamma_1 + \gamma_2)$ is the decay rate of the order parameter, and $d = (\tilde{a}_1 - \tilde{a}_2)/2$ is a diffraction coefficient.

Equation (3.47) is a complex Swift–Hohenberg (CSH) equation, formally identical to the order parameter equation derived for lasers in the preceding chapter.

A multiple-scale expansion is also possible in the case of large pump detuning, leading to

$$\frac{1}{\Gamma} \frac{\partial A}{\partial t} = (E - 1) A - A \left| A \right|^2 - \mathrm{i} d \left(\omega - \nabla^2 - \omega_0 \left| A \right|^2 \right) A$$

$$- \frac{1}{2} \left(\omega - \nabla^2 - \omega_0 \left| A \right|^2 \right)^2 A + \frac{1}{2} \omega_0 \left(A^* \nabla^2 A - A \nabla^2 A^* \right) A , (3.48)$$

which is the CSH equation with a nonlinear resonance, as derived in [6].

3.4 The Order Parameter Equation for Photorefractive Oscillators

3.4.1 Description and Model

A photorefractive crystal is a nonlinear medium that responds to the light intensity via the electro-optic effect, where spatial variations in the refractive index are induced according to the light profile. When the crystal is placed inside a resonator and subjected to an optical pump, this nonlinear optical system is called a photorefractive oscillator. The pump wave, when scattered by the imperfections of the crystal as it passes along the optical axis, initiates an oscillation process, generating a signal wave. During the process, both the pump and the generated waves are present in the resonator.

The total optical field inside the resonator is given by

$$\bar{E}(r, t) = A_{\mathrm{p}}(r, t) \exp(\mathrm{i} k_{\mathrm{p}} r - \mathrm{i} \omega_{\mathrm{p}} t) + A_{\mathrm{s}}(r, t) \exp(\mathrm{i} k_{\mathrm{s}} r - \mathrm{i} \omega_{\mathrm{s}} t) + \mathrm{c.c.} . \quad (3.49)$$

where the indices p and s attributes to the pump and signal waves, respectively. This induces a spatial modulation of the refractive index,

$$\bar{n}(r,t) = n(r,t)\exp(\mathrm{i}qr - \mathrm{i}\Omega t) + \text{c.c.} \ , \tag{3.50}$$

where $\Omega = \omega_\mathrm{p} - \omega_\mathrm{s}$ and $q = k_\mathrm{p} - k_\mathrm{s}$.

In the mean-field limit, the equations describing the evolution of the signal wave and the refractive index are (the details of the derivation can be found in [7])

$$\frac{\partial A}{\partial t} = \kappa\left[-(1 + \mathrm{i}\beta)A + \mathrm{i}n^* + \mathrm{i}a\nabla^2 A\right], \tag{3.51a}$$

$$\frac{\partial n}{\partial t} = -\gamma\left(n - \mathrm{i}n - n_\mathrm{s}\frac{A^*}{1 + |A|^2}\right), \tag{3.51b}$$

where $A = A_\mathrm{s}/A_\mathrm{p}$ is the normalized signal field, n_s is the saturation value of the index grating, β is the detuning of the resonator frequency from the center of the gain line, and κ and γ are the decay rates of the photon and index gratings, respectively. Usually, the condition $\gamma \ll \kappa$ holds, which allows the adiabatic-elimination of the optical field. In the next section, the adiabatic elimination technique is used to derive an order parameter equation for PROs.

3.4.2 Adiabatic Elimination and Operator Inversion

The envelope of the refractive-index grating can be expressed in terms of the optical field by assuming that the field is a fast-relaxing variable, i.e. $\partial A/\partial t = 0$. In this case

$$n = \left(1 - \mathrm{i}\beta + \mathrm{i}a\nabla^2\right)A^* \ . \tag{3.52}$$

Substituting (3.52) in (3.51), and letting the differential operator act on both sides of (3.51) yields

$$\frac{\partial A}{\partial \tau} = -(1 + \mathrm{i})A + \frac{\mathrm{i}n_\mathrm{s}}{1 + \mathrm{i}\beta - \mathrm{i}a\nabla^2}\frac{A^*}{1 + |A|^2} \ , \tag{3.53}$$

where $\tau = \gamma t$ is a normalized time.

The stationary solution of (3.53) is $A(r,t) = A_0\exp(\mathrm{i}kr)$, where $A_0 = n_\mathrm{s}/2 - 1$ and $ak^2 = 1 - \beta$. This means that certain spatial modes with wavenumbers k proportional to the resonator detuning are favored. Note the presence of a constant frequency shift $\beta = 1$, which is different from the case of a laser.

The differential operator in (3.53) can be expanded in a Taylor series,

$$\frac{\mathrm{i}n_\mathrm{s}}{1 + \mathrm{i}\beta - \mathrm{i}a\nabla^2} = \frac{\mathrm{i}n_\mathrm{s}}{(1 + \mathrm{i}) + \mathrm{i}\left(\beta - 1 - a\nabla^2\right)} \tag{3.54}$$

$$\approx (1 + \mathrm{i})\frac{n_\mathrm{s}}{2}\left[1 - \frac{1 + \mathrm{i}}{2}\left(\beta - 1 - a\nabla^2\right) - \frac{\mathrm{i}}{4}\left(\beta - 1 - a\nabla^2\right)^2 + \cdots\right].$$

This is valid when the condition $\beta - 1 - a\nabla^2 \ll 1$ holds. As can be shown by an analysis of (3.53), this is the case for generation near the threshold, when $|A| \ll 1$, and thus the expansion is justified.

The expansion (3.54), truncated at the second order, and inserted into (3.53) leads to the equation

$$
\begin{aligned}
\frac{\partial A}{\partial \tau} = {} & \left(\frac{n_{\mathrm{s}}}{2} - 1 \right) (1 + \mathrm{i}) \, A - \mathrm{i} \frac{n_{\mathrm{s}}}{2} \left(\omega - a\nabla^2 \right) A \\
& + \mathrm{i} \, (1 + \mathrm{i}) \, \frac{n_{\mathrm{s}}}{8} \left(\omega - a\nabla^2 \right)^2 A - \frac{n_{\mathrm{s}}}{2} \, (1 + \mathrm{i}) \, X + \mathrm{i} \frac{n_{\mathrm{s}}}{2} \left(\omega - a\nabla^2 \right) X \\
& - \mathrm{i} \, (1 + \mathrm{i}) \, \frac{n_{\mathrm{s}}}{8} \left(\omega - a\nabla^2 \right)^2 X \;,
\end{aligned}
\tag{3.55}
$$

where $X = A \, |A|^2 / (1 + |A|^2)$ is a small quantity ($X \ll A$) and, in order to keep the analogy with lasers, we have defined $\omega = \beta - 1$.

Retaining in (3.55) only the terms at the leading order and applying the cubic approximation $X \approx (2/n_{\mathrm{s}}) \, A \, |A|^2$, we finally obtain

$$
\begin{aligned}
\frac{\partial A}{\partial \tau} = {} & \left(\frac{n_{\mathrm{s}}}{2} - 1 \right) (1 + \mathrm{i}) \, A - (1 + \mathrm{i}) \, |A|^2 \, A - \\
& \mathrm{i} \frac{n_{\mathrm{s}}}{2} \left(\omega - a\nabla^2 \right) A - \frac{n_{\mathrm{s}}}{8} \left(\omega - a\nabla^2 \right)^2 A \;,
\end{aligned}
\tag{3.56}
$$

which is again the CSH equation. However, there is an important difference between (3.56) and the CSH equations derived for lasers and OPOs: the coefficient of the nonlinear term is complex, which causes self-defocusing in this system.

3.5 Phenomenological Derivation of Order Parameter Equations

The CSH equation (3.47) was first derived for lasers [8]. Afterwards the same equation was derived for photorefractive oscillators [7] and for nondegenerate optical parametric oscillators [6]. The fact that the same order parameter equation has been derived for different types of nonlinear optical system hints at its universality. Its universality becomes evident when we derive the CSH equation phenomenologically from general symmetry assumptions, not restricting ourselves to a specific physical system. Let us assume for this purpose that an isotropic physical system characterized by a complex order parameter loses its stability at a nonzero wavenumber k_0. This means that the maximum of the real part of the dominating (largest and positive) instability branch crosses the $\lambda = 0$ axis at the wavenumber k_0, as illustrated in Fig. 3.1. The dominating instability branch can be approximated by a parabola at its maximum (near to the points where it crosses the $\lambda = 0$ axis),

$$
\lambda_{\mathrm{Re}}(k^2) = p - g \left(ak^2 - k_0^2 \right)^2 \;,
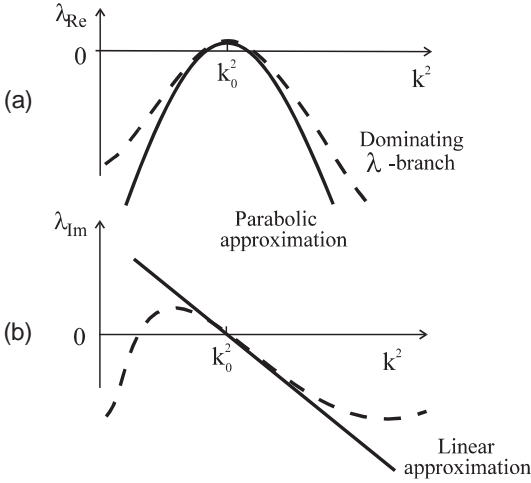\tag{3.57}
$$

Fig. 3.1. (**a**) Real part of the dominating Lyapunov exponents as a function of the transverse wavenumber (*dashed curve*), and the parabolic approximation (*solid curve*). (**b**) Imaginary part of the dominating Lyapunov exponent (*dashed curve*) and its linear approximation (*solid line*). The dashed curves are generic (they are free-hand curves). It is significant that the real part of the dominating Lyapunov exponent just crosses the $\lambda = 0$ axis from below

where p is a control parameter. The spatial isotropy implies that λ depends on $k^2 = |\boldsymbol{k}|^2$ and not on the first power of $\boldsymbol{k}$. The imaginary part of λ can be approximated by the line

$$\lambda_{\text{Im}}\left(k^2\right) = ak^2 - k_0^2 \ . \tag{3.58}$$

λ_{Im} is equal to zero at $k^2 = k_0^2$ if the reference frequency is equal to the central frequency of the gain line of the nonlinear optical system.

If we now substitute λ by the temporal derivative $\partial/\partial t$ (thus returning from the frequency spectrum to the evolution in time), and the wavenumber $\boldsymbol{k}$ by the differential operator $-\mathrm{i}\nabla$ (thus returning from the spatial spectrum to the distributions in space), then the linear part of the order parameter equation is recovered,

$$\frac{\partial A}{\partial \tau} = pA + \mathrm{i}\left(a\nabla^2 + k_0^2\right)A - g\left(a\nabla^2 + k_0^2\right)^2 A \ , \tag{3.59}$$

where $A(r,t)$ is an eigenvector associated with the relevant (most unstable) λ-branch and plays the role of an order parameter.

It remains to close the linear equation (3.59) using some nonlinearity, in order to prevent the infinite growth of unstable modes. If we assume the invariance of the field phase, we obtain a cubic, saturating, nonlinear term $A\left|A\right|^2$ in the lowest order. In fact, the terms $pA - A\left|A\right|^2$ represent a normal

form of the Hopf bifurcation, the bifurcation preserving the invariance of the phase of the order parameter. This closure of the linear equation (3.59) leads to

$$\frac{\partial A}{\partial \tau} = pA - A\left|A\right|^2 + \mathrm{i}\left(a\nabla^2 + k_0^2\right)A - g\left(a\nabla^2 + k_0^2\right)^2 A \;, \tag{3.60}$$

which is exactly equivalent to (3.47).

In such a way the CSH equation can be derived phenomenologically as a universal model that includes, in the lowest-order approximation, all the significant ingredients of a nonlinear optical system: (a) the finite width of the gain line, (b) spatial isotropy and (c) phase invariance. It is a normal form (a minimum equation) for a tunable system with a finite gain line width characterized by a Hopf bifurcation.

The above phenomenological derivation of (3.47) allows one to consider it as not only a simplified model equation for a specific physical system, such as a class A or class C laser, which is valid in a particular parameter range, but also as a universal model equation that describes a class of patterns and a class of phenomena in nonlinear optics in the lowest order of approximation.

In the same spirit, one can derive phenomenologically the real Swift–Hohenberg (RSH) equation, which was derived above for a DOPO. DOPOs are characterized not by a Hopf but by a pitchfork bifurcation (a DOPO favors two values of the phase, differing by π). The normal form of a pitchfork bifurcation is $pA - A^3$, where A is the real-valued order parameter. Adding the spatially dependent term, one obtains

$$\frac{\partial A}{\partial \tau} = pA - A^3 + \left(a\nabla^2 + k_0^2\right)^2 A \;, \tag{3.61}$$

which is the RSH equation. The RSH equation is actually valid not only for DOPOs, but also for degenerate four-wave mixers, for systems showing optical bistability [5], and for other systems showing phase squeezing.

References

1. G.L. Oppo, M. Brambilla, D. Camesasca, A. Gatti and L.A. Lugiato, Spatio temporal dynamics of optical parametric oscillators, J. Mod. Opt. **41**, 1151 (1994). 51
2. K. Staliunas, Transverse pattern formation in optical parametric oscillators, J. Mod. Opt. **42**, 1261 (1995). 53
3. L.A. Lugiato, C. Oldano, C. Fabre, E. Giacobino and R. Horowicz, Bistability, self-pulsing and chaos in optical parametric oscillators, Nuovo Cimento **10D**, 959 (1988). 54
4. J.B. Swift and P.C. Hohenberg, Hydrodynamic fluctuations at the convective instability, Phys. Rev. A **15**, 319 (1977). 55

5. P. Mandel, M. Georgiou and T. Erneux, Transverse effects in coherently driven nonlinear cavities, Phys. Rev. A **47**, 4277 (1993); G.J. de Valcárcel, K. Staliunas, E. Roldán and V.J. Sánchez-Morcillo, Transverse patterns in degenerate optical parametric oscillation and degenerate four-wave mixing, Phys. Rev. A **54**, 1609 (1996); S. Longhi and A. Geraci, Swift–Hohenberg equation for optical parametric oscillators, Phys. Rev. A **54**, 4581 (1996). 55, 63

6. V.J. Sánchez-Morcillo, E. Roldán, G.J. de Valcárcel and K. Staliunas, Generalized complex Swift-Hohenberg equation for optical parametric oscillators, Phys. Rev. A **56**, 3237 (1996). 59, 61

7. K. Staliunas, M.F.H. Tarroja, G. Slekys, C.O. Weiss and L. Dambly, Analogy between photorefractive oscillators and class-A lasers, Phys. Rev. A **51**, 4140 (1995). 60, 61

8. K. Staliunas, Laser Ginzburg-Landau equation and laser hydrodynamics, Phys. Rev. A **48**, 1573 (1993); J. Lega, J.V. Moloney and A.C. Newell, Universal description of laser dynamics near threshold, Physica D **83**, 478 (1995). 61

4 Zero Detuning: Laser Hydrodynamics and Optical Vortices

In this chapter, the properties of vortices in class A and class C lasers at zero detuning are investigated. As shown in the previous chapters, these classes of laser can be described by the complex Swift–Hohenberg equation (2.26), which in the zero-detuning case reads

$$\frac{\partial A}{\partial \tau} = pA + \mathrm{i}a\,\boldsymbol{\nabla}^2 A - \frac{\kappa^2}{(\kappa + \gamma_\perp)^2}a^2\,\boldsymbol{\nabla}^4 A - |A|^2\,A \; . \tag{4.1}$$

This equation is similar to the complex Ginzburg–Landau equation, except for the diffusion term. Instead of the Laplace operator describing the usual diffusion, here one has a second-order Laplace operator, corresponding to super-diffusion. Therefore, adopting the terminology of [1], we call (4.1) the laser Ginzburg–Landau (LGL) equation.

Equation (4.1) can be simplified by using the following normalizations for time, space and the order parameter: $\tau \to t/p$, $x \to x\sqrt{a/p}$ and $A \to A\sqrt{p}$. Now, instead of (4.1), we can deal with an LGL equation with only one free parameter,

$$\frac{\partial A}{\partial t} = A + \mathrm{i}\,\boldsymbol{\nabla}^2 A - g\,\boldsymbol{\nabla}^4 A - |A|^2\,A \; . \tag{4.2}$$

The remaining parameter in (4.2) is $g = p\kappa^2/(\kappa + \gamma_\perp)^2$, and thus all the properties of the solutions of the LGL equation depend on this g-factor, which has the meaning of a super-diffusion coefficient.

4.1 Hydrodynamic Form

The LGL equation (4.2) can be converted into a hydrodynamic form by using the Madelung transformation. Originally, Madelung demonstrated [2] that the transformation of the order parameter $A(\boldsymbol{r}, t) = \sqrt{\rho(\boldsymbol{r}, t)}\exp\left[\mathrm{i}\Phi(\boldsymbol{r}, t)\right]$ brings the nonlinear Schrödinger equation into a hydrodynamic form, where the intensity plays the role of a (super)fluid density, and the phase gradient $\boldsymbol{\nabla}\Phi(\boldsymbol{r}, t)$ the role of a velocity. Performing the same transformation in (4.2), we obtain

$$\frac{\partial \rho}{\partial t} = 2\rho - 2\rho^2 - 2\,\boldsymbol{\nabla}(\rho\,\boldsymbol{\nabla}\Phi) \ , \tag{4.3a}$$

$$\frac{\partial \Phi}{\partial t} = -g\boldsymbol{\nabla}^4\Phi + \frac{\boldsymbol{\nabla}(2\sqrt{\rho})}{\sqrt{\rho}} - (\boldsymbol{\nabla}\Phi)^2 \ . \tag{4.3b}$$

In (4.3) the super-diffusion has been assumed to be small: all the terms containing the coefficient g have been neglected, except for the most significant one ($g\,\boldsymbol{\nabla}^4\Phi$ in (4.3b)). Normalizing again the spatial variables with the change $r/\sqrt{2} \to r$, and rewriting (4.3) in terms of the velocity in the transverse space $\boldsymbol{v} = \boldsymbol{v}_\perp = \boldsymbol{\nabla}\Phi$, we obtain

$$\frac{\partial \rho}{\partial t} + \boldsymbol{\nabla}(\rho\boldsymbol{v}) = 2\rho - 2\rho^2 \ , \tag{4.4a}$$

$$\frac{\partial \boldsymbol{v}}{\partial t} + (\boldsymbol{v}\boldsymbol{\nabla})\boldsymbol{v} = -\frac{g}{2}\boldsymbol{\nabla}^4\boldsymbol{v} + \boldsymbol{\nabla}\left(\frac{\boldsymbol{\nabla}(\sqrt{\rho})}{2\sqrt{\rho}}\right). \tag{4.4b}$$

Equations (4.4) describe, in the hydrodynamic analogy, the evolution of a "photon fluid". The left parts of the equations can be interpreted as the conservation of mass and momentum (the analogues of the continuity and Euler equations, respectively). The right part of (4.4a) describes the presence of sources and sinks: "mass" is created owing to the linear gain and dissipates owing to the saturation of the inversion in the laser. The right part of (4.4b) can be interpreted as the dissipation of momentum due to super-viscosity, which is proportional to the g-factor. The last term in (4.4b), called the "quantum pressure" term, has no analogue in standard fluid mechanics.

The "photon fluid" in a laser as described by the LGL equation does not possess the usual compressibility, where the internal pressure is proportional to some local function of the density (note that the quantum pressure in (4.4b) is nonlocal). However, a classical pressure can occur if we consider an additional self-focusing or self-defocusing mechanism, e.g., if a focusing–defocusing Kerr material is present in the laser resonator. In this case the LGL equation becomes

$$\frac{\partial A}{\partial t} = A + \mathrm{i}\,\boldsymbol{\nabla}^2 A - g\,\boldsymbol{\nabla}^4 A - (1 + \mathrm{i}\alpha)\,|A|^2\,A \ . \tag{4.5}$$

The Euler equation (4.4b) is modified because of this self-focusing/defocusing to

$$\frac{\partial \boldsymbol{v}}{\partial t} + (\boldsymbol{v}\boldsymbol{\nabla})\boldsymbol{v} = -\frac{\boldsymbol{\nabla}p}{\rho} - \frac{g}{2}\boldsymbol{\nabla}^4\boldsymbol{v} + \boldsymbol{\nabla}\left(\frac{\boldsymbol{\nabla}(\sqrt{\rho})}{2\sqrt{\rho}}\right), \tag{4.6}$$

where the classical pressure is proportional to the fluid density, since $p = \alpha\rho^2/2$. For a defocusing medium ($\alpha > 0$) the compressibility relation is "normal", while for a focusing medium ($\alpha < 0$) it is "anomalous".

Looking ahead (this topic will be treated in detail in Chap. 6), in the case of a curved (parabolic) resonator, an additional external potential appears in

the laser hydrodynamic equation. The curved mirrors result in an additional term in the right-hand side of the LGL equation (4.2), given by $-\mathrm{i}c\boldsymbol{r}^2 A$, where c is the curvature of the mirrors. The form of this new term arises from the fact that the curved mirrors correspond to a spatial dependence of the resonator detuning parameter, which is parabolic in a first approximation. Taking the curvature into account leads to the corresponding Euler equation,

$$\frac{\partial \boldsymbol{v}}{\partial t} + (\boldsymbol{v}\boldsymbol{\nabla})\boldsymbol{v} = -\boldsymbol{\nabla}V - \frac{\boldsymbol{\nabla}p}{\rho} - \frac{g}{2}\boldsymbol{\nabla}^4 \boldsymbol{v} + \boldsymbol{\nabla}\left(\frac{\boldsymbol{\nabla}(\sqrt{\rho})}{2\sqrt{\rho}}\right), \qquad (4.7)$$

where $V(\boldsymbol{r})$ is a potential holding the laser fluid inside the resonator (in the lateral direction).

Summarizing, the transverse dynamics of the laser radiation are analogous to the dynamics of a compressible, quantized fluid. The parabolic mirrors of the laser resonator result in a parabolic potential, which localizes the laser fluid. The compressibility law of the laser fluid is nonlocal, and a local compressibility/anticompressibility term appears when additional self-defocusing/focusing effects are included. Finally, the super-viscosity of the laser fluid $p\kappa^2/\left[2(\kappa + \gamma_\perp)\right]^2$ is inversely proportional to the width of the gain line.

4.2 Optical Vortices

The radiation of lasers, being similar to fluids and superfluids, can be expected to show vortices. Optical vortices can indeed be obtained by integrating the LGL equation (4.2) numerically. In the first approximation, an optical vortex has a helical wavefront, and therefore can be described asymptotically (at the core) by

$$A(r) = r\exp(\mathrm{i}m\varphi) , \qquad (4.8)$$

where $m = \pm 1$ is the topological charge of the vortex, and (r, φ) are polar coordinates centered at the vortex core. In general, the distribution of the field in the presence of an optical vortex is

$$A(r) = R(r)\exp\left[\mathrm{i}m\varphi + \mathrm{i}\Phi(r)\right] , \qquad (4.9)$$

where the amplitude $R(r)$ saturates far away from the vortex core, and $\Phi(r)$ is the radial phase responsible for the radiation from the vortex.

When $\Phi(r)$ is a constant (corresponding to a uniform radial phase), the lines of equal phase are directed radially from the vortex core (Fig. 4.1, left), and the flow of the photon fluid around the vortex is purely azimuthal. The vortex does not radiate in this case. In general, however, the flow has a radial component, as shown in Fig. 4.1 on the right. The origin of the radial flow
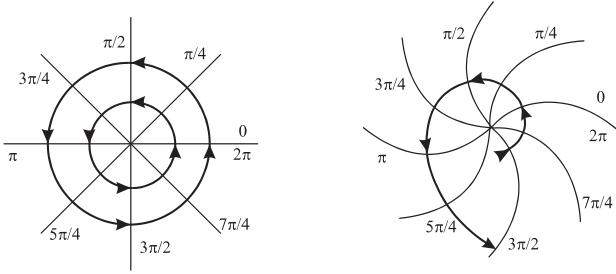
Fig. 4.1. Phase isolines around an optical vortex, shown by *thin lines or curves*, and flow lines (along the phase gradient), shown by *thick lines* with arrows. *Left*: optical vortex with constant radial phase. *Right*: optical vortex with radial phase growing monotonically away from the vortex core

component is that fluid is created at the vortex core (where the amplification (source) dominates over the saturation (sink) in (4.4a)), and flows outwards, where the sources and sinks compensate one another. Such radiating vortices are sometimes called spiral waves, since the equiphase lines are of spiral shape.

The vortex solution (4.9), however, does not posses an explicit algebraic form for the LGL equation in two spatial dimensions. In order obtain insight into the properties of the vortex (e.g. the size of the vortex core, and the vortex radiation), an analysis of a 1D analogue of a vortex is useful. The 1D analogue of a vortex is a kink wave that is equal to zero at the vortex core $(x = 0)$, and approaches asymptotic values with constant amplitude and opposite phases at $x = \pm\infty$.

In the next section, the 1D version of (4.2) is analyzed in two limits separately: (1) in the limit of strong diffraction ($g \ll 1$), and (2) in the limit of strong diffusion ($g \gg 1$).

4.2.1 Strong Diffraction

In the strong-diffraction limit ($g \ll 1$), (4.2) converts to

$$\frac{\partial A}{\partial t} = A + i\frac{\partial^2 A}{\partial x^2} - |A|^2 A \ . \tag{4.10}$$

A solution in the form of a kink can be found straightforwardly using an ansatz of the form $A(x,t) = \tanh(x/x_0)\exp\left[-i\omega t + i\Phi(x)\right]$, with a phase gradient $\Phi_x = (\alpha/x_0)\tanh(x/x_0)$. Inserting the ansatz into (4.10), one obtains the half-width of the kink x_0, the kink radiation factor α and the frequency ω:

$$x_0^2 = 3\sqrt{2}\ , \quad \alpha = \sqrt{2}\ , \quad \omega = \frac{1}{3\sqrt{2}}\ . \tag{4.11}$$

These values apply approximately in the 2D case for an optical vortex, where the half-width of the kink x_0 plays the role of the vortex core radius r_0. The

numerical values of the parameters differ slightly in the 2D case, but the scalings hold.

As follows from this analysis, the radial phase of the vortex is not uniform, since $\Phi_r = (\alpha/r_0)\tanh(r/r_0)$. According to the hydrodynamic analogy, where the phase gradient is equivalent to the velocity of the flow, the vortex creates a flow outwards or, in optical terms, the vortex radiates. The radiation is zero close to the vortex core (the radial phase variation is zero at this point), and increases away from it, saturating at a constant value. The saturation value with the initial normalizations of (4.1) is

$$\Phi_r^{\text{sat}} = \sqrt{\frac{\sqrt{2}p}{3a}} \approx 0.687\sqrt{\frac{p}{a}} \; . \tag{4.12}$$

The equal-phase lines therefore form spirals, as shown in the right-hand side of Fig. 4.1.

This provides an interpretation of the existence of "shocks" between vortices: the radiation from the neighboring vortices propagates, and collides. Owing to the collision, "shocks" appear.

The vortex core radius, expressed in terms of the initial parameters of (4.1), is proportional to the diffraction coefficient in this limit of strong diffraction:

$$r_0^2 = 3\sqrt{2}\left(\frac{a}{p}\right) . \tag{4.13}$$

In Fig. 4.2, several vortex ensembles are shown in the strong-diffraction case, as obtained by numerical integration of (4.1).

It is interesting to note that the motion of the vortices is nearly chaotic. Annihilation of vortices is observed, as well as nucleation of new pairs of vortices. From a statistical point of view, the distribution of vortices remains
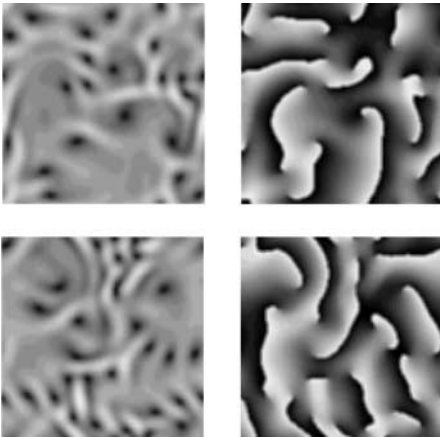

Fig. 4.2. The amplitude (*left*) and the phase (*right*) obtained by numerical integration of the LGL equation (4.2) with $g = 0.2$. The distributions in the *top row* are obtained at time $t = 100$, and those in the *bottom row* at time $t = 300$

unchanged during the calculation: the density of vortices is nearly the same in the top and bottom plots in Fig. 4.2. The chaotic vortex motion in the CGL equation has been shown to be at the root of "defect-mediated turbulence" [3].

In order to check the predicted vortex behavior, several experiments have been performed with a broad-aperture photorefractive oscillator, which, as shown in Chap. 3, is the analogue of a laser described by the LGL equation. In the strong diffraction limit, ensembles of vortices with shocks were observed [4].

Figure 4.3 shows experimentally recorded patterns obtained by tuning the resonator length so that the ring in the far field contracted to a central spot (right). This siuation corresponds to zero resonator detuning. Optical vortices separated by shocks are seen in the near-field pattern (left), in accordance with the theoretical predictions. The orientation of the shock boundaries and the locations of vortices evolved freely in time and were not imposed by the boundaries. The patterns display central symmetry, which is imposed by the confocality of the resonator (see Chap. 6 for a discussion of confocal resonators). The mismatch l from the confocal length in the experiment was around 5 mm. Judging from the observed patterns, the diffraction dominated over diffusion in this case.
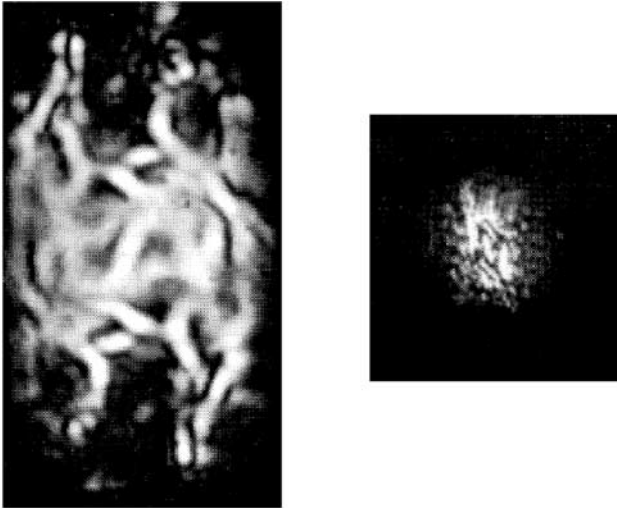

Fig. 4.3. Vortices separated by shocks for zero detuning: the near-field distribution is shown at the *left*, and the far-field distribution at the *right*. The deviation from the confocal length was around 5 mm, and thus diffraction dominates over diffusion. The pump field intensity was twice the threshold value

4.2.2 Strong Diffusion

Consider now the strong-diffusion limit $(g \gg 1)$, in which (4.2) reads

$$\frac{\partial A}{\partial t} = A - g\frac{\partial^4 A}{\partial x^4} - |A|^2 A \ . \tag{4.14}$$

Obviously, one can scale out the parameter g in this limit. However, we keep it in order to avoid misunderstandings, and keep the normalizations defined previously.

The natural guess for the solution of (4.14) in 1D is again a kink, $A\left(r,t\right) = \tanh(x/x_0)$, now with a uniform phase profile. This form of kink, however, is not an exact solution of (4.14), as is easy to find by a direct test. Therefore one can use it only as an approximate solution.

Next, we use the fact that (4.14) is variational, i.e. it can be expressed in variational form as $\partial_t A = -\delta\mathcal{F}/\delta A^*$, where $\mathcal{F}(A)$ is a real-valued variational potential given by

$$\mathcal{F} = \int_{-\infty}^{\infty} \left(-|A|^2 + \frac{1}{2}|A|^4 + \left|\frac{\partial^2 A}{\partial x^2}\right|^2 \right) dx \ . \tag{4.15}$$

This allows us to determine the half-width of the kink solution by inserting the ansatz into the variational functional, and minimizing (4.15) with respect to x_0.

If we substitute the hyperbolic-tangent ansatz into (4.15), an infinite value is obtained for the potential. This is due to the contribution of the homogeneous background of amplitude $|A_0| = 1$. Therefore we calibrate the potential (4.15) by subtracting this constant contribution:

$$\mathcal{F} = \int_{-\infty}^{\infty} \left(-|A|^2 + \frac{1}{2}|A|^4 + \frac{1}{2} + \left|\frac{\partial^2 A}{\partial x^2}\right|^2 \right) dx \ . \tag{4.16}$$

Integration of (4.16) now gives a finite value for the potential,

$$\mathcal{F}(x_0) = \frac{16g + 5x_0^4}{120x_0^3} \ . \tag{4.17}$$

The value of the half-width that minimizes the potential $\mathcal{F}$ is given by $x_0^4 = (24/5)\,g$. The vortex core radius is therefore proportional to the diffusion coefficient in this limit of strong diffusion, if we use the initial normalization of (4.1):

$$r_0^2 = \sqrt{\frac{24}{5}}\frac{a}{\sqrt{p}}\frac{\kappa}{\kappa + \gamma_\perp} \ . \tag{4.18}$$

The radial phase is constant in this limit. Vortices do not radiate when diffusion is the dominating process and, consequently, they do not cause shocks in vortex ensembles.
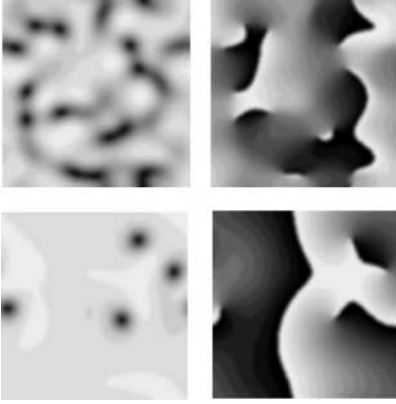
Fig. 4.4. The amplitude and phase, as obtained by numerical integration of (4.1) with $g = 10$. The distributions calculated at $t = 8$ and $t = 150$ are shown in the *top* and *bottom* rows respectively

Figure 4.4 illustrates the dynamics of a vortex ensemble in the strongly diffusive case, as obtained by numerical integration of (4.1).

The number of vortices decreases with time in this diffusive limit. This is in contrast with Fig. 4.2, which shows no variation in the number of vortices, in a statistical sense, in the diffractive limit.

Annihilation of vortices, and a plane wave as the final state can be expected, since the diffusive limit is a variational one. Variational systems develop in such a way that they reach the minimum of the variational potential along the shortest path (along the gradient of the potential).

In experiments, the diffusive case is obtained when the resonator length is precisely tuned to the self-imaging length, as shown in Chap. 6. An example of a pattern recorded under such conditions is shown in Fig. 4.5. An obvious difference from the distribution shown in Fig. 4.3 is the absence of shocks.

4.2.3 Intermediate Cases

It is difficult to perform analytical evaluations of the vortex parameters for arbitrary diffraction–diffusion ratios. However, the vortex behavior in this intermediate case can be extrapolated from the two limits. Qualitatively, one can expect that the closer the parameters are to the diffractive limit (small g), the more the vortices radiate, and the more prominent the shocks in vortex ensembles are. Also, the dynamics are more chaotic. On the other hand, the closer the parameters are to the diffusive limit (large g), the more the vortices tend to annihilate and disappear.

Some quantitative evaluations can be performed with a simplified version of the LGL equation, namely the ordinary CGL equation, which contains normal diffusion. In two dimensions, this equation reads

$$\frac{\partial A}{\partial t} = A + ia_{\mathrm{Im}} \, \boldsymbol{\nabla}^2 A + a_{\mathrm{Re}} \, \boldsymbol{\nabla}^2 A - |A|^2 \, A \; , \tag{4.19}$$

where a_{Im} and a_{Re} are the diffraction and diffusion coefficients, respectively.
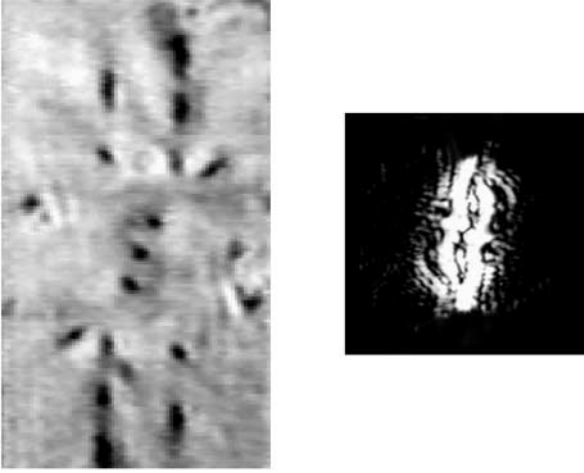
Fig. 4.5. Vortices for zero detuning, for a perfectly confocal resonator, when the diffusion dominates over the diffraction. The pump field intensity was twice the threshold value. Shocks are absent because diffusion dominates

In one transverse dimension, (4.19) possesses an exact kink solution in the form $A(x,t) = \beta \, \tanh(x/x_0) \exp\left[-i\omega t + i\Phi(x)\right]$, where the gradient of the phase is given by $\Phi_x = (\alpha/x_0) \tanh(x/x_0)$. Substitution in (4.19) allows us to evaluate the parameters of the kink:

$$x_0^2 = -\frac{5}{2}a_{\mathrm{Re}} + \sqrt{\left(\frac{9}{2}\right)a_{\mathrm{Re}}^2 + 18a_{\mathrm{Im}}^2} \; , \tag{4.20a}$$

$$\alpha = -\frac{3}{2}\frac{a_{\mathrm{Re}}}{a_{\mathrm{Im}}} + \sqrt{\left(\frac{3a_{\mathrm{Re}}}{2a_{\mathrm{Im}}}\right)^2 + 2} \; . \tag{4.20b}$$

In two transverse dimensions, no algebraic vortex solution exists. However, the parameters obtained for the kink solution can again be supposed to be valid also for the vortex solution, with the width of the kink x_0 corresponding now to the radius of the vortex core r_0.

Consider now the two limiting cases of (4.20).

In the diffractive case, where $a_{\mathrm{Im}} \gg a_{\mathrm{Re}}$, the vortex radius is given by

$$r_0^2 = 3\sqrt{2}a_{\mathrm{Im}} - \frac{5}{2}a_{\mathrm{Re}} \; , \tag{4.21}$$

and is mainly determined by diffraction. The vortex radiation parameter is

$$\alpha = \sqrt{2} - \frac{3}{2}\frac{a_{\mathrm{Re}}}{a_{\mathrm{Im}}} \; , \tag{4.22}$$

which asymptotically approaches its maximum value as the purely diffractive case is approached.

In the diffusive case, where $a_{\mathrm{Im}} \ll a_{\mathrm{Re}}$, the vortex radius is given by

$$r_0^2 = 2a_{\mathrm{Re}} + 2\frac{a_{\mathrm{Im}}^2}{a_{\mathrm{Re}}} \; , \tag{4.23}$$

and is mainly determined by diffusion. The radiation parameter is

$$\alpha = \frac{2a_{\mathrm{Im}}}{3a_{\mathrm{Re}}} \; , \tag{4.24}$$

which is linearly proportional to the diffraction/diffusion ratio. In the purely diffusive limit α tends to zero, corresponding to a uniform phase.

Note that, with the appropriate scalings (the parameter $a_{\mathrm{Im}}/a_{\mathrm{Re}}$ used for asymptotic expansions plays the role of the g-factor of (4.2), as can be easily checked), these results agree with those obtained for the vortices of the LGL equation in the corresponding limits, thus justifying the use of (4.19) to evaluate the vortex parameters.

4.3 Vortex Interactions

A single, isolated vortex on a homogeneous background is stationary. If the spatial symmetry is broken, the vortex starts to move. The symmetry can be broken by a gradient of the background field on which the vortex is superimposed. For the study of vortex interactions, we assume the presence of two vortices; one vortex creates inhomogeneities, and the other vortex moves because of those inhomogeneities, and vice versa.

A vortex creates phase as well as amplitude inhomogeneities. Vortices interact predominantly as a result of phase inhomogeneities, since the amplitude inhomogeneities decay rapidly far away from the vortex core. The phase gradient has an angular component due to the helicity of the vortex, and also a radial component due to the vortex radiation, as discussed in the previous section. Therefore, we already know how the first vortex imposes phase inhomogeneities. To understand the vortex dynamics, one must find out how the second vortex responds to those phase inhomogeneities.

A mathematically rigorous derivation of the vortex–vortex interaction can be found in [5, 6]. Here we sketch a phenomenological theory, which is simpler and more transparent.

We assume that the second vortex is imposed on a tilted wave $\exp(i\boldsymbol{k} \cdot \boldsymbol{r})$, and rewrite (4.19)[1] with the ansatz $A(\boldsymbol{r}, t) = \exp(i\boldsymbol{k} \cdot \boldsymbol{r})\, B(\boldsymbol{r}, t)$:

---

[1] For simplicity, we study the ordinary CGL equation. The main properties of the dynamics of vortices for the LGL equation are analogous, and will be discussed below in the present chapter.

$$\frac{\partial B}{\partial t} + 2a_{\mathrm{Im}}(\boldsymbol{k} \cdot \boldsymbol{\nabla})B - 2\mathrm{i}a_{\mathrm{Re}}(\boldsymbol{k} \cdot \boldsymbol{\nabla})B$$
$$= (1 - a_{\mathrm{Re}}\boldsymbol{k}^2 - \mathrm{i}a_{\mathrm{Im}}\boldsymbol{k}^2)B - |B|^2\,B + \mathrm{i}a_{\mathrm{Im}}\,\boldsymbol{\nabla}^2 B + a_{\mathrm{Re}}\,\boldsymbol{\nabla}^2 B \ . \tag{4.25}$$

The presence of the background tilted wave decreases the gain and shifts the frequency (the first term on the right-hand side in (4.25)), owing to the mismatch from the resonance (a tilted wave is at resonance in a laser with zero detuning). The remaining three terms on the right-hand side indicate that the presence of the background tilted wave does not alter the nonlinearity, the diffraction or the diffusion. Therefore the vortex solution (modified by a change of the gain) makes the right-hand side of (4.25) equal to zero. The terms on the left-side of the equation are responsible for the vortex motion.

The term $2a_{\mathrm{Im}}(\boldsymbol{k} \cdot \boldsymbol{\nabla})B$ implies a uniform translation of the vortex envelope $B(\boldsymbol{r}, t)$ with a velocity $\boldsymbol{v} = 2a_{\mathrm{Im}}\boldsymbol{k}$. Indeed, the solution $B(\boldsymbol{r}, t) = B_{\mathrm{v}}(\boldsymbol{r} - 2a_{\mathrm{Im}}\boldsymbol{k}t)$ makes the first two terms of the left-hand side of (4.25) equal to zero. The vortex envelope $B_{\mathrm{v}}(\boldsymbol{r}, t)$ thus translates at a certain velocity, or, in other words, is advected by the photon flow. In general, not only a vortex but also an arbitrary inhomogeneity is advected by a background flow. Note that no assumption about the form of the perturbation $B(\boldsymbol{r}, t)$ has been made to calculate the advection.

The term with imaginary coefficient $2\mathrm{i}a_{\mathrm{Re}}(\boldsymbol{k} \cdot \boldsymbol{\nabla})B$, evaluated asymptotically close to the vortex core, can be rewritten as follows. The asymptotic form of B_{v} close to the vortex is $B_{\mathrm{v}}(\boldsymbol{r}, t) = x + \mathrm{i}my$ ($m = \pm 1$), and the following relation is valid:

$$\mathrm{i}(\boldsymbol{k} \cdot \boldsymbol{\nabla})B_{\mathrm{v}} = (m\boldsymbol{k}_{\perp} \cdot \boldsymbol{\nabla})B_{\mathrm{v}} \ , \tag{4.26}$$

where $\boldsymbol{k}_{\perp}$ is perpendicular to the gradient of the background tilted wave of wavevector $\boldsymbol{k}$ (it is rotated counterclockwise by $90°$). As a result, we obtain an asymptotic equation for the motion of the vortex envelope,

$$\frac{\partial B_{\mathrm{v}}}{\partial t} + 2a_{\mathrm{Im}}(\boldsymbol{k} \cdot \boldsymbol{\nabla})B_{\mathrm{v}} - 2a_{\mathrm{Re}}m(\boldsymbol{k}_{\perp} \cdot \boldsymbol{\nabla})B_{\mathrm{v}} = 0 \tag{4.27}$$

and, consequently, an expression for the vortex velocity,

$$\boldsymbol{v} = 2a_{\mathrm{Im}}\boldsymbol{k} - 2a_{\mathrm{Re}}\boldsymbol{m} \times \boldsymbol{k} \ , \tag{4.28}$$

where $\boldsymbol{m}$ is a unit vector which is transverse to the (x, y) plane, and directed along the z axis (optical axis) for a vortex with positive topological charge, and in the opposite direction for a negative charge.

From this analysis, it follows that the vortices are advected by the mean flow, and move with the flow velocity. Diffraction is responsible for the hydrodynamic advection. Owing to diffusion, however, the vortices have a velocity component transverse to the flow. The hydrodynamic interpretation of this transverse velocity component of a vortex is the gyroscopic Magnus force: a vortex (and any rotating object in general) adquires a velocity component

transverse to the direction of the force acting on it. The Magnus force depends on the sense of rotation of a rotating body in hydrodynamics and, equivalently, on the topological charge of the optical vortex m in nonlinear optics (4.28). The magnitude of the Magnus force is proportional to the diffusion coefficient.

A similar analysis performed on the LGL equation (4.2) reveals that the vortex motion induced by the phase gradient is described by

$$\boldsymbol{v} = 2\boldsymbol{k} - 4g\,|\boldsymbol{k}|^2\,\boldsymbol{m} \times \boldsymbol{k}, \qquad\qquad (4.29)$$

where the advection along $\boldsymbol{k}$ is the same as for the CGL equation, but the transverse motion is proportional to the third power of the wavenumber $|\boldsymbol{k}|$ of the background tilted wave, since not the usual diffusion but super-diffusion is present in the LGL equation.

In Fig. 4.6, results of numerical calculations based on (4.2) demonstrating vortex motion in a phase gradient are shown.
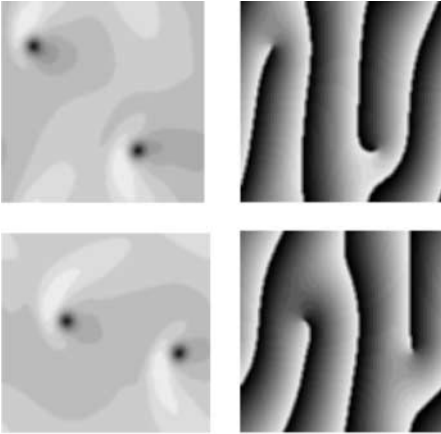
Fig. 4.6. Two vortices advected by a background flow, for $g = 4$. The phase gradient, visible from the phase pictures (*right*), is directed to the right. The time t between pictures is 40

The vortex velocity component directed along the phase gradient is independent of the vortex charge. The transverse (gliding) component depends on the charge: the positively charged vortex at the top left corner of Fig. 4.6 glides downwards, while the negatively charged vortex at the bottom right corner glides upwards.

Vortices gliding perpendicular to the background tilted wave diminish their average tilt. Indeed, below the positively charged vortex in Fig. 4.6, the tilt is larger than above the vortex: above the positively charged vortex there are three vertical interference fringes, while below there are four fringes. The zero-detuned (resonant) laser "prefers" a homogeneous distribution, because this corresponds to a minimum of the variational potential. Thus a vortex glides in such a way as to minimize the potential energy of the laser.
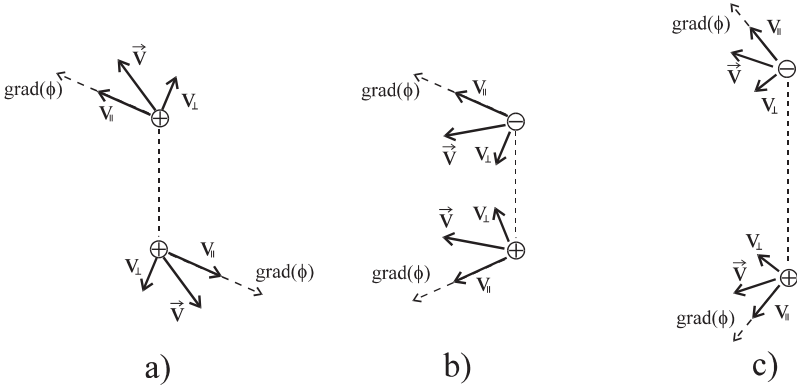
Fig. 4.7. Interaction of two vortices: (**a**) of the same charge; (**b**) of opposite charge at small separation; (**c**) of opposite charge at large separation

Once one knows how vortices create phase gradients and how they move because of phase gradients, one can analyze the interaction of vortices.

A system of two equally charged vortices is shown in Fig. 4.7a. The first vortex imposes an angular and a radial phase variation at the location of the second vortex, and vice versa, as shown by the dashed arrows. The induced velocity components are indicated by solid arrows. It follows that two positively charged vortices rotate one around another anticlockwise; if, on the other hand, both are negatively charged, they rotate clockwise. The vortices also repel one another, and the separation between them grows. This picture of the interaction remains qualitatively the same for different diffusion–diffraction ratios $a_{\mathrm{Re}}/a_{\mathrm{Im}}$ for the CGL equation (4.19) or, equivalently, for different values of g for the LGL equation (4.2).

This also provides evidence that vortices of charge larger than one are never stable in broad-aperture lasers.

The behavior of two vortices with opposite charge is illustrated in Figs. 4.7b,c. It follows that a vortex pair translates in a direction perpendicular to the line connecting the vortex cores. The vortex separation can increase or decrease during the course of translation, depending on the diffusion/diffraction ratio and on their initial separation. For a small initial separation, the vortices attract one another and eventually annihilate. For a sufficiently large separation, the vortices repel one another. This follows from simple geometrical considerations, as illustrated in Figs. 4.7b,c: recall that the radial phase variation increases and the angular phase variation decreases monotonically with the vortex separation.

It is possible to evaluate analytically the critical separation of oppositely charged vortices for the CGL equation. At the critical radius, the relation $a_{\mathrm{Re}}/a_{\mathrm{Im}} = \Phi_r/\Phi_\varphi$ holds. The radial and angular phase variations are $\Phi_r = (\alpha/r_0)\tanh(r/r_0)$, and $\Phi_\varphi = 1/r$. Therefore, the critical separation r_{cr} can

be calculated from the transcendental equation

$$\frac{a_{\mathrm{Re}}}{a_{\mathrm{Im}}} = \alpha \left(\frac{r_{\mathrm{cr}}}{r_0} \right) \tanh \left(\frac{r_{\mathrm{cr}}}{r_0} \right). \tag{4.30}$$

The critical vortex separation increases with increasing diffusion, as (4.30) shows. In the strong-diffusion limit, the equilibrium vortex separation can be expressed analytically, and is given by

$$\frac{r_{cr}}{r_0} = \frac{3}{2} \left(\frac{a_{\mathrm{Re}}}{a_{\mathrm{Im}}} \right)^2. \tag{4.31}$$

A similar analysis for the LGL equation yields the result that the critical vortex separation is linearly proportional to $g : r_{\mathrm{cr}}/r_0 \approx g$.

In all cases, the more diffusive the system is, the more dilute is the vortex gas at equilibrium. The equilibrium density of a vortex gas is thus proportional to $n \approx (r_0/r_{\mathrm{cr}})^2 \approx 1/g^2$.

The above scenario of vortex interaction is, however, valid only in the limit where diffusion dominates. When diffraction dominates, the shocks between neighboring vortices can significantly alter the picture discussed above. Figure 4.8. shows how the presence of shocks can strongly influence the vortex interaction.
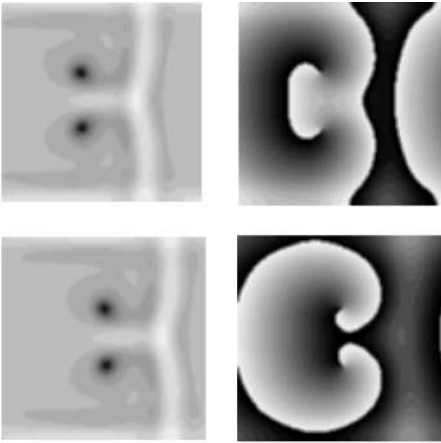

Fig. 4.8. Two vortices interacting with a shock in between them, for $g = 0.5$. In each of the pictures, the upper vortex has a negative topological charge, and the lower has a positive topological charge. The time t between pictures is 40

The vortices in Fig. 4.8 are expected to propagate to the left, according to the analysis given above (Fig. 4.7); since the bottom vortex is of positive charge, it should drive the upper vortex to the left, and since the upper vortex is of negative charge, it should drive the bottom vortex to the left too. This occurs for a large diffusion parameter $g \gg 1$, as numerical integration of (4.2) shows. This is also the case in the initial stage of evolution for the

relatively small diffusion parameter $g = 0.5$ used in the calculations by which Fig. 4.8 was obtained. However, the vortices interact "correctly" only before the shock develops between them. After the shock develops, it begins to screen the vortices from one another, and the phase gradients caused by one vortex are no longer visible to the other vortex. The vortices then move not because of a mutual interaction mediated by phase gradients, but because of interaction with the shock. The bottom vortex then moves to the right, as rolling along the shock. The upper vortex also rolls to the right, for the same reason.

The interaction between vortices and shocks can be understood in terms of vortex motion due to amplitude gradients, as investigated in [7]. An amplitude gradient (a gradient of the fluid density) causes a gradient of the pressure, owing to the compressibility relation in the laser–hydrodynamics analogy. The pressure gradient, according to the laser hydrodynamic equations (4.4), causes a drift of the vortex. The vortex drift has, however, a component perpendicular to the force acting on the vortex. This is the Magnus drift: not only a vortex, but also every rotating object undergoes a drift perpendicular to the force acting on it.

References

1. K. Staliunas, Laser Ginzburg–Landau equation and laser hydrodynamics, Phys. Rev. A **48**, 1573 (1993). 65
2. E. Madelung, Quantentheorie in hydrodynamischer form, Z. Phys. **40**, 322 (1926). 65
3. P. Coullet, L. Gil and J. Lega, Defect-mediated turbulence, Phys. Rev. Lett. **62**, 1619 (1989). 70
4. K. Staliunas, G. Slekys and C.O. Weiss, Nonlinear pattern formation in active optical systems: shocks, domains of tilted waves, and cross-roll patterns, Phys. Rev. Lett. **79**, 2658 (1997). 70
5. S. Rica and E. Tirapegui, Interaction of defects in two-dimensional systems, Phys. Rev. Lett. **64**, 878 (1990). 74
6. S. Aranson, L. Kramer and A. Weber, Interaction of spirals in oscillatory media, Phys. Rev. Lett. **67**, 404 (1991). 74
7. K. Staliunas, Dynamics of optical vortices in a laser beam, Opt. Commun. **90**, 123 (1992). 79

5 Finite Detuning: Vortex Sheets and Vortex Lattices

In this chapter, the spatio-temporal dynamics of the fields emitted by class A and C lasers are investigated in the case of moderate negative detuning. The transverse field dynamics in lasers are described by the CSH equation (2.26), as derived in Chap. 2. In this chapter, the same normalizations as in (4.2) are used, bringing (2.26) into the form

$$\frac{\partial A}{\partial t} = A + \mathrm{i}\left(\boldsymbol{\nabla}^2 + \Delta\right)A - g\left(\boldsymbol{\nabla}^2 + \Delta\right)^2 A - |A|^2 A \,, \tag{5.1}$$

where the normalized detuning $\Delta = -\omega/p$ has also been defined. Note that the laser detuning ω and that of the CSH equation given by (5.1) are defined with opposite signs. As follows from the linear stability analysis in Chap. 2, laser patterns appear in the blue-detuned case $\omega < 0$ (when the cavity resonance frequency is less than the central frequency of the atomic transition). On the other hand, it is customary to write the real and complex Swift–Hohenberg equations in the form (5.1), where patterns occur for positive values of Δ.

The simplest solution of (5.1) is a tilted (or traveling) wave (TW),

$$A(\boldsymbol{r}, t) = \exp(\mathrm{i}\boldsymbol{k}\boldsymbol{r}), \tag{5.2}$$

with a wavevector $\boldsymbol{k}$ pertaining to the resonant ring (the modes obeying $|\boldsymbol{k}| = \sqrt{\Delta}$, which, as predicted by the linear stability analysis in Chap. 2, experience the maximum amplification).

If the wavenumber of the TW is mismatched from that of the maximally amplified mode (the wavelength is shorter or longer than the resonant value), the resulting TW solution is

$$A(\boldsymbol{r}, t) = \left[1 - g\left(|\boldsymbol{k}|^2 - \Delta\right)^2\right]\exp\left[\mathrm{i}\boldsymbol{k}\cdot\boldsymbol{r} - \mathrm{i}\left(k^2 - \Delta\right)t\right], \tag{5.3}$$

which has an amplitude smaller than that of the resonant TWs, and oscillates with a frequency proportional to the mismatch $\Delta\omega = k^2 - \Delta$, where $k = |\boldsymbol{k}|$. The dependence of the amplitude of the TW on the mismatch $\Delta\omega$ in (5.3) is similar to the usual resonance curve of a driven oscillator.

The presence of traveling waves is closely related to the existence and dynamics of vortices, as already discussed in Chap. 4. In Sect. 5.1 the motion

of a single vortex superimposed on a TW is analyzed, in a similar way to the analysis in Sect. 4.3. In this case, the finite detuning introduces new features into the dynamics compared with the zero-detuning case, such as vortex stretching. In Sect. 5.2, the interaction of two TWs with different orientations is studied. It is shown that such an interaction may lead to the formation of TW domains. At a boundary between two domains (where two TWs merge), an array of equally charged vortices is formed, which corresponds to a vortex sheet. Finally, the interaction of four TWs at particular angles is shown to generate a stable cross-roll pattern, which can alternatively be described as a square vortex lattice.

5.1 Vortices "Riding" on Tilted Waves

The evolution of an arbitrary perturbation of a TW can be studied using the change of variable $A(\boldsymbol{r}, t) = \exp(\mathrm{i}\boldsymbol{k}\boldsymbol{r})\, B(\boldsymbol{r}, t)$. In the case of a resonant TW ($|\boldsymbol{k}| = \sqrt{\Delta}$), this change brings (5.1) into the form

$$\frac{\partial B}{\partial t} + 2\boldsymbol{k} \cdot \boldsymbol{\nabla} B = B + \mathrm{i}\boldsymbol{\nabla}^2 B - g(2\mathrm{i}\boldsymbol{k} \cdot \boldsymbol{\nabla} + \boldsymbol{\nabla}^2)^2 B - |B|^2\, B \ , \qquad (5.4)$$

which is the evolution equation for the modulation of a resonant TW. The terms on the left-hand side describe the advection of vortices (and of every structure in general), with the velocity of the TW given by $\boldsymbol{v} = 2\boldsymbol{k}$. The terms on the right-hand side describe the evolution of the envelope in a basis propagating with the underlying TW. The dynamics are similar to those of the nondetuned laser studied in the previous chapter, but not completely identical. Inspecting the right-hand side of (5.4), one can identify local gain and saturation terms, and also diffraction terms identical to those for a laser with zero detuning. The diffusion in (5.4) is, however, different. Expanding the third term on the right-hand side,

$$-g(2\mathrm{i}\boldsymbol{k} \cdot \boldsymbol{\nabla} + \boldsymbol{\nabla}^2)^2 = 4g(\boldsymbol{k} \cdot \boldsymbol{\nabla})^2 - g\boldsymbol{\nabla}^4 - 4\mathrm{i}g(\boldsymbol{k} \cdot \boldsymbol{\nabla}^3) \ , \qquad (5.5)$$

we notice that the vortices diffuse in different ways in the directions parallel and perpendicular to the direction of the advecting TW. The parallel diffusion is stronger (the first order of the Laplacian) than the perpendicular diffusion (the second order of the Laplacian). Therefore vortices can be expected to stretch along the TW direction.

   Figure 5.1 shows two oppositely charged vortices advected by a TW, as obtained by solving numerically the CSH equation (5.1). As expected from (5.4), the vortices are stretched along the direction of advection. For periodic boundary conditions, as in Fig. 5.1, the vortices move periodically through the interaction region. The situation is different for zero boundary conditions. In this case vortices can appear at one boundary, be advected by the tilted wave and be destroyed at the other boundary. Such a case is illustrated by
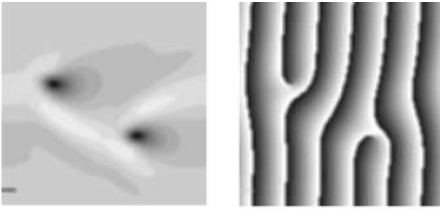
Fig. 5.1. Two vortices advected by a background tilted wave directed to the right, as obtained by numerical integration of (5.1). The phase gradient is visible from the phase picture. The parameters are $\Delta = 0.5$ and $g = 0.4$
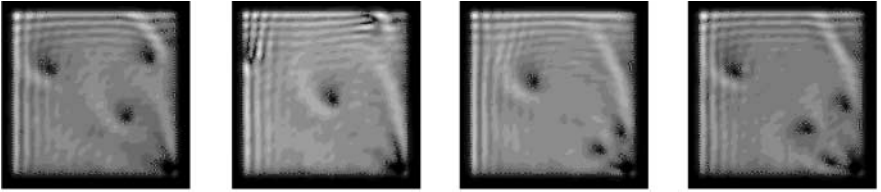

Fig. 5.2. Vortices generated periodically at the *bottom right* corner of the integration region, and advected by a tilted wave in an upward and leftward direction. At the *top left* corner of the integration region, several fringes are visible, which occur because of interference between propagating and reflected TWs. The parameters are $\Delta = 2$ and $g = 0.1$. The time between the plots is $t = 2.5$, and increases from *left* to *right*

a series of snapshots in Fig. 5.2, obtained by numerical integration of the CSH equation (5.1) with zero boundary conditions. Similar results have been obtained in [1] by investigating numerically a Raman laser.

Figure 5.3 shows several vortices advected by a tilted wave, as obtained experimentally with a photorefractive oscillator in a self-imaging cavity (the details of the experimental configuration will be given in Chap. 6). The figure shows three snapshots of vortices, which are continuously created in the central part of the crystal and drift outwards. There is a defect in the central part of the figure, since seemingly the telescope inside the resonator was not
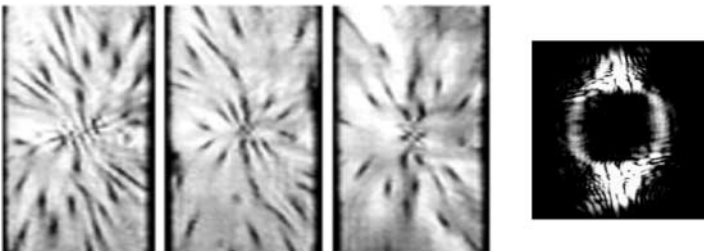

Fig. 5.3. Optical vortices nucleated at the center are advected outwards by a radially tilted wave. The times between three consecutive snapshots (at the *left*) were $t = 5$ s. At the *right*, the corresponding far-field distribution is shown

perfectly tuned in the lateral direction (see Fig. 6.6). The defect in the center nucleates the vortices, which are advected by a radially spreading tilted wave.

5.2 Domains of Tilted Waves

Another natural choice for a basic solution of the CSH equation (5.1) is in the form of two counterpropagating TWs,

$$A(\boldsymbol{r}, t) = a_+(t) \exp(\mathrm{i}\boldsymbol{k} \cdot \boldsymbol{r}) + a_-(t) \exp(-\mathrm{i}\boldsymbol{k} \cdot \boldsymbol{r}) , \qquad (5.6)$$

which corresponds to a standing wave (SW) in the case of equal amplitudes $|a_+| = |a_-|$.

One can easily check the stability of the solution (5.6) by inserting it into (5.1), gathering the terms with the exponents $\exp(\mathrm{i}\boldsymbol{k} \cdot \boldsymbol{r})$ and $\exp(-\mathrm{i}\boldsymbol{k} \cdot \boldsymbol{r})$, and neglecting the terms containing the third spatial harmonics (those with the exponents $\exp(3\mathrm{i}\boldsymbol{k} \cdot \boldsymbol{r})$ and $\exp(-3\mathrm{i}\boldsymbol{k} \cdot \boldsymbol{r})$). In the case of resonant counterpropagating TWs, where $|\boldsymbol{k}| = \sqrt{\Delta}$, the equations for the amplitudes read

$$\frac{\partial a_\pm}{\partial t} = a_\pm - a_\pm(|a_\pm|^2 + 2\,|a_\mp|^2) . \qquad (5.7)$$

A linear stability analysis of (5.7) yields the result that the SW solution $|a_+| = |a_-|$ is unstable against one of the two TW solutions, $|a_+| = 1$, $|a_-| = 0$ or $|a_-| = 1$, $|a_+| = 0$. The system (5.7) possesses a variational potential that has two minima, which correspond to two TWs, and a saddle point, which corresponds to a SW. Therefore, (5.7) leads to a competition between counterpropagating TWs, with the survival of the stronger one.

The competition of counterpropagating TWs can also result in their separation in space. In this case spatial domains appear, each domain characterized by a particular direction of a TW.

TW domains commonly appear in the numerical integration of the CSH equation with periodic boundary conditions, but they exist only as transients: the strongest domain finally wins, and a pure TW remains as the final pattern. With zero (Dirichlet) lateral boundaries, however, coexisting TW domains can be stationary.

Figure 5.4 shows the formation and evolution of TW domains. From the resonant ring, some spots emerge (right column, showing the spectra), corresponding to TW domains (left column). In what follows, the strongest domains survive. However, the domains are not uniform (second and third rows), but contain defects in the form of optical vortices. The optical vortices are advected by the TWs and finally disappear at the domain boundaries.

A domain boundary, as can be seen from the left column in Fig. 5.4, is an array of equally charged vortices, or a vortex sheet. This is so because of the particular phase variation at the boundary between two TWs (center
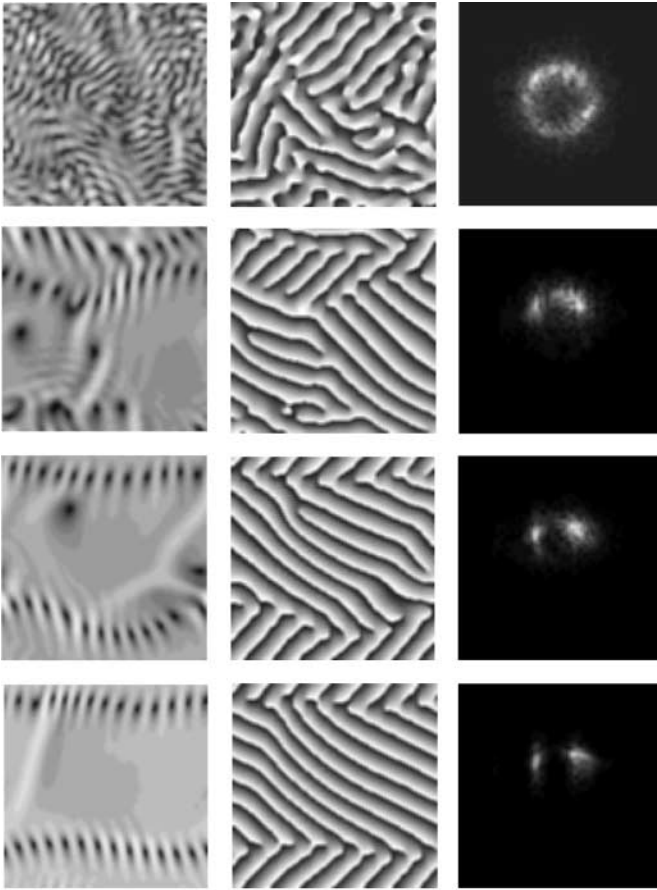
Fig. 5.4. Appearance and dynamics of TW domains, as obtained by numerical integration of (5.1). The parameters are $\Delta = 2$ and $g = 1$, and the time between snapshots is $t = 20$. Time runs from *top* to *bottom*

column, showing the phase pattern). Note also that the size of a vortex in the array is different from that of a freely moving vortex, as can clearly be seen from the third row in Fig. 5.4.

Figure 5.5 shows field distributions containing domains of tilted waves, as observed experimentally. Two domains (left) and four domains (right) are shown together with their corresponding far-field distributions. The directions of the waves traveling inside the domains correspond to the orientations of the spots in the far-field ring. The orientation drifted slowly with time, indicating that the orientation of the domains is independent of the boundaries both in the experiment and in the numerics. The domains are separated by vortex rows, as expected for domains of different flow.
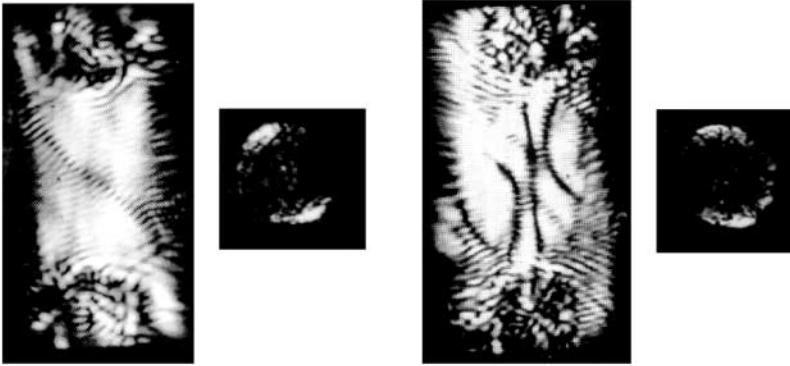
Fig. 5.5. Domains of tilted waves separated by rows of vortices: near-field and far-field pictures. The resonator length was tuned to maintain the ring in the far field. Note the row of vortices separating the two domains of tilt in the snapshot at the *left*. Four domains of different tilt are visible in the *right* snapshot

In the experimental figure (Fig. 5.5) counterpropagating domains were recorded. In general, the directions of the TWs in neighboring domains can be at arbitrary angles. Different angles between domains result in different separations between vortices at the domain boundaries. Figure 5.6 illustrates boundaries between domains characterized by different angles of the TWs, from counterpropagating domains (Fig. 5.6a) to almost copropagating domains (Fig. 5.6d).

The counterpropagating domains in Fig. 5.6a were constructed from TWs with wavenumbers $|\boldsymbol{k}| = 5 \times 2\pi$, directed to the left in the middle of the figure, and to the right at the horizontal periodic boundary. The directions of the TWs can be seen clearly from the phase plots (right column). The vortex sheet contains 10 vortices over the integration range in this case of counterpropagating domains: the integral of the phase gradient over the corresponding closed loop is equal to $10 \times 2\pi$.

In general, the density of vortices in a vortex sheet is proportional to the projection of the difference between the wavevectors $\Delta\boldsymbol{k} = \boldsymbol{k}_1 - \boldsymbol{k}_2$ on the domain boundary; this can be shown by integration of the phase gradient of the field over a closed loop enclosing a unit length of the domain boundary.

The TW of the middle domain in Fig. 5.6b is directed upwards and to the left: it has the same modulus of the wavevector as in Fig. 5.6a ($|\boldsymbol{k}| = 5 \times 2\pi$), but has a horizontal component $k_x = -4 \times 2\pi$. The vortex sheet now contains 9 vortices, which can again be checked by the integration of the phase gradient over the corresponding closed loop.

The TW of the middle domain in Fig. 5.6c is directed upwards. The vortex sheet contains 5 vortices in this case. A peculiar feature is that, for the lower vortex sheet, the TWs "run apart" (in the vertical direction), and thus the vortices are "stretched". This domain boundary corresponds to a
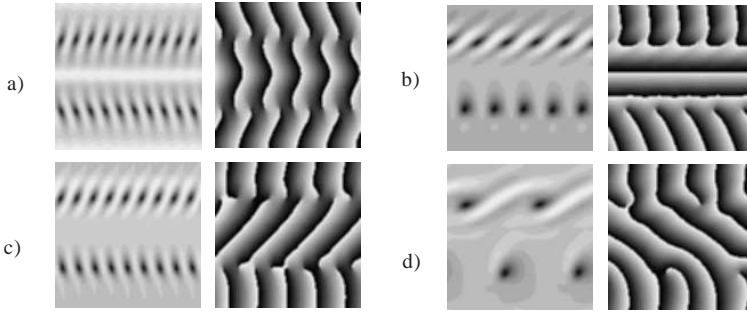
Fig. 5.6. TW domains, as obtained by numerical integration of (5.1). The parameters are $\Delta = 2$ and $g = 1$. Different initial conditions were used to generate different direction of the TW in the domain

source. The upper domain boundary, in contrast, represents a sink, since the corresponding TWs "run together".

Finally, the domain boundaries in Fig. 5.6d contain only two vortices, since the TWs are almost copropagating: for the middle domain, $k_x = 2 \times 2\pi$. The bottom vortex sheet again corresponds to a line of sources, and the top vortex sheet corresponds to a line of sinks, which can be also seen from the size and shape of the vortices.

5.3 Square Vortex Lattices

Two counterpropagating TWs compete and do not result in a stable standing-wave pattern, as shown in the previous section. Instead, they occupy different areas in space. However, four resonant TWs can coexist simultaneously, resulting in a stationary pattern,

$$A(r,t) = \sum_{j=1,4} A_j \exp(\mathrm{i} k_j r) \ . \tag{5.8}$$

The four wavevectors are directed as shown in Fig. 5.7. The pattern consists of two pairs of counterpropagating TWs, crossing at an angle of 90°. Such cross-roll patterns have been found in lasers [2, 3] and in optical parametric oscillators [4].

By inserting (5.7) into (5.1) and neglecting the higher harmonics, we obtain the result that the amplitudes of the TW components of the square vortex lattice (SVL) are all equal to $|A_j|^2 = 1/5$. The phases of the TWs obey the relation

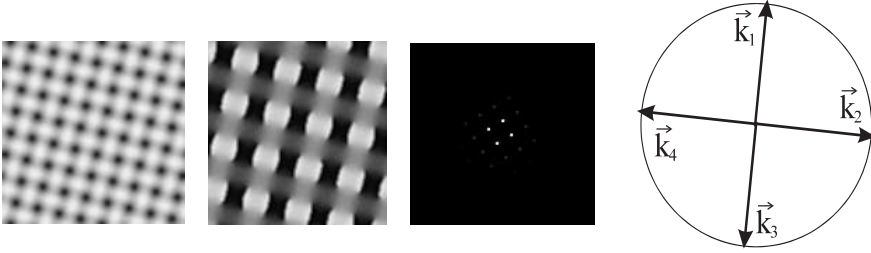$$\Phi = \sum_{j=1,4} \varphi_j = \pi \ . \tag{5.9}$$

Fig. 5.7. Square vortex lattice as obtained by numerical integration of (5.1): amplitude, phase and spatial Fourier spectrum of the field. The parameters are $g = 0.4$ and $\Delta = 2$. At the *right*, a schematic illustration of the four TWs forming the pattern is shown

A stability analysis based on the variational potential yields the result that the SVL corresponds to a local minimum in the parameter space of A_j [2]. Therefore the SVL is stable with respect to small perturbations. The tilted waves correspond to deeper minima of the potential, and standing waves, as discussed in the previous section, correspond to a saddle point.

In Fig. 5.8 the SVL is shown for a pump value significantly larger than that used in Fig. 5.7. Shocks between vortices are visible, as well as higher spatial harmonics in the spatial Fourier spectrum.
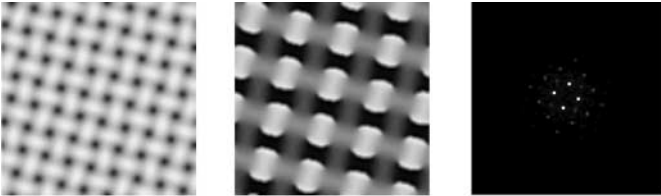
Fig. 5.8. Square vortex lattice as obtained by numerical integration of (5.1). The parameters are the same as in Fig. 5.7, except for the pump value, $p = 9$. Here, a version of (5.1) was used in which the pump parameter was normalized to $p = 1$, and the gain term (the first term on the right-hand side of (5.1)) contained the gain parameter explicitly

Two pairs of counterpropagating TWs can cross not only at an angle of 90°, but also at arbitrary angles. Such angles lead to rhombic vortex lattices, as shown in Fig. 5.9. The picture resembles domains of counterpropagating TWs. Indeed, with increasing detuning, a rhombic vortex lattice becomes unstable and transforms into domains of counterpropagating TWs. The decay of a rhombic vortex lattice and the formation of TW domains is shown in Fig. 5.10.
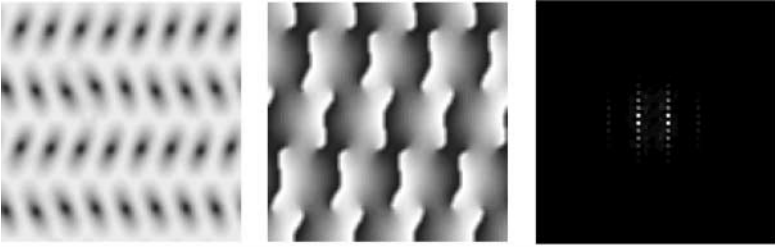
Fig. 5.9. Rhombic vortex lattice as obtained by numerical integration of (5.1). The parameters are the same as in Fig. 5.7. The lattice is constructed from four TWs with wavevectors $\boldsymbol{k}_j = (\pm 4 \times 2\pi, \pm 2\pi)$; however, higher components in spatial Fourier spectrum appear
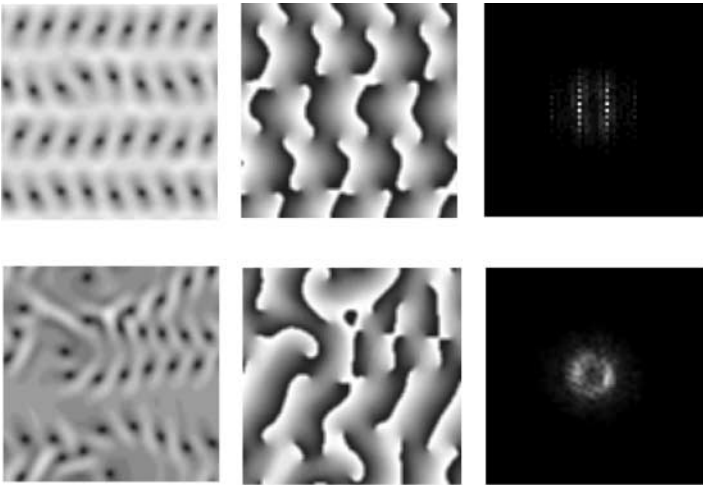

Fig. 5.10. Decay of a rhombic vortex lattice and formation of TW domains, as obtained by numerical integration of an unnormalized version of (5.1). The parameters are the same as in Fig. 5.9, except for the pump value, $p = 4$. The stationary distribution shown in Fig. 5.9 was taken as the initial condition for the calculation

Finally, we present experimental evidence of a square vortex lattice. Figure 5.11 shows the corresponding field distribution. The directions of the four tilted waves correspond to the orientations of the four spots in the far-field ring. The orientation of these spots drifted with time indicating that (1) not only a square but also a rhombic symmetry of the vortex lattice was possible, and (2) the symmetry of the pattern was independent of the boundaries.
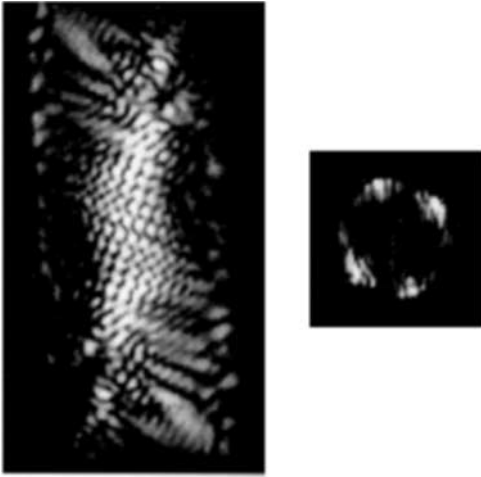
Fig. 5.11. A "cross-roll" pattern or square vortex lattice, as obtained experimentally with a photorefractive oscillator

References

1. P.K. Jakobsen, J. Lega, Q. Feng, M. Staley, J.V. Moloney and A.C. Newell, Nonlinear transverse modes of large-aspect-ratio homogeneously broadened lasers: I. Analysis and numerical simulation, Phys. Rev. A **49**, 4189 (1994). 83
2. K. Staliunas and C.O. Weiss, Tilted and standing waves and vortex lattices in class-A lasers, Physica D **81**, 79 (1995). 87, 88
3. Q. Feng, J.V. Moloney and A.C. Newell, Transverse patterns in lasers, Phys. Rev. A **50**, R3601 (1994). 87
4. S. Longhi, Alternating rolls in nondegenerate optical parametric oscillators, J. Mod. Opt. **43**, 1569 (1996). 87

6 Resonators with Curved Mirrors

All the previous chapters have dealt with pattern formation in plane–plane mirror resonators. The order parameter equations (Chaps. 2 and 3) were derived assuming a plane–plane mirror cavity. The vortex dynamics (Chaps. 4 and 5) were analyzed for a plane–plane mirror resonator too. In reality, however, most nonlinear resonators contain curved mirrors. This chapter is devoted to the transverse patterns in nonplanar resonators.

In the presence of curved mirrors, the Maxwell–Bloch equation system reads

$$\frac{\partial E}{\partial t} = \kappa \left[-\left(1 + \mathrm{i}\omega_0\right) E - \mathrm{i}c\boldsymbol{r}^2 E + \mathrm{i}a\,\nabla^2 E + P \right], \tag{6.1a}$$

$$\frac{\partial P}{\partial t} = -\gamma_\perp \left(P - ED\right), \tag{6.1b}$$

$$\frac{\partial D}{\partial t} = -\gamma_\parallel \left(D - D_0 + \frac{1}{2}\left(EP^* + E^*P\right)\right). \tag{6.1c}$$

The only difference between (6.1) and (2.1) is the additional term $\mathrm{i}c\boldsymbol{r}^2 E$ in (6.1a), which takes into account the presence of a parabolic mirror in the resonator. Here $c = kC/2\kappa$ is the focusing parameter, proportional to the total curvature of the mirrors C (positive for a cavity with focusing mirrors, and negative for a cavity with defocusing mirrors).

The resonator equation, in the absence of nonlinearity ($P = 0$ in (6.1a)), has a simple solution in the form of a decaying Gaussian beam,

$$E\left(\boldsymbol{r}, t\right) = E_0 \, \mathrm{e}^{-(1+\mathrm{i}\omega)t} \mathrm{e}^{-(\boldsymbol{r}/r_0)^2}, \tag{6.2}$$

with a frequency $\omega = \omega_0 - 2\sqrt{ac}$ and a half-width $r_0^2 = 2\sqrt{a/c}$. The Gaussian beam is actually the lowest, fundamental transverse mode of the resonator, named the TEM$_{00}$ mode. In general, the higher-order transverse modes are also exponentially decaying solutions of the linearized version of (6.1a).

In the first two sections of this chapter the case of a quasi-planar resonator, such that the curvature of the resonator mirrors is small, is discussed. The effects of the curved mirrors are weak in one resonator round trip, and can be calculated perturbatively. This fact allows one to derive the order parameter equation for a laser with curved mirrors (Sect. 6.1). It also allows the application of mode expansion techniques in the theoretical treatment of

laser patterns (Sect. 6.2). In Sect. 6.3 the case of a resonator with strongly curved mirrors is investigated, which in some limits (confocal and self-imaging resonators) also leads to important simplifications of the problem.

6.1 Weakly Curved Mirrors

In this case the effects of the curvature may be treated perturbatively. We can take into account of these effects by assuming a weakly varying detuning in the transverse cross section of the resonator, $\omega(\boldsymbol{r}) = \omega_0 + cr^2$. We then (see Fig. 6.1) consider a resonator with focusing parabolic mirrors as a resonator with a length thats varies over the transverse cross section: the resonator is of maximum length along the optical axis, and shorter at some distance from it. This corresponds to a negative detuning that is maximum on the optical axis and decreases away from it.
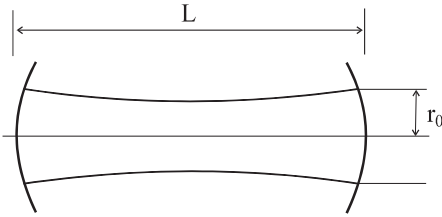

Fig. 6.1. A resonator with focusing curved mirrors can be considered as a resonator with laterally varying length: on the optical axis the length of the resonator is maximum

If the variation of the resonator length over the beam width is small, then the derivation of the order parameter equation is straightforward. We can repeat the adiabatic-elimination procedure in Chap. 2 by using a coordinate-dependent resonator detuning $\omega(\boldsymbol{r}) = \omega_0 + cr^2$. This leads to

$$\frac{\partial A}{\partial \tau} = pA + \mathrm{i}(a\boldsymbol{\nabla}^2 - \omega_0 - cr^2)A \tag{6.3}$$

$$-\frac{\kappa^2}{(\kappa + \gamma_\perp)^2}(a\boldsymbol{\nabla}^2 - \omega_0 - cr^2)^2 A - |A|^2 A \ .$$

The same result was obtained in [1] by using a multiscale expansion. In both derivations the smallness parameter is $\varepsilon = \sqrt{ac}$, which is actually the frequency separation of two adjacent transverse modes.

The transverse modes are the eigenfunctions of the operator $\hat{P} = \mathrm{i}(a\boldsymbol{\nabla}^2 - cr^2)$, in both (6.3) and (6.1a). $\hat{P}$ is the propagation operator in a linear resonator without gain or decay. The eigenfunctions of the propagator $\hat{P}$ are the transverse modes of the resonator, such that the field distributions do not vary in time, and $\hat{P}A_n(\boldsymbol{r}) = -\mathrm{i}\omega_n A_n(\boldsymbol{r})$. For a cylindrically symmetric resonator, the Gauss–Laguerre mode sets can be used:

$$A_{pl}(\rho, \varphi) = \frac{2}{\sqrt{\pi}}(2\rho^2)^{1/2}\left(\frac{p!}{(p+l)!}\right)^{1/2} L_p^l(2\rho^2)\exp(-\rho^2)\exp(\mathrm{i}l\varphi) \ , \tag{6.4}$$

where $p = 0, 1, 2, ...$ is the radial index, and $l = ..., -2, -1, 0, 1, 2, ...$ is the angular index. ρ denotes the radial coordinate normalized to the beam waist $r_0 = (4a/c)^{1/4}$, φ is the angle around the optical axis of the laser, and L_p^l are Laguerre polynomials with the argument indicated. The mode functions are orthonormalized, and obey the condition

$$\int\limits_0^{2\pi} d\varphi \int\limits_0^{\infty} d\rho\, \rho A_{pl}(\rho, \varphi) A_{p'l}^*(\rho, \varphi) = \delta_{pp'}\delta_{ll'} \ . \tag{6.5}$$

Alternatively, one can use the Gauss–Hermite mode set; however, for cylindrically symmetric resonators, the Gauss–Laguerre modes are more convenient.

The eigenfrequencies of the modes are

$$\omega_{p,l} = 2\sqrt{ac}(2p + l + 1) \ , \tag{6.6}$$

which means that the transverse modes can be degenerate. The fundamental Gaussian mode TEM$_{00}$ ($p = 0$, $l = 0$) has a frequency $\omega_0 = 2\sqrt{ac}$; the two single-vortex helical modes TEM$_{0\pm1}^*$ ($p = 0$, $l = \pm1$) have a frequency $\omega = 2\omega_0$; the next mode family consists of the nonhelical mode TEM$_{10}^*$ ($p = 1$, $l = 0$) and two helical double-vortex modes TEM$_{0\pm2}^*$ ($p = 0$, $l = \pm2$), and so on. The nth transverse mode family $n = 2p + l$ is n times degenerate.

6.2 Mode Expansion

Modes are eigenfunctions of a linear resonator. In a nonlinear resonator, the modes become coupled. We can then rewrite (6.3) in terms of coupled mode amplitudes, by expanding the order parameter into modes:

$$A(\boldsymbol{r}, t) = \sum_i f_i(t) A_i(\boldsymbol{r}) \ , \tag{6.7}$$

where i is an arbitrary combination of mode indices p and l. Inserting the expansion (6.7) into (6.3), multiplying both sides by $A_j^*(\boldsymbol{r})$, integrating and taking into account of the orthonormality of the modes, we obtain

$$\frac{\partial f_i}{\partial \tau} = p_i f_i - \mathrm{i}(\omega_i + \omega_0)f_i - \sum_{jkl} \Gamma_{jk}^{il} f_j f_k f_l^* \ , \tag{6.8}$$

where $p_i = p - (\omega_i + \omega_0)^2 \kappa^2/(\kappa + \gamma_\perp)^2$ are the individual gain coefficients of the modes, and Γ_{jk}^{il} are the nonlinear coupling coefficients, given by

$$\Gamma_{jk}^{il} = \int A_j(\boldsymbol{r}) A_k(\boldsymbol{r}) A_i^*(\boldsymbol{r}) A_l^*(\boldsymbol{r})\, d\boldsymbol{r} \ . \tag{6.9}$$

The mode expansion is not very useful if many modes are taken into account. The computer time required to integrate (6.8) numerically is proportional to the fourth power of the number of modes. Therefore, for a large number of modes, the numerical integration of the partial differential equation (6.3) is usually more convenient. However, the mode expansion approach is very useful if a small number of modes is excited. The usefulness of mode expansion is illustrated below with two examples of circling vortices, and with an example of transverse-mode locking.

6.2.1 Circling Vortices

Vortices circling around the optical axis of a laser can be interpreted as the interference of two modes of different helicities. In this case, (6.8) becomes

$$\frac{\partial f_1}{\partial \tau} = p_1 f_1 - \mathrm{i}(\omega_1 + \omega_0)f_1 - f_1(G_{11}\,|f_1|^2 + 2G_{12}\,|f_2|^2) \,, \tag{6.10a}$$

$$\frac{\partial f_2}{\partial \tau} = p_2 f_2 - \mathrm{i}(\omega_2 + \omega_0)f_2 - f_2(G_{22}\,|f_2|^2 + 2G_{12}\,|f_1|^2) \,, \tag{6.10b}$$

where

$$G_{11} = \Gamma_{11}^{11} = \int |A_1(\boldsymbol{r})|^4 \; \mathrm{d}\boldsymbol{r} \,, \tag{6.11a}$$

$$G_{22} = \Gamma_{22}^{22} = \int |A_2(\boldsymbol{r})|^4 \; \mathrm{d}\boldsymbol{r} \,, \tag{6.11b}$$

$$G_{12} = \Gamma_{12}^{12} = \Gamma_{21}^{21} = \int |A_1(\boldsymbol{r})|^2\,|A_2(\boldsymbol{r})|^2 \; \mathrm{d}\boldsymbol{r} \,. \tag{6.11c}$$

From (6.10), one can analyze the behavior of two modes with different helicities. For example, it is found that the frequencies of the modes are not affected by the nonlinear interaction. The particular spatial shapes of the helical modes do not lead to nonlinear mode pulling or locking. The variation of the difference between the phases of the modes only rotates the two-mode interference pattern around the optical axis of the laser, and consequently there is no preferred phase difference.

There are several different solutions for the intensities of the modes $n_i = |f_i|^2$. One solution is trivial, with the amplitudes of both modes equal to zero. This solution is, however, unstable if the laser is above the generation threshold. Another solution corresponds to a single mode, where the intensity of one mode is zero, and the intensity of the other is $n_i = p_i/G_{ii}$. The most interesting solution is that where both modes are excited,

$$n_1 = \frac{p_1 G_{22} - 2p_2 G_{12}}{G_{11}G_{22} - 4G_{12}^2} \,, \tag{6.12a}$$

$$n_2 = \frac{p_2 G_{11} - 2p_1 G_{12}}{G_{11}G_{22} - 4G_{12}^2} \,. \tag{6.12b}$$

A stability analysis of these solutions shows that the two modes can co-exist (and beat, if they have different eigenfrequencies) if $G_{11}G_{22} > 4G_{12}^2$, which means that the modes overlap relatively weakly. For example, the fundamental mode TEM_{00} and the single-vortex mode TEM_{01}^* overlap relatively strongly and the above inequality is invalid. The overlap between these two modes is $G_{12}/\sqrt{G_{11}G_{22}} = 1/\sqrt{2}$, which is larger than the critical overlap of $1/2$ for the coexistence of modes. These two modes, therefore, cannot exist simultaneously. Interference of the modes TEM_{00} and TEM_{01}^* results in an optical vortex rotating around the optical axis of the laser. Such behavior is, however, unstable for a class A laser, as (6.12) shows, and either the vortex spirals in and subsequently remains on the optical axis of the laser (the helical TEM_{01}^* mode wins the competition), or the vortex spirals out and disappears (the fundamental TEM_{00} mode wins). A steadily spiraling vortex is possible only in a class B laser, as shown in Chap. 7.

Instead of one single vortex, however, several circling vortices are easily obtained in the framework of (6.11). A number l of vortices of the same charge arranged symmetrically around the optical axis of the laser corresponds to the interference pattern of a TEM_{0l}^* mode with the fundamental Gaussian mode. The mode overlap decreases with increasing l. For example, the overlap between the TEM_{02}^* and TEM_{00} modes is $1/\sqrt{6}$, that between the TEM_{03}^* and TEM_{00} modes is $1/\sqrt{20}$, and so on.

In Fig. 6.2, an example of multiple circling vortices is shown, taken from [2]. Note that while multiple circling vortices are relatively easily obtained experimentally, a single circling vortex following a circular trajectory has never been observed.
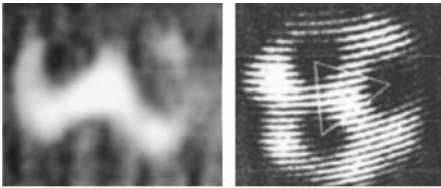

Fig. 6.2. Three vortices circling around the optical axis of a laser. At the *right,* an interference picture with a tilted plane wave is shown. The interference fringes indicate the topological charges of the vortices

6.2.2 Locking of Transverse Modes

Another example concerns the locking of the transverse modes. In this case, instead of helical modes (6.4), a expansion into flowerlike modes is more convenient:

$$
A_{pli}(\rho, \varphi) = \frac{2}{\sqrt{\pi}}(2\rho^2)^{1/2}\left(\frac{p!}{(p+l)!}\right)^{1/2} L_p^l(2\rho^2)\mathrm{e}^{-\rho^2} \times \begin{cases} \cos(l\varphi), i = 1 \\ \sin(l\varphi), i = 2 \end{cases},
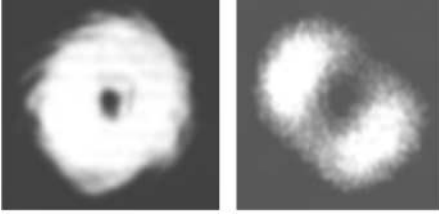$$

$$
(6.13)
$$

Fig. 6.3. Perfectly locked vortex (*left*) and a vortex locked with some nonzero angle between the phases of the "flower" modes of which it is composed (*right*). The experiments were done with a photorefractive oscillator

which are also orthogonal and normalized. Taking now two modes from the same transverse mode family, we obtain, instead of (6.11),

$$\frac{\partial f_1}{\partial \tau} = p_1 f_1 - \mathrm{i}(\omega_1 + \omega_0) f_1 - f_1 (G_{11} |f_1|^2 + 2G_{12} |f_2|^2) - G'_{12} f_2^2 f_1^* \;, \tag{6.14a}$$

$$\frac{\partial f_2}{\partial \tau} = p_2 f_2 - \mathrm{i}(\omega_2 + \omega_0) f_2 - f_2 (G_{22} |f_2|^2 + 2G_{12} |f_1|^2) - G'_{12} f_1^2 f_2^* \;, \tag{6.14b}$$

where the phase-sensitive terms (the last term in the right-hand side) are included. The phase-sensitive coupling coefficient is given by

$$G'_{12} = \Gamma_{11}^{22} = \Gamma_{22}^{11} = \int A_1^2(\boldsymbol{r}) A_2^{*2}(\boldsymbol{r}) \, \mathrm{d}\boldsymbol{r} \;. \tag{6.15}$$

The role of the phase-sensitive terms is to lock the frequencies of the two modes (i.e. to synchronize the modes) if their eigenfrequencies do not differ too much. If we restrict our considerations, for simplicity, to the case of symmetric modes ($p_1 = p_2 = p$, $G_{11} = G_{22}$), the solution of (6.14) is

$$p - n\left[G_{11} + 2G_{12} + G'_{12} \cos\left(4\,\Delta\varphi\right)\right] = 0 \;,$$
$$\frac{\Delta\omega}{2} - nG'_{12} \sin\left(4\,\Delta\varphi\right) = 0 \;. \tag{6.16}$$

Here $\Delta\omega = \omega_1 - \omega_2$ is the frequency mismatch between the two modes, n is the intensity of each of the modes, and $\Delta\varphi = \varphi_1 - \varphi_2$ is their phase difference.

The solution (6.16) indicates that the modes lock with the same phase if the frequency detuning is equal to zero. In general, the phase-locking angle is proportional to the detuning. Figure 6.3 (left) shows a perfectly locked vortex and (right) a vortex where the corresponding "flower" modes are locked at a nonzero angle.

Evidently, there exists a maximum value of the mode frequency mismatch for which the modes are still locked,

$$\Delta\omega_{\mathrm{thr}} = \frac{2pG'_{12}}{G_{11} + 2G'_{12}} \;. \tag{6.17}$$

Figure 6.4 shows examples of mode-locked patterns involving a small number of modes, obtained experimentally [3].

Fig. 6.4. Mode-locked patterns: vortex quadrupole (*left*) and a vortex quadrupole that has degenerated into two vortices of the same charge (*middle*). Both of these plots belong to the mode family $2p + l = 2$. The distribution at the *right* belongs to transverse mode family $2p + l = 3$

When the frequency detuning is larger than the threshold value given by (6.17), the modes continue to beat, despite their phase-sensitive coupling. Figure 6.5 shows the evolution of the phase difference between two modes when the mode detuning is close to the locking threshold. The modes are unlocked but do not evolve freely: the phase difference, during its cycle of 2π, sometimes varies faster, and sometimes varies more slowly (for favored values of the phase). The intensity of the field also oscillates correspondingly.
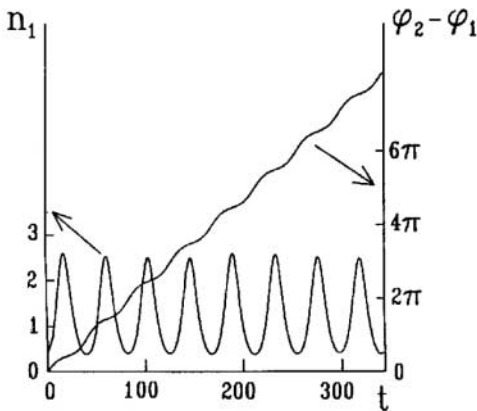

Fig. 6.5. Evolution of the phase difference between the two modes, and of the intensity of one (arbitrary) mode close to the locking threshold

6.3 Degenerate Resonators

The use of resonators with curved mirrors allows one to observe the simplest transverse patterns containing several optical vortices (e.g. as shown in Figs. 4.2 and 4.3). The observed patterns are the result of the interference of transverse modes of the resonator. The patterns are either stationary, if the

modes are locked, or periodic, if the modes are beating. These patterns are weakly nonlinear patterns: role of the nonlinearity is only that of allowing mode competition. The spatial scale of the patterns (e.g. the size of the vortices) does not depend on the nonlinearity, but only on the boundary conditions. This means, equivalently, that the temporal spectrum is a collection of discrete frequencies. These frequencies may be shifted (for frequency-pulling modes) or locked. However, these patterns have a discrete set of frequencies and not a continuous spectrum, which indicates a dependence on the boundaries.

Patterns that are essentially nonlinear, such as those investigated in Chaps. 3 and 4, are of a different nature. They depend weakly on the boundaries and, equivalently, their temporal spectrum degenerate into a continuum. These patterns were predicted and calculated for a plane–plane mirror resonator.

Let us now estimate the width of the aperture of a plane–plane resonator necessary to observe at least one vortex. The evaluation of the vortex core radius in Chap. 4 gives $r_0^2 = 3\sqrt{2}a/p$, which for a pump intensity of two times the threshold value ($p = 1$) yields $r_0 \approx 2\sqrt{a}$. Remembering that the diffraction coefficient is $a = QL\lambda/(4\pi)$ (where $L \approx 1$ m is a typical resonator length, $\lambda \approx 1\,\mu$m is a typical wavelength of the radiation, and $Q \approx 10$ is a typical resonator finesse), we obtain $r_0 \approx 3$ mm. A minimum width of the aperture of order of 1 cm is then necessary to observe one vortex. Correspondingly, for observation of ensembles of vortices, such as those calculated in Chaps. 4 and 5, unrealistically broad apertures are needed.

It is difficult experimentally to build a laser with such a broad aperture, and therefore one must think of some other configuration. In fact, the requirement of a broad-aperture cavity can be achieved not only with a plane–plane mirror resonator, but also with a curved cavity in a self-imaging or near-self-imaging configuration, as will be shown in this section.

The main reason why configurations other than a quasi-planar resonator are mistrusted for experimental investigation of transverse pattern formation concerns the theoretical assumptions. In deriving the order parameter equation (2.26) for lasers and other nonlinear optical systems, the mean-field approximation is used. It is assumed that the radiation changes very little during a resonator roundtrip. The question is whether order parameter equations derived for a mean-field case can be used to describe resonators where the fields vary strongly with propagation. Indeed, for self-imaging resonators (e.g. a confocal resonator) the field changes significantly over a roundtrip. On one roundtrip, the field changes from the near field in a reference plane to the far field in the Fourier-conjugated plane, and back to the near-field.

However, the variation of the field along the cavity can be neglected if the nonlinear material is short enough compared with the length of the cavity. In this case the diffractive propagation in the linear part of the resonator is completely irrelevant. What is significant is how much the fields change over

a complete roundtrip in the cavity. If the fields change just a little, then order parameter equations derived using a mean-field approximation are valid. In near-self-imaging resonators, the fields indeed change very little in a round trip. In a precisely self-imaging resonator, the fields do not change at all (they are imaged on themselves).

In order to derive an order parameter equation for a near-self-imaging resonator, we must rewrite the field propagation equation (6.1a) for a more general case:

$$\frac{\partial E}{\partial t} = \kappa \left(-(1 + \mathrm{i}\omega)E - \frac{\mathrm{i}kC r^2}{2\kappa}E + \mathrm{i}\frac{B}{2k\kappa}\nabla^2 E + P \right), \tag{6.18}$$

where the coefficients B and C are the off-diagonal elements of the propagation ($ABCD$) matrix. For a near-planar resonator, the ABCD matrix is

$$ABCD = \begin{pmatrix} A & B \\ C & D \end{pmatrix} = \begin{pmatrix} 1 & L \\ -c & 1 \end{pmatrix}, \tag{6.19}$$

where the element B is equal to the total resonator length, and the element C is the total curvature of the resonator c. From this, one can retrieve the propagation equation from (6.18), and for small L and c one can derive the CSH equation as the order parameter equation (6.3). In experiments, the so-called $8f$ resonator, shown in Fig. 6.6, is very convenient.
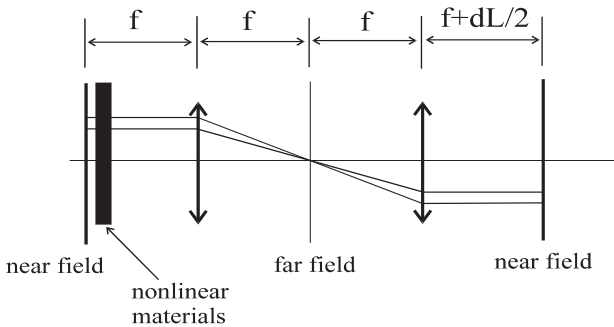

Fig. 6.6. The $8f$ resonator. The cavity is self-imaging for a linear length equal to $4f$ (the full length is equal to $8f$); $\mathrm{d}L$ is a small deviation from the self-imaging length

The $ABCD$ matrix for a perfectly self-imaging case is the diagonal unitary matrix. If a small deviation from the self-imaging length is present, then the $ABCD$ matrix is

$$ABCD = \begin{pmatrix} 1 & \mathrm{d}L \\ 0 & 1 \end{pmatrix}, \tag{6.20}$$

where the element B, which is proportional to the diffraction, is equal to the deviation from the focal length. In the precise self-imaging case, the diffraction vanishes. A slightly longer resonator is equivalent to a planar resonator with a total length equal to the deviation $\mathrm{d}L$. A resonator slightly shorter than the length of a self-imaging resonator is equivalent to a planar resonator with a negative length. A negative length of the equivalent resonator means a negative diffraction coefficient.[1]

The sign of the diffraction has no influence on the linear propagation (spreading) properties. However, combined with a focusing nonlinearity, a change between diffraction and antidiffraction allows one to change between focusing and defocusing.

Some experiments have been performed with a nearly confocal resonator, as shown in Fig. 6.7. The $ABCD$ matrix in this case is

$$ABCD = \begin{pmatrix} -1 & \mathrm{d}L \\ -\mathrm{d}L/f^2 & -1 \end{pmatrix}, \tag{6.21}$$

which, for the precisely confocal configuration, corresponds to an antiunitary matrix. Confocal resonators are not completely degenerate. They self-image only after two resonator roundtrips. In one roundtrip, they invert the image. Therefore a confocal resonator can support only patterns that have central symmetry or antisymmetry.
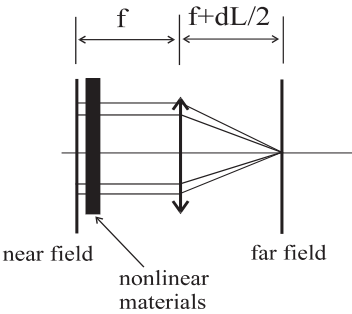

Fig. 6.7. Confocal resonator

Summarizing, one can expect that the nonlinear light dynamics in a self-imaging $(4f)$ resonator are described by the CSH equation (2.26), with a

---

[1] A negative diffraction coefficient has the following physical sense: the usual diffraction of a resonator, in a geometrical approach, relates the angle of the incident ray (with respect to the optical axis) to the lateral shift of the ray in the resonator after one round trip. An incident ray inclined to the right normally returns shifted to the right after a round trip. The larger the resonator diffraction is, the larger is the shift. For a resonator slightly shorter than the corresponding self-imaging resonator, an incident ray inclined to the right returns shifted to the left. This can be interpreted as propagation in a resonator with negative diffraction.

diffraction coefficient calculated using the deviation from the self-imaging length instead of the total length. The dynamics in a confocal resonator can also be described by (2.26), but with additional symmetry restrictions, such that central symmetry, $A(\boldsymbol{r}, t) = A(-\boldsymbol{r}, t)$, or antisymmetry $A(\boldsymbol{r}, t) = -A(-\boldsymbol{r}, t)$, is imposed.

This insight inspired the use of self-imaging resonators for observing essentially nonlinear vortex patterns (Chaps. 4 and 5), bright spatial solitons (Chap. 9), and phase domains and phase solitons (Chap. 11). For example, in some experiments to observe essentially nonlinear patterns we have used a photorefractive oscillator with BaTiO$_3$ as the active medium. In the confocal case, the resonator consisted of two highly reflecting mirrors with a radius of curvature of 350 mm. In the self-imaging case, a resonator with four highly reflecting plane mirrors and four identical intracavity lenses (with focal length $f = 100$ mm), arranged in a near-self-imaging geometry, was used (Fig. 6.8). The total length of the resonator is $L = 8f + l$, where l is a small shift from the self-imaging configuration ($l \ll f$).
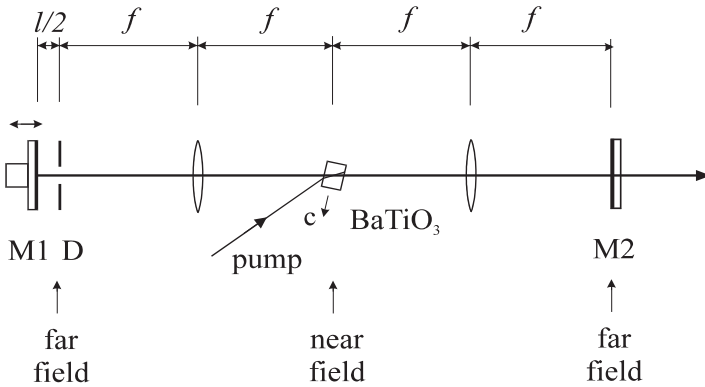

Fig. 6.8. Schematic illustration of the experimental arrangement used in the $8f$ resonator geometry

For a totally open aperture, we observe in the near field (at the plane where the crystal is located) a random small-scale structure, as is typically observed in large-Fresnel-number photorefractive oscillators. In the far field (Fourier-conjugated plane), we observe a set of concentric rings (Fig. 6.9). The rings in the far field indicate the slight deviation from the self-imaging length and are comparable to the rings observed in plane Fabry–Pérot resonators. Different rings correspond to different longitudinal orders of the resonant spatial wavevectors (or different longitudinal modes). A variation of the resonator length leads to a change of the tilt angles of the resonant wavevectors and a change of the ring diameters in the far field.
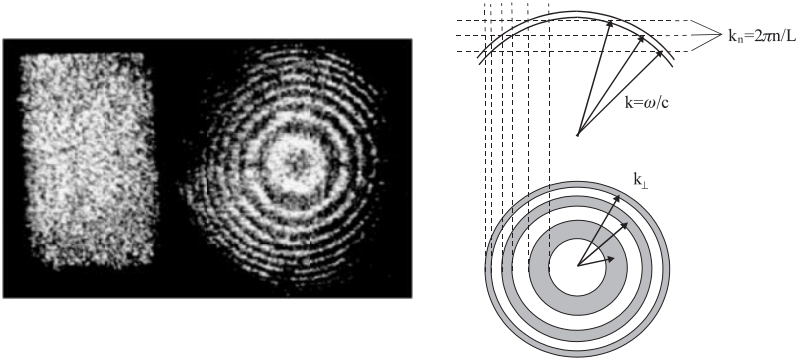
Fig. 6.9. *Left*: a transverse pattern (near field at the *left*, far field at the *right*) recorded experimentally in a PRO with a nearly confocal resonator. The intracavity aperture was completely open. *Right:* schematic interpretation of the Fresnel rings in the PRO resonator. The PRO emits in a narrow frequency band, which is related to the wavenumber of the emitted light $k = \omega/c$. The light is radiated at angles such that the longitudinal component of the wavevector matches the longitudinal-mode condition of the resonator

To realize the case of a single-longitudinal mode (but with multiple transverse modes) describable by the CSH equation, the emission was restricted to a single ring by an aperture in the far-field plane. Under these conditions the PRO displayed the typical patterns predicted by CSH equation, which depended on the resonator tuning.

References

1. G.J. de Valcárcel, Order-parameter equations for transverse pattern formation in nonlinear optical systems with nonplanar resonators, Phys. Rev. A **56**, 1542 (1997). 92
2. M. Brambilla, F. Battipede, L.A. Lugiato, V. Penna, F. Prati, C. Tamm and C.O.Weiss, Transverse laser patterns. I. Phase singularity crystals, Phys. Rev. A **43**, 5090 (1991). 95
3. K. Staliunas, G. Slekys and C.O. Weiss, Nonlinear pattern formation in active optical systems: shocks, domains of tilted waves, and cross-roll patterns, Phys. Rev. Lett. **79**, 2658 (1997). 96

7 The Restless Vortex

A single, isolated vortex in a class A or C laser, as described by the CSH equation (2.26), is stationary. However, in the case of a class B laser, the situation is different. Free vortices are not stationary but are in permanent motion. Also, a lattice of vortices experiences permanent self-sustained motion, leading to various oscillation modes.

For class B lasers, the population inversion decays slowly, and the following relations hold: $\gamma_\parallel/\kappa = \mathcal{O}(\varepsilon)$ and $\gamma_\parallel/\gamma_\perp = \mathcal{O}(\varepsilon)$, where ε is a smallness parameter. The eigenvalue associated with the population inversion D in the linear stability analysis, $\lambda(k) = -\gamma_\parallel$, does not lie sufficiently deep below the zero axis. Consequently, the population inversion is not enslaved by the fast variables, namely the field and the polarization, and cannot be adiabatically eliminated. The CSH equation is therefore an oversimplified model for a class B laser and does not describe adequately its spatio-temporal phenomena.

It is well known that single-transverse-mode class B lasers show relaxation oscillations with a frequency

$$\omega_{\mathrm{rel}} = \sqrt{2\kappa\gamma_\parallel(D_0 - 1) - \frac{\gamma_\parallel^2}{4}} \, , \tag{7.1}$$

where the polarization is assumed to relax infinitely fast, i.e. $\gamma_\perp \to \infty$. On the other hand, a single-transverse-mode laser, as described by the CSH equation, reaches its stationary state monotonically, and does not show relaxation oscillations. It is plausible to expect also that the spatio-temporal dynamics of class B lasers are different from those of lasers of class A and class C, which are described by the CSH equation.

7.1 The Model

An order parameter equation system describing the spatio-temporal dynamics of a class B laser close to the emission threshold can be obtained by applying the techniques presented in Chap. 2. We use here the method of adiabatic elimination used in Sect. 2.3 in the limit of a class A laser.

For a class B laser, owing to the slowness of the population inversion, one can consider the equations of the field and polarization ((2.1a) and (2.1b))

separately from the equation of the population inversion (2.1c), and diagonalize the system formed by (2.1a) and (2.1b), considering $D(\boldsymbol{r}, t)$ as a parameter. This leads to the following growth rate of perturbations:

$$\lambda_{1,2}(\Delta\omega) = -\frac{\kappa}{2}\left(2 + \mathrm{i}\,\Delta\omega \pm \sqrt{4D - \Delta\omega^2}\right). \tag{7.2}$$

Here, as in Chap. 2, the particular case $\kappa = \gamma_\perp$ is considered for simplicity. Generalization to arbitrary values of κ and $\gamma_\perp$ (but keeping $\mathcal{O}(\kappa) = \mathcal{O}(\gamma_\perp)$) is straightforward. The eigenvector system associated with (7.2) is, in matrix form,

$$V = \begin{pmatrix} 1 & (1/2)\left(\mathrm{i}\,\Delta\omega + \sqrt{4D - \Delta\omega^2}\right) \\ 1 & (1/2)\left(\mathrm{i}\,\Delta\omega - \sqrt{4D - \Delta\omega^2}\right) \end{pmatrix}, \tag{7.3}$$

and its adjoint transformation matrix $S = (V^{-1})^{\mathrm{T}}$ is given by

$$S = \frac{1}{\sqrt{\kappa}\sqrt{4D - \Delta\omega^2}} \begin{pmatrix} (1/2)\left(-\mathrm{i}\,\Delta\omega + \sqrt{4D - \Delta\omega^2}\right) & 1 \\ (1/2)\left(\mathrm{i}\,\Delta\omega + \sqrt{4D - \Delta\omega^2}\right) & 1 \end{pmatrix}. \tag{7.4}$$

The expressions for the eigenvalues (7.2), the eigenvectors (7.3) and the transformation matrix (7.4) are analogous to the expressions (2.10), (2.15) and (2.16) for class A and class C lasers in Chap. 2. The difference is that here a time- and space-dependent population inversion $D(\boldsymbol{r}, t)$ appears instead of a homogeneous, stationary population inversion D_0.

Now, we define a new set variables $\boldsymbol{A} = (A, B)^{\mathrm{T}}$, related to the old ones by the transformation $\boldsymbol{A} = S\boldsymbol{E}$ and viceversa, $\boldsymbol{E} = S^{-1}\boldsymbol{A}$.

The equations for the field and polarization can now be rewritten, in terms of the new variables, as

$$\frac{2}{\kappa}\frac{\partial A}{\partial t} = -\mathrm{i}\,\Delta\omega\,A + \left(\sqrt{4D - \Delta\omega^2} - 2\right)A\,, \tag{7.5a}$$

$$\frac{2}{\kappa}\frac{\partial B}{\partial t} = -\mathrm{i}\,\Delta\omega\,B - \left(\sqrt{4D - \Delta\omega^2} + 2\right)B\,. \tag{7.5b}$$

The equation for the population inversion transforms to

$$\frac{\partial D}{\partial t} = -\gamma_\parallel\left[D - D_0 + \frac{\kappa}{2}\sqrt{4D - \Delta\omega^2}\left(|A|^2 - |B|^2\right)\right]. \tag{7.6}$$

As follows from (7.5b), the stable variable B decays rapidly to zero and can be neglected. Now, expanding the term with the square root in (7.5a) and (7.6) as a Taylor series, assuming the near-threshold condition $p = D - 1 = \mathcal{O}(\varepsilon^2)$ and the near-to-resonance condition $\Delta\omega = \mathcal{O}(\varepsilon)$, we obtain

$$\frac{2}{\kappa}\frac{\partial A}{\partial t} = (D-1)A + \mathrm{i}\left(a\nabla^2 - \omega\right)A - \frac{1}{4}\left(a\nabla^2 - \omega\right)^2 A \,, \tag{7.7a}$$

$$\frac{\partial D}{\partial t} = -\gamma_\parallel\left(D - D_0 + |A|^2\right). \tag{7.7b}$$

If we remove the assumption of $\kappa = \gamma_\perp$ (but assume that these two coefficients are of the same order, $\mathcal{O}(1)$) we obtain the order parameter equation for the general case of a class B laser:

$$\frac{\partial A}{\partial \tau} = (D-1)A + \mathrm{i}\left(a\nabla^2 - \omega\right)A - \frac{\kappa^2}{(\kappa + \gamma_\perp)^2}\left(a\nabla^2 - \omega\right)^2 A, \tag{7.8a}$$

$$\frac{\partial D}{\partial \tau} = -\gamma\left(D - D_0 + |A|^2\right), \tag{7.8b}$$

where we recall that the variables appearing in (7.8) are related to the original ones through the relations $\tau = t\kappa\gamma_\perp/(\kappa + \gamma_\perp)$, $\gamma = (\kappa + \gamma_\perp)\gamma_\parallel/\kappa\gamma_\perp$, and a normalized field intensity $\kappa\,|A|^2 \to |A|^2$ has been used.

The two coupled equations (7.8) have also been derived in [1] using the multiscale expansion technique. They are the basic equations used for the study of the spatio-temporal dynamics in class B lasers throughout this chapter.

During the diagonalization procedure, the time-dependent transformation matrix S was used, which obviously does not commute with the operator of the time derivative $\partial/\partial t$. In fact, the commutation of these operators was assumed in obtaining (7.8). Assuming the above near-threshold condition $D - 1 = \mathcal{O}(\varepsilon^2)$, however, we obtain the result that the commutator is of higher order of smallness than the rest of the terms in (7.8), and thus can be neglected. Therefore, in the framework of the near-threshold assumption used here, the system (7.8) is valid for a class B laser.

7.2 Single Vortex

A numerical study of a single vortex in a class B laser (in the framework of (7.8), and also in the framework of the complete Maxwell–Bloch equations (2.1)) reveals a surprising result: a single, isolated vortex, placed in a homogeneous background, is not stationary as in a class A laser, but shows a self-induced, permanent motion. For some values of the parameters, the motion resembles a "stochastic meandering" of the vortex core. Sometimes the motion is circular or flower-like. In order to understand the origin of this self-induced motion we inspect the distributions of the optical field A and of the population inversion D at the vortex core.

Figure 7.1a shows the fields along a line crossing the center of a stationary vortex. At the vortex center the order parameter A, which is proportional to the optical field, is zero. As the population inversion does not decay in the
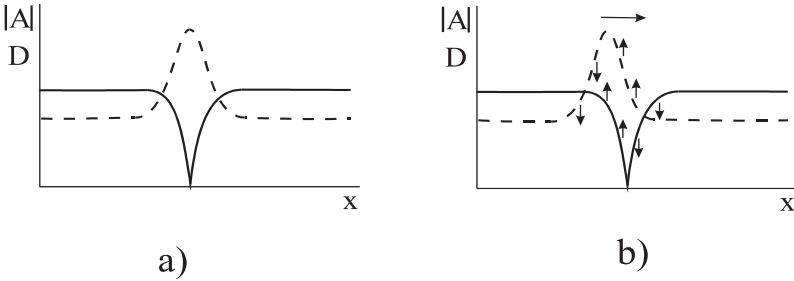
Fig. 7.1. Electric-field modulus (*solid line*) and population inversion (*dashed line*), corresponding to (**a**) a stationary optical vortex, and (**b**) a vortex moving to the right, on the axis along which the vortex moves in (**b**). The changes of the field are shown by *arrows*

absence of an optical field, an inversion maximum builds at the location of the optical vortex.

If we perturb the envelope of the field by shifting the "optical part" of the vortex, as shown in Fig. 7.1b, restoring forces appear, represented by vertical arrows in the figure. The inversion builds up at the new location of the zero of the optical field. In this way, the inversion profile tends to follow the motion of the "optical part" of the vortex. The restoring forces on the optical fields are such that the shifted zero of the field is pushed further in the same direction: the trailing slope is amplified more since the inversion is larger there, and the leading edge is attenuated more, since the inversion is smaller there.

As a consequence, the zero of the optical field moves away from the maximum of the population inversion. Its escape velocity is proportional to κ, the buildup rate of the optical field. The population inversion follows the escaping zero of the field. Its maximum velocity is proportional to the buildup rate of the population inversion, $\gamma_\parallel$. If the population inversion is faster than the optical field, i.e. $\gamma_\parallel \geq \kappa$, its maximum cannot escape the zero of the optical field, and thus the location of the optical vortex is stabilized. In the case of a class B laser, where $\gamma_\parallel \leq \kappa$, the population inversion relaxes more slowly than the field, and the race between the zero of the optical field and the maximum of the population inversion continues forever.

The velocity of the vortex motion can be estimated by assuming that the laser field at a particular location goes through half a period of a relaxation oscillation during the passage of a restless vortex through it. Since the radius of the vortex is proportional to $r_0 \approx \sqrt{a/(D_0 - 1)}$, and the relaxation oscillations have a frequency $\omega_{\mathrm{rel}} = \sqrt{2\gamma(D_0 - 1) - \gamma^2/4}$, the velocity of the self-induced motion estimated in this way is

$$|\boldsymbol{v}| = \frac{2r_0\omega_{\mathrm{rel}}}{\pi} = \frac{2\sqrt{2a\gamma}}{\pi}\sqrt{1 - \frac{\gamma}{8(D_0 - 1)}} \ . \tag{7.9}$$
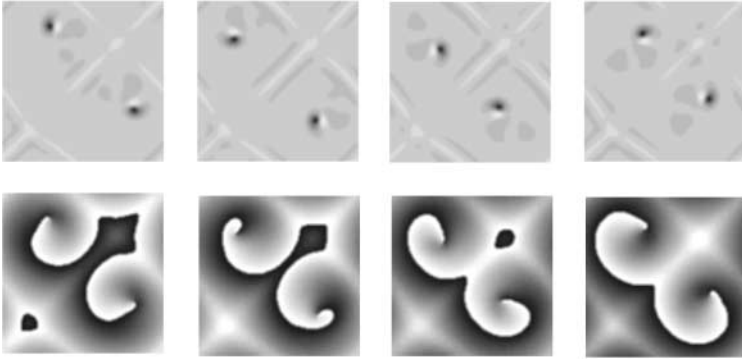
Fig. 7.2. Restless motion of two vortices. Two vortices with opposite topological charge have been considered, since the periodic boundary conditions require zero total charge. The positively charged vortex at the *bottom right* corner moves clockwise, and the other, negatively charged vortex, moves anticlockwise. The parameters are $D_0 = 2, \gamma = 0.1$, $a = 0.0001$ and $g = 1.25$; the time between successive plots is $t = 20$
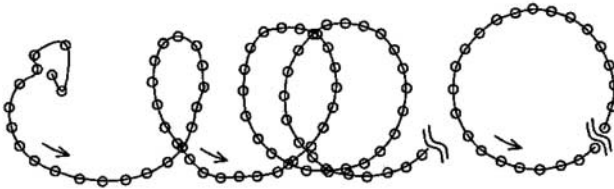

Fig. 7.3. Trajectory of a restless vortex with positive topological charge: the transient toroidal trajectory and the final circular trajectory. The parameters are as in Fig. 7.2, and time between successive points is $\Delta t = 3.5$

Numerical calculations show that the estimation (7.9) works well concerning the velocity of the vortex $|v| \approx 2\sqrt{2a\gamma}/\pi$, and also concerning the threshold condition for self-induced vortex motion, $\gamma = 8(D_0 - 1)$. In Fig. 7.2, the motion of two restless vortices, obtained numerically, is shown.

Figure 7.3 shows the trajectory of a restless vortex. The direction in which the vortex starts to move is given by an initial symmetry breaking. After a transient toroidal motion, the asymptotic vortex trajectory is circular. Apparently, the rotatory nature of the vortex motion is related to the fact that the vortex itself is a rotating object.

The vortex is squeezed in the direction of motion. Figure 7.4 shows the field amplitude (a magnified part of the first plot of Fig. 7.2), where this squeezing is visible. The field maximum behind the vortex corresponds to the maximum of the population inversion. The optical and material parts of the vortex are shifted, so that the population inversion maximum lags behind.
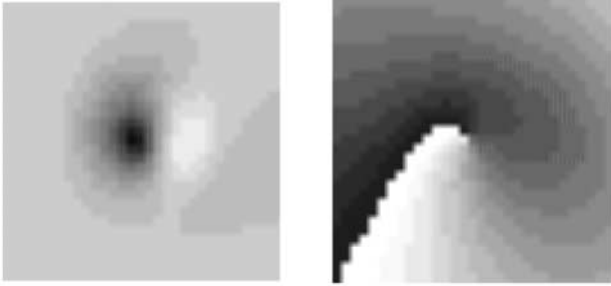
Fig. 7.4. A restless vortex taken from the first plot in Fig. 7.2, and magnified four times. The vortex moves to the *left*, and is squeezed along the direction of motion

The radius of the circular orbit of the vortex depends in general on the diffusion coefficient in the equation for the field (the g-factor), and also on the decay rate of the population inversion, γ. The exact dependence is unclear. The numerical calculations indicate that the radius of the vortex orbit increases with a decrease of the diffusion factor g and the population inversion decay rate γ. However, even in the purely diffractive case $g = 0$, the vortex trajectory is a curved, not a straight line. This is related to the fact that a spatially dependent gain occurs because of the spatial mismatch between the field zero and the maximum of the population inversion. This creates a spatial profile of both the background field intensity and the background field phase. The gradients of both the intensity and the phase push the optical vortex in accordance with the results of Chap 2: the vortex motion induced by the phase inhomogeneity is parallel to the phase gradient, and should result in a parallel motion of the restless vortex in the purely diffractive case. However, the inhomogeneity of the intensity causes a vortex motion perpendicular to the intensity gradient. The amplitude and phase gradients together cause a circular vortex motion, even in the purely diffractive case.

7.3 Vortex Lattices

The nonstationarity of a single vortex in a class B laser suggests that vortices arranged in a lattice will also be, in general, nonstationary. Numerical integration of the class B laser equations confirms this suggestion.

As shown in [2], vortex oscillations in a vortex lattice can be synchronized in different ways. "Optical", "acoustic" and several "mixed" oscillation modes have been identified here, on the basis of numerical integration of the laser equations with reflecting (zero flux) boundary conditions. When periodic boundaries are used, two pure cases of self-induced dynamics of vortex lattices are observed: (1) an "optical" oscillation mode, where neighboring vortices along a diagonal (with the same topological charge) oscillate in antiphase, and (2) a parallel translation of the vortex lattice. The analogue of

this translational motion in the case of reflecting boundaries is an "acoustic" oscillation mode.

7.3.1 "Optical" Oscillation Mode

Figure 7.5 shows four snapshots of a vortex lattice, where neighboring vortices along the diagonal oscillate in antiphase. The motion resembles the oscillation of atoms in a crystal when an "optical" oscillation mode is excited.

An interesting fact is that the vortices in the oscillating square vortex lattice are arranged hexagonally most of the time. The average intensity distribution is, however, of square symmetry.
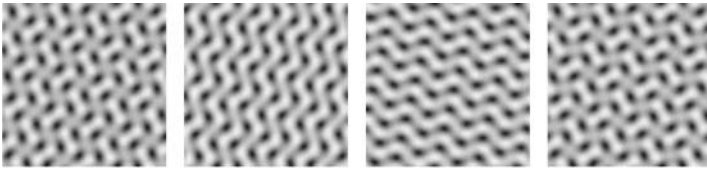
Fig. 7.5. Oscillations of a vortex lattice as obtained by numerical integration of (7.8). The parameters are $g = 0.2$, $D_0 = 2$, $\omega = 0.335$, $\gamma = 0.1$. The time between snapshots is $t = 5$

The oscillation frequency of the "optical" oscillation mode can be found by noting that the far field of an oscillating vortex lattice, as shown in Fig. 7.6, is a superposition of two cross-roll patterns rotated by $45°$. One cross-roll has a resonant transverse wavenumber, with eigenfrequency $\omega_0 = ak^2$; the wavenumber of the other pair of cross-rolls is larger by a factor of $\sqrt{2}$, which corresponds to the eigenfrequency $\omega_1 = 2ak^2$. This leads to a beat frequency $\Delta\omega = ak^2$.
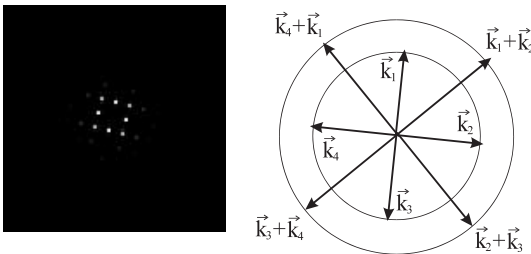

Fig. 7.6. Spatial Fourier spectrum of the optical field in the oscillating vortex lattice shown in Fig. 7.5 (*left*). *Right*, the composition of the wavevectors in the oscillating vortex lattice

7.3.2 Parallel translation of a vortex lattice

If the gain line is extremely narrow ($\Delta\omega \ll ak^2$), then both cross-rolls cannot be simultaneously excited, and the "optical" oscillation mode does not appear. Instead of oscillating, the vortices start to drift. Drift occurs if the tilted-wave components of the vortex lattice have different frequencies.

To investigate the drift of a vortex lattice, we use the ansatz

$$A(\boldsymbol{r},t) = \sum_{j=1,4} A_i \exp(\mathrm{i}\,\boldsymbol{k}_j \cdot \boldsymbol{r} - \mathrm{i}\omega_j t) \,, \tag{7.10a}$$

$$D(\boldsymbol{r},t) = d_0 + \sum_{j=1,4}\sum_{l=1,4} d_{j,k} \exp\left[\mathrm{i}\,(\boldsymbol{k}_j - \boldsymbol{k}_l) \cdot \boldsymbol{r} - \mathrm{i}\,(\omega_j - \omega_l)\,t\right], \tag{7.10b}$$

where the frequencies obey $\sum \omega_j = 0$. For a parallel translation of the vortex lattice, the frequencies of antiparallel TW components are of opposite sign: $\omega_1 = -\omega_3$ and $\omega_2 = -\omega_4$. The drift direction depends on the frequency ratio: $\boldsymbol{v} \cdot \boldsymbol{k}_j = \omega_j/\omega$, where $\omega = \sqrt{\omega_1^2 + \omega_2^2}$ is the total oscillation frequency, and

$$\omega^2 = \frac{\gamma\,(D_0 - 1)}{4 + \gamma} \,. \tag{7.11}$$

As (7.10) and (7.11) indicate, oscillations of the intensity of the optical field appear at every location, and are related to the translational motion of the pattern. The frequency of the intensity oscillations in the limit of slow population inversion is $\omega_{\mathrm{osc}} = 2\omega = \sqrt{\gamma(D_0 - 1)}$, and thus this frequency is smaller than the frequency of the relaxation oscillation by a factor of $\sqrt{2}$.

The corresponding velocity of the pattern is $|\boldsymbol{v}| = \omega/k$, given by

$$|\boldsymbol{v}| = \frac{\sqrt{\gamma_\parallel\,(D_0 - 1)}}{2k} \,. \tag{7.12}$$

A parallel translation of a square vortex lattice is possible for periodic boundary conditions only. For reflecting boundaries, a square vortex lattice either is fixed if the area is too small, or oscillates periodically as a whole. The latter oscillation mode of the vortex lattice has been called an "acoustic" oscillation mode in [2].

Figure 7.7 illustrates the "acoustic" oscillation mode in the case of one spatial dimension. In this case we can excite a standing-wave pattern (owing to the reflecting boundaries). The standing wave oscillates back and forth, as shown in the figure. A vortex lattice in 2D oscillates in a similar way.

Summarizing, the vortex lattice either oscillates in an "optical" mode or undergoes a parallel translation, for periodic boundary conditions and a class B laser. The vortex lattice is never at rest. For reflecting (zero flux) boundary conditions, the lattice can also oscillate in an "optical" mode. A parallel translation is impossible in this case, and therefore the lattice either displays an "acoustic" oscillation mode or is at rest. For boundaries different
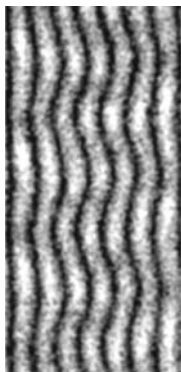
Fig. 7.7. Temporal oscillations of a 1D optical pattern (a standing wave) as obtained by numerical integration of the 1D version of (7.8) with reflecting lateral boundaries. The spatial coordinate is horizontal; the time varies from *top* to *bottom* by $t = 100$. The parameters are $D_0 = 1.5$, $\gamma = 0.16$ and $g = 0.1$

from those discussed above, the vortex oscillations can synchronize in different ways. For example, in the case of a rotationally symmetric boundary (a circular aperture, or a spherical mirror), small vortex ensembles can rotate.

All self-induced oscillations of vortices and vortex lattices in the case of a class B laser occur at a frequency of the order of the relaxation oscillation frequency.

7.4 Experimental Demonstration of the "Restless" Vortex

The "restless vortex" phenomenon suggests that simple transverse patterns consisting of one or several optical vortices, which are stationary in class A lasers, may be nonstationary (periodic or chaotic) in class B lasers. In a class A laser, the frequencies of the transverse modes are pulled towards one another and may lock to a common frequency, owing to the nonlinear coupling via the population inversion common to both modes, as described in Chap. 6. In contrast, in a class B laser, a vortex is nonstationary, and transverse modes may not lock in this case.

In this section, a cavity with curved mirrors is considered. In this case, vortex solutions correspond to the excitation of high-order modes in the cavity. Many of the expressions used here have already been derived in Chap. 6.

7.4.1 Mode Expansion

We look for solutions of (7.8) containing a small number of transverse modes, using a mode expansion technique for the optical field, represented by

$$A(\boldsymbol{r}, t) = \sum_i f_i(t) A_i(\boldsymbol{r}) , \qquad (7.13)$$

where i is an arbitrary combination of the mode indices p and l.[1] The expansion (7.13) was used in Chap. 6 in the limit of a class A laser, where the population inversion can be adiabatically eliminated. In this case $D(\boldsymbol{r}, t)$ was expressed as a function of the field $A(\boldsymbol{r}, t)$,

$$
\begin{aligned}
D(\boldsymbol{r}, t) &= \frac{D_0}{1 + |A(\boldsymbol{r}, t)|^2} \approx D_0 - |A(\boldsymbol{r}, t)|^2 \\
&= D_0 - \sum_i f_i(t) f_j(t) A_i(\boldsymbol{r}) A_j^*(\boldsymbol{r}) \ .
\end{aligned}
\tag{7.14}
$$

Since the population inversion is not enslaved by the optical field in a class B laser, we expand the population inversion too:

$$
D(\boldsymbol{r}, t) = D_0 - \sum_i d_{ij}(t) A_i(\boldsymbol{r}) A_j^*(\boldsymbol{r}) \ .
\tag{7.15}
$$

The motivation for the expansion (7.15) is the expression (7.14), since in the limiting case of a class A laser $d_{ij} = f_i f_j^*$. We insert the expressions (7.13) and (7.15) into (7.8), multiply (7.8a) by A_k^* and integrate over the two-dimensional space. This leads to the following equations for the mode coefficients $f_i(t)$ and $d_{ij}(t)$:

$$
\frac{\partial f_i}{\partial \tau} = p_i f_i - \mathrm{i} \left(\omega_i - \omega_0 \right) f_i - \sum_{jkl} \Gamma_{jk}^{il} f_j d_{kl} \ ,
\tag{7.16a}
$$

$$
\frac{\partial d_{ij}}{\partial \tau} = -\gamma_\parallel \left(d_{ij} - f_i f_j^* \right) ,
\tag{7.16b}
$$

where p_i and the nonlinear coupling coefficients Γ_{jk}^{il} have been defined in (6.8).

The model (7.16) is, to our knowledge, the simplest one capable of describing a multi-transverse-mode class B laser. In principle, it describes an arbitrary number of transverse modes, but in practice it is useful if a small number of modes is excited. We analyze two-mode states in this section, for which the equations (7.16) read

$$
\frac{\partial f_1}{\partial \tau} = p_1 f_1 - \mathrm{i}(\omega_1 + \omega_0) f_1
\tag{7.17a}
$$
$$
\qquad -f_1(G_{11} d_{11} + G_{12} d_{22}) - f_2(G_{12} d_{12} + G'_{12} d_{21}) \ ,
$$
$$
\frac{\partial f_2}{\partial \tau} = p_2 f_2 - \mathrm{i}(\omega_2 + \omega_0) f_2
\tag{7.17b}
$$
$$
\qquad -f_2(G_{22} d_{22} + G_{12} d_{11}) - f_1(G_{12} d_{21} + G'_{12} d_{12}) \ ,
$$
$$
\frac{\partial d_{ij}}{\partial \tau} = -\gamma_\parallel \left(d_{ij} - f_i f_j^* \right) ,
\tag{7.17c}
$$

where the coupling coefficients are as defined in (6.9).

---

[1] Actually we expand (7.8a) here, but take into account of a spatially dependent detuning corresponding to the curved mirrors of the resonator.

We recall that the coefficient G'_{12} vanishes for phase-insensitive (helical) modes (6.3), and is nonzero for phase-sensitive (flower) modes (6.12).

7.4.2 Phase-Insensitive Modes

In a class A laser, the frequencies of phase-insensitive modes are not affected by the nonlinear coupling. The vortices rotate around the optical axis with a frequency exactly equal to the difference of the eigenfrequencies of the two corresponding modes. In the degenerate case the vortices stop rotating. We show below that for a class B laser, the vortices behave differently.

We look for solutions of (7.17) in the form $f_i(t) = n_i \exp(i\Omega_i t)$. The coefficients of the population inversion become

$$d_{ii} = f_i f_i^* \,, \tag{7.18a}$$

$$d_{ij} = -f_i f_j^* \frac{\gamma}{\gamma + i(\Omega_i - \Omega_j)} \,, \tag{7.18b}$$

and the mode beat frequency $\Delta\Omega = \Omega_i - \Omega_j$ obeys the equation

$$\left(1 - \frac{\Delta\omega}{\Delta\Omega}\right)\left[\gamma^2\left(\frac{G_{11}}{G_{12}} + 2\right) + \Delta\Omega^2\left(\frac{G_{11}}{G_{12}} + 1\right)\right] = 2\gamma(D_0 - 1), \quad (7.19)$$

where $\Delta\omega = \omega_i - \omega_j$ is the mode degeneracy here [2], or, in other words, the difference of the eigenfrequencies of the modes.
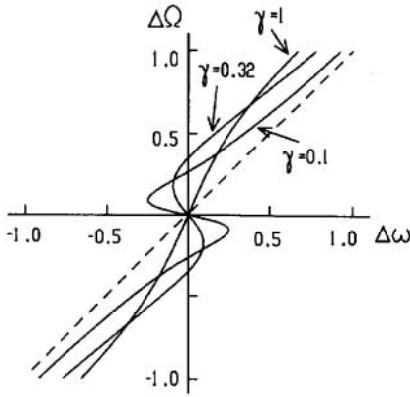

Fig. 7.8. The mode beat frequency $\Delta\Omega$ versus the mode frequency detuning $\Delta\omega$ for different values of γ. The mode-coupling coefficients correspond to the beating of the TEM_{01} and TEM_{01}^* modes (a circling vortex)

A family of curves of $\Delta\Omega$ versus $\Delta\omega$ for different values of γ is plotted in Fig. 7.8. The curves clearly show the mode-pushing phenomenon in the case of a class B laser. The pushing is weaker in the intermediate case between a class A and a class B laser ($\gamma \approx 1$) and grows with decreasing γ. When

---

[2] Do not confuse this $\Delta\omega$ with $\Delta\omega = \omega - a\nabla^2$ used previously in this chapter.

$$\gamma < \frac{2\,(D_0 - 1)}{G_{11}/G_{12} + 2} \ , \tag{7.20}$$

bistability appears. In this case the beat frequency is never zero, which means that a stationary pattern consisting of helical modes is never generated.

The frequency of the self-induced mode beat in the case $\Delta\omega = 0$ is given by

$$\Delta\Omega_0^2 = \frac{2\gamma\,(D_0 - 1) - \gamma^2\,(G_{11}/G_{12} + 2)}{G_{11}/G_{12} + 1} \ , \tag{7.21}$$

which is proportional to the frequency of the relaxation oscillations in the limit $\gamma \ll 1$.

7.4.3 Phase-Sensitive Modes

Mode pushing also occurs for the modes which frequency-pull for class A lasers. For a class B laser, the relation between the mode beat frequency and the detuning is modified with respect to the class A laser, as shown in Fig. 7.9. The mode-locking region shrinks with decreasing γ and bistability appears, similarly to the case of no mode-locking.
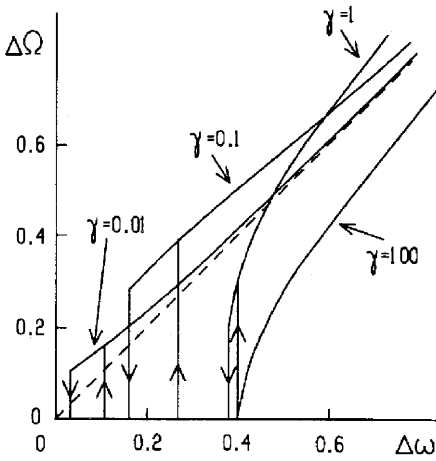

Fig. 7.9. The mode beat frequency $\Delta\Omega$ versus the mode frequency detuning $\Delta\omega$ for different values of γ in the mode-pulling case. The mode-coupling coefficients correspond to the TEM_{10} and TEM_{01} Gauss–Hermite modes, and their locking to the helical TEM_{01}^* mode

A numerical analysis leads to the conclusion that the transition between mode locking and unlocking occurs at a mode beat frequency proportional to the relaxation oscillation frequency: the pattern either oscillates at a frequency larger than the relaxation frequency or locks to a stationary pattern. A pattern consisting of nonlocking modes is never at rest for a class B laser.

The mode locking was investigated experimentally by studying the vortex behavior in a CO_2 laser [3]. Figure 7.10 shows the frequency of the spatial

oscillations of the laser pattern as the frequency mismatch of the modes was varied (by varying the astigmatism of the resonator). The experiment shows the predicted hysteresis in the locking and unlocking of the vortex. The experiment also shows that the smallest possible frequency of the oscillations is proportional to the relaxation oscillation frequency.
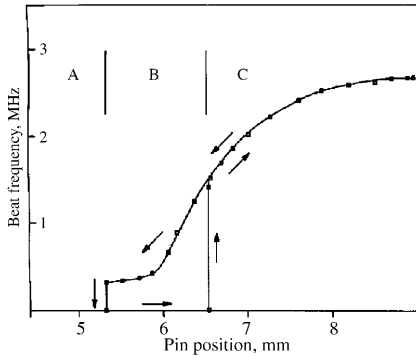

Fig. 7.10. Locking and unlocking of the "doughnut" in a CO_2 laser. The pin position controls the astigmatism of the resonator, and correspondingly the frequency detuning between the Gauss–Hermite modes

References

1. J. Lega, J.V. Moloney and A.C. Newell, Universal description of laser dynamics near threshold, Physica D **83**, 478 (1995).   105
2. K. Staliunas and C.O. Weiss, Nonstationary vortex lattices in large-aperture class B lasers, J. Opt. Soc. Am. B **12**, 1142 (1995).   108, 110
3. G. Slekys, K. Staliunas, M.F.H. Tarroja and C.O. Weiss, Cooperative frequency locking and tristability in a class-B laser, Appl. Phys. B **59**, 11 (1994).   114

8 Domains and Spatial Solitons

This chapter is devoted to the description of the general properties of a particular class of solutions of extended nonlinear systems, namely spatial solitons, or localized structures. In contrast to extended patterns, such as rolls or hexagons, spatial solitons are solutions where the field is inhomogeneous only in a localized region of the space and is homogeneous in the rest of the space.

The stability of spatial solitons is due to a balance between linear and non-linear effects. In transverse nonlinear optics, these balancing effects are usually the spreading caused by diffraction and the compression (self-focusing) caused by a focusing nonlinearity.

Spatial solitons have been theoretically predicted for a variety of nonlinear optical cavities [1]. In this chapter we present some general concepts concerning spatial domains and solitons, and the next three chapters are devoted to the implementation of these ideas in concrete optical systems.

The study of optical solitons is relevant not only from a fundamental viewpoint but also because of their potential applications in information processing technology. Such practical applications will be discussed in Chaps. 9 and 11.

8.1 Subcritical Versus Supercritical Systems

The existence of spatial solitons is closely related to the character of the bifurcation from the nonlasing (trivial) to the lasing regime. It is useful to review here some basic concepts of bifurcation theory [2].

A bifurcation is supercritical if the transition from one solution to another, obtained by varying the control parameter (the pump intensity in the optical case), is continuous, and the solutions connect at the bifurcation point. Equivalently, an infinitesimal variation of the control parameter leads to an infinitesimal change in the amplitude of the solution in the case of a supercritical bifurcation. Examples of a supercritical bifurcation are shown in Figs. 8.1a,c. A supercritical bifurcation corresponds to a phase transition of type II. In contrast, a bifurcation is subcritical if, at the bifurcation point, the amplitudes of the solutions differ by a finite quantity (i.e. they are disconnected). In this case, both solutions may coexist below the bifurcation
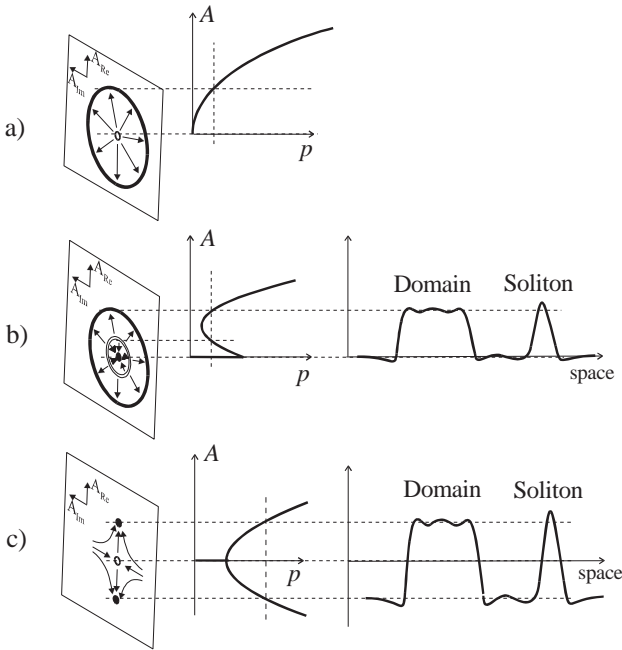
Fig. 8.1. Different types of bifurcation in nonlinear systems. (**a**) Supercritical Hopf bifurcation, (**b**) subcritical Hopf bifurcation, (**c**) supercritical pitchfork bifurcation. A is the amplitude of the solution, and is p the pump (criticality) parameter

point, the system showing bistability or hysteresis (Fig. 8.1b, center). The corresponding phase transition is of type I.

Another possible classification of bifurcations takes into account the symmetry of the phase of the emerging solution. When the phase of the solution is invariant (not fixed by the system), a Hopf bifurcation occurs, as shown in the phase diagrams at the left in Figs. 8.1a,b. If two opposite values of the phase are preferred, a pitchfork (static) bifurcation occurs instead, and a real-valued order parameter is obtained.

As discussed in the following sections, some kind of bistability is always needed for the existence of domains and of spatial solitons. The order parameter equations derived in Chaps. 2 and 3 (the Ginzburg–Landau and Swift–Hohenberg equations, either real or complex), which are representative of most nonlinear optical systems, possess a primary bifurcation of supercritical type.

8.2 Mechanisms Allowing Soliton Formation

There are two basic mechanisms that may cause subcriticality, and consequently may lead to soliton formation. Both are related to the existence of

absolute bistability between two different extended solutions (which may or not be homogeneous). In order to show this, let us consider the complex Swift–Hohenberg equation, and analyze the properties of its simplest non-trivial solution: a traveling wave.

8.2.1 Supercritical Hopf Bifurcation

Consider the simplest form of the complex Swift–Hohenberg equation, as obtained in Chaps. 2 and 3:

$$\frac{\partial A}{\partial t} = pA - A\,|A|^2 + \mathrm{i}\left(a\nabla^2 - \Delta\right)A - g\left(a\nabla^2 - \Delta\right)^2 A \ . \tag{8.1}$$

Consider also a solution of (8.1) in the form of a traveling wave,

$$A = |A|\exp(\mathrm{i}k_0 x - \mathrm{i}\omega t) \ . \tag{8.2}$$

The intensity of the traveling wave can be found from (8.1), and plotted in terms of the various parameters. Figure 8.2a shows the usual bifurcation diagram, with the intensity as a function of the criticality parameter p. Another useful representation, shown in Fig. 8.2b, is the dependence of the intensity on the squared wavenumber. It is evident that no bistability is possible here, since the trivial solution is always unstable against a traveling wave when the latter exists. Consequently, solitons cannot be stable under supercritical conditions, and subcriticality of the emerging solution is then required. In order to introduce subcriticality, an external effect is usually added to the system, such as an intracavity saturable absorber, an intracavity focusing/defocusing material or parametric forcing. The corresponding equation modeling the dynamics is a modified Ginzburg–Landau or Swift–Hohenberg equation, with additional terms describing the subcriticality.
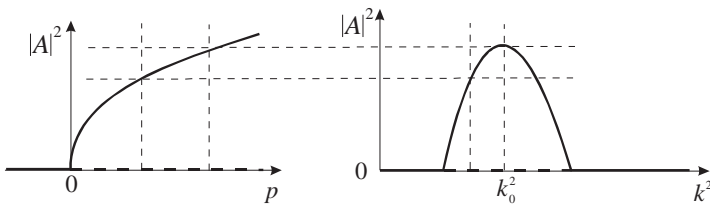

Fig. 8.2. Dependence of the intensity on the criticality parameter p and on the squared wavenumber k^2, in the case of a supercritical Hopf bifurcation

8.2.2 Subcritical Hopf Bifurcation

We consider two possible modifications of (8.1) that lead to subcritical solutions: (a) a modification of the local nonlinear terms, and (b) a modification of the nonlocal terms, containing spatial derivatives.

(a) The Quintic Complex Swift–Hohenberg Equation. In this case, a nonlinear term of fifth order is considered:

$$\frac{\partial A}{\partial t} = pA - bA\,|A|^2 - A\,|A|^4 + \mathrm{i}\left(a\nabla^2 - \Delta\right)A - g\left(a\nabla^2 - \Delta\right)^2 A \ . \quad (8.3)$$

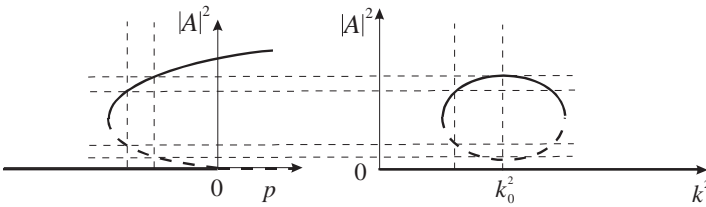The traveling-wave solution behaves as depicted in Fig. 8.3.

Fig. 8.3. Dependence of the intensity on the criticality parameter p and on the squared wavenumber k^2, in the case of a subcritical Hopf bifurcation generated by a quintic nonlinear term

The subcritical character of the bifurcation follows from the left-hand graph in Fig. 8.3 (there is a coexistence of solutions for $p < 0$). Differently from the supercritical case, the traveling-wave branch is disconnected from the trivial-solution branch (see the right-hand graph in Fig. 8.3). As a consequence, the trivial solution is stable for any wavenumber, reflecting an absolute bistability (bistability is not absolute if the upper branch connects with the trivial branch, as will be discussed in the next example).

A physical system showing this behavior is a laser with a saturable absorber, whose corresponding order parameter equation is

$$\frac{\partial A}{\partial t} = \frac{pA}{1 + |A|^2/I_\mathrm{p}} - \frac{\alpha A}{1 + |A|^2/I_\mathrm{s}} - A$$
$$+ \mathrm{i}\left(a\nabla^2 - \Delta\right)A - g\left(a\nabla^2 - \Delta\right)^2 A \ . \quad (8.4)$$

The effect of this type of nonlinearity will be analyzed in detail in the following chapter. Note that the fifth-order nonlinearity corresponds to the first terms in the Taylor expansion of the first two terms in (8.4).

In this example, the gain must be larger than the losses for stable solitons. This condition can be visualized by plotting the first and second terms in (8.4), as shown in Fig. 8.4.
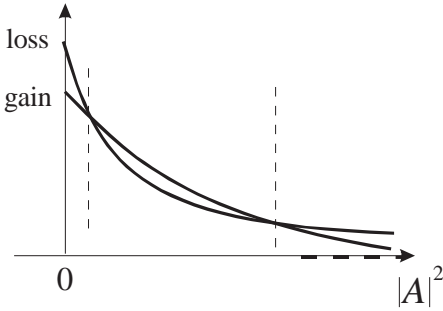
Fig. 8.4. Gain and losses in a laser with a saturable absorber

(b) Spatial Nonlinear Resonance. Usually the resonant wavenumber, corresponding to the solution selected by the system, is constant and given by $k_0^2 = -\Delta/a$. In some cases, however, the resonant wavenumber is intensity-dependent, a phenomenon known as nonlinear resonance. The complex Swift–Hohenberg equation then takes the form

$$\frac{\partial A}{\partial t} = pA - A\left|A\right|^2 + \mathrm{i}\left(a\nabla^2 - \Delta - \Delta_0\left|A\right|^2\right)A$$
$$- g\left(a\nabla^2 - \Delta - \Delta_0\left|A\right|^2\right)^2 A \ . \tag{8.5}$$

The properties of the traveling-wave solution of (8.5) are illustrated in Fig. 8.5: the nonlinear resonance results in a tilt of the resonance curve (a linear resonance corresponds to a symmetric parabola).

Note that, unlike the case of the quintic complex Swift–Hohenberg equation, the instability now is not absolute: there always exist a wavenumber (in fact, the band of wavenumbers between the two intersections of the resonance
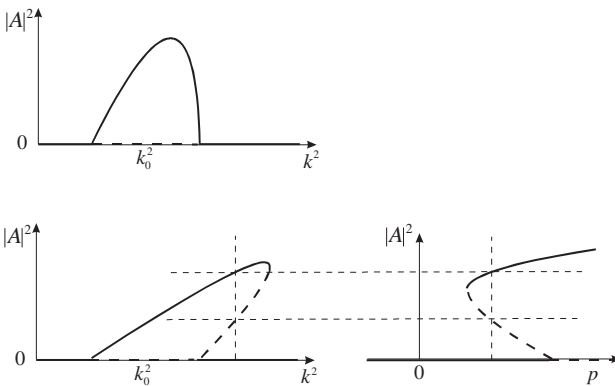

Fig. 8.5. Dependence of the intensity on the criticality parameter p and on the squared wavenumber k^2, in the case of a subcritical Hopf bifurcation generated by a nonlinear resonance term

curve with the axis) where the trivial solution is unstable. In order to have absolute bistability, this instability region must be removed.

One way of doing this is by shifting the curve to the left, since negative values of k_0^2 have no physical meaning. We then deal with a "cut" nonlinear resonance (Fig. 8.6). The bistability is now absolute, since the traveling-wave branch is completely disconnected from the trivial solution.

An example of a physical system showing a nonlinear resonance is a laser (or, in general, a nonlinear resonator) with intracavity focusing. This case will be treated in detail in Chap. 10.
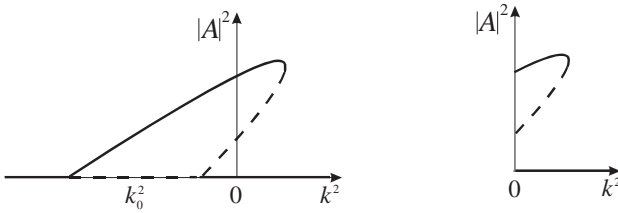

Fig. 8.6. The effect of shifting of the nonlinear resonance curve: (**a**) the whole curve, including unphysical solutions; (**b**) Cut nonlinear resonance, showing absolute bistability

8.3 Amplitude and Phase Domains

A spatial soliton can be regarded as a limiting case of a more general solution, a domain. A domain is a region of space of arbitrary size or shape (in a system with one or two spatial degrees of freedom, respectively) where a field of given amplitude and phase is separated from regions with a different field amplitude and phase by domain boundaries or domain walls. The domain walls correspond to the connections between two stable solutions.

The classification of bifurcations given in Sect. 8.1 (see Fig. 8.1) can be used to classify the different types of domains. When the fields inside and outside the domain differ only in their phase (thus having the same intensity in all of the space except at the walls), we refer to phase domains. Phase domains are related to a pitchfork bifurcation, as shown in Fig. 8.1c. Subcriticality is not required for phase domains. A detailed discussion of phase patterns is left to Chap. 11.

When, however, the fields differ in their amplitude, we refer to amplitude domains. In this case, a subcritical bifurcation is always needed.

Domains can be generated by means of a hard-excitation mechanism: a sufficiently strong spatially localized perturbation of the lower state can bring a portion of the system into the other state, even though a weak perturbation will not. Once a domain has been formed, it shows a dynamic behavior. The

domain walls expand or contract, depending on the parameters, eventually bringing the entire system into one of the two homogeneous states.

If the system parameters are not far away from a modulational stability boundary, the switching fronts connecting two homogeneous states show damped spatial oscillations on either side of the front.

Although a complete characterization of solitons requires, in general, a numerical solution of the model, some important predictions can be made by analyzing (i) the character of the bifurcation, as was done in Sect. 8.1, and (ii) the stability of the homogeneous solutions, to be discussed in the next section.

8.4 Amplitude and Phase Spatial Solitons

Usually, amplitude and phase solitons are referred to as bright solitons and dark ring solitons, respectively. This terminology comes from their intensity distribution: amplitude solitons connect solutions with different amplitudes (and also different intensities), and they appear as bright spots surrounded by a background of lower intensity (usually zero) (see Fig. 8.7a). On the other hand, phase solitons connect solutions of opposite phase (but of the same intensity), and they appear as dark rings (in 2D) or lines (in 1D) on a background of finite intensity (see Fig. 8.7b). As already stated, amplitude solitons always require subcriticality, but this is not necessary for phase solitons.
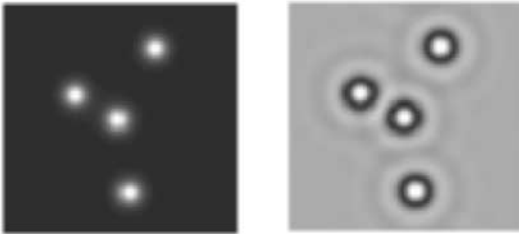

Fig. 8.7. Amplitude (*left*) and phase (*right*) solitons that are solutions of the equations for a degenerate optical parametric oscillator in different parameter regions. For the plot at the *left*, $E = 1.2$, and for the plot at the *right*, $E = 2.0$

Depending on the stability of the homogeneous solutions, amplitude spatial solitons can be interpreted in two ways. First, if a homogeneous solution corresponding to one of two bistability branches is modulationally unstable, then a soliton can occur as a homoclinic connection between a stable homogeneous state and a modulated (stripe or hexagon) state, as shown by Fauve and Thual in [3]. A soliton in this interpretation is a single, isolated band of

a stripe pattern in the 1D case, or a single isolated spot of a hexagonal pattern in the 2D case. The background solution (the solution far away from the soliton) corresponds to the stable solution branch in this interpretation. For bright solitons, the upper branch is usually modulationally unstable, and the radiation corresponding to the stable lower branch serves as a background. In the case of dark solitons, the unstable (modulated) solution is the lower branch [1].

In the case when both the upper and the lower branches are modulationally stable, solitons (or domains in general) can be interpreted as homoclinic connections between the two homogeneous states, as shown by Rosanov [4]. A spatial domain corresponding to one solution branch can contract to a minimum size and not contract further, owing to the interaction between domain boundaries. The bright soliton in this interpretation is a spatial domain of minimum size corresponding to the upper bistability branch, whereas the radiation corresponding to the lower branch acts as the background. For dark solitons, the opposite is true. The mechanisms of the interaction between domain walls that leads to stable solitons are under investigation, but it is more or less clear that a nonmonotonic spatial decay of the domain boundary plays a significant role in the stability of solitons. The stronger the spatial oscillations of a nonmonotonically decaying domain boundary are, the larger is the stability range of a spatial soliton of the Rosanov type. The effect of modulations will be treated in detail in Chap. 12.

Both type of solitons (amplitude and phase) can coexist in the same optical system if it is characterized by a subcritical pitchfork bifurcation. In this case the subcriticality is responsible for bright solitons, and the pitchfork bifurcation for phase solitons. The example shown in Fig. 8.7 corresponds to intensity distributions found by numerical integration of the equation for a DOPO in two transverse dimensions, with the same initial conditions but different parameters.

References

1. M. Tlidi, P. Mandel and R. Lefever, Localized structures and localized patterns in optical bistability, Phys. Rev. Lett. **73**, 640 (1994); K. Staliunas and V.J. Sánchez-Morcillo, Localized structures in degenerate optical parametric oscillators, Opt. Commun. **139**, 306 (1997); W.J. Firth and A.J. Scroggie, Optical bullet holes: robust controllable localized states of a nonlinear cavity, Phys. Rev. Lett. **76**, 1623 (1996). 117, 124
2. G. Ioos and D.D. Joseph, *Elementary Stability and Bifurcation Theory* (Springer, New York, 1990). 117
3. S. Fauve and O. Thual, Solitary waves generated by subcritical instabilities in dissipative systems, Phys. Rev. Lett. **64**, 282 (1990). 123
4. N.N. Rosanov, *Transverse Patterns in Wide-Aperture Nonlinear Optical Systems*, Progress in Optics, vol. 35, ed. by E. Wolf (North-Holland, Amsterdam, 1996). 124

9 Subcritical Solitons I: Saturable Absorber

In the previous chapter, the existence of solitons in subcritical systems was discussed from a general viewpoint. In this and the next chapter, we apply these concepts to concrete nonlinear optical systems. In the present chapter, a laser with a saturable absorber is analyzed. This system shows amplitude bistability, owing to the subcritical character of the bifurcation. Experimental results are also discussed, confirming the theoretical predictions.

9.1 Model and Order Parameter Equation

A simple theoretical model of a laser with an intracavity saturable absorber follows from the Maxwell–Bloch equation system after the adiabatic elimination of the fast atomic variables [1]:

$$\frac{\partial A}{\partial t} = -\left(\alpha + \beta\right)A + \frac{pA}{1 + \left|A\right|^2/I_{\mathrm{p}}} + \left(a_{\mathrm{Re}} + \mathrm{i}a_{\mathrm{Im}}\right)\nabla^2 A \ , \tag{9.1a}$$

$$\frac{\partial \beta}{\partial t} = \gamma\left(\beta_0 - \beta - \beta\frac{\left|A\right|^2}{I_{\mathrm{s}}}\right) , \tag{9.1b}$$

where β represents the nonlinear saturable absorption (nonlinear losses), which relaxes at a rate γ to β_0, its maximum value, in the absence of a field; p is the gain parameter; I_{p} and I_{s} are the gain and absorption saturation intensities, respectively; α represents the linear losses; and a_{Re} and a_{Im} are the diffusion and diffraction coefficients, respectively.

A single order parameter equation for a laser with a saturable absorber can be found by neglecting the inertia of the absorber (i.e. when $\gamma \gg 1$). In this case, the adiabatic elimination of β in (9.1b) leads to [2, 3]

$$\frac{\partial A}{\partial t} = -\alpha A + \frac{pA}{1 + \left|A\right|^2/I_{\mathrm{p}}} - \frac{\beta_0 A}{1 + \left|A\right|^2/I_{\mathrm{s}}} + \left(a_{\mathrm{Re}} + \mathrm{i}a_{\mathrm{Im}}\right)\nabla^2 A \ . \tag{9.2}$$

In the derivation of (9.1) and (9.2), a cavity with plane mirrors was assumed. However, as discussed in Sect. 6.3, the validity of these equations can be extended to systems in a self-imaging resonator, just by using a diffraction coefficient $a_{\mathrm{Im}} = l/2k$, where l is the displacement of the mirrors from the

self-imaging case, instead of the total cavity length in a plane–plane mirror cavity. Then, in a quasi-self-imaging configuration (with l small), the diffraction is correspondingly small.

The diffusion term a_{Re} is introduced phenomenologically in (9.2). Its physical sense is a spatial frequency filtering. In the case of a self-imaging resonator with an aperture located in the far field, the aperture imposes a localized profile of the gain in the Fourier domain. In the most convenient case of a parabolic profile, we can write

$$\frac{\partial A(\boldsymbol{k}_\perp, t)}{\partial t} = -a_{\mathrm{Re}} k^2 A(\boldsymbol{k}_\perp, t) \ , \tag{9.3}$$

where a_{Re} is related to the size of the aperture. Converting (9.3) to the spatial domain by an inverse Fourier transform, we obtain

$$\frac{\partial A(\boldsymbol{r}, t)}{\partial t} = a_{\mathrm{Re}} \nabla^2 A(\boldsymbol{r}, t) \ , \tag{9.4}$$

which is a diffusion term, phenomenologically included in (9.1a).

Owing to this equivalence, the diffusion of the field can be controlled by varying the boundary conditions, either by using a finite pump area or by introducing an aperture into the resonator.

The model (9.2), although derived for a class A laser, is also valid, as shown in [4], for a photorefractive oscillator. This equivalence was discussed in Chap. 3.

An important restriction on the validity of (9.1) and (9.2) is that both nonlinear processes, gain and absorption saturation, must occur in the same location of the resonator along its optical axis. In some experimental situations, however, it is convenient to place the nonlinear elements in Fourier-conjugate planes, and thus at different locations. This near-field–far-field separation can be taken into account if, in (9.1a), the nonlinear gain operator $\hat{N}(p, I_{\mathrm{p}})$, defined as

$$\hat{N}(p, I_{\mathrm{p}}) = \frac{pA}{1 + |A|^2 / I_{\mathrm{p}}} \ , \tag{9.5}$$

acts not on the field but on its Fourier image. This particular configuration is then modeled by the equation

$$\frac{\partial A}{\partial t} = -\left(\alpha + \beta\right) A + \hat{F}^{-1} \hat{N} \hat{F} A + \left(a_{\mathrm{Re}} + \mathrm{i} a_{\mathrm{Im}}\right) \nabla^2 A \ , \tag{9.6}$$

together with (9.1b). Here the operators $\hat{F}$ and $\hat{F}^{-1}$ represent the direct and inverse Fourier transforms, defined by

$$\hat{F} A = \frac{1}{2\pi} \iint A(x, y, t) \exp(\mathrm{i} k_x x + \mathrm{i} k_y y) \mathrm{d}x \, \mathrm{d}y \ , \tag{9.7a}$$

$$\hat{F}^{-1} A = \frac{1}{2\pi} \iint A(k_x, k_y, t) \exp(-\mathrm{i} k_x x - \mathrm{i} k_y y) \mathrm{d}k_x \, \mathrm{d}k_y \ . \tag{9.7b}$$

The models (9.2) and (9.6), which correspond to two different experimental configurations, are the basic models used for the investigation of amplitude domains and spatial solitons in this chapter.

9.2 Amplitude Domains and Spatial Solitons

In both configurations described above, when the system starts from a random initial condition, an ensemble of solitons can be excited in the near field, a situation that dominates in the initial stage of the evolution. For the first configuration, when both nonlinearities act in the near-field domain of a self-imaging resonator, solitons behave nearly independently, and the nonlinear evolution leads to an ensemble of weakly interacting solitons.

A different scenario is observed when the gain medium is located in the far-field domain. In this case, in the nonlinear evolution, a strong competition between solitons occurs. The solitons, although well separated in the spatial domain, overlap completely in the focal plane, where the gain medium is placed. The gain saturation depends on the total energy of the radiation. As a result, several solitons well separated from one another in the spatial domain share the same population inversion. The more solitons in the ensemble, the smaller the average energy (and the peak intensity) of a soliton. Owing to the nonlinear absorption, the weaker solitons are more strongly discriminated, initiating a competition, which proceeds until a single soliton survives.

We start the analysis by obtaining the homogeneous lasing solution of (9.2). Neglecting spatial and temporal derivatives, we find that the intensity is given by

$$I_{\pm} = \frac{I_s}{2\alpha} \left(\frac{I_p}{I_s} (p - \alpha) - \beta_0 - \alpha \right)$$
$$\pm \frac{I_s}{2\alpha} \sqrt{4\alpha \frac{I_p}{I_s} (p - \beta_0 - \alpha) + \left(\frac{I_p}{I_s} (\alpha - p) + \alpha + \beta_0 \right)^2}. \tag{9.8}$$

The bifurcation from the trivial solution to (9.8) is subcritical (and the lasing solution is bistable) if

$$\frac{I_p}{I_s} > \frac{1 + \alpha}{\alpha} . \tag{9.9}$$

When (9.9) holds, bistability occurs in a pump parameter range given by

$$1 + \frac{I_s}{I_p} \left(\alpha - 1 + \sqrt{4\alpha \left(\frac{I_p}{I_s} - 1 \right)} \right) < p < \alpha + 1 , \tag{9.10}$$

which corresponds to the parameter region where bright solitons can exist.

An exact soliton solution does not exist for (9.2) or (9.6), and therefore an analytical treatment is possible only using an approximate profile of the

soliton. One reasonable choice is a Gaussian envelope with unknown time-dependent parameters,

$$A(r,t) = \sqrt{I(t)}\,e^{-c(t)r^2}\;.\tag{9.11}$$

Inserting the ansatz (9.11) into (9.6) leads to a set of equations for the complex parameters of the soliton. A handleable system of equations can be found by assuming the following conditions:

1. A fast saturable absorber $(\gamma \gg 1)$. In this case, the absorption variable can be adiabatically eliminated from (9.1b), leading to (9.2).
2. Diffusion is strong compared with diffraction, $a_{\mathrm{Re}} \gg a_{\mathrm{Im}}$. This is the case when the resonator length is tuned to correspond to a self-imaging resonator, where diffraction almost vanishes. In this limit the parameters of the soliton take real values.
3. The soliton can be approximated by a parabolic profile if we use, instead of (9.11), the ansatz $A(r,t) \approx \sqrt{I(t)}\left[1 - c(t)\,r^2\right]$. In this case, the saturating nonlinear terms can be simplified by a series expansion.

Finally, gathering terms in r, we obtain the following system:

$$\frac{dI}{dt} = -2\alpha I - \frac{2\beta_0 I}{1 + I/I_s} + \frac{2pI\left(1 + 3I/4c^2 I_p\right)}{\left(1 + I/4c^2 I_p\right)^2} - 8Ica_{\mathrm{Re}}\;,\tag{9.12a}$$

$$\frac{dc}{dt} = -\frac{2\beta_0 I/I_s}{\left(1 + I/I_s\right)^2} + \frac{pI/2cI_p}{\left(1 + I/4c^2 I_p\right)} - 4c^2 a_{\mathrm{Re}}\;.\tag{9.12b}$$

The system (9.12) is still too complicated to obtain analytically tractable steady-state solutions. However, an analysis of this system is useful for obtaining some preliminary conclusions concerning the role of the diffusion parameter, a_{Re}.

If diffusion is absent $(a_{\mathrm{Re}} = 0)$, the system (9.12) leads to singular solutions, as (9.12b) results in a continuous increase of the curvature $c(t)$ and a corresponding shrinking of the soliton. For $p > \alpha + \beta_0/(1 + I/I_s)$, the intensity $I(t)$ also grows, leading to an unphysical singularity. This can be understood by analyzing the different saturating effects involved: the absorption leads to a narrowing of the soliton, since it acts more strongly in the parts with less amplitude (far from the peak). If the saturating gain were at the same location in the resonator, it would lead to a broadening of the soliton, since in this case the pumping would be stronger in the tails and weaker at the peak. The balance of these two effects allows soliton formation in a quasi-planar laser cavity. However, in the present case the saturating gain acts in the Fourier plane, and a broadening in the Fourier domain corresponds to a narrowing of the soliton in the spatial domain. Hence, both nonlinear processes contribute to narrowing the soliton, and lead to a singularity if no other physical

phenomena balance this double narrowing effect. The balance in the present model comes from the diffusion, as (9.12b) shows.

The counterbalance between nonlinearities on the one hand, and diffusion on the other hand, can be seen in a plot of the vector field generated by (9.12), as shown in Fig. 9.1. When the diffusion is large enough to compensate the narrowing effect of the nonlinearities, a node point appears, signaling the possibility of stable solitons.
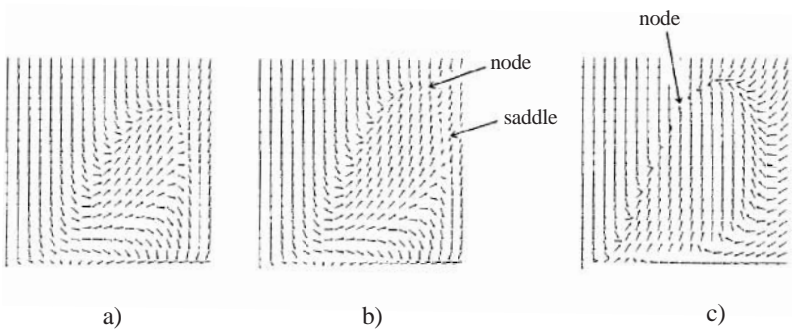

Fig. 9.1. The vector field of the evolution of the parameters of the spatial soliton (amplitude $a(t)$ in the vertical direction, and inverse width $c(t)$ in the horizontal direction) as given by the parabolic expansion (9.12). (**a**) Below the threshold, $p = 0.75$, $a_{Re} = 0.127$; (**b**) situation corresponding to bistability, $p = 0.79$, $a_{Re} = 0.13$; (**c**) in the monostable regime, $p = 1.6$, $a_{Re} = 0.29$. Other parameters are $I_p = 1$, $I_s = 1$; the amplitude $a(t)$ varies from 0 to 8.4; and the inverse width $c(t)$ from 0 to 1.4 in all three cases

9.3 Numerical Simulations

In order to check the analytical results described above, the models (9.2) and (9.6) were integrated numerically by using the split-step method with periodic boundary conditions. Two stages can be distinguished: (1) the process of soliton formation starting from noisy initial conditions, and (2) the manipulation of a single soliton once it has been formed. Experiments corresponding to these results are described in Sect. 9.4.

9.3.1 Soliton Formation

We start by considering simulations of a laser in the first configuration (with both nonlinear elements located in the near field of the resonator), described by (9.2). In this case no competition between localized structures is expected.

The emission was initiated with a large pump value ($p = 2.5$), at which the absorber was completely saturated. The field developed several optical
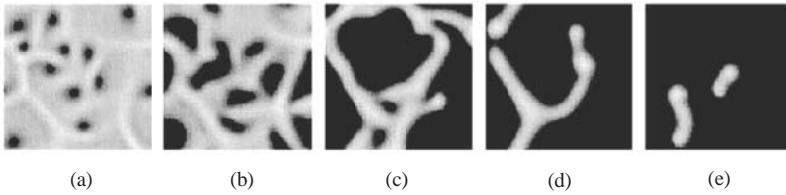
(a)   (b)   (c)   (d)   (e)

Fig. 9.2. Evolution of an initial randomly distributed field as obtained by numerical integration of (9.2). The parameters are $a_{\mathrm{Re}} = 0.5$, $a_{\mathrm{Im}} = 2$, $I_{\mathrm{p}} = 1$, $I_{\mathrm{s}} = 0.06$, $\alpha = 3$. The first plot was calculated for a relatively large value of the pump intensity ($p = 2.5$), corresponding to an almost saturated absorber. Later the pump intensity was lowered to $p = 2.15$. The time between plots is $t = 30$

vortices at arbitrary locations, separated by shocks, as Fig. 9.2a shows. Next, the pump value was decreased to $p = 2.15$, at which value the absorber was unsaturated, and field discrimination occurred. The vortices converted into dark domains, and the shocks into bright domains, the precursors of the solitons (Figs. 9.2b,c). The bright domains take the form of arbitrarily oriented stripes, which correspond to one-dimensional solitons (Fig. 9.2d,e). If the pump is left unchanged, the stripes shorten during the evolution and finally disappear, leaving the system in a homogeneous state. The excitation of two-dimensional solitons requires a slight increase of the pump in the final stage of contraction. The shortening of the stripes then stops, allowing the formation of stationary solitons.

The need for this complicated procedure, based on variations of the pump intensity, to control the patterns and obtain stable solitons, can be under-
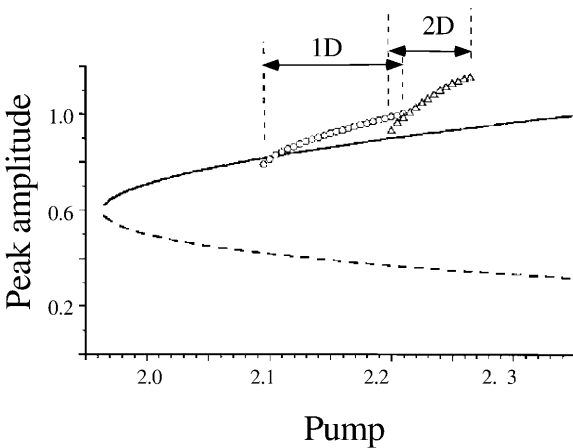

Fig. 9.3. The peak amplitude of a stable soliton versus the pump parameter in the case of one spatial dimension (*circles*) and two spatial dimensions (*triangles*), as obtained by numerical integration of (9.2). The parameters are as in Fig. 9.2

stood from an analysis of single solitons in 1D and 2D. In Fig. 9.3 the peak amplitudes of 1D and 2D solitons, evaluated numerically, are plotted together with the amplitude of the homogeneous solution given by (9.8), as a variation of the pump parameter. We clearly see that localized stripes (1D solitons) are stable for pump values smaller than those required for localized spots (2D solitons), and that their existence ranges do not coincide. The explanation lies in the fact that the solitons have larger losses (diffractive and diffusive) in two dimensions than in one, and therefore require a larger pump value to compensate such losses. It is also important to note that the existence range of the solitons corresponds only to a small portion of the full bistability range (9.10).

Let us now consider the other laser configuration (with a near-field–farfield separation), where, as discussed in the previous section, competition among solitons is expected. The numerical integration of (9.6) in this case shows the formation of a single soliton from a noisy spatial distribution (Fig. 9.4).
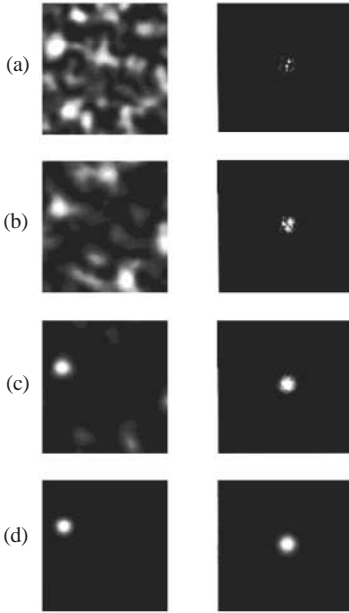

Fig. 9.4. Formation of a symmetric, stable, localized structure from an initial randomly distributed field, as obtained by numerical integration of (9.6) in the case of two spatial dimensions: the *left column* shows the spatial distributions (near field), and the *right column* the spatial spectra (far field)

The temporal series shown in Fig. 9.4 shows the near field (left) and the far field (right), where the absorber and the gain medium, respectively, are placed. Figure 9.4a shows the initial random distribution. During the linear evolution, several bright spots emerge, and a filtering in the Fourier plane is observed, which corresponds to a broadening of the spots in the spatial domain (Fig. 9.4b). In the nonlinear stage, the saturation of both the gain and the absorption contributes to a broadening of the spatial spectrum (or, equivalently, to a narrowing of the spots), forming an ensemble of round spots

or solitons (Fig. 9.4c). Finally, owing to the nonlinear absorption, only the strongest soliton survives the competition (Fig. 9.4d).

We remark that this scenario of the developement of a single soliton in the transverse plane is analogous to the temporal pulse-formation process in lasers with passive mode locking. In both cases one starts with a random field distribution (a random ensemble of pulses or solitons). A spectral filtering in the frequency spectrum or in the spatial Fourier spectrum occurs in the linear stage of the evolution. In both cases, only one pulse or soliton survives in the nonlinear stage of the evolution. Competition occurs because several pulses or solitons share a common population inversion. For a mode-locked laser the amplifying medium is relatively slow, and the amplification depends on the integral energy. In our pattern-forming laser, the spatial spectra of individual pulses overlap in the focal plane, and the amplification again depends on the integral characteristics (in space) of the radiation.

9.3.2 Soliton Manipulation: Positioning, Propagation, Trapping and Switching

One of the most promising applications of transverse spatial solitons is expected in the field of information processing and storage, where the solitons would be used as bits or basic information units [5]. To realize such practical applications, one needs to be able to manipulate solitons by external actions. In this section we show how such external actions can be incorporated into the numerical simulations, and how the solitons can be influenced in the desired way.

An important property of a spatial soliton is its position: in the absence of spatial inhomogeneities, a soliton has spatial multistability, i.e. it is stable independently of its location in the laser cross section. Consequently, it is expected that a soliton will move under the action of gradient forces, in particular those produced by phase gradients. We have tested the drift of a soliton under the influence of two different phase gradients: a linear (ramped) and a parabolic gradient.

The easiest way to physically introduce a linear phase gradient is by tilting one of the resonator mirrors. This effect can be taken into account in the model by adding phenomenologically a symmetry-breaking term to (9.1), which now reads

$$\frac{\partial A}{\partial t} = -\boldsymbol{k}_\mathrm{t}\,\boldsymbol{\nabla}A - \alpha A + T_\mathrm{NL} + (a_\mathrm{Re} + \mathrm{i}a_\mathrm{Im})\,\nabla^2 A \;, \tag{9.13}$$

where T_NL represents the same nonlinear terms as in (9.1) and $\boldsymbol{k}_\mathrm{t}$ describes the tilt of the mirror, which has the dimensions of a velocity. The first term in (9.13) results in the drift of a soliton in a direction determined by the mirror tilt, with a constant velocity proportional to $\boldsymbol{k}_\mathrm{t}$.

Similarly, a phase trough can be modeled by placing one of the intracavity lenses closer to the resonator center or, alternatively, by a spatially dependent

pump. In this case the soliton drifts towards the resonator axis, independently of its initial position and even without mirror tilting.

The most important characteristic that we require of the system, from the information-processing point of view, is the possibility of "writing" and "erasing" the solitons. This can be achieved by exploiting the characteristics of a resonator with spatially extended nonlinearities, which induces a strong competition between solitons, independent of their separation. In this case, a strong enough localized perturbation, externally injected into the system, can be used to create (or write) a new soliton at a desired location, which competes with another soliton previously existing at a different place, the latter soliton discriminated against (or erased) by the new one. This switching process is shown in Fig. 9.5.
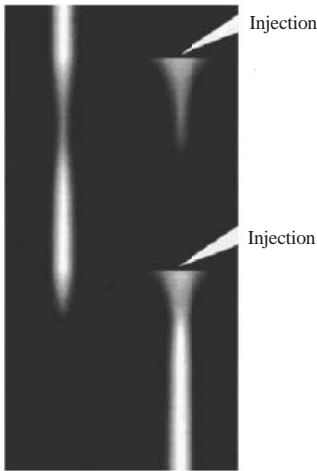

Fig. 9.5. The dynamics of switching of solitons by injection as obtained by numerical integration of (9.6) in the case of one spatial dimension. A first injection flash occurs at $t = 40$, and a second at $t = 80$. The peak amplitude of the first injection beam was 4.1, and that of the second beam was 4.4; the widths of the injection beams were the same in both cases

9.4 Experiments

All of the theoretical results presented in the previous sections have been experimentally reproduced. For the experiments, a self-imaging resonator configuration was used containing a photorefractive crystal as the amplifying medium, and a saturable absorber consisting of bacteriorhodopsin [6] or a dye cell. The amplifying medium and the absorber were placed either in the same place in the resonator (corresponding to model (9.2)) or in separate places (corresponding to model (9.6)). A schematic illustration of the experimental setup is shown in Fig. 9.6.

The saturation of the transmission of the intracavity saturable absorber was initiated by an additional (bleaching) unfocused beam controlled by a shutter.
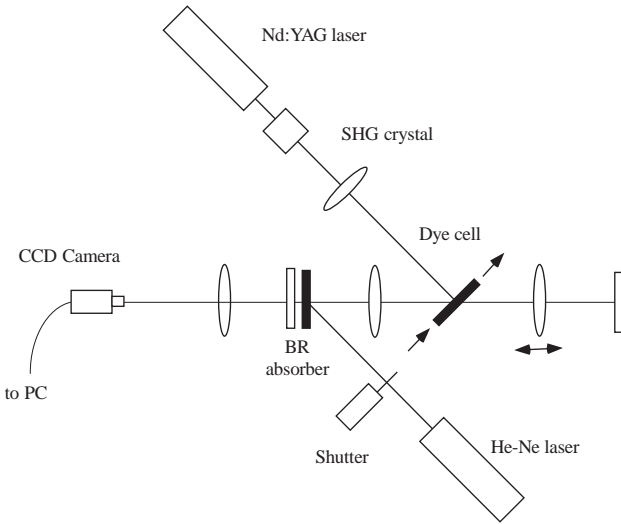
Fig. 9.6. Experimental setup used in the studies of solitons

We consider first some experiments with a PRO, located close to the absorber. Initially, the bleaching beam completely saturates the absorber, and the observed emission is a speckle structure, with optical vortices separated by shocks. When the bleaching beam is blocked, the absorber unsaturates and a domain structure develops, evolving into contracting stripes (the field density decreases with time). This experimental scenario is shown in Fig. 9.7, in good agreement with the numerical result (compare with Fig. 9.2).
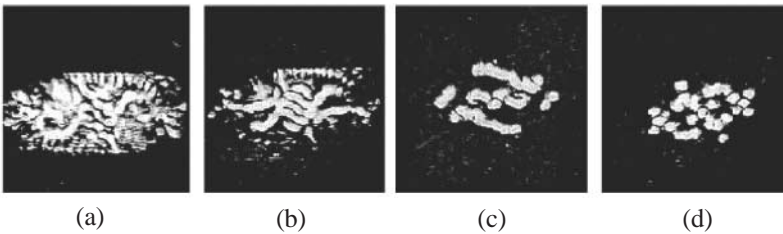

(a)   (b)   (c)   (d)

Fig. 9.7. Experimentally observed evolution of the field after the bleaching beam is switched off. The time interval between successive plots is 10 s

When the pump intensity is increased, two-dimensional solitons can be stabilized, as discussed in the previous section. Depending on the pump value and, mainly, on the moment at which it is increased, a single soliton or a cluster of solitons can be stabilized. If the pump intensity is increased
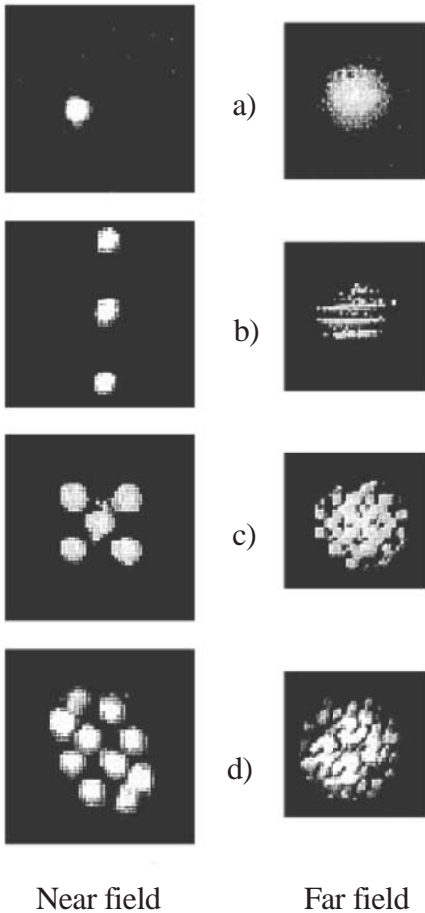
Near field   Far field

Fig. 9.8. Stationary solitons and ensembles of solitons, observed experimentally in the near and far field of the resonator

relatively late, one or a few coexisting solitons are obtained (Figs. 9.8a,b). If the change is made earlier, larger soliton ensembles appear (Figs. 9.8c,d).

The properties of single solitons were studied experimentally with a dye laser in the near-field–far-field configuration. The dependence of the average laser output on the average pump power was measured experimentally, showing the bistability or hysteresis loop predicted by the theory (Fig. 9.9).

The transverse structure of the output field was also measured, at three characteristic pump values. For pump values in the bistability region, a quasi-Gaussian spatial soliton develops, as Fig. 9.9a shows. At the border between bistability and monostability, a super-Gaussian structure appears (Fig. 9.9b), while in the monostability domain a large-size structure with a strongly structured profile is observed (Fig. 9.9c). To create the soliton, the absorber cell was locally bleached for a short time. After the bleaching was removed, the soliton remained.
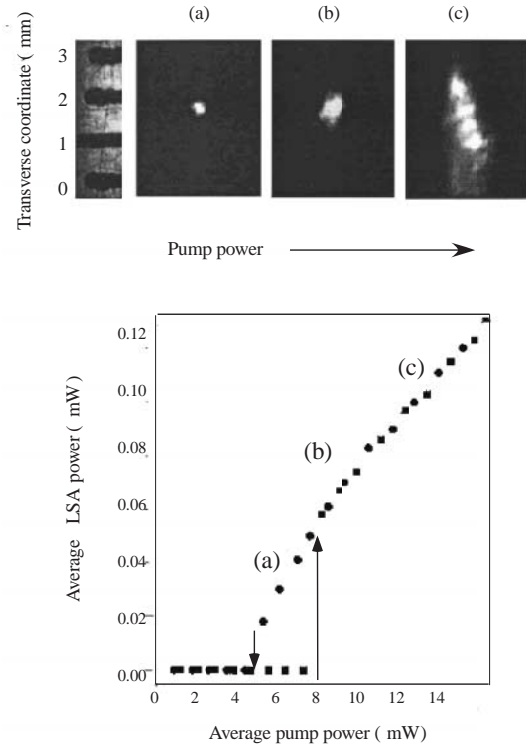
Fig. 9.9. Experimentally measured hysteresis in the dependence of the laser output on the pump power, and the transverse structure of the output laser beam for three fixed pump powers: (**a**) small, quasi-Gaussian spatial soliton in the bistable region, (**b**) intermediate-size, super-Gaussian soliton at the border between bistability and monostability, and (**c**) large-size structure with a strongly structured profile in the monostable region

The size of the soliton depends on the diffusion coefficient (note that, for small diffraction, the diffusion is nothing but a spatial scaling; see (9.4)), which, as discussed previously, is a function of the pump area. This dependence has been also observed in the experiments. As Fig. 9.10 shows, a focusing of the pump results in a broadening of the soliton.

The possibility of manipulating the solitons has been also demonstrated experimentally. Figure 9.11 shows the switching of a soliton. Once a soliton is "written" in a given place in the resonator cross section, the bleaching of the absorber at a different location results in the "erasing" of the first soliton and the creation of the new one.

Finally, the motion or drift of a soliton under the action of a phase gradient has been also tested. When one of the resonator mirrors is tilted, the soliton drifts at a constant velocity in the direction of the tilt (Fig. 9.12a). The
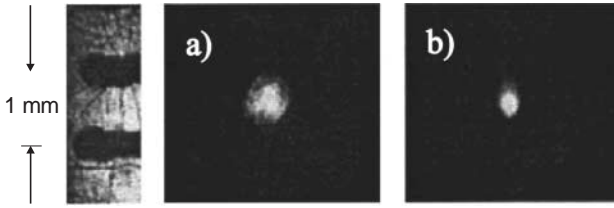
Fig. 9.10. Experimental observation of the spatial soliton structure in a laser: (**a**) for small pump area in the dye cell, and (**b**) for large pump area, illustrating the dependence of soliton size on diffusion
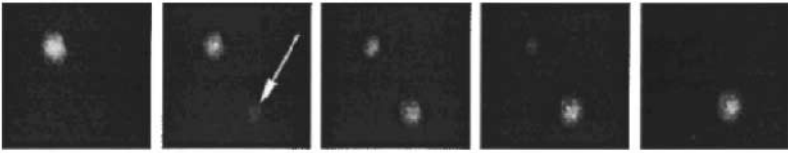

Fig. 9.11. Switching of a soliton initiated by an external bleaching beam in a new position across the laser aperture. The *arrow* in the second picture indicates the place of incidence of the initiating beam. The time interval between neighboring pictures is 2.5 s
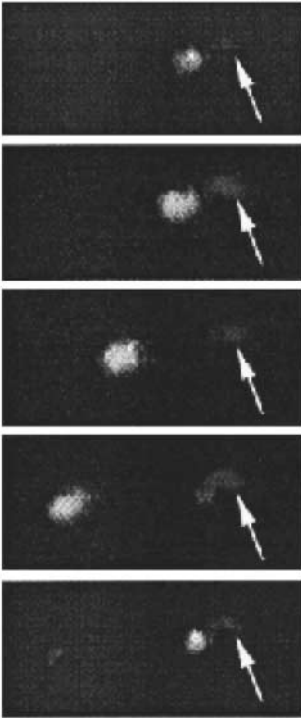

Fig. 9.12. The periodic soliton. Unidirectional drift motion and switching off occurs for a tilted resonator mirror when the bacteriorhodopsin absorber cell is subjected to permanent local bleaching by a laser beam

snapshots here were taken at equally spaced times, and demonstrate the constant transverse velocity of the soliton under the linear gradient.

On the other hand, changing the length of the resonator away from the precise self-imaging length creates a phase trough with a minimum at the resonator center. The soliton then moves towards the center of the phase trough, and becomes trapped at the cavity axis.

References

1. V.B. Taranenko, K. Staliunas and C.O. Weiss, Spatial soliton laser: localized structures in a laser with a saturable absorber in self-imaging resonator, Phys. Rev. A **56**, 1582 (1997). 125
2. H.R. Brand and R.J. Deissler, Stable localized solutions in nonlinear optics with large dissipation, Physica A **204**, 87 (1994); N.N. Rosanov, *Transverse Patterns in Wide-Aperture Nonlinear Optical Systems*, Progress in Optics, vol 35, ed. by E. Wolf (North-Holland, Amsterdam, 1996). 125
3. G. Slekys, K. Staliunas and C.O. Weiss, Spatial solitons in optical photorefractive oscillators with saturable absorber, Opt. Commun. **149**, 113 (1998). 125
4. K. Staliunas, M.F.H. Tarroja, G. Slekys, C.O. Weiss and L. Dambly, Analogy between photorefractive oscillators and class-A lasers, Phys. Rev. A **51**, 4140 (1995). 126
5. W.J. Firth and A. Scroggie, Optical bullet holes: robust controllable localized states of a nonlinear cavity, Phys. Rev. Lett. **76**, 1623 (1996). 132
6. N. Hampp, C. Brauchle and D. Oesterhelt, Biophys. J. **58**, 83 (1990). 133

10 Subcritical Solitons II:
Nonlinear Resonance

In this chapter we study the formation of bright solitons in an optical system where amplitude bistability occurs because of a nonlinear resonance mechanism. One system showing this property is a degenerate optical parametric oscillator with a detuned pump [1, 2]. The model equations for this system in the mean-field limit were presented in Chap. 3. The existence of a nonlinear resonance in a DOPO was also shown in Chap. 3, by the derivation of an order parameter equation in the limit of large pump detuning (3.24). This equation is the real version of (8.5), and therefore the general ideas presented in the previous chapter are applicable in the case of a DOPO. In particular, bright solitons can also be expected in DOPOs.

Throughout this chapter we analyse the degenerate case of an OPO only. However, since the order parameter equation for a nondegenerate OPO shows a nonlinear resonance too, the main conclusions of this chapter (about solitons) are easily extendable to the nondegenerate case [3].

10.1 Analysis of the Homogeneous State.
Nonlinear Resonance

As stated earlier, the mean-field model of a DOPO can be reduced to an order parameter equation in the form of a modified Swift–Hohenberg equation (3.24), which we rewrite here for convenience:

$$\frac{\partial A}{\partial t} = pA - A^3 - \frac{1}{2}\left(\omega_1 - \nabla^2 - \omega_0 A^2\right)^2 A \ . \tag{10.1}$$

This equation describes the evolution of the order parameter A, which proportional to the signal field, close to the oscillation threshold; $p = E - 1$ is the amount by which the pump intensity is above the threshold, and ω_0 and ω_1 are the pump and signal detunings, respectively.[1] For nonzero ω_0, (10.1) possesses a nonlinear resonance, since the frequency-selection operator (the

---

[1] Remember that the pump and signal fields appearing in the order parameter equation (10.1) are scaled with respect to their original values as defined in the mean-field model of the DOPO (3.1); the changes are given by (3.3).

last term) is intensity-dependent. Corresponding plots of the spatial nonlinear resonance effect were given in Figs. 8.5 and 8.6.

In order to find the necessary conditions for the existence of solitons in a DOPO, we proceed as in the laser case considered in the previous chapter. First, we analyze the properties of the homogeneous nontrivial solution, which for (10.1) is given by

$$A_\pm^2 = \frac{1}{\omega_0^2}\left(-1 + \omega_0\omega_1 \pm \sqrt{1 - 2\omega_0\omega_1 + 2p\omega_0^2}\right). \tag{10.2}$$

Depending on the values of the detunings, the solution (10.2) can appear via a supercritical bifurcation (when $\omega_0\omega_1 < 1$) or via a subcritical one (when $\omega_0\omega_1 > 1$). In the latter case, the system shows bistability between (10.2) and the trivial solution $A = 0$ for pump values in the range

$$\frac{\omega_0\omega_1 - 1/2}{\omega_0^2} \leq p \leq \frac{\omega_1^2}{2} , \tag{10.3}$$

as follows from (10.2).

The lower branch of (10.2) (the solution with the minus sign) is unstable, as usual. The stability of the upper branch against space-dependent perturbations can be analyzed by substituting $A = A_+ + \delta A\exp(\lambda t + i\mathbf{k}\cdot\mathbf{r})$ in (10.2), and linearizing in the perturbations δA. The growth rate of a perturbation is governed by the real part of the eigenvalue λ, given by

$$\lambda(k) = p - \frac{1}{2}\left(k^2 - \omega_1\right)^2 - \frac{A_+^2}{2}\left[6 - 2\omega_0\left(2k^2 + 3\omega_1\right) + 5\omega_0^2 A_+^2\right], \tag{10.4}$$

where $k^2 = k_x^2 + k_y^2$. Note that the following analysis is valid for either one or two transverse dimensions, owing to the rotational symmetry of the problem.

From (10.4) it follows that a perturbation can grow (λ can be positive), and develop into a pattern only when $\omega_1 > 0$, which, together with the bistability condition $\omega_0\omega_1 > 1$, requires that the pump detuning must be positive.

The growth rate (10.4) is maximal at a wavenumber $k_{\max}$, which, as found by setting $\partial\lambda/\partial k = 0$ in (10.4), is

$$k_{\max}^2 = \omega_1 + 2\omega_0 A_+^2 , \tag{10.5}$$

or, using (10.2),

$$k_{\max}^2 = \omega_1 + 2\left(-1 + \sqrt{1 - 2\omega_0\omega_1 + 2p\omega_0^2}\right)\frac{1}{\omega_0} . \tag{10.6}$$

This corresponds to the characteristic spatial-modulation wavenumber of the pattern. It is clear from (10.5) that, for $\omega_0 \neq 0$, the modulation wavenumber depends on the intensity of the solution, indicating the nonlinear resonance mentioned above.

If the pump power is increased, the real part of the eigenvalue decreases, vanishing at a threshold value $p = p_{\mathrm{mod}}$, where

$$p_{\mathrm{mod}} = \frac{\omega_1^2}{2} \left(24 - 8\omega_0\omega_1 + \omega_0^2\omega_1^2 \right). \tag{10.7}$$

For $p > p_{\mathrm{mod}}$, the homogeneous solution is stable. Since p_{mod} is always larger than the pump value given by the upper limit of (10.3) for an arbitrary detuning value, the trivial and modulated solutions coexist in the whole bistability domain. We therefore expect soliton formation in this parameter region.

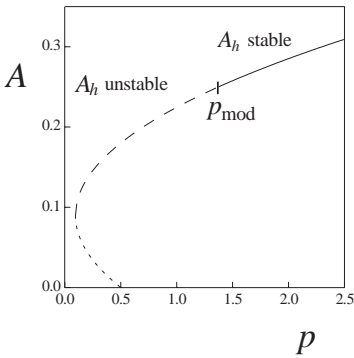The bifurcation diagram of the homogeneous solution is depicted in Fig. 10.1.

Fig. 10.1. Bifurcation diagram of homogeneous solution, for $\omega_0 = 10$, $\omega_1 = 1$. The trivial solution is stable for $p < 0.5$

10.2 Spatial Solitons

From the viewpoint of soliton formation, an important difference between the DOPO and the laser studied in the previous chapter is that the solitons in a DOPO are closely related to a modulational instability, which is absent in the case of a laser with a saturable absorber. To show this and to test the above predictions derived from the order parameter equation (10.1), the mean-field model for a DOPO (3.1) has been numerically integrated. We present the results for one and two transverse dimensions.

10.2.1 One-Dimensional Case

In 1D (representing, for example, a resonator with cylindrical mirrors or a system with a slab waveguide configuration), a roll (or stripe) pattern develops for pump values below p_{mod}, sustained by the homogeneous solution. In Fig. 10.2, several periodic solutions obtained for different pump values are
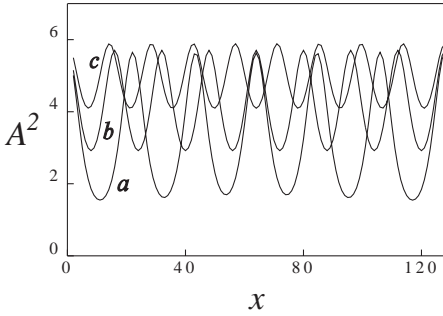
Fig. 10.2. Stable rolls on a finite background for different pump values: (**a**) $E = 1.4$, (**b**) $E = 1.6$, (**c**) $E = 2$. The other parameters are $\omega_0 = 10$, $\omega_1 = 1$, $a_1 = 0.001$, $a_0 = a_1/2$. Note the dependence of the wavenumber on the pump value

shown. Note that not only the wavenumber depends on the pump value (see (10.5)), but also the amplitude of the modulation.

The modulation depth of the stationary pattern, defined as

$$C = \frac{I_{\max} - I_{\min}}{I_{\max} + I_{\min}} \, , \tag{10.8}$$

increases with decreasing pump value. At the pump value $p = p_{\lim}$, the modulation equals unity ($I_{\min} = 0$); here the point of zero intensity of the envelope of the roll pattern connects with the trivial solution. Below this pump value, the rolls are no longer stable, and owing to the attracting character of the trivial solution, a dynamical regime appears, shown in Fig. 10.3.
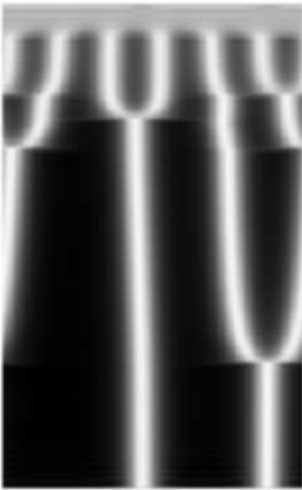

Fig. 10.3. Modulational instability of the homogeneous solution, and soliton formation via annihilation of neighboring solitons. Time runs from *top* ($t = 0$) to *bottom* ($t = 75$). The pump value is $E = 1.2$, and the other parameters are as in Fig. 10.2

The initial homogeneous solution is modulationally unstable, and thus in an initial stage a roll pattern emerges, with a wavenumber given by k_{max}, and with a modulation increasing with time (top part of the figure). Since the pump value is below p_{lim}, the roll breaks into independent units, and each of the local maxima of the pattern behaves independently from the others; the maxima interact and merge with their nearest neighbors, and develop into an ensemble of weakly interacting solitons. After a long transient, only one soliton survives.

This scenario of spontaneous soliton formation is not possible in the absence of modulational instability. In the latter case, only localized perturbations strong enough to connecting the two homogeneous branches can lead to soliton formation.

For pump values $p_{lim} < p < p_{mod}$, the solitons are stable, but require a hard localized excitation, as in the case of a laser, as described in the previous chapter.

The spatial profile of the solitons is given in Fig. 10.4. Apart from the single soliton usually found (Fig. 10.4a), higher-order solitons can also be stable (although they are less probable). A double-peaked soliton is shown (Fig. 10.4b); this exist in a narrower pump domain. The peak-to-peak distance is close to the width of an individual soliton, and the double-peaked soliton resembles a portion of a periodic pattern.
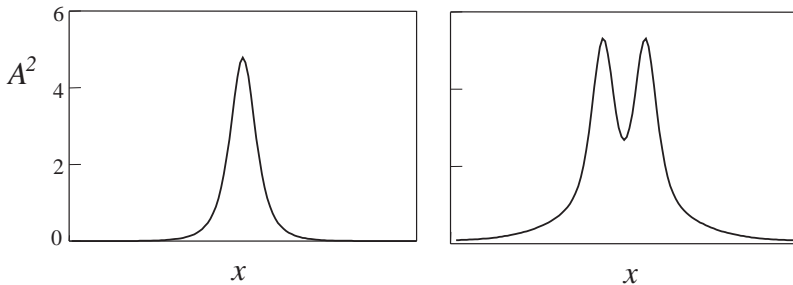

Fig. 10.4. Soliton profiles: (**a**) single, for $E = 1.2$, and (**b**) double, for $E = 1.35$. The other parameters are as in Fig. 10.2

A roll pattern can be interpreted as a periodic array of equally spaced solitons, an idea supported by the numerical results described above (Figs. 10.3 and 10.4). This relation between extended and localized patterns allows estimation of the width of a soliton on the basis of results of a linear stability analysis. To perform this estimation, we consider the asymptotic relations

$$A \approx A_+ \left[1 + \cos\left(kx\right)\right] \approx A_+ \left[1 + \left(1 - \frac{k^2 x^2}{2}\right)\right]$$

$$= 2A_+ \left(1 - \frac{k^2 x^2}{4}\right) \approx 2A_+ \mathrm{sech}\left(\frac{x}{\sqrt{2}/k}\right), \tag{10.9}$$

from which the width of the soliton is found to be

$$x_0 = \frac{\sqrt{2}}{k}, \tag{10.10}$$

where $k = k_{\max}$, given by (10.6).

These results are consistent with an alternative analysis [4, 5], where a parametrically driven Ginzburg–Landau equation was derived as an order parameter equation for the DOPO, under different assumptions from those used in the derivation of (10.1). As shown in [5], this equation supports an exact hyperbolic-secant solution, in agreement with the asymptotic solution (10.9).

In Fig. 10.5, the width of the soliton as evaluated numerically (dots) is compared with the analytical value given by (10.10) (full line). Note that the correspondence is better for pump values close to the threshold, in accordance with the assumption made in the derivation of the model (10.1). The dashed lines represent limiting values of the width, those widths corresponding to the largest and smallest wavenumbers that may experience growth (neutrally stable eigenvalues).

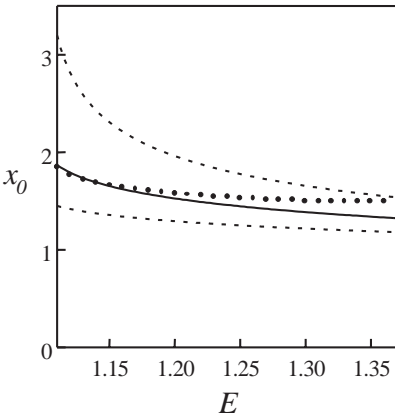**Fig. 10.5.** Width of the soliton as a function of the pump amplitude. Numerical values (*dots*) are compared with analytical values (*line*) derived from the linear stability analysis. Other parameters as in Fig. 10.2

10.2.2 Two-Dimensional Case

The above treatment of 1D solitons can be extended to the 2D case. In 2D, the pattern that coexists with solitons has hexagonal symmetry. Analogously

to the 1D case, below a certain value of the pump, the pattern breaks up into an ensemble of weakly interacting solitons, resembling a "soliton gas". Neighboring solitons merge, leaving a single soliton after a long transient.

The most straightforward extension of the 1D soliton is a solitary spot. Another extension would be a solitary stripe. However, this kind of soliton is always unstable in 2D, and breaks up into an array of spots which eventually evolve into a single soliton. A scenario of a modulational instability of a localized stripe is shown in Fig. 10.6, where only the initial evolution is shown.

Fig. 10.6. Instability of a localized stripe in two dimensions, and formation of solitons in the form of spots, evaluated at $E = 1.3$. Other parameters as in Fig. 10.2

The extension of the double soliton to 2D is a localized ring (Fig. 10.7a), and corresponds to Fig. 10.4b in a rotationally symmetric case. If the pump is increased, the ring-shaped soliton can experience a modulational instability in the azimuthal direction, forming an ensemble of single solitons located around the ring (Fig. 10.7b).

More generally, curved solitary lines (of arbitrary shape) in 2D are affected by modulational instabilities along the direction of the soliton axis, and the straight or circular shapes we have studied are just particular cases.

In conclusion, we have shown that bright spatial solitons can be stable solutions of a model of the degenerate optical parametric oscillator when the pump wave is positively detuned with respect to the closest frequency of the resonator. This result can be explained by noticing the existence of
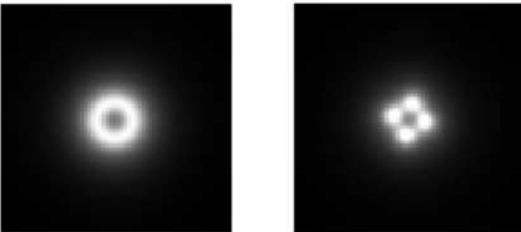

Fig. 10.7. Higher-order 2D solitons: (**a**) annular soliton for $\omega_0 = 5$; (**b**) modulated annular soliton for $\omega_0 = 10$. Other parameters are $E = 1.32$ and $\omega_1 = 1$

a nonlinear resonance effect, as revealed by the order parameter description of the DOPO derived in this limit. This mechanism is not exclusive to this system, but should be present in other resonators that contain nonlinear focusing media, thus producing an intensity-dependent detuning.

References

1. G.J. de Valcárcel, K. Staliunas, E. Roldán and V.J. Sánchez-Morcillo, Transverse patterns in degenerate optical parametric oscillation and degenerate four-wave mixing, Phys. Rev. A **54**, 1609 (1996). 139
2. K. Staliunas and V.J. Sánchez-Morcillo, Localized structures in degenerate optical parametric oscillators, Opt. Commun. **139**, 306 (1997). 139
3. V.J. Sánchez-Morcillo, G.J. de Valcárcel, E. Roldán and K. Staliunas, Generalized complex Swift–Hohenberg equation for optical parametric oscillators, Phys. Rev. A **56**, 3237 (1997). 139
4. K. Staliunas, Transverse pattern formation in optical parametric oscillators, J. Mod. Opt. **42**, 1261 (1995). 144
5. S. Longhi, Localized structures in degenerate optical parametric oscillation, Phys. Scr. **56**, 611 (1997). 144

11 Phase Domains and Phase Solitons

11.1 Patterns in Systems with a Real-Valued Order Parameter

The radiation emitted by lasers and other laser-like nonlinear optical systems, such as nondegenerate optical parametric oscillators and photorefractive oscillators, has a free phase: above the generation threshold the field intensity is fixed, but the phase can take an arbitrary value. The generation threshold in laser-like systems is usually characterized by a supercritical Hopf bifurcation (Fig. 8.1a). As a consequence, the corresponding order parameter equation is the complex Ginzburg–Landau or the complex Swift–Hohenberg equation (or a generalization of one of those equations) as discussed in Chaps. 2 and 3. In Chaps. 8–10 we have seen that for some kinds of systems (e.g. in the presence of an intracavity saturable absorber or with an intracavity focusing/defocusing material), the bifurcation from the nonlasing to the lasing state can also be subcritical (Fig. 8.1b). Owing to this subcriticality, or equivalently owing to the amplitude bistability, switching waves between bistable states, amplitude domains, and spatial solitons in the form of amplitude domains of minimum size are possible.

This chapter deals with a different class of systems in nonlinear optics, those characterized by a real-valued order parameter. Such systems display not a subcritical or supercritical Hopf bifurcation, but a pitchfork one at the generation threshold (Fig. 8.1c). Typical examples of systems with a real-valued order parameter are degenerate optical parametric oscillator and a degenerate four-wave mixer (DFWM). The radiation in such systems prefers two values for the phase, differing by π and associated with the two branches of the pitchfork bifurcation. Consequently, patterns associated with a real-valued order parameter such as stripes, hexagons and phase domains are favored, while laser-like patterns such as tilted waves, optical vortices and vortex lattices, of the kind studied in Chaps. 4–6, are suppressed in such systems with phase selection properties.

We now analyze patterns analogous to the amplitude domains discussed in Chap. 8, namely phase domains, and their limiting case, phase solitons [1, 2].

11.2 Phase Domains

As an example of a system displaying a pitchfork bifurcation we consider again the DOPO, whose mean-field model, introduced in Chap. 3, reads

$$\frac{\partial A_0}{\partial t} = \gamma_0 \left[-\left(1 + i\omega_0\right) A_0 + \bar{E} - A_1^2 + i a_0 \nabla^2 A_0 \right], \tag{11.1a}$$

$$\frac{\partial A_1}{\partial t} = \gamma_1 \left[-\left(1 + i\omega_1\right) A_1 + A_0 A_1^* + i a_1 \nabla^2 A_1 \right]. \tag{11.1b}$$

The spatially homogeneous stationary solution of (11.1) can be found by elimination of the pump field A_0 from (11.1), and by using the ansatz $A_1 = A \exp(i\varphi)$ for the subharmonic field. We obtain

$$A^2 = -1 + \omega_0\omega_1 + \sqrt{E^2 - (\omega_0 + \omega_1)^2}\,, \tag{11.2a}$$

$$\sin\left(2\varphi\right) = -\frac{\omega_0 + \omega_1}{E}\,, \tag{11.2b}$$

with an additional constraint on the phase, $\cos(2\varphi) > 0$ [3]. The stationary intensity of the pump corresponding to (11.2) is $|A_0|^2 = 1 + \omega_1^2$. This solution is exact for the mean field-model, and coincides with (10.2) when the appropriate limits are taken.

The expressions (11.2) represent two physically equivalent solutions with the same amplitude but different phases, $\varphi_1 = -\arcsin\left[(\omega_0 + \omega_1)/2E\right]$ and $\varphi_2 = \varphi_1 + \pi$. In the case of zero (or sufficiently small) detuning, the numerical solution of (11.1) leads asymptotically to one of the two homogeneous distributions given by (11.2) as the final state. However, in a transient stage of the evolution, when the system starts from a random field distribution, the field shows separate domains, characterized by one of the two values of the phase inside each domain.

In Fig. 11.1, the amplitude and phase distributions of the subharmonic (signal) radiation in a DOPO are shown during a transient. The field vanishes along the lines separating the two phases, which are called domain boundaries (and also dark switching waves). The stability of domain boundaries in DOPOs was first investigated in [4]. The domains here are essentially dynamic, and can move, reconnect or disappear during the nonlinear evolution. This chapter is devoted to the nonlinear dynamics of these domains.

For the sake of simplicity, and also for the sake of generality of the results, in the following the domain dynamics are studied not by solving the mean-field DOPO model (11.1), but by solving the corresponding order parameter equation. As shown in Sect. 3.3, the dynamics of a DOPO are described, close to the threshold, by the real Swift–Hohenberg equation, which can be written as

$$\frac{\partial A}{\partial t} = A - A^3 - \left(\Delta + \nabla^2\right)^2 A\,, \tag{11.3}$$
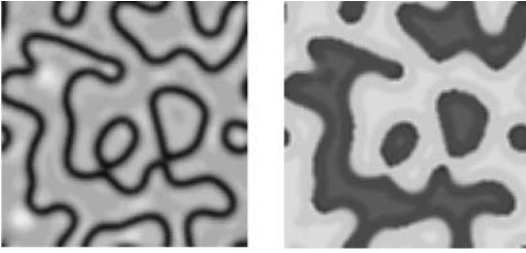
Fig. 11.1. Phase domains in a DOPO for small signal detuning. The intensity (*left*) and phase (*right*) distributions are shown. The calculations started from a random distribution of the optical field (with a broadband spatial spectrum). A transient stage of the evolution is shown. The parameters used were $E = 2$, $\omega_0 = 0$, $\omega_1 = -0.3$, $\gamma_1 = \gamma_0 = 1$, $a_1 = 0.0005$ and $a_0 = a_1/2$. The integration was performed using periodic boundary conditions in a region of unit size

Notice that this equation is valid for zero or moderate pump detuning. Otherwise, nonlinear resonance effects must be taken into account.

Owing to the universal character of the Swift–Hohenberg equation as a basic pattern-forming model, the results derived from (11.3) are applicable not only to DOPOs, but also to other nonlinear optical systems such as DFWMs [5] and to physical systems of different natures, such as systems showing Rayleigh–Bénard convection in hydrodynamics [6].

The order parameter $A(\boldsymbol{r}, t)$ is proportional to the complex amplitude of the subharmonic field, $A_1(\boldsymbol{r}, t)$. The normalization of the time $\tau = (E - 1)\gamma_1 t$ scales out the pump value E in (11.3). The coefficient of the Laplace operator is equal to unity, owing to the normalization of the spatial coordinates. The parameter Δ is proportional to the subharmonic detuning ω_1 in (11.1): $\Delta = -\omega_1/\sqrt{2(E-1)}$. Note that the detuning parameter in (11.3) is sign-reversed with respect to the detuning in the DOPO model (11.1). Extended patterns, such as rolls and hexagons, now occur for positive Δ in (11.3), whereas equivalent patterns occur for negative detunings in the DOPO equations.

The solutions of (11.3) are analogous to the patterns generated by the DOPO equations discussed above. For a relatively large positive detuning, the RSH equation has a spatially modulated solution in the form of stripes with amplitude $A(\boldsymbol{r}) = \sqrt{4/3}\cos(\boldsymbol{k} \cdot \boldsymbol{r})$, where the resonant wavenumber $|\boldsymbol{k}| = \sqrt{\Delta}$ is dependent on the detuning. For a negative or relatively small positive detuning Δ, the RSH equation has two physically equivalent homogeneous solutions with equal amplitude $A = \sqrt{1 - \Delta^2}$, but with different phases $\varphi = (0, \pi)$, the analogue of the domains in the DOPO (Fig. 11.1). In the following sections the evolution of domains or, equivalently, the motion of the domain boundaries is studied.

11.3 Dynamics of Domain Boundaries

Before investigating the dynamics of phase domains in 2D, let us analyze
the case of stationary, straight boundaries, which is actually the 1D case.
Straight boundaries between sufficiently large domains are stationary, since
two phases (two stationary solutions) corresponding to neighboring domains
are always in equilibrium here.[1] Domain boundaries can move either because
of curvature effects (as investigated in Sect. 11.4), or because of their mutual
interaction (Sect. 11.5).

   No analytic expression exists for a straight domain boundary in the case
of the RSH equation. However, such boundaries can be found analytically in
the case of the real Ginzburg–Landau (RGL) equation,

$$\frac{\partial A}{\partial t} = A - A^3 + \nabla^2 A . \tag{11.4}$$

Equation (11.4) has a kink-form solution in 1D, corresponding to a straight
domain boundary in 2D,

$$A(x) = \pm \tanh\left(\frac{x}{\sqrt{2}}\right), \tag{11.5}$$

which represents a solution directed along the y axis.

   The RSH equation in the limit of large negative detuning actually trans-
forms into the RGL equation (11.4). Therefore, let us assume that the domain
boundary solution of the RSH equation possess a form similar to the kink
solution of the RGL equation. This suggest the use of the following ansatz:

$$A(x) = \sqrt{1 - \Delta^2} \tanh\left(\frac{x}{x_0}\right), \tag{11.6}$$

where $\sqrt{1 - \Delta^2}$ is the modulus of the homogeneous solution of the RSH
equation and x_0 is the (unknown) half-width of the domain boundary.

11.3.1 Variational Approach

The RSH equation is a variational equation, and thus it can be also written
in the gradient form $\partial A/\partial t = -\delta F/\delta A$, with a potential $F(A)$ given by [7]

$$F = \int_{-\infty}^{\infty} \left(-\frac{A^2}{2} + \frac{A^4}{4} + \frac{\left[(\nabla^2 + \Delta) A\right]^2}{2} \right) dx \, dy . \tag{11.7}$$

---

[1] This is not always true in DOPOs, since in a certain parameter range the Ising–
Bloch transition can be present, leading to a drift of the walls at constant velocity.
However, this transition requires a complex order parameter, and thus cannot
be obtained from the Swift-Hohenberg equation.

We use a variational approach in order to (i) determine the half-width x_0 of the straight domain boundary that minimizes the potential (11.7) in 1D, and (ii) to analyze the motion of curved domain boundaries in 2D.

After the ansatz (11.6) is substituted into (11.7), the integration results in an infinite value for the potential. This is due to the contribution of the homogeneous background A_0. Therefore we need to calibrate the potential (11.7) by subtracting this constant contribution [8], which in the 1D case yields

$$F = \int_{-\infty}^{\infty} \left(-\frac{A^2 - A_0^2}{2} + \frac{A^4 - A_0^4}{4} + \frac{\left[(\partial^2/\partial x^2 + \Delta) A \right]^2}{2} - \frac{\Delta^2 A_0^2}{2} \right) \mathrm{d}x \ . \tag{11.8}$$

Integration of (11.8) with the ansatz (11.6) now gives a finite value for the potential,

$$F = \frac{1 - \Delta^2}{15 x_0^3} \left[5 x_0^4 \left(1 - \Delta^2 \right) + 8 - 20 \Delta x_0^2 \right], \tag{11.9}$$

which depends on the unknown parameter x_0 and on the detuning Δ. The value of the half-width can be found by minimizing the potential (11.9), and is given by

$$x_0^2 = \frac{2}{\sqrt{5}} \frac{\sqrt{6 - \Delta^2} - \sqrt{5}\Delta}{1 - \Delta^2} \ . \tag{11.10}$$

Substituting (11.10) into (11.9), we find the corresponding potential,

$$F_{1D} = \frac{8}{3\sqrt{2\sqrt{5}}} \frac{\left(1 - \Delta^2 \right)^{(3/2)} \left(2 + 3\Delta^2 - \sqrt{6 - \Delta^2}\sqrt{5}\Delta \right)}{\left(\sqrt{6 - \Delta^2} - \sqrt{5}\Delta \right)^{(3/2)}} \ . \tag{11.11}$$

The dependences (11.10) and (11.11) are plotted in Fig. 11.2. As expected, the dark line broadens monotonically with decreasing detuning. The calibrated potential (11.8) is positive over almost the whole detuning range. This is plausible, since the dark line is a defect in a homogeneous pattern, and thus increases the potential energy of the system. However, for large values of the detuning the potential becomes negative, which has profound consequences for the dynamics of domains in 2D. Indeed, if for a small detuning the presence of a kink in 1D increases the variational potential, then in 2D a domain wall should tend to be as short as possible, and the domains should contract. On the other hand, if for a large detuning the presence of a kink in 1D decreases the variational potential, then in 2D a domain wall should, correspondingly, tend to be as long as possible, and thus the domains should expand. This dynamic behavior of 2D domains is investigated in the next section.
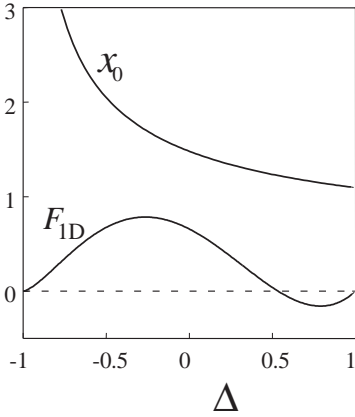
Fig. 11.2. The half-width x_0 of the dark line given by (11.10), and the calibrated 1D functional (11.11), as a function of the detuning Δ

11.3.2 Two-Dimensional Domains

To study analytically the motion of a domain boundary in 2D, we assume a ring-shaped form. This represents, equivalently, a circular domain centered at the origin of a polar coordinate system. Such a dark ring can be described by the ansatz

$$A(r) = \sqrt{1 - \Delta^2} \tanh\left(\frac{r - r_0}{x_0}\right) \tanh\left(\frac{r + r_0}{x_0}\right), \qquad (11.12)$$

where r_0 is the radius of the ring, and the half-width x_0 is given by (11.10). Owing to the cylindrical symmetry of the ansatz (11.12), the variational potential can be written as

$$F = 2\pi \int_0^\infty \left(-\frac{A^2}{2} + \frac{A^4}{4} + \frac{1}{2}\left[\left(\frac{\partial^2}{\partial r^2} + \frac{1}{r}\frac{\partial}{\partial r} + \Delta \right) A \right]^2 \right) r \, dr, \quad (11.13)$$

which has to be calibrated in the same way as in the 1D case, to avoid the background contribution.

Analytical integration of (11.13) using the ansatz (11.12) is not possible in the 2D case; however, two other complementary approaches can be used. One possibility is to evaluate approximately the integral in some limiting cases. The other possibility is to calculate the integral (11.13) numerically.

When the radius of the ring is large enough (when $r_0/x_0 \gg 1$), the order parameter $A(r)$ is nearly an odd function with respect to the ring radius r_0. Making the change of variables $x = r - r_0$, assuming the integrated function $f(x)$ to be even, and extending the integration limits to the whole space, we obtain

$$F_{2D} = 2\pi \int_{-\infty}^\infty f(x)(x + r_0) \, dx = 2\pi r_0 \int_{-\infty}^\infty f(x) \, dx = 2\pi r_0 F_{1D}. \qquad (11.14)$$

This result is not exact, because the integration limits in reality do not extend to infinity, and also because the integrated function is not even, but has a small odd part. The errors occurring because of these two assumptions give corrections to (11.14) of orders $\mathcal{O}(\exp{(-r_0/x_0)})$ and $\mathcal{O}(1/r_0)$, respectively. Therefore, for an asymptotically large radius of the ring r_0, and for a width of the dark line $x_0 = \mathcal{O}(1)$, we obtain the potential

$$F_{2D} = 2\pi r_0 F_{1D} + \mathcal{O}\left[\exp\left(-\frac{r_0}{x_0}\right)\right] + \mathcal{O}\left(\frac{1}{r_0}\right) . \tag{11.15}$$

Thus the potential in 2D is roughly equal to the potential in 1D (11.11) multiplied by the length of the weakly curved (circular) dark line. In this approximation, the sign of F_{1D} determines the evolution of the ring. As can be seen from Fig. 11.2, around zero detuning F_{1D} is positive, and thus the longer the domain boundary is, the larger the 2D potential is. As the solution tends to minimize the potential, the domains contract. For a detuning larger than some Δ_c, the 1D potential is negative, and the domains expand. The particular case of stationary rings occurs at $\Delta_c = \sqrt{2/7} \approx 0.535$.

The result of numerical integration of the RSH equation (11.4) shows contraction or expansion of the domains, depending on the detuning. In Fig. 11.3, an example of domain contraction for a small value of the detuning is given.

Figure 11.4, in contrast, shows domain expansion for a large detuning value. The asymptotic pattern in this case is a labyrinth structure. The numerical results indicate that rings of large radius are marginally stable at a detuning $\Delta_c = 0.45 \pm 0.05$, which differs from the analytically evaluated
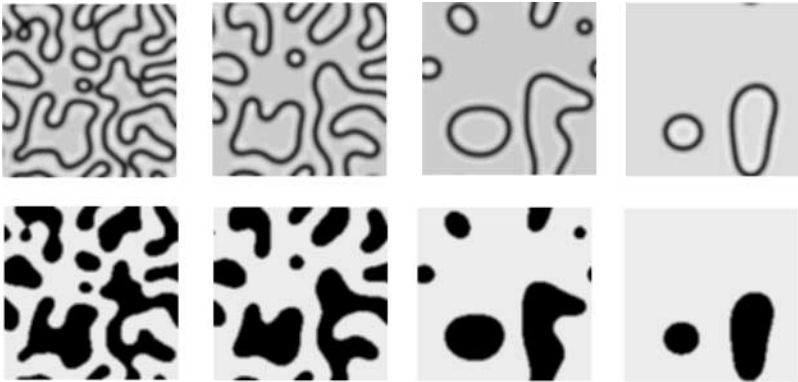

Fig. 11.3. Evolution of phase domains obtained using the RSH equation for a small signal detuning, $\Delta = 0.25$. The integration was performed in a box of size 70 units (the integration grid contained 128×128 points), with periodic boundaries. Time increases from *left* to *right*. In the *upper row* the field intensity is plotted, and the *lower row* shows the field phase. The pictures were obtained at times $t = 0$ (the initial distribution), $t = 20$, $t = 100$ and $t = 250$. The last domains disappear at $t = 370$
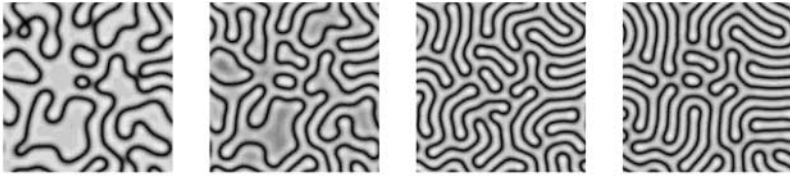
Fig. 11.4. Evolution of phase domains obtained using the RSH equation for a large signal detuning, $\Delta = 0.65$. Other parameters as in Fig. 11.3. The initial picture at time $t = 0$ was prepared by integrating the RSH equation with a detuning $\Delta = 0.25$ (as in the previous figure), and further calculations were then performed with the new detuning value. The other plots were obtained at times $t = 20$, $t = 150$ and $t = 1000$

equilibrium detuning value given above. This difference occurs because of the inexact form of the ansatz. The domain boundaries are not exactly of hyperbolic-tangent form (with monotonically decaying tails), but show an oscillatory decay of the tails. A more accurate analysis that takes account of these spatial oscillations and leads to a better correspondence with the numerical values is performed in Sect. 11.5.

In this way, by varying the detuning Δ, one can manipulate the domain dynamics, forcing the domains to expand or to shrink. Expanding domains keep their topological properties during the evolution for moderate values of the detuning: the number of domains in a finite labyrinth pattern is equal to that in the initial pattern, as can be seen in Fig. 11.4.

The situation is different for larger values of the detuning, in particular when $\Delta > \sqrt{2/3}$. In this case, as follows from the linear stability analysis, the homogeneous solution is modulationally unstable. Domain growth and labyrinth formation are now accompanied by the appearance of new domains (nucleation), as shown in Fig. 11.5. Another peculiarity of the large-detuning case is that the dark lines in the labyrinths can break and reconnect, which also leads to topological changes of the domains.
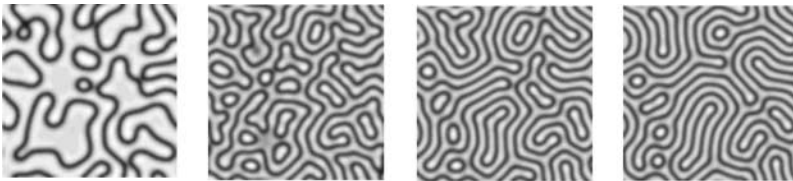

Fig. 11.5. Evolution of phase domains obtained using the RSH equation a for large signal detuning, $\Delta = 0.85$. Other parameters as in Fig. 11.3. The plots were obtained at times $t = 0$, 20, 150 and 1000

An expression for the velocity of the moving fronts in a potential system can also be derived. In the case of a cylindrically symmetric ring, the radial velocity $v = dr_0(t)/dt$ is [7]

$$v = -\frac{\partial F/\partial r_0}{2\pi \int (\partial A/\partial r)^2 r \, dr} \; , \tag{11.16}$$

and is proportional to the force acting on the ring (the gradient of the variational potential) and inversely proportional to the "mass", or inertia, of the ring. In the limit of large ring radius, the velocity can be evaluated analytically. In this case, using (11.14) for the potential, and evaluating the integral in the denominator in (11.16) in the same way as above, we obtain

$$v = -\frac{2}{r_0}\frac{2 + 3\Delta^2 - \sqrt{6 - \Delta^2}\sqrt{5}\Delta}{\sqrt{5}\sqrt{6 - \Delta^2} - 5\Delta} \; , \tag{11.17}$$

that is, the velocity is inversely proportional to the ring radius.

The behavior of a circular domain boundary can be generalized to domains of arbitrary form. Assuming that the curvature of the dark line is sufficiently small, the equation for the local motion of the curve is $\partial \boldsymbol{R}/\partial t = -v\boldsymbol{c}$, where the local motion of the dark line is directed along its normal and is proportional to the local curvature $\boldsymbol{c} = \partial^2 \boldsymbol{R}/\partial l^2$, with the proportionality coefficient given by (11.17).

11.4 Phase Solitons

The above analysis predicts either the contraction or the expansion of domains. This conclusion is valid, however, only for a sufficiently large radius of a domain or, equivalently, for a sufficiently small curvature of a dark line. In other words, when diametrically opposite segments of the domain boundary do not interact. For small domains, when the diameter is of the same order of magnitude as the width of the domain boundary, the situation may be different. Indeed, numerical integration of the RSH equation sometimes shows that the dark rings stop contracting at some small radius. Figure 11.6 shows such a scenario, where an ensemble of stable dark rings of fixed radius evolves. We call these stationary small domains phase solitons, by analogy with the amplitude solitons studied in Chap. 9. A comparison of the profiles of the two types of solitons was shown in Figs. 8.1 and 8.7.

The variational approach of the previous section cannot predict analytically the existence of solitons, since the assumption $r_0/x_0 \gg 1$ is no longer valid. Numerical integration of (11.3), however, shows that phase solitons exist for detuning values in the range $0.287 \pm 0.001 < \Delta < 0.460 \pm 0.001$.

The interaction of opposite segments of the ring results in a repulsive force that balances the attraction between the fronts due to the tendency to contraction, allowing soliton formation.
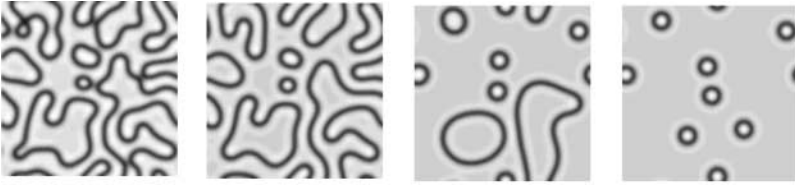
Fig. 11.6. Evolution of phase domains obtained using the RSH equation for an intermediate signal detuning, $\Delta = 0.35$. Other parameters as in Fig. 11.3. The plots were obtained at times $t = 0, 20, 150$ and 1000

To demonstrate the repulsive effect of the interaction, the potential (11.13) has been integrated numerically using the ansatz (11.12). Three characteristic plots are given in Fig. 11.7, showing the dependence of the potential on the radius of the ring for different values of the detuning Δ, together with the analytical approximation (11.14) (dashed lines).

As predicted from the 1D analytical calculations, for small detuning, the potential increases with the radius, leading to a contraction of the ring. Correspondingle, for large detuning, the potential decreases with increasing radius, leading to an expansion However, for some intermediate values of the detuning, the potential exhibits a minimum at some radius of the ring (the middle curve in Fig. 11.7; see also the inset). This potential minimum indicates the existence of phase solitons, with a radius corresponding to the potential minimum. The final distribution in the series shown in Fig. 11.6 is an ensemble of such solitons. These solitons are similar to those found in systems showing optical bistability, whose order parameter equation is also of Swift–Hohenberg type [9].

Although a variational analysis using the ansatz (11.12) yields a potential minimum at some radius of the dark ring, thereby predicting its stability, the evaluated stability range $0.39 \pm 0.01 < \Delta < 0.52 \pm 0.01$ does not coincide with the numerically calculated stability range $0.287 \pm 0.001 < \Delta < 0.460 \pm 0.001$.
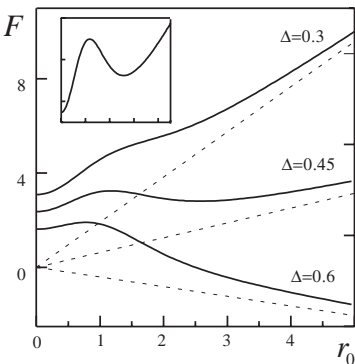

Fig. 11.7. The potential obtained by evaluating (11.13) numerically with the ansatz (11.12), for a small detuning $\Delta = 0.3$, for a large detuning $\Delta = 0.6$ and for an intermediate value of detuning $\Delta = 0.45$. The 1D potentials calculated analytically (11.11) are shown by *dashed lines*. The case of $\Delta = 0.45$ is magnified in the *inset*

The discrepancy between the numerically calculated soliton existence range and that obtained from the "monotonic" ansatz (11.12) suggests that some other mechanism is responsible for the stability of solitons. We consider next the nonmonotonic (oscillatory) spatial decay of the domain boundaries as a possible stabilizing mechanism.

11.5 Nonmonotonically Decaying Fronts

As can be seen from Fig. 11.8, numerical integration of the RSH equation in 1D indeed shows small amplitude oscillations in the decay of the fronts. The larger the detuning is, the larger is the spatial modulation of the tails of the domain boundaries.
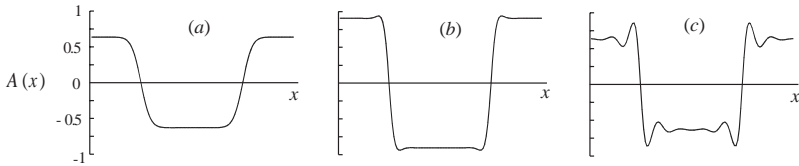

Fig. 11.8. The order parameter A corresponding to a phase domain, as calculated from (11.3) in the 1D case, for different values of detuning. (**a**) $\Delta = -0.75$: domain boundaries are monotonic functions. (**b**) $\Delta = 0$: small spatial oscillations close to domain boundaries are visible. (**c**) $\Delta = 0.75$: strong spatial oscillations are visible. The detuning value in the last case c) is close to the modulational-instability threshold at $\Delta = \sqrt{2}/3$

Since the monotonic ansatz (11.6) in the form of a hyperbolic tangent does not describe these spatial oscillations correctly, an "oscillatory" ansatz must be used instead [10]. We use the ansatz

$$A(x) = \text{sign}(x)\sqrt{1 - \Delta^2} f(x) , \tag{11.18}$$

where the profile function f, given by

$$f(x) = 1 - e^{-\sigma|x|} \cos(kx) , \tag{11.19}$$

is characterized by a spatial decay rate σ and a spatial frequency k. In general, the ansatz (11.18) means that the domain boundaries decay with a complex-valued decay parameter $\Lambda = \sigma + ik$. The real part of Λ indicates the spatial decay of a perturbation, while the imaginary part indicates the spatial frequency of oscillation. These two unknown parameters can be found by minimizing the corresponding potential. Integration of (11.8) with the ansatz (11.18) gives a value for the potential which depends on the detuning Δ and
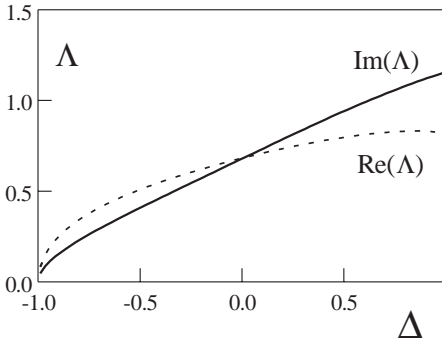
Fig. 11.9. The real and imaginary parts of the spatial decay rate $\Lambda = \sigma + ik$ of a domain boundary, as a function of the detuning Δ

on the soliton parameters σ and k. The potential has a minimum corresponding to the correct values of σ and k. These values are given in Fig. 11.9 as a function of the detuning.

From Fig. 11.9, it follows that oscillatory behavior is more prominent for positive detuning, since $\sigma < k$. For negative detuning, $\sigma > k$, and the oscillations are relatively strongly damped, in accordance with Fig. 11.8. The dependence of the potential on the detuning is qualitatively the same as in Fig. 11.2, obtained with the monotonic ansatz. The difference is only quantitative: the potential changes its sign from positive (domain contraction) to negative (domain expansion) at a detuning value $\Delta_c \approx 0.4616$. Comparing this value with the numerically obtained value $\Delta_c = 0.45 \pm 0.05$, we see that the results obtained from the nonmonotonic ansatz agree well with the numerically obtained results.

The nonmonotonic ansatz can be extended to 2D to analyze the stability of ring-shaped domain boundaries in 2D. In this case we take

$$A(r) = \text{sign}\,(r - r_0)\,\sqrt{1 - \Delta^2} f(r - r_0) f(r + r_0)\;, \tag{11.20}$$

where f is given by (11.19), r_0 is the radius of the ring as in (11.12), and the decay parameters σ and k are taken from the results of the 1D variational study. The oscillatory ansatz and the numerically calculated soliton profile are compared in Fig. 11.10.

A calculation of the potential (11.8) using the ansatz (11.20) yields again a minimum at some ring radius, indicating the existence of solitons. This minimum exists in the detuning range $0.27 < \Delta < 0.46$, which corresponds well to that obtained numerically, $0.287 \pm 0.001 < \Delta < 0.460 \pm 0.001$. Again we note that the existence range calculated in the previous section by using the monotonic ansatz was very different from the existence range calculated numerically. Therefore one may conclude that a nonmonotonic decay of domain boundaries is essential for a correct description of solitons. The assumption of nonmonotonic decay allows one to calculate precisely the critical detuning value for contraction or expansion of domains, and also the existence range of localized solutions.
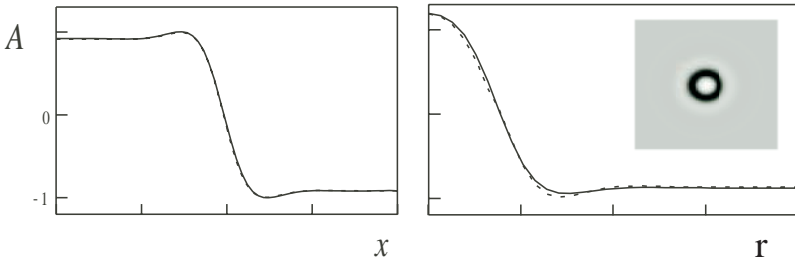
Fig. 11.10. *Left*: profile of a dark line (kink) in 1D (*solid line*) and its approximation by the oscillatory ansatz (11.18) (*dashed line*), for $\Delta = 0.3$. *Right*: profile of a spatial soliton in 2D and its approximation by the ansatz (11.20), for $\Delta = 0.4$

Next we explore how, in general, the soliton stability range depends on the modulation of the tails. For this purpose, we assume that the dynamics of domain boundaries are described by the RSH equation, but that the modulation of the domain boundaries is enhanced (or reduced) by some additional (let us say, nonvariational) effects [10]. This occurs, for example, in degenerate optical parametric oscillators (see Chap. 12). For this purpose, we keep the value of the k obtained from the variational analysis of the RSH equation (in which case $k(\Delta)$ is a function only of the detuning), but allow arbitrary values of the decay parameter σ. The approach is somewhat artificial, but it allows one to understand qualitatively the role of the oscillatory fronts in the stabilization of solitons.

The resulting diagram is plotted in Fig. 11.11, which shows the soliton stability range in the plane $(\Delta, 1/\sigma)$. The existence range grows with increasing oscillation of the decaying domain boundary (decreasing σ). The dashed curve corresponds to the decay rate calculated from the variational analysis of the RSH equation. The region above the dashed line corresponds to enhanced
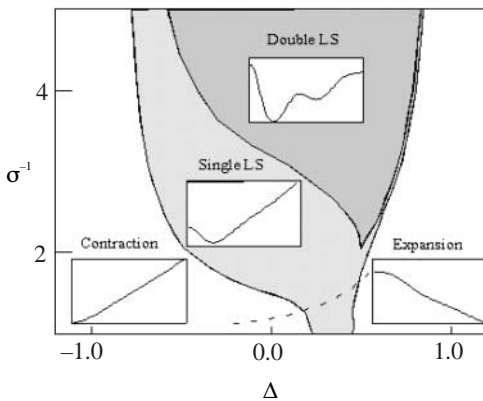

Fig. 11.11. The soliton existence range in the plane $(\Delta, 1/\sigma)$, for a single- and a double-radius ring soliton. The potentials corresponding to different cases are shown in the *insets*

spatial oscillations relative to the predictions of the RSH equation, and the region below the dashed line corresponds to reduced spatial oscillations.

For sufficiently strong spatial oscillations, the soliton stability range may extend even the negative values of detuning. This is in good correspondence with results derived in the case of a DOPO, where a significant increase of the existence range is predicted (Chap. 12). Also, besides the fundamental soliton (a ring of minimum radius), higher-order solitons appear, characterized by a set of discrete values of the ring radius $r = nr_0$, where $n = 1, 3, 5, ...$ and r_0 is the radius of the fundamental soliton. The potential corresponding to a double-size ring soliton is shown in the inset. These higher-order solitons have been found numerically in a DOPO in [11] (see also Sect. 11.7).

The distributions in Fig. 11.12 show ensembles of solitons calculated from a model of a DOPO [2]. Besides the single-ring soliton, double-ring solitons are also possible here. Also, locked states of two single-ring solitons and even more complicated "molecules" were obtained.
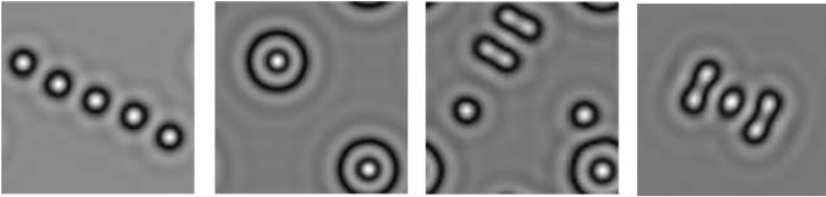

Fig. 11.12. Ensembles of phase solitons in a DOPO. The parameters are $E = 2$, $\omega_0 = 0$, $\gamma_1 = \gamma_0 = 1$, $a_1 = 0.0005$ and $a_0 = 0.00025$. The integration was performed with periodic boundary conditions in a unit-size region. The signal detunings ω_1, from *left* to *right,* are -0.3, -0.5, -0.6 and -0.6

11.6 Experimental Realization of Phase Domains and Solitons

Although theoretical investigations of phase domains and solitons were initiated by studying the concrete example of a DOPO system, the first experiments on domains were performed with a degenerate four-wave mixer [12]. The equivalence of these two systems near the threshold was demonstrated theoretically in [5], on the basis of the common order parameter equation for both systems. Experimentally, the slow dynamics of the field in a DFWM based on a slow photorefractive material ($BaTiO_3$) are very convenient for the observation of transients. The characteristic timescale of the system is about 1 s, which allows recording with ordinary video equipment.

The experimental scheme is shown in Fig. 11.13. Two counterpropagating pump beams (from a single-frequency Ar^+ laser at 514.5 nm) illuminate
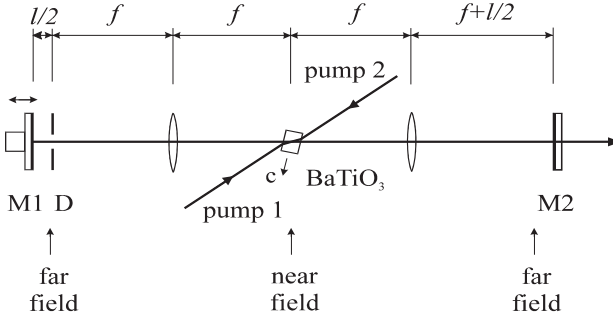
Fig. 11.13. Schematic illustration of near-self-imaging resonator used for experiments to study phase domains and solitons. M, mirrors; f, focal length of lenses; l, deviation from self-imaging length; D, diaphragm, which filters the high transverse modes. The photorefractive crystal was pumped by two counterpropagating beams. This scheme is similar to that discussed in Chap. 9, but the pumping by two counterpropagating beams used here results in degenerate four-wave mixing

a photorefractive $BaTiO_3$ crystal mounted inside a near-self-imaging linear resonator. In the limit of precise self-imaging, such a resonator has an infinite Fresnel number (within the limits of the paraxial approximation). All the transverse modes are exactly degenerate, allowing resonance for arbitrary images with complicated structure. Changing the resonator length with respect to the self-imaging length by l makes the resonator equivalent to a plane-mirror resonator of length l. In the experiment l was 30 mm, which corresponds to a characteristic spatial scale $x_0 = 100\,\mu\mathrm{m}$ ($\Delta x_0 \approx \sqrt{\lambda l}$). Variation of the resonator length on the scale of an optical wavelength allowed us to vary the detuning parameter.

Typically, domains separated by black lines of irregular shape were observed in the emission. The domain boundaries can have quite complicated forms, including self-crossings, and in general they move. Figure 11.14 shows the intensity of a portion of the emitted radiation (left), and an interferogram made with a plane wave (right), showing a phase difference of π between do-
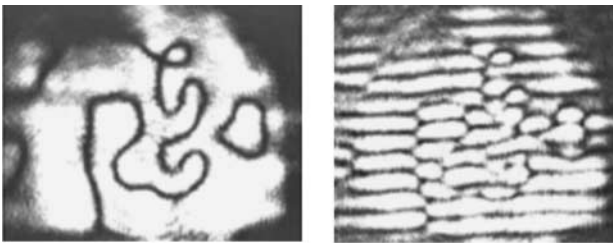

Fig. 11.14. Snapshots of the field intensity (*left*) and interferogram (*right*). A phase shift of π between neighboring domains is visible in the interference picture
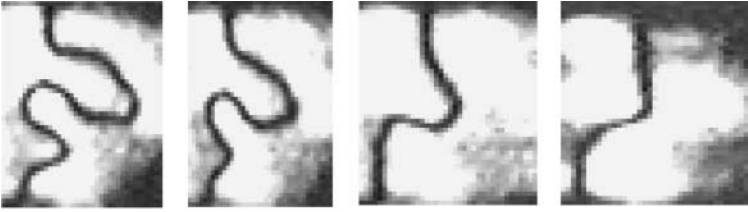
Fig. 11.15. A contracting domain boundary for small resonator detuning. The domain boundary straightens, and the domains contract and disappear for such values of the detuning
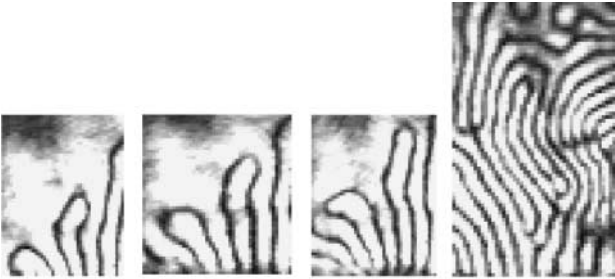
Fig. 11.16. Expanding domains for large resonator detuning. The domains grow and a final labyrinth structure sets in

mains, thus proving the real-valued nature of the order parameter of the emitted field.

The dynamics of the domains depend strongly on the detuning, as follows from the theoretical treatment discussed above. For near-zero detuning a domain coarsening occurs. Experimental recordings in this regime are given in Fig. 11.15, showing the shrinking of a domain boundary (compare with Fig. 11.3). The domain boundaries finally disappear, and a homogeneous field results as the final state.

For moderately large detuning, the topology-preserving expansion of domain boundaries, as recorded experimentally, is shown in Fig. 11.16 (compare with Fig. 11.4). The domains expand until the whole space is filled, and a "labyrinth" pattern is reached as the final state.

The formation of solitons was also observed when the detuning was increased (Fig. 11.17). In the left plot a transient state is shown, in which some domains shrink and some domains have already shrunk to the minimum radius. In the plot at the right, a stationary state containing two solitons is shown.

In order to prove the stability of the solitons, the evolution of the length of a domain boundary was studied. In these experiments, a long domain boundary and one soliton were simultaneously present. As Fig. 11.18 shows, the long domain shrinks, whereas the soliton remains unchanged. The lengths
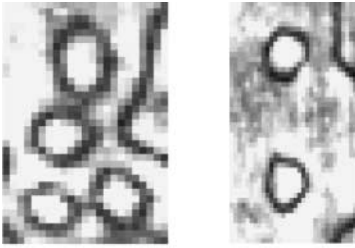
Fig. 11.17. Spatial localized structures. *Left*: the transient stage is shown, where one domain (the upper one) is contracting, and three other domains have already contracted to minimum radius. *Right*: two stationary solitons are visible
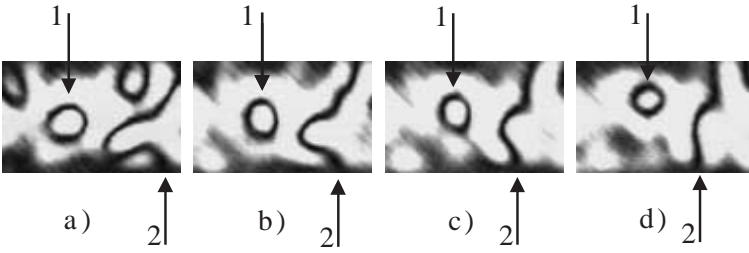
Fig. 11.18. A contracting domain boundary (2), and a stable soliton (1). Time increases from (**a**) to (**d**)
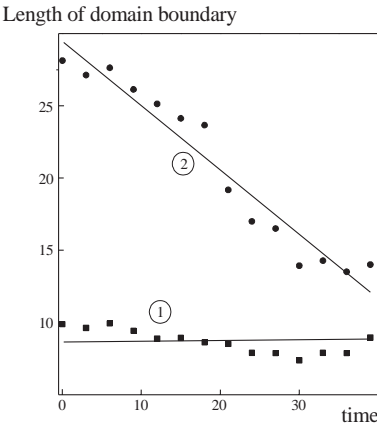
Fig. 11.19. Length of the domain boundaries of (1) and (2) from Fig. 11.18 as a function of time. The *lines* are to guide the eye

of the domain boundaries are plotted as a function of time in Fig. 11.19. This evidences that the solitons are not marginally stable small domains, but really are stable formations (with a finite stability range).

11.7 Domain Boundaries and Image Processing

Phase domains and spatial solitons in the form of dark rings could be a useful tool for parallel analog information processing [13], which could be applied to all-optical artificial vision, optical neural networking or optical sensing. Here
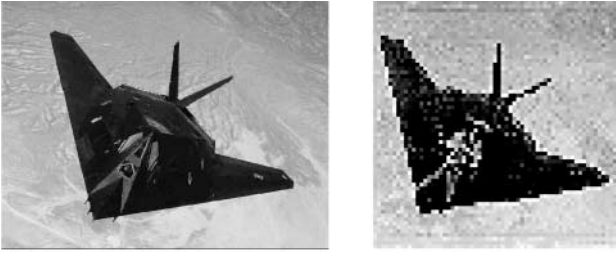
Fig. 11.20. A photo of an airplane (*left*) and a reduced-resolution version (on a grid of (128×128 points). The reduced-resolution version was processed (see Fig. 11.21)

we give just an example that shows the potential of this technique to locate and track stationary and moving objects. In Fig. 11.20, an original photo of an airplane (left) and its reduced-resolution version on a grid of 128×128 points (right) are shown. The DOPO equations (11.1) were solved using the distribution in Fig. 11.20 as the initial condition for the subharmonics. In practice, this could be achieved by a short injection of a field with a distribution of subharmonic frequency corresponding to the image to be processed.

The temporal evolution of the spatial distribution of subharmonics is shown in Fig. 11.21, as obtained from the numerical integration of (11.1). The contour of the object (the airplane) is automatically reproduced by dark curves (the domain boundaries). In the nonlinear evolution (which in a experiment using a DOPO could take just few picoseconds), the dark curves contract into a phase soliton positioned at the center of the object (targeting).
The detailed scenario is as follows:

1. $t = 1$. There is essentially an image of the injected field distribution. The amplitude of the subharmonics at the beginning of the processing is 0.1% of the saturation value of the subharmonic amplitude (the corresponding value in terms of intensities).
2. $t = 3$. Linear stage of amplification: a smoothing of the field due to spatial filtering is observed. The form of the spatial filter is a ring or a central spot in the far field, depending on the detuning.
3. $t = 10$. Nonlinear saturation is reached: the amplitude distribution in the domains becomes more and more regular (more "flat"). The nonlinear evolution of domains begins.
4. $t = 30$. The domain begins contracting.
5. $t = 90$. The domain boundary becomes smoother, and contraction continues.
6. $t = 130$. At a particular size of the domain, the contraction slows down. This particular radius is roughly $3r_0$, where r_0 is the radius of the final soliton. The evolution, however, does not stop at this size of the domain, but the domain continues contracting.
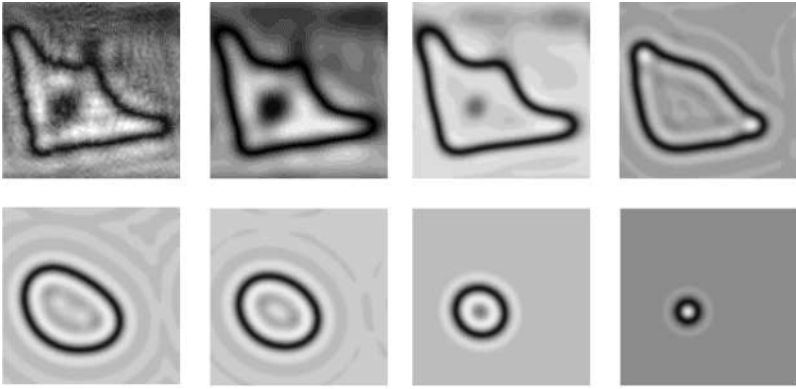
Fig. 11.21. Domain evolution as obtained by numerical integration of DOPO equations (11.1). Spatial intensity distributions are shown. The initial distribution of subharmonics is taken (injected) from Fig. 11.21. Parameters are: $E = 2$, $\omega_0 = 0$, $\omega_1 = -0.2$, $\gamma_1 = \gamma_0 = 1$. Diffraction coefficients are: $a_1 = 0.001$ and $a_0 = 0.0005$. Integration was performed with periodic boundary conditions in unit size region

7. $t = 190$. The contraction again slows down, this time at a radius $2r_0$.
8. Finally, at $t = 250$, the domain contracts to the final state, a stable soliton, at the geometrical center of the object.

An interesting point is that the evolution of the domain does not exactly follows the velocities (11.16) and (11.17), but slows down at some stages of evolution. This slowing down can be explained by the modulation of the slope of the variational potential shown in Fig. 11.11. At some radii of the domain, roughly equal to integer multiples of the radius of the fundamental soliton ($r = nr_0$, where $n = 1, 2, 3 \ldots$), the slope of the potential is minimum (it is maximum at radii $r = (n + 1/2) r_0$). The force causing contraction (the derivative of the potential) is minimum at radii that are integer multiples of r_0, and here the contraction velocity is also minimum. The modulation of the slope of the potential is due to the spatial modulation of the tails of the domain boundaries, as discussed above in Sect. 11.5.

For sufficiently strong modulation of the tails, the potential can have multiple local minima, at radii $r = nr_0$. In this case a domain can stop contracting at those radii. Figure 11.22 shows some snapshots of the evolution of domains with larger spatial modulation of the tails of the domain boundaries (e.g. because of larger pump diffraction, as will be discussed in the next chapter).

This simple example shows the unique possibilities of phase domains in analog image processing. Domain boundaries may simulate the margins of an object. Discrete solitons can count the objects of interest in the field of vision. A (stroboscopic) array of solitons can be left behind to track a moving object and the trajectory of the moving object can be recorded by discrete positions
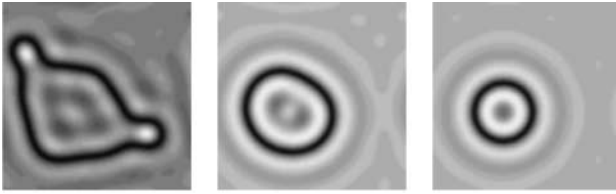
Fig. 11.22. Some snapshots from domain evolution as obtained by numerical integration of the DOPO equations. The parameters and initial conditions are as in Fig. 11.21 except for the pump diffraction coefficient, $a_0 = 0.0015$ (three times as large as in the previous case). The larger diffraction of the pump enhances spatial modulation (see Chap. 12), and consequently enables not only a stable fundamental soliton (of minimum radius), but also stable solitons with twice (or even three or more times) the minimum radius

of solitons. In general, solitons can discretize the properties of objects. And, finally, moving (inertial) solitons may be employed to forecast the trajectory of an object or the evolution of an image in general by all-optical means.

References

1. K. Staliunas and V.J. Sánchez-Morcillo, Dynamics of domains in Swift–Hohenberg equation, Phys. Lett. A **241**, 28 (1998).   147
2. K. Staliunas and V.J. Sánchez-Morcillo, Spatial localized structures in degenerate optical parametric oscillators, Phys. Rev. A **57**, 1454 (1998).   147, 160
3. L.A. Lugiato, C. Oldano, C. Fabre, E. Giacobino and R. Horowicz, Bistability, self-pulsing and chaos in optical parametric oscillators, Nuovo Cimento **10D**, 959 (1988).   148
4. S. Trillo, M. Haelterman and A. Sheppard, Stable topological spatial solitons in optical parametric oscillators, Opt. Lett. **22**, 970 (1997).   148
5. G.J. de Valcárcel, K. Staliunas, E. Roldán and V.J. Sánchez-Morcillo, Transverse patterns in degenerate optical parametric oscillation and degenerate four-wave mixing, Phys. Rev. A **54**, 1609 (1996).   149, 160
6. J.B. Swift and P.C. Hohenberg, Hydrodynamic fluctuations at the convective instability, Phys. Rev. A **15**, 319 (1977).   149
7. M.C. Cross and P.C. Hohenberg, Pattern formation outside of equilibrium, Rev. Mod. Phys. **65**, 851 (1993).   150, 155
8. Y.S. Kivshar and X. Yang, Perturbation-induced dynamics of dark solitons, Phys. Rev. E **49**, 1657 (1994).   151
9. P. Mandel, M. Georgiou and T. Erneux, Transverse effects in coherently driven nonlinear cavities, Phys. Rev. A **47**, 4277 (1993); M. Tlidi, P. Mandel and R. Lefever, Localized structures and localized patterns in optical bistability, Phys. Rev. Lett. **73**, 640 (1994).   156
10. V.J. Sanchez-Morcillo and K. Staliunas, Stability of localized structures in Swift–Hohenberg equation, Phys. Rev. E **60**, 6153 (1999).   157, 159

11. G.L. Oppo, A.J. Scroggie and W.J. Firth, From domain walls to localized structures in degenerate optical parametric oscillators, J. Opt. B: Quantum Semiclass. Opt. **1**, 133 (1999).   160

12. V.B. Taranenko, K. Staliunas and C.O. Weiss, Pattern formation and localized structures in degenerate optical parametric mixing, Phys. Rev. Lett. **81**, 2236 (1998).   160

13. W.J. Firth and A.J. Scroggie, Optical bullet holes: robust controllable localized states of a nonlinear cavity, Phys. Rev. Lett. **76**, 1623 (1996).   163

12 Turing Patterns in Nonlinear Optics

12.1 The Turing Mechanism in Nonlinear Optics

A well-known transverse-pattern formation mechanism in broad-aperture lasers and other nonlinear resonators is off-resonance excitation. If the central frequency of the gain line of the laser ω_A is larger than the resonator resonance frequency ω_R, then the excess of frequency $\Delta\omega = \omega_A - \omega_R$ causes a transverse (spatial) modulation of the laser fields, with a characteristic transverse wavenumber $\boldsymbol{k}$ obeying a dispersion relation $ak^2 = \Delta\omega$, where a is the diffraction coefficient of the resonator. The patterns that occur in such a way play the role of a "bridge" between the excitation and the dissipation, which occur at different frequencies, and these patterns enable maximum energy transfer through the system.

In all the previous chapters, patterns due to off-resonance excitation have been studied. These were patterns in lasers, photorefractive oscillators, degenerate and nondegenerate optical parametric oscillators, and four-wave mixers. For a degenerate OPO, the excitation frequency is equal to half of the pump radiation frequency $\omega_A = \omega_0/2$, and its mismatch from ω_R leads to the same macroscopic pattern formation mechanism as in lasers. The off-resonance mechanism not only excites extended patterns (such as tilted waves, rolls, square vortex lattices and hexagons), but is also responsible for the stability of localized structures in the above systems.

The off-resonance pattern formation mechanism is essentially a geometrical one. It resembles the formation of rolls in Rayleigh–Bénard convection, where the width of the convection rolls is fixed mainly by the distance between the upper and lower plates. In optical resonators, the propagation angles of off-axis components are fixed by the resonance conditions. The spatial scale is thus fixed not by nonlinearity, but by linear geometric effects.

The pattern formation mechanism discovered by Turing for reaction–diffusion systems [1] has a different origin from the mechanism discussed above. Here, at the root, is an interplay between the diffusions of two (or more) interacting components. The coupling between a strongly diffusing (lateral) inhibitor and a weakly diffusing (local) activator is responsible for the pattern formation.

The simplest (linearized) representation of such a reaction–diffusion equations displaying a Turing instability is given by the model [2]

$$\frac{\partial u_1}{\partial t} = a_1 u_1 - b_1 u_2 + d_1 \nabla^2 u_1 \ , \tag{12.1a}$$

$$\frac{\partial u_2}{\partial t} = b_2 u_1 - a_2 u_2 + d_2 \nabla^2 u_2 \ . \tag{12.1b}$$

In this system u_1 plays the role of the activator and u_2 the role of the inhibitor, with diffusion coefficients d_1 and d_2 respectively. The particular form of the cross-coupling matrix (where a_i and b_i have positive values) leads to maximum amplification of the wavenumbers obeying

$$|\boldsymbol{k}|^2 = \frac{1}{2} \left(\frac{a_1}{d_1} - \frac{a_2}{d_2} \right) , \tag{12.2}$$

as follows from a stability analysis of (12.1).

Motivated by this analysis, one might ask the following question: is the Turing mechanism possible in nonlinear optics too? Let us take as an example the equation for a class B laser from Chap. 7,

$$\frac{\partial A}{\partial t} = (D - 1) A + \mathrm{i} \left(a\nabla^2 - \omega \right) A - g \left(a\nabla^2 - \omega \right)^2 A \ , \tag{12.3a}$$

$$\frac{\partial D}{\partial t} = -\gamma \left(D - D_0 + |A|^2 \right) , \tag{12.3b}$$

with an unsaturated population inversion D_0 and a spatial-wavenumber selection factor g. Let us simplify (12.3) by assuming a very narrow gain line, i.e. $g \gg 1$, which makes diffraction negligible when compared with diffusion, and zero detuning, $\omega = 0$. Also, which is very significant here, let us assume that the population inversion also diffuses, which results in adding a Laplacian to (12.3b). In this case, if we define the field diffusion constant $d_1 = gd^2$, (12.3) converts to

$$\frac{\partial A}{\partial t} = (D - 1)A - d_1 \nabla^4 A \ , \tag{12.4a}$$

$$\frac{\partial D}{\partial t} = -\gamma \left(D - D_0 + |A|^2 \right) + d_2 \nabla^2 D \ , \tag{12.4b}$$

a system of two nonlinearly coupled diffusing components. The field diffusion is governed not by the usual Laplace operator, but by the second power of the operator (sometimes called super-diffusion, as mentioned earlier); however, this makes no essential difference compared with normal diffusion.

Consider a perturbation of the stationary solution $A = \bar{A} + a$, $D = \bar{D} + d$, where $\left(\bar{A}, \bar{D} \right) = \left(\pm\sqrt{D_0 - 1}, 1 \right)$. Linearizing (12.4) with respect to the perturbations leads to

$$\frac{\partial a}{\partial t} = d\sqrt{D_0 - 1} - d_1 \nabla^4 a \ , \tag{12.5a}$$

$$\frac{\partial a}{\partial t} = -\gamma \left(d + 2a\sqrt{D_0 - 1} \right) + d_2 \nabla^2 d \ . \tag{12.5b}$$

The similarity to the Turing system (12.1) becomes more evident if we change the sign of the perturbation of the population inversion d. This results

in the linear coupling matrix

$$
L = \begin{pmatrix} 0 & -\sqrt{D_0 - 1} \\ 2\gamma\sqrt{D_0 - 1} & -\gamma \end{pmatrix},
\tag{12.6}
$$

and a diagonal diffusion matrix

$$
D = \begin{pmatrix} -d_1\nabla^4 & 0 \\ 0 & d_2\nabla^2 \end{pmatrix} = \begin{pmatrix} -d_1 k^4 & 0 \\ 0 & -d_2 k^2 \end{pmatrix}.
\tag{12.7}
$$

The form of the linear coupling matrix, compared with (12.1), allows us to identify the optical field with the activator variable in a reaction–diffusion system, and the population inversion with the inhibitor variable.

The main requirement for Turing pattern formation in a reaction–diffusion system is that the inhibitor diffuses faster than the activator. This requirement is often called the principle of "local activator and lateral inhibitor" (LALI). Consequently, it seems reasonable that for observation of similar patterns in nonlinear optics, one must require that the inhibitor (the population inversion in a laser) diffuses more strongly than the optical field.

The purpose of this chapter is to generalize the LALI principle to arbitrary forms of nonlocalities. Indeed, both diffusion and diffraction are nonlocal operators responsible for the communication of fields in the transverse plane. In the original study by Turing, the usual form of diffusion was considered for the two interacting components. In optics one can have more complicated situations: even the model (12.4) and (12.5) shows such complications, since besides the normal diffusion of the population inversion there is a super-diffusion of the optical field. One can also have a situation where the inversion is diffusing but the optical field is diffracting (for a laser with a broad gain line). And, finally, one can have both components diffracting, as in the case of optical parametric oscillators.

These cases are investigated below. In the next section, a laser with diffusing inversion is studied under subcritical and supercritical conditions, and it is shown that Turing patterns are possible in the subcritical case. It is also shown that the diffusion of the population inversion stabilizes spatial solitons. In Sect. 12.3, the optical parametric oscillator is investigated. It is shown that the diffraction of the pump field (playing the role of inhibitor) may lead to the excitation of Turing patterns, which are different from the off-resonance patterns studied in previous chapters.

12.2 Laser with Diffusing Gain

It is often supposed intuitively that diffusion in a gain material (e.g. diffusion of the population inversion in a gas laser or diffusion of free charge carriers in a

semiconductor laser) should weaken the spatial inhomogeneity of the emitted optical field. As a consequence, gain diffusion should reduce or suppress a modulational instability, and might destroy spatial solitons that would exist in its absence.

The opposite phenomenon is shown to be true in this section, namely that the diffusion of a saturating gain enhances the spatial modulation of the optical field. This enhancement of modulation supports solitons and increases their stability range.

12.2.1 General Case

Consider a general model, where the mean-field equations for an optical system with saturable gain are given by [3]

$$\frac{\partial A}{\partial t} = F(A, \nabla^2 A) + DA ,$$ (12.8a)

$$\frac{\partial D}{\partial t} = \gamma(D_0 - D - D |A|^2 + d\nabla^2 D) ,$$ (12.8b)

where $A(\boldsymbol{r}, t)$ is the optical field (order parameter) and $D(\boldsymbol{r}, t)$ is the gain field (e.g. the population inversion). The operator $F(A, \nabla^2 A)$ is a given nonlinear and nonlocal function of the order parameter $A(\boldsymbol{r}, t)$, d is the diffusion coefficient for the saturable gain, and γ is its relaxation rate. The complex conjugate equation of (12.8a) must also be taken into account when the optical field is complex (if diffraction or focusing/defocusing nonlinearities are present in the function $F(A, \nabla^2 A)$).

For simplicity, it is assumed below that the gain relaxation is fast ($\gamma = \mathcal{O}(1/\varepsilon)$, with $\varepsilon \ll 1$), and the gain variable D can be adiabatically eliminated from (12.8b) by requiring that $\partial D/\partial t = 0$. However, as numerical calculations show, the main conclusions are valid even for moderate gain relaxation, i.e. $\gamma = \mathcal{O}(1)$. The adiabatic elimination from (12.8b), neglecting gain diffusion ($d = 0$), is straightforward, and gives

$$D = \frac{D_0}{1 + |A|^2} .$$ (12.9)

In general (for $d \neq 0$), the adiabatic elimination requires the inversion of the operator

$$N = 1 + |A|^2 - d\nabla^2 ,$$ (12.10)

since (12.8b) can be written, in the stationary case, as $ND = D_0$. The inversion can be performed for small diffusion, assuming that $d\nabla^2 = \mathcal{O}(\varepsilon)$ and all the other variables are of $\mathcal{O}(1)$, yielding

$$N^{-1}D = \frac{D_0}{1 + |A|^2} \left[1 + d\nabla^2 \left(\frac{1}{1 + |A|^2} \right) \right] + d\nabla^2 \left[\frac{1}{\left(1 + |A|^2\right)^2} \nabla D_0 \right] ,$$

(12.11)

where the Laplace operator acts on the variables to the right of it. It is easy to verify that $N^{-1}ND_0 = D_0\left(1 + \mathcal{O}(\varepsilon^2)\right)$, which confirms the validity of the inverse operator (12.11) at $\mathcal{O}(\varepsilon)$.

For a spatially homogeneous pump parameter D_0, the last term on the right-hand side of (12.11) vanishes, and the population inversion becomes

$$D = \frac{D_0}{1 + |A|^2} + \frac{D_0}{1 + |A|^2} d\nabla^2 \left(\frac{1}{1 + |A|^2}\right). \tag{12.12}$$

Inserting (12.12) into (12.8a), we finally obtain the order parameter equation

$$\frac{\partial A}{\partial t} = F'(A, \nabla^2 A) + \frac{D_0 A}{1 + |A|^2} d\nabla^2 \left(\frac{1}{1 + |A|^2}\right), \tag{12.13}$$

where $F'(A, \nabla^2 A) = F(A, \nabla^2 A) + D_0/(1 + |A|^2)$. The last term on the right-hand side of (12.13) is due to the diffusion of the saturable gain.

Equation (12.13) will be used as a basis to investigate how the gain diffusion affects the stability of the homogeneous solutions of that equation.

Linearization of (12.13) around the homogeneous stationary solution (which now depends on the explicit form of F', and is assumed to be real-valued without loss of generality), with perturbations of the form $A = \bar{A} + a_1 \exp(\lambda t + \mathrm{i}kr) + a_2^* \exp(\lambda t - \mathrm{i}kr)$, leads to

$$\lambda \boldsymbol{a} = L\boldsymbol{a} + D\boldsymbol{a}, \tag{12.14}$$

where $\boldsymbol{a} = (a_1, a_2)^{\mathrm{T}}$ is the column vector of the perturbation amplitudes. L is the linear evolution matrix generated by the nondiffusive part of (12.13),

$$L = \begin{pmatrix} \delta F'/\delta a_1 & \delta F'/\delta a_2 \\ \delta F'^*/\delta a_1 & \delta F'^*/\delta a_2 \end{pmatrix}, \tag{12.15}$$

and D is the perturbation matrix due to gain diffusion,

$$D = \frac{D_0 \bar{A}^2}{\left(1 + \bar{A}^2\right)^3} d\nabla^2 \begin{pmatrix} 1 & 1 \\ 1 & 1 \end{pmatrix}. \tag{12.16}$$

A useful representation can be found by rewriting (12.14)–(12.16) in terms of the new basis $a_\pm = a_1 \pm a_2$ (corresponding to perturbations of the amplitude and the phase, respectively), in which one obtains, instead of (12.16),

$$D = \frac{D_0 \bar{A}^2}{\left(1 + \bar{A}^2\right)^3} d\nabla^2 \begin{pmatrix} 2 & 0 \\ 0 & 0 \end{pmatrix}. \tag{12.17}$$

From this general analysis, we can draw some conclusions:

1. The sum of the Lyapunov exponents is always equal to the trace of the linear evolution matrix. The perturbation (12.17) increases the sum of the Lyapunov exponents by an amount $2dk^2 D_0 A^2 / \left(1 + A^2\right)^3$. This indicates that, overall, the gain diffusion works as "antidiffusion" of the order parameter, and spatial components with nonzero transverse wavenumbers (off-axis modes) may be amplified because of gain diffusion.
2. If the amplitude and the phase of the order parameter A are decoupled from one another, then the gain diffusion affects only the amplitude perturbations. Therefore the gain diffusion always increases the amplitude modulations, and as a consequence may stabilize spatial solitons. On the contrary, it does not affect purely phase perturbations at all.
3. If the amplitude and phase perturbations of the order parameter A are coupled, then the eigenvalues are complex and form a conjugate pair, i.e. $\lambda_{1,2} = \lambda_{\mathrm{Re}} \pm i\lambda_{\mathrm{Im}}$. The sum of the eigenvalues is proportional to the real part, i.e. $\lambda_1 + \lambda_2 = 2\lambda_{\mathrm{Re}}$. Therefore (12.17) indicates also the destabilization of coupled amplitude and phase perturbations. The gain diffusion thus increases (or initiates) a modulational instability of oscillatory (Hopf) type.
4. In the case of bistability, the gain diffusion affects predominantly the upper bistability branch: the coefficient of the effective "antidiffusion" of the order parameter $2dk^2 D_0 A^2 / (1 + A^2)^3$ depends on the intensity of the optical field, and is evidently larger for the upper branch.

The above conclusions are now set out in detail for the case of a bistable laser (a laser with an intracavity saturable absorber).

12.2.2 Laser with Saturable Absorber

We consider first the simplest case of a monostable laser (with linear losses), represented by

$$F(A, \nabla^2 A) = -A + i a \, \nabla^2 A + g \, \nabla^4 A \ . \tag{12.18}$$

A linear stability analysis of the full system ((12.8) and (12.18)) shows that, although the λ-branch related to the amplitude perturbation is shifted upward, its maximum value can never become positive. As a consequence, amplitude modulations (due to lateral boundaries or other reasons) can be enhanced, but never cause absolute instabilities. Some bistability mechanism is required to reach an instability. As an example, we consider the case of a laser with a saturable absorber, discussed in Chap. 9. The functional $F(A, \nabla^2 A)$ is now given by

$$F(A, \nabla^2 A) = -A - \frac{\alpha_0 A}{1 + |A|^2 / I_\mathrm{s}} + i a \, \nabla^2 A - g \, \nabla^4 A \ , \tag{12.19}$$

where α_0 is the coefficient of the unsaturated losses and I_s is the saturation intensity. Again, zero detuning is assumed in (12.19).

For $g = 0$, one has a purely diffractive case, as studied by Rosanov [4]. For $a = 0$, the purely diffusive case is obtained instead. In optics, the purely diffusive case can be realized using a self-imaging resonator, as described in Chap. 6.

First we investigate the purely diffusive case, where the amplitude and phase perturbations are decoupled. In this case we have

$$\frac{\partial A}{\partial t} = \frac{D_0 A}{1 + |A|^2} - A - \frac{\alpha_0 A}{1 + |A|^2 / I_\mathrm{s}} - g \nabla^4 A + \frac{D_0 A}{1 + |A|^2} d\nabla^2 \left(\frac{1}{1 + |A|^2} \right). \tag{12.20}$$

A linear stability analysis of the homogeneous upper-branch solution of (12.20) gives

$$\lambda = \frac{2D_0 \bar{A}^2}{\left(1 + \bar{A}^2\right)^2} + \frac{2\alpha_0 (\bar{A}^2 / I_\mathrm{s})}{\left(1 + \bar{A}^2 / I_\mathrm{s}\right)^2} - gk^4 + \frac{2D_0 \bar{A}^2}{\left(1 + \bar{A}^2\right)^3} dk^2 \tag{12.21}$$

for amplitude perturbations. The phase perturbations are not affected by the gain diffusion in this purely diffusive case.

A family of plots of (12.21) is given in Fig. 12.1a, showing the modulational instability, which appears and grows with increasing gain diffusion d. For sufficiently large gain diffusion, the upper branch can be modulationally unstable.

In order to test whether the above procedure of operator inversion reveals the correct results, a linear stability analysis of the full problem ((12.8) and (12.19)) was also performed. Figure 12.1b shows the results of the stability analysis of the full system. Evidently, the instability spectra for small gain diffusion and small transverse wavenumbers coincide well in the two cases (the smallness parameter in the adiabatic elimination (12.11)–(12.13) is indeed $d\nabla^2 = -dk^2 = \mathcal{O}(\varepsilon)$). Discrepancies appear for relatively large values of the gain diffusion, leading to different quantitative (but not different qualitative) results.
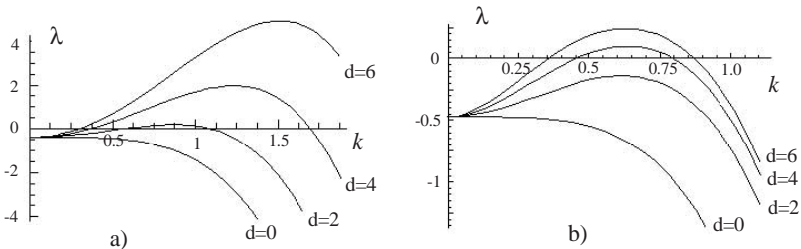

Fig. 12.1. Growth rate of a perturbation as a function of the transverse wavenumber for different values of gain diffusion d, obtained from a linear stability analysis of (**a**) the simplified model (12.20) and (**b**) of the full system (12.8). The parameters are $D_0 = 2.8$, $\gamma = 5$, $I_\mathrm{s} = 0.1$ and $\alpha_0 = 5.0$

12.2.3 Stabilization of Spatial Solitons by Gain Diffusion

Two different interpretations of spatial solitons were discussed in Chap. 8: a spatial soliton can be considered either as a part of an extended pattern, such as a pattern of rolls or hexagons (Fauve and Thual type [5]), or as a homoclinic connection between two stable homogeneous states, forming a domain of minimum size (Rosanov type [4]).

In the first case, the background amplitude (the solution far away from the soliton) corresponds to the stable solution branch. For bright solitons, the upper branch is usually modulationally unstable, and the radiation corresponding to the stable lower branch serves as the background. For dark solitons, the opposite is valid. In the second case, an interaction between locked fronts results from the nonmonotonic decay of the background field far from a front.

In both cases, a spatial modulation is involved in the soliton formation process. As shown in Chap. 11, solitons are more robust, and their stability range is larger, in the case of strong spatial modulation. Consequently, from the analysis of the previous section, it follows that gain diffusion must enhance the stability of solitons, since in all cases an increase in the gain diffusion always leads to an increase in the growth exponents of the off-axis perturbation modes, i.e. to the enhancement of the spatial modulation. Three different situations can be realized:

1. Positive growth exponents become larger, and the parameter range of the modulational instability, and that for solitons of the Fauve and Thual type, increases.
2. Negative growth exponents decrease in magnitude, and spatial oscillations become less damped, resulting in the stabilization of Rosanov-type solitons.
3. Negative growth exponents may become positive. One can then obtain a transformation of solitons of the Rosanov type into solitons of the Fauve and Thual type (this is actually more a transformation of the interpretation than a qualitative transformation of the soliton itself). In all cases, the stability range of the bright solitons is increased.

In order to check the statements above, a numerical investigation of the full system ((12.8) and (12.19)) was performed. The results are summarized in Fig. 12.2, where the existence ranges of bright and dark solitons are plotted on the plane (D_0, d), together with the modulational-instability boundary (squares) and the domain equilibrium boundary (full circles). Typical field profiles corresponding to different parameter values are shown in Fig. 12.3.

In region A of Fig. 12.2, amplitude spatial solitons of the Fauve and Thual type exist. Their profile is shown in Fig. 12.3d. In region B, the spatial solitons are of the Rosanov type. A contraction of amplitude domains occurs in this region. In region C, the spatial solitons are still of the Rosanov type (shown in Fig. 12.3c), but amplitude domains expand. In regions C and D, dark spatial
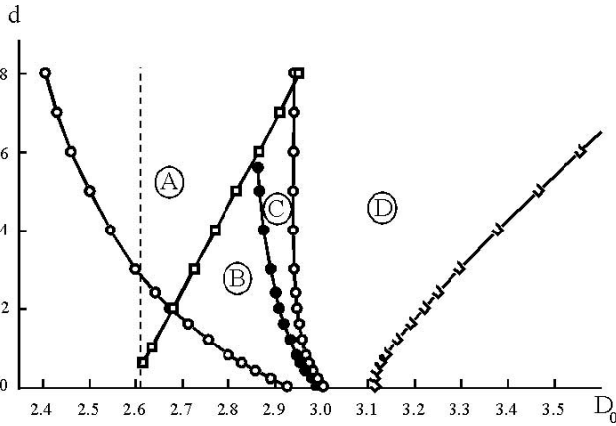
Fig. 12.2. Regions corresponding to different regimes of localized solutions in the plane (D_0, d), as obtained from numerical integration of (12.8) in the purely diffusive case. The parameters are as in Fig. 12.1

solitons exist. The line marked by squares (separating region A from regions B and C in Fig. 12.2) corresponds to the modulational-instability threshold. The line marked by filled circles (separating regions B and C) corresponds to the equilibrium state of the two phases corresponding to the upper and lower solution branches, and thus domains neither contract nor expand. The dashed vertical line separates the monostable and bistable regimes of the homogeneous solutions.

In the case of small domains, the domain boundaries lock and result in stable solitons. As Fig. 12.2 indicates, this locking can occur for contracting domains (in region B) and also for expanding domains (in region C).

We note that the spatial solitons in regions A, B, and C appear visually identical: no abrupt changes of the soliton parameters are observed when the modulational-instability threshold line is crossed. The existence range of bright solitons increases with diffusion, and the Rosanov-type solitons transform into Fauve and Thual type solitons at the onset of the modulational instability of the upper solution branch.

Figures 12.3a,b show domains at equilibrium, which occurs between region B (contraction) and region C (expansion). However, the domain boundaries do not decay monotonically, but show spatial oscillations. These oscillations are stronger for larger diffusion of the gain, as is evident from comparison between Fig. 12.3a and Fig. 12.3b. We note that spatial oscillations are much more prominent on the upper bistability branch, in correspondence with the predictions above.

Dark solitons have also been found numerically. They exist in regions C and D. Curiously enough, enhancement of the modulation of the upper-branch solution stabilizes the dark solitons too. The upper (modulated) so-
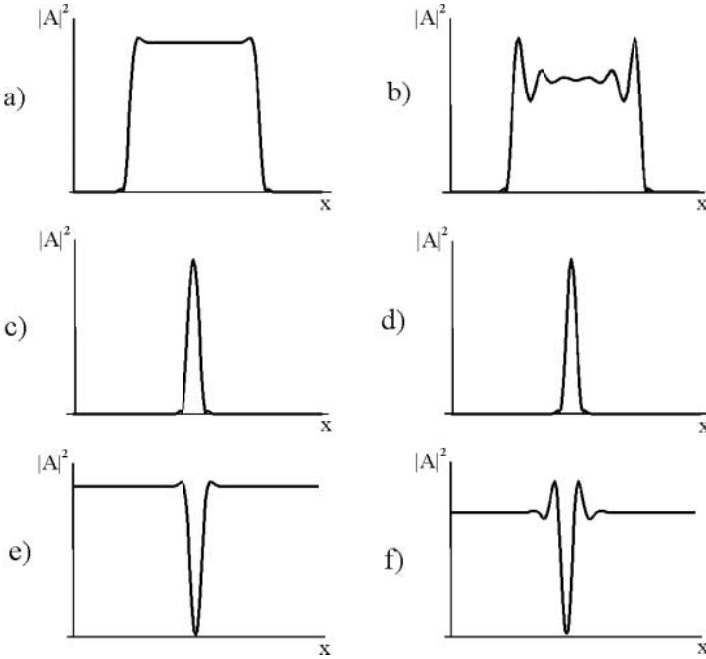
Fig. 12.3. Stationary solutions obtained by numerical integration of the initial equations in the case of one spatial dimension. The parameters are as in Fig. 12.1. (**a**) Amplitude domain with weakly nonmonotonic tails, for $D_0 = 2.99$, $d = 0$. (**b**) Amplitude domain with strongly nonmonotonic tails (close to the modulational-instability boundary), for $D_0 = 2.85$, $d = 5$. (**c**) Soliton in region B (of Rosanov type), for $D_0 = 2.95$, $d = 0$. (**d**) Soliton in region A (of Fauve and Thual type), for $D_0 = 2.7$, $d = 5$. (**e**) Dark soliton in region D for zero gain diffusion (weak spatial modulation), for $D_0 = 3.05$, $d = 0$. (**f**) Dark soliton in region D for strong gain diffusion (strong spatial modulation), for $D_0 = 2.15$, $d = 5$

lution now serves now as the background for the dark solitons. It is usually presumed that a modulation of the solution branch other than that corresponding to the background stabilizes solitons. What follows generally from this study is that enhancement of the modulation of the background also increases the stability of dark solitons.

Figures 12.3e,f show numerically calculated field profiles corresponding to dark solitons. As in the case of large domains, the enhancement of the spatial modulation with gain diffusion is also clearly visible in this case.

The above results correspond to the purely diffusive case. In the presence of diffraction, the mathematical expressions obtained from the linear stability analysis are not so transparent. The corresponding plots are given in Fig. 12.4. In general, a relatively small ammount of diffraction of the field does not bring about qualitative changes: an enhancement of the modulational instability
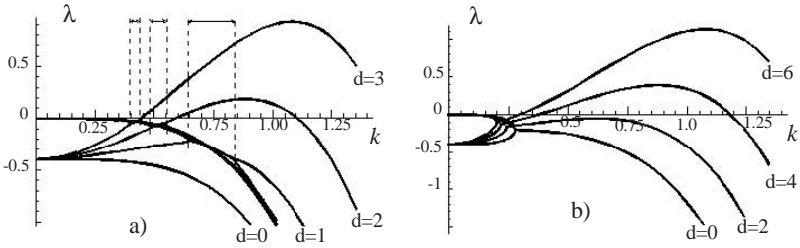
Fig. 12.4. Growth rate of perturbations in the diffractive case. Parameters as in Fig. 12.1, except for the diffraction coefficient. (**a**) Weak diffraction, $a = 0.25$; for nonzero gain diffusion, a small region of locking between amplitude and phase perturbations appears (indicated by *vertical dashed lines*). (**b**) Strong diffraction, $a = 2.5$; the amplitude and phase perturbations are locked everywhere except for relatively small transverse wavenumbers k

(Fig. 12.4a) is observed because of gain diffusion, as in the purely diffusive case studied above. The additional feature compared with the purely diffusive case is a locking between amplitude and phase instabilities in a certain band of transverse wavenumbers (where the amplitude and phase λ-branches are sufficiently close). As the numerical calculations show, the enhancement of the soliton stability range due to gain diffusion is similar to that in the purely diffusive case.

For larger diffraction (Fig. 12.4b), the locking between amplitude and phase perturbations is stronger. As a consequence, a nonstationary modulational instability is predicted (an instability of Hopf type). One may, therefore, expect oscillatory solitons in the case of strong diffraction.

Some general conclusions following from the above analytical and numerical study are:

1. Diffusion of the saturable gain enhances the growth of the off-axis field components. Overall, gain diffusion results in "antidiffusion" of the order parameter. As a result, gain diffusion can enhance and/or initiate a modulational instability. In the monostable case, a modulational instability is never achieved; however, the maximum growth rate can approach very close to the zero axis from below, thus causing weakly decaying spatial oscillations. In the bistable case, a modulational instability can appear in some band of transverse wavenumbers.
2. The solution corresponding to the upper bistability branch is predominantly affected by gain diffusion. The solution corresponding to the lower branch is less affected, or almost unaffected, since its amplitude is significantly smaller than that of the upper branch.
3. As a result, gain diffusion increases the stability range of solitons of both types: in the case of a Fauve and Thual type soliton, which a priori requires modulationally unstable solutions, the enhancement of the modulational instability obviously increases its existence range. In the case of

solitons of the Rosanov type, where the stabilization is due to the non-monotonic decay of the domain fronts, an increase of the gain diffusion results in an increase of the spatial oscillations, and the existence range of solitons increases correspondingly.

4. The transition between the solitons of the two types is smooth (no singular behavior appears at the boundary between solitons of Rosanov type and solitons of Fauve and Thual type). This suggests that distinguishing the two types of solitons is only a matter of interpretation. In essence, the solitons of the two types are similar, as they convert one into another smoothly.

5. As the analysis of bright solitons shows, an enhancement of the modulation of the upper state (unlike a enhancement of the modulaton of the background solution) increases the stability of a soliton. However, the analysis of dark solitons shows that an enhancement of the background modulation can also stabilize those solitons.

6. In the diffractive case, pump diffusion can enhance or initiate not only stationary modulational instabilities, but also nonstationary ones (instabilities of Hopf type).

12.3 Optical Parametric Oscillator with Diffracting Pump

Consider now a system where the two competing fields are diffracting. One example is given by a DOPO, whose mean-field dynamical equations for the signal (subharmonic) $A_1(\boldsymbol{r}, t)$ and the pump wave $A_0(\boldsymbol{r}, t)$ are

$$\frac{\partial A_0}{\partial t} = \gamma_0 \left[-(1 + i\omega_0) A_0 + \bar{E} - A_1^2 + i a_0 \nabla^2 A_0 \right], \tag{12.22a}$$

$$\frac{\partial A_1}{\partial t} = \gamma_1 \left[-(1 + i\omega_1) A_1 + A_0 A_1^* + i a_1 \nabla^2 A_1 \right], \tag{12.22b}$$

where the parameters are defined in Chap. 3.

Throughout this section, the case of a resonant pump $\omega_0 = 0$ and equal decay rates $\gamma_1 = \gamma_0$ is considered to simplify the analysis. Also, we normalize the spatial coordinates to $\sqrt{a_1}$, which is equivalent to setting $a_1 = 1$ and $a_0 = a$ in (12.22), where $a = a_0/a_1$ is the relative diffraction parameter.

We note here that, as diffraction in a laser depends on the resonator length in the case of a self-imaging cavity, in a DOPO the use of such a cavity allows one to choose freely the value of the diffraction parameter a. In fact, when the optical cavity is formed by plane mirrors, the diffraction coefficients of the signal and pump fields are related by $a_1 = 2a_0$, as a result of the phase-matching condition [7]. In the present case, in order to study the influence of diffraction, we assume that each field resonates in a near-self-imaging cavity, with different lengths for the two fields, and consider $a = a_0/a_1$ a free parameter.

12.3.1 Turing Instability in a DOPO

An initial comparison with the Turing system suggests that a LALI instability might be observed in a DOPO when the ratio between the pump (inhibitor) and subharmonic (activator) diffraction coefficients a reaches a critical value [8].

We proceed again by analyzing the stability of the homogeneous solution of (12.22) against space-dependent perturbations of the form $\delta \boldsymbol{A}(\boldsymbol{r}, t) \propto \exp(\lambda t + \mathrm{i}\boldsymbol{k} \cdot \boldsymbol{r})$, where $\delta \boldsymbol{A} = (\delta A_0, \delta A_0^*, \delta A_1, \delta A_1^*)$. The resulting linear matrix leads to a fourth-order polynomial in the eigenvalues and then to explicit (although lengthy) analytical expressions for the growth rate $\lambda(k)$.

In Fig. 12.5 we represent the real part of λ as a function of the perturbation wavenumber k, for three different values of the diffraction parameter and a fixed positive value of the signal detuning. The parameters are such that an off-resonance instability does not occur (the signal detuning is positive). For zero pump diffraction, $a = 0$ (dotted curve), the homogeneous solution is stable. The off-axis modes are strongly damped, and no LALI instability occurs. For a diffraction parameter $a = 1/2$ (dashed curve in Fig. 12.5), corresponding to the plane-mirror configuration, the homogeneous solution is still stable; the off-axis modes are damped, but the damping around some wavenumbers is weak. This corresponds to a situation where a LALI instability is detectable, but below the threshold (an underdeveloped LALI instability). If the value of the diffraction parameter is increased, the largest of the real parts of the eigenvalues grows, until it becomes positive at a critical wavenumber $k = k_{\mathrm{c}}$. This situation is shown by the continuous curve in Fig. 12.5, obtained for a diffraction parameter $a = 10$.
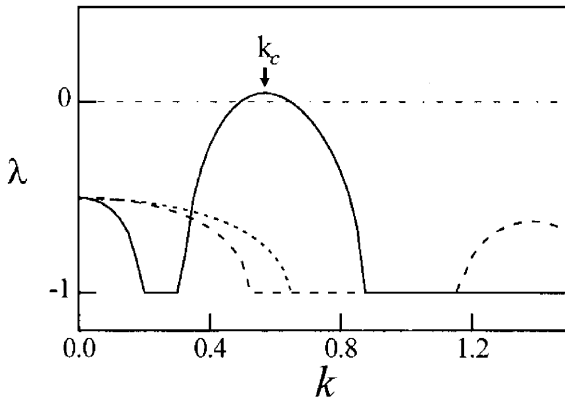

Fig. 12.5. Real part of the eigenvalue as a function of the perturbation wavenumber, for different values of the diffraction parameter: $a = 0$ (*dotted curve*), $a = 0.5$ (*dashed curve*) and $a = 10$ (solid curve). The other parameters are $\omega_1 = 1$, $\omega_0 = 0$, $E = 2.5$

At the threshold of the pattern-forming instability, the real part of the eigenvalue of the wavenumber with maximum growth is zero. In Fig. 12.6, the off-resonance and LALI instability regions are plotted in the parameter space (ω_1, E) for a specific value of the diffraction parameter. The regions are well separated in the parameter space, and therefore can be associated with different mechanisms. The off-resonance instability exists for all values of the pump intensity above threshold, whereas the LALI instability appears only at some critical pump value that depends on the diffraction parameter a.
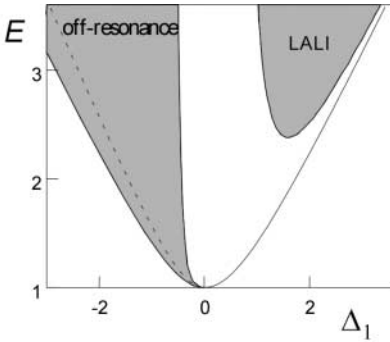

Fig. 12.6. Instability regions in the parameter space (ω_1, E) for nonzero diffraction parameter $a = 5$, evaluated from a linear stability analysis. There are two instability regions: for negative detuning, the traditional off-resonance instability; for positive detuning, the Turing instability

We note that pump diffraction not only creates the LALI instability, but also modifies the off-resonance instability range, as can be seen from Fig. 12.6. For zero pump diffraction the off-resonance instability occurs between the dashed curve and the left part of the solid curve corresponding to the neutral-stability line, as follows from the standard analysis. Pump diffraction increases significantly the off-resonance instability region. However, the spatial scale of the off-resonance pattern is not modified by the presence of pump diffraction.

Another important feature that reveals the different nature of the patterns on both sides of the resonance is the corresponding wavelength. In the case of off-resonance patterns, this wavelength depends mainly on the resonator detuning and the diffraction coefficient of the signal wave. In contrast, the wavelength of the pattern in the LALI region depends essentially on the pump and on the ratio of the diffraction coefficients a, and very weakly on the resonator detuning. This behavior is shown in Fig. 12.7, where the squared wavenumber of the maximally growing mode is plotted against the detuning (full line). The broken part of the curve, in the neighborhood of the resonance, corresponds to negative eigenvalues.

Some analytical expressions can be found in different limits. For negative detuning, the wavenumber is given by

$$k^2 = -\omega_1 ,$$

$$(12.23)$$
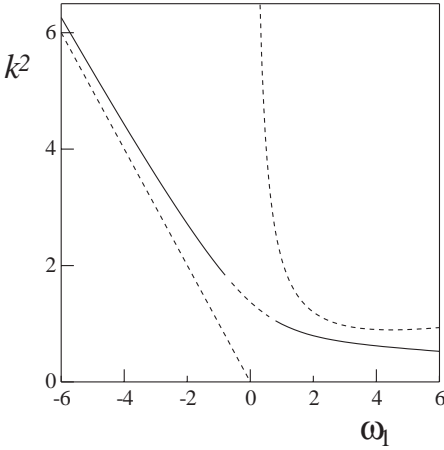
Fig. 12.7. The wavenumber of the pattern, given by a linear stability analysis for $a = E = 10$. The exact value is given by the *solid line*. The *dashed lines* correspond to analytical expressions given in the text

which clearly corresponds to the off-resonance patterns selected by the cavity. For positive detuning,

$$k^2 = \frac{\omega_1}{a} + \frac{2E}{a\omega_1} \ . \tag{12.24}$$

The asymptotic expressions (12.23) and (12.24) are represented by dashed curves in Fig. 12.7, to be compared with the exact result (full line).

Turing patterns were found by numerical integration of (12.22). In Fig. 12.8 we show the threshold for the emergence of spatial patterns, for a fixed value of signal detuning. Results obtained from the linear stability analysis described above (full line) are shown, together with numerical results for some values of the diffraction parameter (represented by symbols). In all cases, the final LALI patterns have hexagonal symmetry, such as the one shown in the
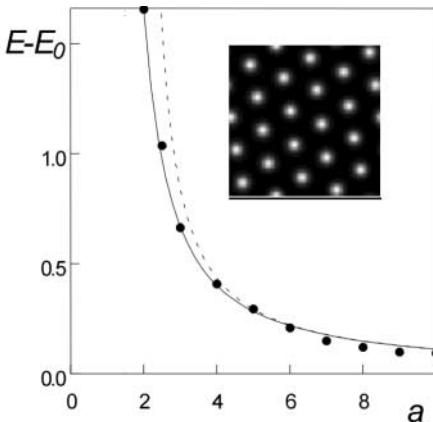
Fig. 12.8. Critical pump value for Turing instability as a function of the diffraction parameter, for fixed signal detuning $\omega_1 = 2$. The *symbols* represent the result of numerical integration of the DOPO equations. The *solid curve* represents the result of a semianalytical calculation based on a linear stability analysis, and the *dashed curve* corresponds to the boundary of the instability domain given by (12.27). The *inset* shows a hexagonal pattern obtained numerically for $a = 5$, $E = 3$

inset of Fig. 12.8. For comparison, the preferred patterns occurring in the off-resonance region are not hexagons, but stripes.

The threshold condition for a LALI instability can be evaluated analytically, but is in general a complicated function of the parameters. However, Fig. 12.8 indicates two main features: (i) there exists a hyperbolic relation between the pump and diffraction parameters, and (ii) a minimum value of the diffraction parameter a_m is required to reach the instability for a fixed detuning. This guided our search for an asymptotic expression, where we introduced a smallness parameter related to the deviation from the threshold, given by $E_0 = \sqrt{1 + \omega_1^2}$. Assuming that $R = E_0 (E - E_0) \approx \mathcal{O}(\varepsilon)$ and $D = a - a_m \approx \mathcal{O}(1/\varepsilon)$, and expanding the eigenvalue, we find, at leading order in ε, that the homogeneous solution is unstable whenever

$$27 D^2 R^2 - \omega_1^2 (2DR - 1)^3 < 0 . \tag{12.25}$$

The minimum value of the diffraction parameter a_m, which depends on the detuning, can be evaluated by analyzing the opposite limit, i.e. at large values of the pump parameter above the threshold. In this case we find that the instability can be observed only when $a > a_m$, where

$$a_m (E_0 - 1) = 1 . \tag{12.26}$$

From (12.26) it follows that a_m grows monotonically when the detuning is decreased, and that $a > 1$ (and consequently $a_0 > a_1$) when $\omega_1 < \sqrt{3}$.

Finally, the instability domain (12.25) in the original variables is

$$(a - a_m) (E - E_0) < \eta , \tag{12.27}$$

where η is a positive function of the signal detuning. In the limit of small detuning, (12.25) yields an asymptotic value $\eta = 27/8\omega_1^2$.

The expression (12.27) is plotted in Fig. 12.8 (as the dashed line) for $\omega_1 = 2$ (for which $\eta = 2$). Notice the good correspondence with the exact (full line) and numerical (symbols) results.

12.3.2 Stochastic Patterns

The Turing instability in a DOPO occurs only for nonzero signal detuning, as follows from the stability analysis and also from (12.25). However, in resonance, some transverse wavenumbers are weakly damped for nonzero pump diffraction. The wavenumber of the weakly damped modes can be obtained from a linear stability analysis of (12.22). In the limit of far above the threshold ($E \gg 1$), this wavenumber is given by

$$k^2 = \sqrt{\frac{2E}{a}} , \tag{12.28}$$

which is valid also for small values of the detuning ω_1, where pattern formation is expected.

Equation (12.28) corresponds to a ring of weakly damped wavevectors, in the spatial Fourier domain. To check the existence of the ring numerically one must introduce a permanent noise. We can expect that the homogeneous solution will then be weakly modulated by a filtered noise, with a characteristic wavenumber given by (12.28).

In order to incorporate the noise, we have modified (12.22) by adding a term $\sqrt{\gamma_i}\Gamma_i$ to the evolution equation for each field component A_i. These terms, introduced phenomenologically, represent stochastic Langevin forces defined by

$$\langle \Gamma_i(r_1, t_1) \rangle \langle \Gamma_i^*(r_2, t_2) \rangle = \frac{\delta(r_1 - r_2)\delta(t_1 - t_2)}{2T_i} \ , \tag{12.29}$$

where T_i are the corresponding temperatures.

A typical result of numerical integration of the Langevin equations is shown in Fig. 12.9, where a snapshot of the amplitude and the corresponding averaged spatial power spectrum $\langle |A(\boldsymbol{k})|^2 \rangle$ are shown. As expected, no spatial wavenumber selection was visible in the case of zero pump diffraction. For nonzero pump diffraction, the DOPO filters the off-axis noise components, and a ring emerges in the far field (Fig. 12.9, right). If the pump diffraction parameter is increased, the induced wavenumber ring decreases in radius and becomes more dominant, in accordance with (12.28).

The above calculations were performed for zero detuning for both waves. Therefore all possible pattern formation mechanisms due to off-resonance excitation are excluded.

The expression (12.28) for the wavenumber, although evaluated at resonance, is a good approximation to the wavenumber of the patterns for moderate values of the signal detuning, and corresponds to a characteristic length of the emerging pattern $L_{\mathrm{p}} = k_{\mathrm{c}}^{-1}$. Returning to the initial normalizations of
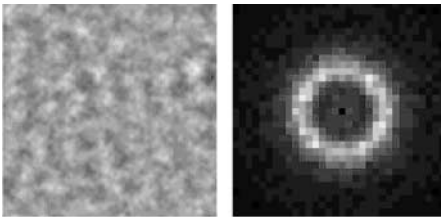

Fig. 12.9. Stochastic spatial distribution (*left*) and averaged spatial Fourier power spectrum (*right*) obtained by numerical integration of the DOPO Langevin equations, for $\omega_1 = 0$, $E = 2$, $a_0 = 0.005$, $a_1 = 0.0005$ ($a = 10$). The averaging time was $t = 300$. The zero spectral component has been removed

the spatial variables in (12.22), this length can be expressed as

$$L_{\mathrm{p}}^2 = \sqrt{\frac{a_0 a_1}{2E}} \; , \tag{12.30}$$

which, together with (12.27), is strikingly similar to the conditions derived in [9] for the Brusselator, a paradigmatic model of chemical pattern formation.

Clearly, the scale of the pattern given by (12.30) depends on the diffraction coefficients of both fields. It is interesting to compare the scale of the Turing pattern with the characteristic scales of the components, given by their spatial evolution in the absence of interaction. For this purpose, we consider first a deviation from the trivial solution, $A_0 = E + X$, $A_1 = Y$. In the resonant case and neglecting the nonlinear interaction, (12.22a) leads to

$$-Y + EY^* + ia_1 \nabla^2 Y = 0 \; , \tag{12.31}$$

or, equivalently,

$$\left[1 - \left(\frac{a_1}{E} \nabla^2 \right)^2 \right] Y = 0 \; . \tag{12.32}$$

Similarly, from (12.22b) we find

$$-X + ia_0 \nabla^2 X = 0 \; . \tag{12.33}$$

From the solutions of (12.32) and (12.33), we can define a characteristic spatial scale for the activator, $L_{\mathrm{a}} = \sqrt{a_1/E}$, and for the inhibitor, $L_{\mathrm{i}} = \sqrt{a_0}$, corresponding to the signal and pump fields, respectively. Now the scale of the generated pattern can be written in terms of the scales of the activator and the inhibitor, as

$$L_{\mathrm{p}}^2 = \frac{L_{\mathrm{a}} L_{\mathrm{i}}}{\sqrt{2}} \; , \tag{12.34}$$

revealing that the characteristic spatial scale of the pattern is the geometric mean of the spatial scales of the interacting components.

It is possible to find a simple relation between L_{a} and L_{i} in the limit of $a \gg a_m$ and $E \gg E_0$ (large diffraction and pump parameters, and moderate detuning). In this case, the instability domain (12.27) takes the form $aE > \eta$, which can be expressed in terms of the characteristic lengths to give the threshold condition

$$L_{\mathrm{i}} > \sqrt{\eta} L_{\mathrm{a}} \; . \tag{12.35}$$

The value of η depends on the signal detuning and can be evaluated from (12.25). We find that $\eta > 1/2$ always and, in particular, that $\eta > 1$ for $\omega_1 < 3\sqrt{3}$. Therefore, for small (and also moderate) detuning, the inhibitor range must be larger than the activator range for the occurrence of the LALI

instability. This is in accordance with the assumptions made in the derivation of (12.28).

The conditions defined by (12.34) and (12.35) are typically found in reaction–diffusion systems, and are a signature of the Turing character of the instabilities described above.

12.3.3 Spatial Solitons Influenced by Pump Diffraction

The spatial modulation induced by pump diffraction also influences the stability of solitons [10], in accordance with the results of Chap. 11. In order to show this, we performed a numerical integration of the DOPO equations (12.22) for different values of a_0. The amplitude along a line crossing the center of a soliton is plotted in Fig. 12.10, showing that the diffraction enhances the spatial oscillations strongly.

The parameters that define the shape of a soliton are the exponent of the spatial decay and the wavenumber of the oscillating tails. These parameters can be analytically evaluated by means of a spatial stability analysis. We assume that the intensity of the field is perturbed from its stationary value in some place in the transverse space (owing to the effects of boundaries, a spatial perturbation or a defect in the patterns), and look at how this perturbation decays (or grows) in space. For this purpose, we consider evolution in space instead of time. When the system has reached a stationary state, the solution, which we assume to have radial symmetry, can be written in the time-independent form

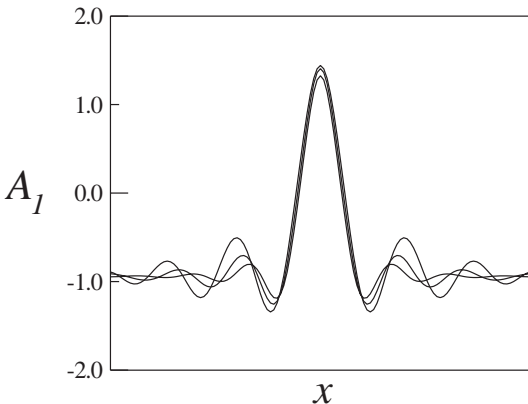$$A_i = \bar{A}_i + \delta A_i(r) \; , \tag{12.36}$$

Fig. 12.10. Amplitude profile of a soliton across a line crossing its center, evaluated numerically for different pump diffraction coefficients, $a_0 = 0.0005$, 0.002 and 0.01. The amplitude of the modulation of the tails increases with increasing diffraction. The other parameters are $a_1 = 0.001$, $E = 2$, $\omega_1 = -0.6$, $\omega_0 = 0$

where $\bar{A}_i$ represents the stationary homogeneous solution for the pump and signal fields, given in (11.2).

After substitution of (12.36) in (12.22), if we consider regions in space not close to the domain boundary, the resulting system can be linearized in the deviation, and the spatial evolution can be described by the system

$$\nabla^2 \, \delta \boldsymbol{A} = L \, \delta \boldsymbol{A} \; , \tag{12.37}$$

where $\delta \boldsymbol{A}$ is the four-component perturbation vector and L is a linear matrix. In the case of a resonant pump, i.e. $\omega_0 = 0$, L is given by [10, 11]

$$L = \begin{pmatrix} -\mathrm{i}/a & 0 & -(2\mathrm{i}/a)\,\bar{A}_1 & 0 \\[2mm] 0 & \mathrm{i}/a & 0 & (2\mathrm{i}/a)\,\bar{A}_1^* \\[2mm] \mathrm{i}\bar{A}_1^* & 0 & -\mathrm{i}\,(1+\mathrm{i}\omega_1) & \mathrm{i}\bar{A}_0 \\[2mm] 0 & -\mathrm{i}\bar{A}_1 & -\mathrm{i}\bar{A}_0^* & \mathrm{i}\,(1-\mathrm{i}\omega_1) \end{pmatrix} . \tag{12.38}$$

The solutions of the linear system (12.37) are of the form

$$\delta \boldsymbol{A}(r) \propto \mathrm{e}^{qr} \; , \tag{12.39}$$

where the wavevector q can be complex, in the form $q = \mathrm{Re}(q) + \mathrm{i}\,\mathrm{Im}(q)$. From (12.39), it follows that a negative value of $\mathrm{Re}(q)$ indicates a spatial decay of the perturbation and is responsible for localization, while a nonvanishing value of $\mathrm{Im}(q)$ indicates the presence of a nonmonotonic (oscillatory) decay [12]. Thus, the solution (12.36), with the deviation given by (12.39), represents the asymptotic profile of the soliton far from its core.

Expressions for the spatial decay and modulation follow from a study of the eigenvalues of L, which are the solutions of the characteristic equation

$$a^2\mu^4 - 2a^2\omega_1\mu^3 + (1-4aI_1)\,\mu^2 - 2\omega_1\,(1-2aI_1)\,\mu + 4I_1\,(1+I_1) = 0 \; , \tag{12.40}$$

where $I_1 = A_1^2$. Comparing with the ansatz (12.40), we identify $q = \sqrt{\mu}$.

A simple analytical solution of (12.40) exists in the case of a resonant signal, i.e. $\omega_1 = 0$, only, and can be written as

$$a\mu^2 = \frac{1}{\sqrt{2}}\sqrt{-1 + 4aI_1 \pm \sqrt{1 + 8a\,(2a+1)\,I_1}} \; . \tag{12.41}$$

We see from (12.41) that the size of the soliton depends on the diffraction ratio a in a nontrivial way. This is in contrast with previous studies of pattern formation in many nonlinear optical systems (the Lugiato–Lefever approach [13]), where diffraction appears simply as a scale factor in the wavevector, in the form ak^2.

In Fig. 12.11 a comparison between analytical results (dashed curve) and numerical results (continuous curve) for the spatial oscillations of the decaying tail of a domain boundary is given. The peak of the localized structure is omitted. Note that the correspondence is very good, even close to the domain boundary (the line of zero intensity). In this particular case, four minima of the intensity are visible. The opposite segment of a dark ring can be locked by each of the minima. Obviously, the soliton of minimum size, locked by the first maximum, which is the strongest, is the most stable one. However, dark rings with larger radii can also be stable.
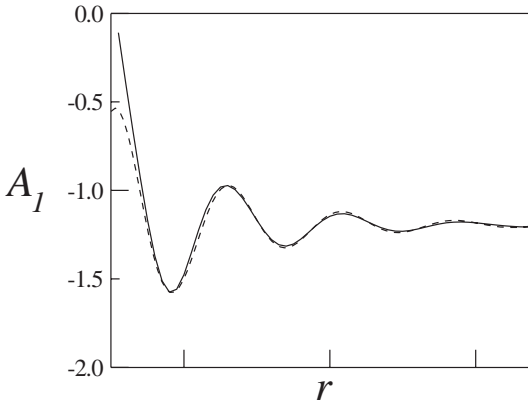
Fig. 12.11. Spatial oscillations of the field outside a soliton, as evaluated numerically (*continuous line*) and analytically from the spatial stability analysis (*dashed line*), for $E = 2.5$, $\omega_1 = 0.5$, $\omega_0 = 0$, $a_1 = 0.00025$ and $a_0 = 0.00125$ ($a = 5$)

The stability range of solitons is limited on one hand by the contraction and annihilation of domains, and on the other hand by either the presence of modulational instabilities (the modulations grow, and fill the whole space) or expansion of domains. Since modulational instabilities are favored by diffraction, it may seem that diffraction has a negative effect on the stability of solitons. However, for pump values at which instabilities are absent, the increase in the modulation of the tails could prevent full contraction, thus contributing to an enhancement of the stability range. Numerical calculations performed for a large pump diffraction parameter show that the stability is always enhanced, at least up to some value of the pump parameter.

The presence of strong modulations in the tails also allows the formation of more complex structures, in the form of bound states of single solitons, or "molecules" of light. Some examples of molecules of varying complexity are shown in Fig. 12.12. Examples with two and three maxima are shown in Figs. 12.12a,b, and a chain composed of five maxima is shown in Fig. 12.12c.
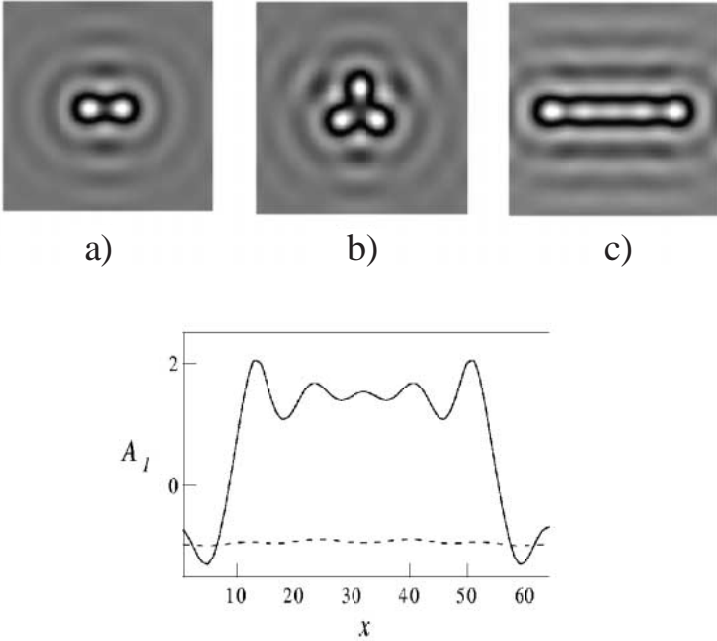
Fig. 12.12. Several bound states (molecules) of solitons, obtained for $a = 5$, $E = 2.5$, $\omega_1 = 0.5$, $\omega_0 = 0$: (**a**) Double; (**b**) triple; (**c**) a chain. The field amplitude along a cross section $y = 0$ of the chain is shown the graph by the *solid line*. The *dashed line* represents a section across the space outside the dark line

The internal structure of the chain shown in Fig. 12.12c is more clearly visible in a section along the middle ($y = 32$). Five maxima at equidistant points are seen. The field along a line outside the domain boundary is given by the dashed line, evaluated at $y = 20$.

In all cases, the large value of the pump diffraction parameter is responsible for the stability of such complex structures, by amplifying the spatial oscillations and thus preventing their collapse. To show this, we have followed the evolution of the soliton "molecules" shown in Figs. 12.12b,c by decreasing the diffraction parameter to $a = 1$ while keeping the other parameters unchanged. The resulting scenario is shown in Fig. 12.13, where the pictures have been taken at equally spaced times. The final state corresponds to a single soliton.
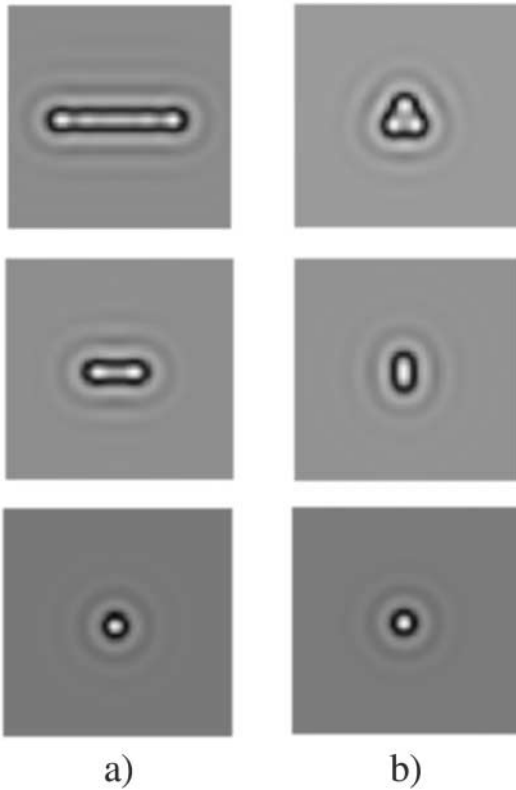
Fig. 12.13. Temporal evolution showing the decay to a single soliton of the molecules shown in Figs. 12.12b,c when the diffraction parameter is decreased to $a = 1$

References

1. A.M. Turing, The chemical basis of morphogenesis, Phil. Trans. R. Soc. London B **237**, 37 (1952). 169
2. M.C. Cross and P.C. Hohenberg, Pattern formation outside of equilibrium, Rev. Mod. Phys. **65**, 851 (1993). 169
3. K. Staliunas, Stabilization of spatial solitons by gain diffusion, Phys. Rev. A **61**, 053813 (2000). 172
4. N.N. Rosanov, *Transverse Patterns in Wide-Aperture Nonlinear Optical Systems*, Progress in Optics, vol. 35, ed. by E. Wolf (North-Holland, Amsterdam, 1996). 175, 176
5. S. Fauve and O. Thual, Solitary waves generated by subcritical instabilities in dissipative systems, Phys. Rev. Lett. **64**, 282 (1990); M. Tlidi, P. Mandel and R. Lefever, Localized structures and localized patterns in optical bistability, Phys. Rev. Lett. **73**, 640 (1994). 176
6. D. Michaelis, U. Peschel and F. Lederer, Multistable localized structures and superlattices in semiconductor optical resonators, Phys. Rev. A **56**, R3366 (1997); M. Brambilla, L.A. Lugiato, F. Prati, L. Spinelli and W.J. Firth, Spatial soliton pixels in semiconductor devices, Phys. Rev. Lett. **79**, 2042 (1997).

7. L.A. Lugiato, C. Oldano, C. Fabre, E. Giacobino and R. Horowicz, Bistability, self-pulsing and chaos in optical parametric oscillators, Nuovo Cimento **10D**, 959 (1988).   180

8. K. Staliunas and V.J. Sánchez-Morcillo, Turing patterns in nonlinear optics, Opt. Commun. **177**, 389 (2000).   181

9. I. Prigogine and R. Lefever, Symmetry breaking instabilities in dissipative systems, J. Chem. Phys. **48**, 1696 (1968).   186

10. V.J. Sánchez-Morcillo and K. Staliunas, Role of pump diffraction on the stability of localized structures in degenerate optical parametric oscillators, Phys. Rev. E. **61**, 7076 (2000).   187, 188

11. G.L. Oppo, A.J. Scroggie and W.J. Firth, From domain walls to localized structures in degenerate optical parametric oscillators, J. Opt. B: Quantum Semiclass. Opt. **1**, 133 (1999).   188

12. G.T. Dee and W. van Saarloos, Bistable systems with propagating fronts leading to pattern formation, Phys. Rev. Lett. **60**, 2641 (1988).   188

13. L.A. Lugiato and R. Lefever, Spatial dissipative structures in passive optical systems, Phys. Rev. Lett. **58**, 2209 (1987).   188

13 Three-Dimensional Patterns

In the previous chapters, only 1D and 2D structures of light were investigated; when the fields depend on one or two transverse spatial coordinates and evolve slowly in time. A single family of longitudinal modes was assumed in the theoretical models, where the fields change negligibly along length of the resonator. The experimental measurements were also 2D; the two-dimensional distributions were recorded with a video camera. Very little is known about three-dimensional spatial light structures of the fields associated with the simultaneous emission of a large number of longitudinal and transverse modes of the resonator. Some analysis of 3D Turing structures has been done in [1] for nonoptical systems, and recently in [2] for lasers.

Emmision of multiple longitudinal modes can occur in lasers and other nonlinear optical systems when the gain line is broader than the free spectral range of the resonator. The gain line for OPOs (the line of phase synchronism) is usually very broad, and therefore this system is suited very well for generating 3D structures. The case of degenerate OPOs is the main case discussed in this chapter; we restrict our considerations of the nondegenerate case and other nonlinear optical systems to a short discussion at the end of the chapter.

13.1 The Synchronously Pumped DOPO

For simplicity, a synchronously pumped DOPO, as sketched in Fig. 13.1, is discussed here. 3D subharmonic pulses travel around a resonator filled with a medium with a second-order nonlinearity, being feed from the energy of a sequence of pump pulses. The pump pulses are resonant: a new pump pulse meets a resonating subharmonic pulse at the entrance of the nonlinear crystal on each resonator round trip. 3D structures are expected to reside within the propagating subharmonic pulses. We show below that the spatio-temporal dynamics of the field within the resonating pulses are governed by a 3D Swift–Hohenberg (SH) equation. We then analyze 3D extended (periodic) and localized structures as solutions of the order parameter equation.

The model of a synchronously pumped DOPO is used for simplicity and clarity only. It covers pump pulses of infinitely long duration, which corresponds to continuous pumping. The model of a continuously pumped DOPO

Synchronously pumped   OPO:
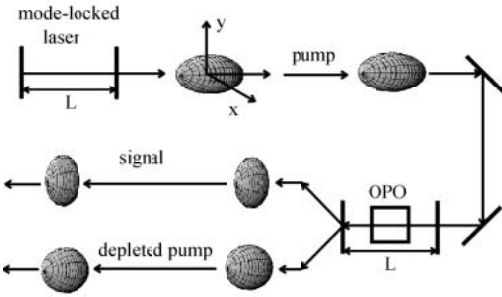
cw-pumped OPO:

Fig. 13.1. Schematic illustration of a synchronously pumped (*left*) and continuously pumped (*right*) degenerate optical parametric oscillator
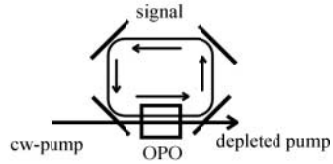
is also shown in Fig. 13.1. Therefore the analysis applies for synchronously and continuously pumped DOPOs.

The interaction of the three-dimensional slowly varying envelopes of the 3D pump and subharmonic pulses, $A_0(\boldsymbol{r}_\perp, \tau, z)$ and $A_1(\boldsymbol{r}_\perp, \tau, z)$, respectively, is described by the following set of equations:

$$\frac{\partial A_0}{\partial z} = \mathrm{i}a_{\parallel,0}\frac{\partial^2 A_0}{\partial \tau^2} + \mathrm{i}a_{\perp,0}\nabla_\perp^2 A_0 - \chi A_1^2 \, , \tag{13.1a}$$

$$\frac{\partial A_1}{\partial z} = (v_0 - v_1)\frac{\partial A_1}{\partial \tau} + \mathrm{i}a_{\parallel,1}\frac{\partial^2 A_1}{\partial \tau^2} + \mathrm{i}a_{\perp,1}\nabla_\perp^2 A_1 + \chi A_0 A_1^* \, . \tag{13.1b}$$

Here $v_j = \partial k_j/\partial\omega_j$ are the group velocities for the pump ($j = 0$) and subharmonic ($j = 1$) waves, $a_{\parallel,j} = \partial k_j/\partial\omega_j$ are the longitudinal dispersion coefficients, $a_{\perp,j} = 1/2k_j$ are the transverse diffraction coefficients, and χ is the nonlinear coupling coefficient. Evolution occurs along z, the longitudinal coordinate. The fields are defined in the 2D transverse space $\boldsymbol{r}_\perp = (x, y)$, in which the Laplace operator $\nabla_\perp^2 = \partial^2/\partial x^2 + \partial^2/\partial y^2$ acts, and in the longitudinal space τ, representing a retarded time in a frame propagating with the group velocity of the pump pulses.

The changes of the fields during one resonator round trip are assumed to be small. This allows us, first, to obtain a mapping describing the discrete changes of the subharmonic pulse in successive resonator round trips. Second, it allows us to replace the discrete mapping by a continuous evolution, and thus to obtain an order parameter equation in the form of a partial differential equation.

13.1.1 Order Parameter Equation

Diffractive and dispersive changes of the pump are neglected during the propagation over the crystal length Δl, which is assumed to be small com-

pared with the total length of the resonator L. Assuming that the subharmonic field changes negligibly along the crystal, i.e. $A_1(\boldsymbol{r}_\perp, \tau, z) \approx A_1(\boldsymbol{r}_\perp, \tau)$, (13.1a) can be integrated to give

$$A_0(\boldsymbol{r}_\perp, \tau, z) = A_0(\boldsymbol{r}_\perp, \tau, 0) - \chi A_1^2(\boldsymbol{r}_\perp, \tau) \, z \;. \tag{13.2}$$

The mean value of the pump envelope is then given by

$$A_0(\boldsymbol{r}_\perp, \tau, z) = A_0(\boldsymbol{r}_\perp, \tau, 0) - \chi A_1^2(\boldsymbol{r}_\perp, \tau) \frac{\Delta l}{2}. \tag{13.3}$$

This approximation of the mean pump value (13.3) allows us to obtain a mapping of the subharmonic pulse for successive resonator round trips. Taking into account the nonlinear interaction in the crystal (13.1a), the diffractive propagation in the resonator, the losses in the mirrors α_1, and the phase shift $\Delta\varphi$ due to resonator length detuning, we obtain the following mapping:

$$A_{1,(n+1)} = A_{1,(n)} + (\nu_0 - \nu_1) \, \Delta l \frac{\partial A_{1,(n)}}{\partial \tau} + \mathrm{i} \, \Delta A_{1,(n)} - \alpha_1 A_{1,(n)} \tag{13.4}$$

$$+ \mathrm{i} a_{\parallel,1} \, \Delta l \frac{\partial^2 A_{1,(n)}}{\partial \tau^2} + \mathrm{i} a_{\perp,1} L \, \nabla_\perp^2 A_{1,(n)} + \chi \, \Delta l \left(A_0 - \chi \frac{\Delta l}{2} A_{1,(n)}^2 \right) A_{1,(n)}^* \;.$$

Dispersion is assumed to occur in the nonlinear crystal only. In contrast, diffraction occurs throughout the propagation over the whole resonator length L.

The mapping (13.4) can be transformed into a continuous evolution in time t (where $t = nL\alpha_1/c$ is normalized to the photon lifetime in the resonator). After renormalizing the fields, one obtains

$$\frac{\partial A}{\partial t} = P A^* - A + \mathrm{i}(\nabla^2 + \Delta)A - |A|^2 A \;, \tag{13.5}$$

which is a parametrically driven Ginzburg–Landau equation similar to that obtained for the corresponding problem in 2D [3, 4]. In (13.5) we have made the following changes of variables:

$$P(\boldsymbol{r}_\perp, \eta) = A_0(\boldsymbol{r}_\perp, \eta, 0)\chi \frac{\Delta l}{\alpha_1} \;, \tag{13.6a}$$

$$A(\boldsymbol{r}_\perp, \tau, \eta) = A_1(\boldsymbol{r}_\perp, \eta, t)\chi \frac{\Delta l}{\sqrt{2}} \;, \tag{13.6b}$$

$$(X, Y) = (x, y) \sqrt{\frac{\alpha_1}{d_\perp L}} \;, \quad \eta = \tau \sqrt{\frac{\alpha_1}{d_\parallel \Delta l}} \;, \quad \Delta = \frac{\Delta\varphi}{\alpha_1} \;. \tag{13.6c}$$

The 3D Laplace operator $\nabla^2 = \partial^2/\partial X^2 + \partial^2/\partial Y^2 + \partial^2/\partial \eta^2$ is calculated in a coordinate frame propagating with the subharmonic pulse, $\boldsymbol{r} = (X, Y, \eta)$.

A further simplification of (13.5) is possible for a pump value close to the generation threshold ($|P - 1| \ll 1$). This can be done by adiabatically eliminating the small imaginary part of the field, as in [3]. Applying directly

the derivation procedure for the 2D case from [3] to the 3D parametrically driven Ginzburg–Landau equation, we obtain

$$\frac{\partial A}{\partial t} = (P - 1)A - \frac{1}{2}(\nabla^2 + \Delta)^2 A - A^3 \, , \tag{13.7}$$

which is a real Swift–Hohenberg equation in 3D.

The spatio-temporal structure of the pump pulses is included in $P(\boldsymbol{r}, t)$, and therefore (13.7) is valid for both synchronously and continuously pumped OPOs. The boundary conditions in the lateral coordinates depend on the details of the experiment: for example, the aperture of the resonator implies boundaries where the fields are zero, and systems with an infinitely broad aperture (and pump profile) require no lateral boundaries at all. In the longitudinal direction, periodic boundaries must be used, corresponding to a periodic repetition of the pattern.

Further, in the analytical treatment of the patterns, a pump that is homogeneous in 3D is assumed. This assumption is legitimate when the typical size of the spatial structures is much smaller than the spatial size of the pump pulse. This occurs for a sufficiently broad pump beam ($|\partial P/\partial X|, |\partial P/\partial Y| \ll |P|$) and also for a sufficiently long pump pulse ($|\partial P/\partial \eta| \ll |P|$). Under these conditions, one can consider the pump parameter to be constant in the central region of the pulse. This allows us to scale out the pump parameter and write (13.7) in the form

$$\frac{\partial A}{\partial t} = A - (\nabla^2 + \Delta)^2 A - A^3 \, , \tag{13.8}$$

which has only one free parameter, the detuning Δ.

The validity of the linear part of (13.7) can be tested by comparison of the spectrum of the Lyapunov growth exponents calculated from (13.7), with the round-trip increments of the fields calculated from (13.1) and (13.3). Such a comparison shows that (13.7) describes well the linear pattern-forming properties (transverse wavenumber selection) of a DOPO not only near the threshold, where $(P - 1) \ll 1$, where (13.7) is strictly mathematically valid, but also moderately above the threshold, where $(P - 1) \approx \mathcal{O}(1)$.

13.2 Patterns Obtained from the 3D Swift–Hohenberg Equation

In the limit of small detuning, a homogeneous distribution with amplitude $|A| = \pm\sqrt{1 - \Delta^2}$ and one of two phase values, $\varphi = (0, \pi)$, is a stable solution of the 3D SH equation (13.8). However, in a transient stage of the evolution, if one starts from a random field distribution, the subharmonic field can consist of separated domains, each with one of two phase values. The phase domains in 2D patterns are separated by domain boundaries (or dark switching waves),
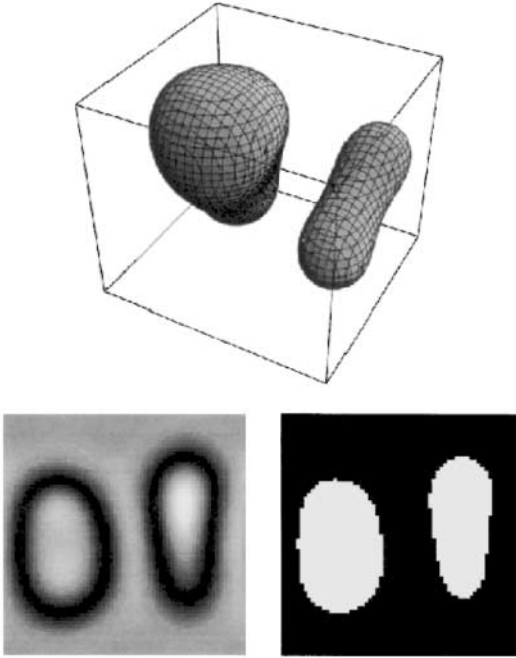
Fig. 13.2. Phase domains as obtained by numerical integration of (13.8), depicted by surfaces of zero field. At the *bottom* a 2D section is shown, showing the field intensity (*left*), and the field phase (*right*). The detuning is $\Delta = 0.4$. Periodic boundaries were used on a box of size $\Delta x = \Delta y = \Delta \eta = 20$

as analyzed in Chap. 11. Analogously, similar 3D domains exist, separated by 2D domain walls.

A numerical integration of the 3D SH equation (13.8) was performed to test the idea of domains in 3D. A split-step technique was used on a spatial grid of $32 \times 32 \times 32$ points. The result is showm in Fig. 13.2 for a particular time in the transient evolution. Two domains of uniform phase, embedded in a background of the opposite phase, are apparent.

The dynamics of the 3D domains depend on the detuning parameter in a similar way to those of 2D domains (see Chap. 11). A negative or small positive detuning leads to the contraction and eventual disappearance of domains. A large positive detuning leads to the growth of domains and formation of a 3D "labyrinth" structure, as discussed below. However, in a particular detuning range the contracting domains can stabilize at a particular size. In this case we obtain spherically symmetric, stable "bubbles", which are the localized structures (spatial solitons) of the 3D SH equation. Such an ensemble of stable bubbles is shown in Fig. 13.3, as obtained numerically.

The stability limits of the spatial solitons were analyzed, by solving the 3D SH equation (13.8) numerically. The bubbles are stable in the interval
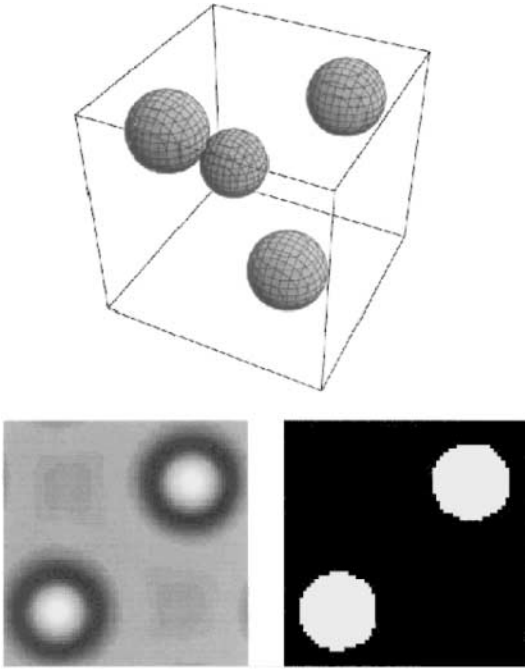
Fig. 13.3. 3D spatial phase solitons (bubbles). The same conditions as in Fig. 13.2 were used, except for the detuning value $\Delta = 0.45$

$0.430 < \Delta < 0.460$. This stability range is much narrower than that for the corresponding dark rings in 2D found in Chap. 11, which is $0.287 < \Delta < 0.460$.

Large detuning values lead to periodic patterns with a dominant nonzero spatial wavenumber $|\boldsymbol{k}| = \sqrt{\Delta}$. In two dimensions, a parallel stripe pattern occurs and has a spatial distribution $A(\boldsymbol{r}) \approx \sqrt{4/3}\cos(\boldsymbol{k}\boldsymbol{r})$. Hexagonal patterns are not supported by the SH equation in 2D, since the nonlinearity is purely cubic here. (It is known that a square nonlinearity is necessary for supporting stable hexagons, unless an additional neutral mode is included.) A direct continuation to the 3D case gives the analogue of a stripe pattern, a standing-wave pattern also called "lamellae". However, besides lamellae another stable periodic structure is possible in 3D, a structure made up of four resonant standing waves, with wavevectors as illustrated in Fig. 13.4a,

$$A(\boldsymbol{r}) \approx \sum_{j=1,4} \left(A_j e^{\mathrm{i}\boldsymbol{k}_j \boldsymbol{r}} + \text{c.c.} \right) . \tag{13.9}$$

The four $\boldsymbol{k}$-resonant standing waves, for which $|\boldsymbol{k}_j| = \sqrt{\Delta}$, do not lie in the same plane, and thus such a tetrahedral structure can exist only in 3D space. The phases of the four nonplanar standing waves, with complex
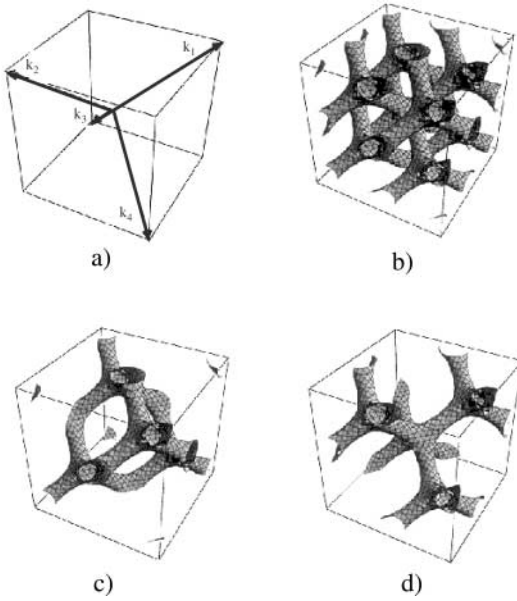
Fig. 13.4. (a) $\boldsymbol{k}$-resonant wavevectors forming a tetrahedral structure. **(b)** Isolines at 85% of maximum field intensity, and isolines at **(c)** 93% and **(d)** −93% of maximum amplitude, obtained by numerical integration of the 3D SH equation for $\Delta = 1.2$ and a box size $\Delta x = \Delta y = \Delta \eta = 10$

amplitudes $A_j = |A_j| e^{i\varphi_j}$, obey

$$\varphi = \sum_{j=1,4} \varphi_j = \pi \ . \tag{13.10}$$

A stability analysis shows that both lamellae and tetrahedral structure are stable. For the stability analysis, a variational potential for (13.8) was calculated, namely

$$F = \int \left(-\frac{A^2}{2} + \frac{A^4}{4} \right) \mathrm{d}\boldsymbol{r} \ . \tag{13.11}$$

Note that Laplace operators do not appear in the variational potential, if we are dealing with the $\boldsymbol{k}$-resonant structures.

Calculation of the variational potential yields the potential minima associated with these structures in the parameter space of A_j. The minimum values of the potential are $F_1 = -1/6 = -0.1666...$ for lamellae, and $F_4 = -2/15 = -0.1333...$ for the tetrahedral structure. Lamellae are thus more stable than the tetrahedral structure. For comparison, the 3D continuations of the resonant square pattern, and of the hexagonal pattern have potentials $F_2 = -1/10 = -0.1$ and $F_3 = -1/9 = -0.1111...$, respectively.

However, these unstable patterns correspond not to local potential minima in the parameter space of A_j but to saddle points.

Numerical integration of (13.8) confirms the stability of the tetrahedral structure. The numerical results are given in Fig. 13.4b, in the form of isolines at 85% of the maximum field intensity. This intensity structure actually consists of two nested structures, shown in Fig. 13.4c and Fig. 13.4d, where the isolines at 93% of the maximum and minimum amplitude are plotted.

13.3 The Nondegenerate OPO

In the case of a nondegenerate OPO, the interaction between the slowly varying envelope of the 3D pump, signal and idler pulses, $A_0(\boldsymbol{r}_\perp, \tau, z)$, $A_1(\boldsymbol{r}_\perp, \tau, z)$ and $A_2(\boldsymbol{r}_\perp, \tau, z)$, respectively, must be considered. This is described by the following set of equations:

$$\frac{\partial A_0}{\partial z} = \mathrm{i}a_{\parallel,0}\frac{\partial^2 A_0}{\partial \tau^2} + \mathrm{i}a_{\perp,0}\,\nabla_\perp^2 A_0 - \chi A_1 A_2 \; , \tag{13.12a}$$

$$\frac{\partial A_1}{\partial z} = (v_0 - v_1)\frac{\partial A_1}{\partial \tau} + \mathrm{i}a_{\parallel,1}\frac{\partial^2 A_1}{\partial \tau^2} + \mathrm{i}a_{\perp,1}\,\nabla_\perp^2 A_1 + \chi A_0 A_2^* \; , \tag{13.12b}$$

$$\frac{\partial A_2}{\partial z} = (v_0 - v_2)\frac{\partial A_2}{\partial \tau} + \mathrm{i}a_{\parallel,2}\frac{\partial^2 A_2}{\partial \tau^2} + \mathrm{i}a_{\perp,2}\,\nabla_\perp^2 A_2 + \chi A_0 A_1^* \; . \tag{13.12c}$$

Here the coefficients are analogous to those in (13.1), but now correspond to the pump ($j = 0$), signal ($j = 1$) and idler ($j = 2$) waves. The assumption that the changes in the fields during one resonator round trip are small may be made as in (13.1), which allows us to obtain a mapping describing the discrete changes of the subharmonic pulse in successive resonator round trips, and to derive equations of continuous evolution (the order parameter equation).

The analogue of (13.3) is

$$A_0(\boldsymbol{r}_\perp, \tau, z) = A_0(\boldsymbol{r}_\perp, \tau, 0) - \chi A_1(\boldsymbol{r}_\perp, \tau) A_2(\boldsymbol{r}_\perp, \tau)\frac{\Delta l}{2} \; , \tag{13.13}$$

and the analogue of (13.5) is

$$\frac{\partial A}{\partial t} + v_1 \frac{\partial A}{\partial \eta} = PB - A + \mathrm{i}(\nabla_1^2 + \Delta_1)A - |B|^2 A \; , \tag{13.14a}$$

$$\frac{\partial B}{\partial t} + v_2 \frac{\partial B}{\partial \eta} = PA - B + \mathrm{i}(\nabla_2^2 + \Delta_2)A - |A|^2 B \; , \tag{13.14b}$$

which is a system of two coupled Ginzburg–Landau equations for the variables

$$A(\boldsymbol{r}_\perp, \tau, z) = A_1(\boldsymbol{r}_\perp, \eta, t)\chi\frac{\Delta l}{\sqrt{2}} \; , \tag{13.15a}$$

$$B(\boldsymbol{r}_\perp, \tau, z) = A_2^*(\boldsymbol{r}_\perp, \eta, t)\chi\frac{\Delta l}{\sqrt{2}} \; . \tag{13.15b}$$

Unlike the case of (13.5), two 3D Laplace operators must be defined if the two waves have different diffraction and/or diffusion coefficients.

A further simplification of (13.14) is possible for equal group velocities of the signal and idler waves. This leads to

$$\frac{\partial A}{\partial t} = (P - 1)A + \mathrm{i}(\nabla_-^2 + \Delta_-)A - \frac{1}{2}(\nabla_+^2 + \Delta_+)^2 A - |A|^2 A ,\quad (13.16)$$

which is the complex Swift–Hohenberg equation in 3D. The resulting detunings depend on the detunings of the signal and idler field components: $\Delta_\pm = \Delta_1 \pm \Delta_2$. The same is true for the resulting components of the Laplace operators.

A numerical integration of (13.16) has been performed. The extended patterns obtained consisted of 3D tilted waves, completely analogous to those in 2D studied in Chap. 5, and also the 3D analogue of the square vortex lattice. The latter consists of a grid of parallel vortex lines with alternating directions. The localized structures obtained here correspond to vortex rings. These vortex rings can stabilize at some equilibrium radius dependent on the value of the detuning parameter. Sometimes these vortex rings can form complicated structures, two of which are shown in Fig. 13.5.

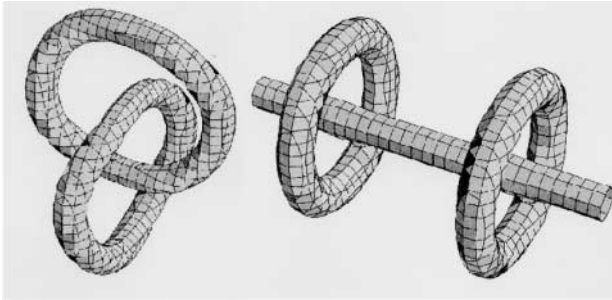**Fig. 13.5.** Stable vortex rings, as obtained by numerical integration of the 3D complex Ginzburg–Landau equation (13.16)

13.4 Conclusions

This investigation of synchronously pumped OPOs leads to the following conclusions.

13.4.1 Tunability of a System with a Broad Gain Band

A DOPO in reality has a very broad gain line width (the line of phase synchronism), typically many orders of magnitude larger than the free spectral

range of the resonator. Nevertheless, variation of the resonator length (on the scale of the optical wavelength) allows one to change the detuning parameter in (13.5) and (13.13), and thus allows the manipulation of the 3D structures.

This seeming paradox can be understood in the following way. The maximum gain for a plane wave of the subharmonic field occurs when its phase has a particular value $\varphi = 0, \pi$ with respect to the pump phase at the entrance of the nonlinear crystal. Tuning of the resonator length breaks the optimum phase relation for the plane wave. Therefore a modulation appears in the subharmonic field, causing a Guoy phase shift, which brings the phase to its optimum value. The Guoy phase shift is proportional to the spatial wavenumber of the modulation appearing. This modulation can appear in the transverse or longitudinal direction, or in both directions simultaneously, resulting in oblique lamellae or a tetrahedral structure.

13.4.2 Analogy Between 2D and 3D Cases

The order parameter equation derived here for a 3D DOPO is analogous to that derived for a DOPO in the 2D case [3]. The only difference is the dimensionality of the problem. This suggests that this analogy between 2D and 3D systems is valid not only for DOPOs, but also for other nonlinear optical systems. A requirement is that the nonlinear processes should be fast compared with the time of light propagation over the typical length scales of the longitudinal modulation. In this case the order parameter equations derived for other nonlinear optical systems in 2D (e.g. externally driven nonlinear resonators containing focusing or defocusing media or saturable absorbers [5]) can be straightforwardly extended to the 3D case, and used to simulate a broad gain line in a synchronously or continuously pumped system. Instead of extended or localized structures in 2D, one should the obtain the corresponding 3D structures, propagating cyclically in the resonator.

The 3D extension of the equations results in the corresponding 3D extension of the structures. the 3D structures that have direct counterparts in 2D are phase domains, localized structures in the form of "bubbles", and lamellar structures. However, the family of 3D structures is richer than that in 2D. An example of a 3D structure that does not have a counterpart in 2D is the resonant tetragonal pattern, which is supported by a cubic nonlinearity.

References

1. A. De Wit, G. Dewel, P. Borckmans and D. Walgraef, Three-dimensional dissipative structures in reaction–diffusion systems, Physica D **61**, 289 (1992).   193
2. N.L. Komarova, B.A. Malomed, J.V. Moloney and A.C. Newell, Resonant quasiperiodic patterns in a three-dimensional lasing medium, Phys. Rev. A **56**, 803 (1997).   193

3. K. Staliunas, Transverse pattern formation in optical parametric oscillators, J. Mod. Opt. **42**, 1261 (1995).   195, 196, 202

4. S. Longhi and A. Geraci, Swift–Hohenberg equation for optical parametric oscillators, Phys. Rev. A **54**, 4581 (1996).   195

5. P. Mandel, M. Georgiou and T. Erneux, Transverse effects in coherently driven nonlinear cavities, Phys. Rev. A **47**, 4277 (1993).   202

14 Patterns and Noise

All of the previous chapters of the book have dealt with patterns in nonlinear resonators in the absence of noise. In reality, noise is always present in experiments. First of all, vacuum noise is inevitable. Noise due to technological limitations is often also present, and causes spatio-temporal fluctuations of the field. Also, the optical elements (e.g. mirrors) always have nonzero roughness of their surfaces, which causes spatial (stationary) noise. Last but not least, the optical elements are of limited size, causing aperture effects, which can also be considered as spatial (constant in time) perturbations of the field.

In the simplest case the influence of noise on the patterns is the following:

1. Above the modulational-instability threshold, where extended ordered patterns are expected (rolls, hexagons, tilted waves or square vortex lattices), noise destroys the long-range order in the pattern. Rolls and other extended structures can still exist in the presence of noise, but may display defects (dislocations or disclinations) with a density proportional to the intensity of the noise [1].
2. Below the modulational-instability threshold, where no patterns are expected in the ideal (noiseless) case, the noise is amplified and can result in (noisy) patterns. The symmetries of the patterns may show themselves even below the pattern formation threshold, thanks to the presence of noise [2]. This can be compared with the case of a single-transverse-mode laser, where the coherence of the radiation develops continuously, and the spectrum of the luminescence narrows continuously when the generation threshold is approached from below.
3. The presence of noise can modify (shift) the threshold of pattern formation [3].

In this chapter, several novel phenomena related to the influence of noise on pattern formation (specifically, stripe-pattern formation) are considered. It is shown that:

- Above the pattern formation threshold, the far field shows singularities asymptotically obeying a k^{-2} law. This is shown concretely for stripe (roll) patterns, where two singularities in the spatial Fourier distribution are present; however, the results may be extended to other patterns. For

example, the far-field distributions of hexagonal patterns show distributions of the form $(\boldsymbol{k} - \boldsymbol{k}_i)^{-2}$, where $\boldsymbol{k}_i$ $(i = 1, ..., 6)$ are the locations of singularities of the far field, arranged on the vertices of a hexagon.

- The spatial power spectra of the noise show a $1/f^\alpha$ distribution, where the exponent α is close to unity, and depends on the dimensionality and symmetry of the pattern.
- The stochastic drift of the patterns is sub-Brownian: it is well known that the stochastic drift of the position of a Brownian particle obeys a square root law,

$$\sqrt{\left\langle x\left(t\right)^2\right\rangle} \propto t^{1/2} \ .$$

We show that the stochastic drift of nonlinear patterns is in general different (weaker) than the Brownian; for example the stripe pattern has a root mean wandering $\propto t^{1/4}$ in the case of one spatial dimension.

The analysis of noisy stripes is performed by solving the stochastic Swift–Hohenberg equation as the order parameter equation for a stripe pattern in a spatially isotropic system [4], or the Newell–Whitehead–Segel equation as an amplitude equation for perturbations of stripe a pattern [5]. However, we start from an analysis of a noisy homogeneous state or, in other words, of a nonzero-temperature condensate. The main results (spatio-temporal spectra) in the case of the condensate (the first part of the chapter), are then applied to calculate the noise properties of stripe patterns.

14.1 Noise in Condensates

An order–disorder transition in a condensate or, in general, in a spatially extended nonlinear system can be described in the lowest order by a complex Ginzburg–Landau equation with a stochastic term:

$$\frac{\partial A}{\partial t} = pA - (1 + \mathrm{i}c)\left|A\right|^2 A + (1 + \mathrm{i}b)\nabla^2 A + \Gamma(\boldsymbol{r}, t) \ . \tag{14.1}$$

Here $A(\boldsymbol{r}, t)$ is a complex-valued order parameter defined in an n-dimensional space $\boldsymbol{r}$, evolving with time t. The control parameter is p (the order–disorder transition occurs at $p = 0$). The Laplace operator $\nabla^2 A$ represents the non-locality in the system, and $\Gamma(\boldsymbol{r}, t)$ is an additive noise, δ-correlated in space and time and of temperature T, such that

$$\langle\Gamma(\boldsymbol{r}_1, t_1)\Gamma^*(\boldsymbol{r}_2, t_2)\rangle = 2T\,\delta(\boldsymbol{r}_1 - \boldsymbol{r}_2)\delta(t_1 - t_2) \ . \tag{14.2}$$

Below the transition threshold ($p < 0$), the CGL equation (14.1) yields a disordered state: the order parameter $A(\boldsymbol{r}, t)$ is essentially noise filtered in space and time, with an exponential (thermal) intensity distribution. Above

the transition threshold ($p > 0$), (14.1) yields an ordered, or coherent, state (or a condensate) in modulationally stable cases, with the intensity distributed around its mean value $\left\langle |A|^2 \right\rangle = p$.

The CGL equation (14.1), with complex-valued coefficients, has been investigated in the previous chapters to describe the dynamics of optical vortices in the case of zero or negative detuning. Here, however, we consider the CGL equation as a universal model describing an order–disorder phase transition. The first two terms, $pA - |A|^2 A$, approximate to the lowest order a supercritical Hopf bifurcation, a bifurcation that brings the system from a trivial state to a state with phase invariance of the order parameter $A(\boldsymbol{r}, t)$. The complex-valued character of the order parameter is important, since every ordered, or coherent, state, both in classical and in quantum mechanics, is characterized not only by the modulus of the order parameter, but also by its phase. The diffusion term $\nabla^2 A$ describes the simplest possible nonlocality term in a spatially isotropic and translationally invariant system.

The real Ginzburg–Landau equation was introduced [6] as the normal form for a second-order phase transition between two arbitrary spatially extended states and can be derived systematically for many systems, as well as phenomenologically from symmetry considerations. The real Ginzburg–Landau equation does not contain information about the coherence properties of the system. Thus, analogously, we try to find a simple model for the order–disorder phase transition, a normal form that can be derived systematically for particular systems, as well as phenomenologically from symmetry considerations. The complex Ginzburg–Landau equation is just that. It describes, as a normal form, systems characterized by (1) a supercritical phase transition between a disordered and an ordered state, (2) phase invariance of the order parameter, and (3) isotropy and homogeneity in space.

14.1.1 Spatio-Temporal Noise Spectra

For the analytical treatment, we assume that the system is sufficiently far above the order–disorder transition, i.e. $p >> T$. Then the homogeneous component $|A_0| = \sqrt{p}$ dominates, and we can look for a solution of (14.1) in the form of a perturbed homogeneous state, $A(\boldsymbol{r}, t) = A_0 + a(\boldsymbol{r}, t)$. After linearization of (14.1) around A_0 and diagonalisation, we obtain the linear stochastic equations for the amplitude and phase perturbations, $b_+ = (a + a^*)/\sqrt{2}$ and $b_- = (a - a^*)/\sqrt{2}$, respectively:

$$\frac{\partial b_+}{\partial t} = -2pb_+ + \nabla^2 b_+ + \Gamma_+(\boldsymbol{r}, t) , \tag{14.3a}$$

$$\frac{\partial b_-}{\partial t} = \nabla^2 b_- + \Gamma_-(\boldsymbol{r}, t) . \tag{14.3b}$$

Equation (14.3a) gives the evolution of the amplitude fluctuations b_+, which decay at a rate $\lambda_+ = -2p - k^2$ (where k is the spatial wavenumber

of the perturbation). Asymptotically, long-lived amplitude perturbations are possible only at the Hopf bifurcation point (in the critical state), but never above or below it. Equation (14.3b) is the equation for phase fluctuations b_- which decay at a rate $\lambda_- = -k^2$ above the Hopf bifurcation point. This means that the long-wavelength modes decay asymptotically slowly, with a decay rate approaching zero as $k \to 0$, which is a consequence of the phase invariance of the system. The phase, as a result, is in a critical state for all $p > 0$.

From (14.3) one can calculate the spatio-temporal noise spectra, by rewriting (14.3) in terms of the spatial and temporal Fourier components,

$$b_\pm(\boldsymbol{r}, t) = \int b_\pm(\boldsymbol{k}, \omega) \mathrm{e}^{\mathrm{i}\omega t - \mathrm{i}\boldsymbol{k}\boldsymbol{r}} \, \mathrm{d}\omega \, \mathrm{d}\boldsymbol{k} \;, \tag{14.4}$$

where the coefficients of the fourier components follow directly from (14.5):

$$b_+(k, \omega) = \frac{\Gamma_+(k, \omega)}{\mathrm{i}\omega + k^2 + 2p} \;, \tag{14.5a}$$

$$b_-(k, \omega) = \frac{\Gamma_-(k, \omega)}{\mathrm{i}\omega + k^2} \;. \tag{14.5b}$$

The coefficients of the spatio-temporal power spectra (sometimes called the "structure function") are

$$S_+(\boldsymbol{k}, \omega) = |b_+(\boldsymbol{k}, \omega)|^2 = \frac{|\Gamma_+(\boldsymbol{k}, \omega)|^2}{\omega^2 + (2p + k^2)^2} \;, \tag{14.6a}$$

$$S_-(\boldsymbol{k}, \omega) = |b_-(\boldsymbol{k}, \omega)|^2 = \frac{|\Gamma_-(\boldsymbol{k}, \omega)|^2}{\omega^2 + k^4} \;, \tag{14.6b}$$

for the amplitude and phase fluctuations, respectively. If we assume δ-correlated noise in space and time, $|\Gamma_\pm(\boldsymbol{k}, \omega)|^2$ are simply proportional to the temperature T of the random force.

Spatial Power Spectra. The spatial spectra are obtained by integration of (14.6) over all the temporal frequencies ω:

$$S(\boldsymbol{k}) = S_+(\boldsymbol{k}) + S_-(\boldsymbol{k}) = \int S_+(\boldsymbol{k}, \omega) \, \mathrm{d}\omega + \int S_-(\boldsymbol{k}, \omega) \, \mathrm{d}\omega \;. \tag{14.7}$$

The total power spectrum here is the sum of the power spectrum of the amplitude, $S_+(\boldsymbol{k})$, and that of the phase, $S_-(\boldsymbol{k})$, since the spectral components $b_\pm(\boldsymbol{r}, t)$ are mutually uncorrelated, as follows from (14.5). For clariry, the integration is performed here separately for the amplitude and phase fluctuations, and yields

$$S_+(k) = \int_{-\infty}^{+\infty} \frac{T}{\omega^2 + (k^2 + 2p)^2} \mathrm{d}\omega = \frac{T\pi}{k^2 + 2p} \;, \tag{14.8a}$$

$$S_-(k) = \int_{-\infty}^{+\infty} \frac{T}{\omega^2 + k^4} \mathrm{d}\omega = \frac{T\pi}{k^2} \;. \tag{14.8b}$$

This means that the spectrum of phase fluctuations is of the form $1/k^2$ (14.8b). The spatial spectrum of amplitude fluctuations is Lorentzian: in the short-wavelength limit, $|k|^2 \gg 2p$, the amplitude spectrum is equal to the phase spectrum, i.e. $S_+(k) = S_-(k)$. The total spectrum is then $S(k) = 2S_+(k)$ in the short-wavelength limit. In the long-wavelength limit $|k|^2 \ll 2p$, the amplitude fluctuation power spectrum saturates at $S_+(k \approx 0) = T\pi/2p$, and is negligibly small compared with phase fluctuation spectrum. Therefore the total spectrum is essentially determined by the phase fluctuations in this long-wavelength limit.

Temporal Power Spectra. The temporal power spectra are obtained by integration of (14.6) over all possible spatial wavevectors $\boldsymbol{k}$. In the case of one spatial dimension,

$$S_{+1\mathrm{D}}(\omega) = \int_{-\infty}^{\infty} \frac{T}{\omega^2 + (2p + k^2)^2}\,\mathrm{d}k = \frac{T\pi}{\omega}\,\mathrm{Im}\left[(2p - \mathrm{i}\omega)^{-1/2}\right], \qquad (14.9\mathrm{a})$$

$$S_{-1\mathrm{D}}(\omega) = \int_{-\infty}^{\infty} \frac{T}{\omega^2 + k^4}\,\mathrm{d}k = \frac{T\pi}{2^{1/2}\omega^{3/2}}\ . \qquad (14.9\mathrm{b})$$

This results in a power spectrum of phase fluctuations (14.9b) of precisely the form $\omega^{-3/2}$ over the entire frequency range. The spectrum of amplitude fluctuations (14.9a) is more complicated: in the limit of large frequencies $|\omega| \gg 2p$ it is equal to the phase spectrum, i.e. $S_{+1\mathrm{D}}(\omega) = S_{-1\mathrm{D}}(\omega)$. In the limit of small frequencies $|\omega| \ll 2p$, the amplitude power spectrum saturates at

$$S_{+1\mathrm{D}}(\omega \approx 0) = \frac{T\pi}{2\,(2p)^{3/2}}\ , \quad |\omega| \ll 2p\ . \qquad (14.10)$$

In this way, (14.9a) represents a Lorentz-like spectrum (with an $\omega^{-3/2}$ frequency dependence) for the amplitude fluctuations of a system extended in one-dimensional space.

Integration of (14.6) in two spatial dimensions yields

$$S_{+2\mathrm{D}}(\omega) = \frac{T\pi}{2\omega}\left(\pi - 2\arctan\frac{2p}{\omega}\right), \quad S_{-2\mathrm{D}}(\omega) = \frac{T\pi^2 2^{1/2}}{2\omega}\ . \qquad (14.11)$$

This results in a power spectrum of the phase fluctuations of the form $1/\omega$ over the entire frequency range, and in a Lorentz-like spectrum of the amplitude fluctuations with an ω^{-1} frequency dependence.

Finally, integration of (14.6) in three spatial dimensions yields

$$S_{+3\mathrm{D}}(\omega) = \frac{2T\pi^2}{\omega}\,\mathrm{Im}\left[(2p + \mathrm{i}\omega)^{1/2}\right], \quad S_{-3\mathrm{D}}(\omega) = \frac{T\pi^2 2^{1/2}}{\omega^{1/2}}\ . \qquad (14.12)$$

This results in an exponent $1/2$ of the Lorentz-like amplitude and phase power spectra.

Generalizing, the power spectrum of phase fluctuations for a D-dimensional systems (e.g. for a fractal-dimensional system) is of the form $S_{-D}(\omega) \approx \omega^{-\alpha}$ where $\alpha = 2 - D/2$. For the amplitude fluctuations, one obtains a Lorentz-like power spectrum, saturating for low frequencies, and with an $\omega^{-\alpha}$ dependence for high frequencies. The width of the Lorentz-like power spectrum of amplitude fluctuations depends on the supercriticality parameter p: $\omega_0 \approx 2|p|$.

14.1.2 Numerical Results

The spectral densities (14.8)–(14.12) calculated from the linearization were compared with densities obtained directly by numerical integration of the CGL equation (14.1) in one, two and three spatial dimensions. A CGL equation with real-valued coefficients $b = c = 0$ was numerically integrated with a supercriticality parameter $p = 1$.

Temporal Power Spectra. The numerically calculated temporal power spectra are plotted in Fig. 14.1. The $1/\omega^\alpha$ character of the noise spectra is most clearly seen in the case of a 1D system (here $\alpha = 3/2$). In two dimensions the $1/\omega^\alpha$ noise ($\alpha = 1$) is visible over almost three decades of frequency, and in three dimensions ($\alpha = 1/2$) over almost two decades. The dashed lines in Fig. 14.1 indicate the expected slopes.
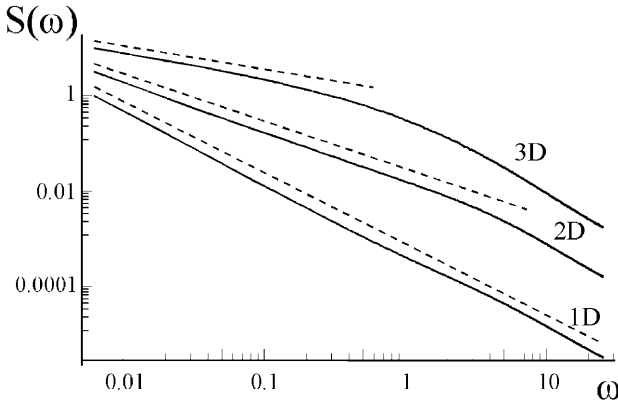

Fig. 14.1. Total temporal power spectra of the noise in one, two and three spatial dimensions, as obtained by numerical integration of the CGL equation. The *dashed lines* show the slopes $\alpha = 1/2$, $\alpha = 1$ and $\alpha = 3/2$. The spectra are arbitrary displaced vertically to distinguish between them. The integration period was $t = 1000$, and averaging was performed over 2500 realizations

The main obstacle to calculating the noise spectra numerically over the entire frequency range is the discretization of the spatial coordinates and of the

time in the integration scheme. Discretization of space imposes a truncation of the higher spatial wavenumbers, and thus affects the high-frequency components of the temporal spectra. Therefore, to obtain numerically the spectra over the entire frequency range, a series of separate calculations for different integration regions was performed, and the spectra in the corresponding frequency ranges were combined into one plot. The calculations shown Fig. 14.2 were performed for the 2D case with four different sizes of integration regions $l = l_n = 2\pi \times 10^{2.5-n/2}$ ($n = 1, 2, 3, 4$). The spectrum constructed by combining partially overlapping pieces results in a $1/\omega$ dependence extending over more than five decades in frequency. A "kink" separating the low-frequency range (where the amplitude fluctuations are negligible compared with the phase fluctuations) and the high-frequency range (where the amplitude fluctuations are equal to the phase fluctuations) is visible in the power spectrum in Fig. 14.2a, and especially in the normalized power spectrum $\omega S(\omega)$ in Fig. 14.2b.
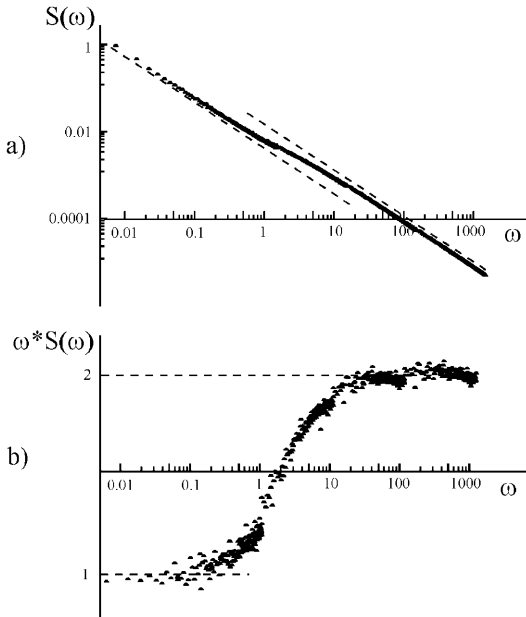
Fig. 14.2. Total temporal power spectra of noise in 2D, as obtained by numerical integration of the CGL equation. The integration period was 10^7 temporal steps; averaging was performed over 2500 realizations. The calculations were performed with four different sizes of the integration region with different temporal steps

A multiscale numerical integration of the CGL equation in 1D and 3D was also performed. This showed the $1/\omega^{3/2}$ and $1/\omega^{1/2}$ dependences, respectively, over more than five decades of frequency (not shown).

Spatial Power Spectra. Numerical discretization also distorts the spatial spectra, since it restricts the range of spatial wavenumbers. Therefore we also performed a series of calculations with different sizes of integration region, and combined the calculated averaged spatial spectra into one plot. The results shown in Fig. 14.3 (2D case) were calculated with five different sizes of the integration region $l = l_n = 2\pi \times 10^{2.5-n/2}$ ($n = 1, ..., 5$). In this way we obtained spectra by combining partially overlapping pieces, extending in total over around four decades.

Figure 14.3a shows the spectra on a $\log - \log$ scale, where a $1/k^2$ character can be clearly seen, especially in the limits of long and short wavelengths. A "kink" at intermediate values of k, most clearly seen in Fig. 14.3b, joins spectra in the limits of long and short wavelengths which are both of the same slope but of different intensities.

One more reason to construct the spectra by combining pieces calculated separately is the finite size of the temporal step used in the split-step numerical technique. In order to obtain the correct spatial spectra in the long-wavelength limit, a time-consuming integration is required. The long waves
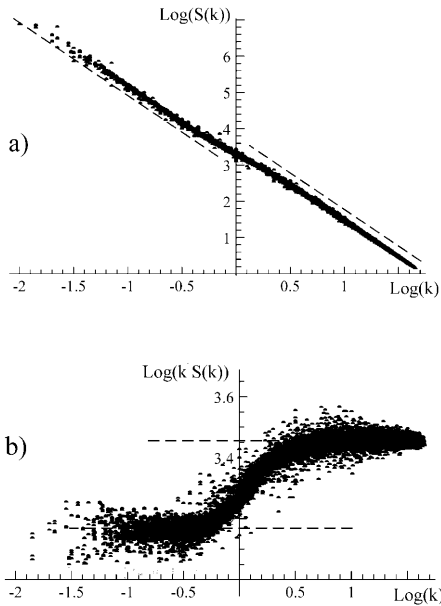
Fig. 14.3. Total spatial power spectra of noise in two spatial dimensions, as obtained by numerical integration of the CGL equation. Averaging was performed over the time of the temporal steps. Each point corresponds to the averaged intensity of a discrete spatial mode. The calculations were performed with five different values of the size of the integration region, with different temporal steps. These spectra were combined into one plot. The *dashed lines* correspond to a $1/k^2$ dependence and are to guide the eye

are very slow, the characteristic buildup time being of the order of $\tau_b \approx 1/k^2$, as can be seen from (14.6) and (14.8), and this time diverges as $k \to 0$. Thus one has to average for a very long time to obtain the correct statistics for the long waves. On the other hand, the characteristic buildup times for short wavelengths are very small, since the same relation $\tau_b \approx 1/k^2$ holds. Here, correspondingly, in order to obtain the correct statistics of the mode occupation, one has to decrease the size of the temporal step as $k \to \infty$. We thus come to the conclusion that one can never obtain the analytically predicted (correct) $1/k^2$ statistical distribution in a single numerical run with finite temporal steps (i.e. with a limited time resolution). A spectrum calculated with a fixed temporal step is shown in Fig. 14.4. In a $\log - \log$ representation (Fig. 14.4a), a sharp decrease of the occupation of the large wavenumbers occurs. In a representation of the logarithm of the spectral density versus k^2 (Fig. 14.4b), a straight line indicating an exponential decrease is obtained for large wavenumbers. The spectrum shown in Fig. 14.4, curiously enough, is thus precisely a Bose–Einstein distribution, which decays with a power law for long wavelengths, i.e. $S(k \to 0) \propto k^{-2}$, and exponentially for short wavelengths, i.e. $S(k \to \infty) \propto \exp(k^{-2})$.
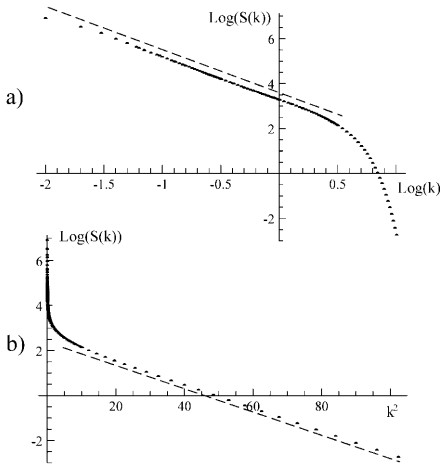
Fig. 14.4. The total spatial spectrum as obtained by numerical integration of the CGL equation in 1D for a fixed temporal step of $\Delta t = 0.05$, but combined from four calculations with different sizes of integration region. Averaging was performed over a time $t = 10^6$. Plot (**a**) shows the spectrum in a $\log - \log$ representation, and the *dashed line* corresponds to a $1/k^2$ dependence, and (**b**) shows the spectrum in a single-log representation and the *dashed line* corresponds to an $\exp(-k^2)$ dependence

We note that the linear stability analysis does not lead to the Bose–Einstein distribution found numerically with finite temporal steps. The finite

temporal step Δt is equivalent to a particular cutoff frequency $\omega_{\max}$ of the temporal spectrum, with $\omega_{\max} = 2\pi/\Delta t$. In order to account for this finite temporal resolution, the integration of (14.9) should be performed not over all frequencies, but over $[0, \omega_{\max}]$. This integration, however, leads to a power-law decay for short wavenumbers, and not to the expected exponential decay. We have no explanation for this discrepancy between the analytical and numerical results.

We performed a series of numerical calculations in which the size of the temporal step was varied, in order to interpolate the spectra over the total range of spatial frequencies. The result can be represented as

$$S(k) = \frac{T\pi C/\omega_{\max}}{\exp\left(k^2 C/\omega_{\max}\right) - 1} . \tag{14.13}$$

Here C is a constant of order one. Equation (14.13) reproduces correctly the numerically obtained spectra in both asymptotic limits of $k \to 0$ and $k \to \infty$. For intermediate values of wavelength, a transition between a power law and an exponential decay is predicted by (14.11), exactly as found in the numerical calculations. In this way, the numerical results show that the spatial spectrum of the CGL equation in the case of limited temporal resolution coincides precisely with a Bose–Einstein distribution, whereas the spectrum in the case of unlimited temporal resolution follows a power law.

14.1.3 Consequences

To conclude this section, we show analytically and numerically that the power spectra of spatially extended systems with order–disorder transitions obey power laws: the spatial noise spectra are of $1/k^2$ form, thus being Bose–Einstein-like. The temporal noise spectra of the CGL equation are shown to be of $1/\omega^\alpha$ form, with the exponent $\alpha = 2 - D/2$ depending explicitly only on the dimension of the space D. Spatially extended systems with order–disorder transitions are described by a CGL equation with stochastic forces (14.1); this equation accounts for the symmetries of the phase space (Hopf bifurcation) and the symmetries of the physical space (rotational and translational invariance).

All ordered states in nature are, presumably, one- to three-dimensional. This corresponds to exponents of the $1/\omega^\alpha$ noise satisfying $1/2 < \alpha < 3/2$, according to our model, which corresponds well with the experimentally observed exponents of $1/\omega^\alpha$ noise (for reviews of $1/f$ noise, see [7]). The exponent is found experimentally to lie in the range $0.6 < \alpha < 1.4$ [7], depending on the particular system. Another prominent feature of $1/\omega$ noise is that the spectrum usually extends over many decades of frequency with constant α, which also follows simply and naturally from our model.

The model presented here for $1/\omega$ noise comprises the two most accepted models for $1/\omega$ noise. In [8], $1/\omega$ noise is interpreted as a result of a superposition of Lorentzian spectra, requiring a somewhat unphysical assumption of

a specific distribution of damping rates. In our model, the $1/\omega$ spectrum also results formally from a superposition of stochastic spatial modes (see (14.5) and (14.6)). However, the distribution of the damping rates $f(\gamma)$ ($\gamma = k^2$ in our case) results naturally from the dimensionality of the space and is universally valid.

There is also a relation to the model of self-organized criticality [9], in that the phase variable in our model is always in a critical state, as (14.3b) indicates. This analogy with self-organized criticality for the phase variable is a consequence of the phase invariance in the Hopf bifurcation. Consequently, one would expect that the noise power spectra of models of self-organized criticality would show the same dependence on the spatial dimension, $\alpha = 2 - D/2$, as found here. To our knowledge, no detailed investigations of the dependence of α on the dimension of the space have been performed for self-organized criticality.

The above dependence of α on the dimension of the space leads to general conclusions concerning the stability of the ordered state of the system. The integral of the $1/\omega^\alpha$ power spectrum always diverges in the limit of either large or small frequency, indicating a breakup of the ordered state in the limit of small or of large times, respectively. For example, in the case of a low-dimensional system with $D < 2$, $\alpha > 1$, the integral of the temporal power spectrum diverges at low frequencies, which means that the average size of the fluctuations of the order parameter grows to infinity for large times. The average size of a fluctuation is

$$\left\langle |a(t)|^2 \right\rangle \approx \int_{\omega_{\min}}^{\infty} S(\omega) \mathrm{d}\omega \; , \tag{14.14}$$

where $\omega_{\min} = 2\pi/t$ is the lower cutoff boundary of the temporal spectrum; thus this average size grows as

$$\left\langle |a(t)|^2 \right\rangle \propto t^{\alpha-1} \tag{14.15}$$

with increasing time. This generalizes the Wiener stochastic diffusion process,

$$\left\langle |a(t)|^2 \right\rangle \propto t \; , \tag{14.16}$$

well known for zero-dimensional systems, and predicts that diffusion in spatially extended systems is weaker than in zero-dimensional systems. For example, the fluctuations of the order parameter in a 1D system ($\alpha = 1.5$) should diffuse as

$$\left\langle |a(t)|^2 \right\rangle \propto t^{1/2} \; . \tag{14.17}$$

This also means that for large times, the fluctuations of the order parameter become, on average, of the order of magnitude of the order parameter

itself. Defects must then appear in the ordered state, even for a small temperature.

For high-dimensional systems with $D > 2$, $\alpha < 1$, in contrast, the integral over the temporal power spectrum diverges at large frequencies. It may be expected that large fluctuations of the order parameter occur at small times, given by

$$\left\langle |a(t)|^2 \right\rangle \approx \int_0^{\omega_{max}} S(\omega) d\omega \ , \tag{14.18}$$

where $\omega_{max} = 2\pi/t$ is the upper cutoff boundary of the temporal spectra. This results in the diffusion law

$$\left\langle |a(t)|^2 \right\rangle \propto \frac{1}{t^{1-\alpha}} \tag{14.19}$$

for $\alpha < 1$, which diverges for small times. The fluctuations of the order parameter in a 3D system ($\alpha = 0.5$) should diverge as

$$\left\langle |a(t)|^2 \right\rangle = t^{-1/2} \tag{14.20}$$

for small times. This means that a continuous creation and annihilation of pairs of defects in the ordered state can be predicted for $D > 2$. These defects are termed "virtual defects", since they appear on a short timescale only and do not have any dynamical significance.

The case $D = 2$ is marginal. The integral over the spectrum diverges weakly (logarithmically) in the limits of both small and large frequencies. A specific such low-frequency divergence in this kind of 2D patterns was investigated in [10], and is termed the Kosterlitz–Thouless transition.

14.2 Noisy Stripes

An analysis of the stochastic dynamics of stripes may be performed by solving a stochastic Swift–Hohenberg equation [4],

$$\frac{\partial A}{\partial t} = pA - A^3 - \left(\Delta + \nabla^2\right)^2 A + \Gamma(\boldsymbol{r}, t) \ , \tag{14.21}$$

for the temporal evolution of the real-valued order parameter $A(\boldsymbol{r}, t)$, defined in the D-dimensional space $\boldsymbol{r}$. Again, p is the control parameter (the stripe formation instability occurs at $p = 0$); Δ is the detuning parameter, determining the resonant wavenumber of the stripe pattern given by $\boldsymbol{k}_0^2 = \sqrt{\Delta}$; and $\Gamma(\boldsymbol{r}, t)$ is an additive noise, δ-correlated in space and time, and of temperature T, defined as in (14.2).

Analytical results are obtained by solving the stochastic amplitude equation for the stripes,

$$\frac{\partial B}{\partial t} = pB - |B|^2\, B - \left(2\mathrm{i}\boldsymbol{k}_0\nabla + \nabla^2\right)^2 B + \Gamma(\boldsymbol{r},t) \ , \qquad (14.22)$$

for the slowly varying complex-valued envelope $B(\boldsymbol{r},t)$ of the stripe pattern corresponding to the resonant wavevector $\boldsymbol{k}_0$. The amplitude equation (14.22) can be obtained directly from (14.21), by inserting $A(\boldsymbol{r},t) = [B(\boldsymbol{r},t)\exp(\mathrm{i}\boldsymbol{k}_0\cdot\boldsymbol{r})+\text{c.c.}]/\sqrt{3}$, or directly from the microscopic equations of various stripe-forming systems (e.g. [11]). Equation (14.22) can also be obtained phenomenologically on the basis of symmetry considerations for arbitrary stripe patterns [5].

14.2.1 Spatio-Temporal Noise Spectra

We again assume that the system is sufficiently far above the stripe-forming transition, and that $p \gg T$. The homogeneous component dominates in (14.22) (and, correspondingly, one stripe component dominates in (14.21)), and one can look for a solution of (14.22) in the form of a perturbed homogeneous state, $B(\boldsymbol{r},t) = B_0 + b(\boldsymbol{r},t)$. After linearization of (14.22) around B_0 and diagonalization, we obtain the linear stochastic equations for the perturbations of the amplitude, $b_+ = (b + b^*)/\sqrt{2}$, and phase, $b_- = (b - b^*)/\sqrt{2}$:

$$\frac{\partial b_+}{\partial t} = -2pb_+ + \hat{L}_+(\nabla)b_+ + \Gamma_+(\boldsymbol{r},t) \ , \qquad (14.23\mathrm{a})$$

$$\frac{\partial b_-}{\partial t} = \hat{L}_-(\nabla)b_- + \Gamma_-(\boldsymbol{r},t) \ . \qquad (14.23\mathrm{b})$$

Here the nonlocality operators are given by

$$\hat{L}_\pm(\boldsymbol{k}_0,\nabla) = -p + (2\boldsymbol{k}_0\nabla)^2 - \nabla^4 \mp \sqrt{p^2 - \left(4\boldsymbol{k}_0\nabla^3\right)^2} \ , \qquad (14.24)$$

and their spectra by

$$\hat{L}_\pm(\boldsymbol{k}_0,\boldsymbol{k}) = -p - (2\boldsymbol{k}_0\,\mathrm{d}\boldsymbol{k})^2 - \mathrm{d}k^4 \mp \sqrt{p^2 - (4\boldsymbol{k}_0^3\,\mathrm{d}\boldsymbol{k})^2} \ , \qquad (14.25)$$

as obtained by the substitution $\nabla \to \mathrm{i}\,\mathrm{d}\boldsymbol{k}$, where $\mathrm{d}\boldsymbol{k} = \boldsymbol{k} - \boldsymbol{k}_0$ is the wavevector of the perturbation mode in (14.22).

Asymptotic values of the the nonlocality operator $\hat{L}_-(\nabla)$ for phase perturbations can be found in two opposite limits, namely the strong- and weak-pump limits, where

$$\hat{L}_-(\boldsymbol{k}_0,\nabla) = (2\boldsymbol{k}_0\nabla)^2 - \nabla^4 \quad \text{for } \left|4\boldsymbol{k}_0\nabla^3\right| \ll p \ , \qquad (14.26\mathrm{a})$$

$$\hat{L}_-(\boldsymbol{k}_0,\nabla) = -\left(2\mathrm{i}\boldsymbol{k}_0\nabla + \nabla^2\right)^2 \quad \text{for } \left|4\boldsymbol{k}_0\nabla^3\right| \gg p \ . \qquad (14.26\mathrm{b})$$

Equation (14.23a) is an equation for the amplitude fluctuations b_+ corresponding to the modulation amplitude of the stripe pattern, while (14.23b) is an equation for the phase fluctuations b_- corresponding to parallel translation of the stripes. Equation (14.25) indicates that the phase fluctuations

decay at a rate $\hat{L}_-(\boldsymbol{k}_0, \boldsymbol{k}) = -(2\boldsymbol{k}_0\,\mathrm{d}\boldsymbol{k})^2 - \mathrm{d}\boldsymbol{k}^4$ in the strong-pump limit, or $\hat{L}_-(\boldsymbol{k}_0, \boldsymbol{k}) = -(2\boldsymbol{k}_0\,\mathrm{d}\boldsymbol{k} + \mathrm{d}\boldsymbol{k}^2)$ in the weak-pump limit. This means that the long-wavelength phase perturbation modes decay asymptotically slowly, with a decay rate approaching zero as $\mathrm{d}\boldsymbol{k} \to 0$, which is a consequence of the phase invariance of the system.

Next, we consider only the phase perturbations. These perturbations determine the stochastic dynamics of the stripe pattern above the stripe formation threshold, i.e. for $p > 0$. More precisely, the amplitude fluctuations are small compared with the phase fluctuations if $\left|4\boldsymbol{k}_0^3\,\mathrm{d}\boldsymbol{k}\right| \ll p$, as follows from (14.26).

We calculate the spatio-temporal power spectra of the phase fluctuations by rewriting (14.23b) in terms of the spatial and temporal Fourier components,

$$b(\boldsymbol{r}, t) = \int b_-(\boldsymbol{k}, \omega) \mathrm{e}^{\mathrm{i}\omega t - \mathrm{i}\boldsymbol{k}\cdot\boldsymbol{r}}\,\mathrm{d}\omega\,\mathrm{d}\boldsymbol{k}\ , \tag{14.27}$$

and

$$S(\boldsymbol{k}, \omega) = |b_-(\boldsymbol{k}, \omega)|^2 = \frac{|\Gamma_-(\boldsymbol{k}, \omega)|^2}{\omega^2 + |L_-(\boldsymbol{k}_0, \boldsymbol{k})|^2}\ . \tag{14.28}$$

Assuming δ-correlated noise in space and time, $|\Gamma_-(\boldsymbol{k}, \omega)|^2$ is simply proportional to the temperature T of the random force.

The spatial power spectrum is obtained by integration of (14.28) over all temporal frequencies:

$$S(\boldsymbol{k}) = \int\limits_{-\infty}^{\infty} \frac{T}{\omega^2 + |L_-(\boldsymbol{k}_0, \boldsymbol{k})|^2}\mathrm{d}\omega = \frac{T\pi}{2\,|L_-(\boldsymbol{k}_0, \boldsymbol{k})|}\ . \tag{14.29}$$

This results in a divergence of the spatial spectrum as $\mathrm{d}\boldsymbol{k} \to 0$ (and, equivalently, in a divergence of the spatial spectrum of a roll pattern obtained from (14.21) as $\boldsymbol{k} \to \boldsymbol{k}_0$). As follows from (14.29), perturbations of the stripe pattern $\mathrm{d}\boldsymbol{k}$ diverge differently, depending on whether the perturbations are parallel or perpendicular to the wavevector of the stripe pattern $\boldsymbol{k}_0$. This follows from the isotropic form of the nonlocality operator (14.25). The parallel perturbations (corresponding to compression and undulation of the stripes) diverge as $\mathrm{d}\boldsymbol{k}^{-2}$, while the perpendicular perturbations (corresponding to a zigzagging of the stripes) diverge as $\mathrm{d}\boldsymbol{k}^{-4}$. This results in an anisotropic form of the singularity at $\mathrm{d}\boldsymbol{k} = 0$, which can actually be expected from the anisotropic form of the amplitude equation for rolls (14.22). Figure 14.5 shows the spatial power spectrum of the noise of the stripe pattern as obtained from a numerical integration of the SH equation (14.21) and illustrates the anisotropy. The anisotropy results in the fact that the stability conditions of the stripes depend on the number of spatial dimensions. The
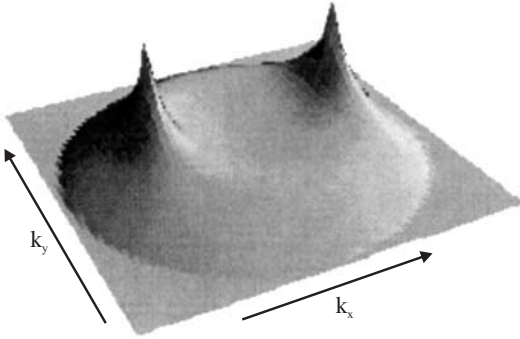
Fig. 14.5. Spatial noise power spectrum of stripes in 2D obtained numerically by solving the stochastic SH equation (14.1) with $p = 1$ and $\Delta = 0.7$. The averaging time was $t_{av} = 5000$. The intensity of the spatial spectral components is represented logarithmically

integral of (14.29) over the spatial wavenumbers $d\mathbf{k}$ diverges for spatial dimensions $D < 4$, and converges for $D \geq 4$ only. Only for four (or more) dimensions of space are the stripes absolutely stable against additive noise. This is in contrast to a well-known theorem concerning the stability of a "condensate": a condensate (a homogeneous distribution) is known to be stable for all spatial dimensions larger than two.

The temporal power spectra are obtained by integration of (14.28) over all possible wavevectors $d\mathbf{k}$:

$$S(\omega) = \int\limits_{-\infty}^{\infty} \frac{T}{\omega^2 + |L_-(\mathbf{k}_0, \mathbf{k})|^2} d\mathbf{k} \ . \tag{14.30}$$

However, this has no analytic form, even for one spatial dimension.

Asymptotically, in the limit of small frequencies $\omega \to 0$, when the term $(2\mathbf{k}_0 \, d\mathbf{k})^2$ dominates in the denominator of the integral (14.30), an analytical integration is possible, and leads to the following results. For 1D, the spectrum is $S_{1D}(\omega) = c_{1D}T\omega^{-3/2}$, with a coefficient $c_{1D} = \pi/(2\sqrt{2}k_0^2)$. For 2D, $S_{2D}(\omega) = c_{2D}T\omega^{-1.25}$; for 3D, $S_{3D}(\omega) = c_{3D}T\omega^{-1}$; and in the general case of D dimensions, $S_D(\omega) = c_D T\omega^{-\alpha}$, where $\alpha = 1 + (3 - D)/4$ and the coefficients c_D is of order unity.

The integral (14.30) has been evaluated numerically, and the results for one, two and three dimensions are given in Fig. 14.6; $1/\omega^\alpha$ dependences are obtained. In the small-frequency limit $\omega \to 0$, the exponents obey $\alpha = 1 + (3 - D)/4$; in the large-frequency limit $\omega \to \infty$, the spectra also show a power-law form, but with exponents $\alpha = 1 + (4 - D)/4$. The exponents change abruptly from the small-frequency value to the large-frequency value at a critical frequency $\omega_c \approx 4k_0^2$, as follows from an analysis of (14.29), and as seen from Fig. 14.6.
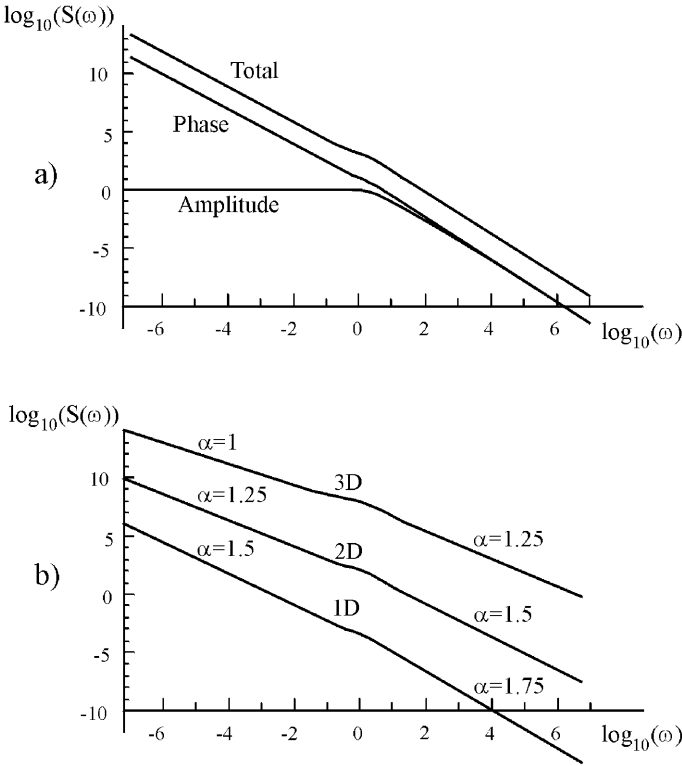
Fig. 14.6. Temporal spectra obtained by numerical calculation of the integral (14.9) with $p = 1$ and $\Delta = 1$. (**a**) 1D case. The phase power spectrum (obtained from integration of (14.23b)), the amplitude power spectrum (obtained from integration of (14.23a)) and the total spectrum are shown. (**b**) The phase power spectra as calculated for one, two and three spatial dimensions

Comparing these results with the noise spectra of condensates (Sect. 14.1) one can conclude that:

1. One-dimensional stripes have the same exponent of noise power spectra as one-dimensional condensates. This is plausible, since the amplitude equation for stripes is similar to a complex Ginzburg–Landau equation, and the two equations coincide in the limit of $d\boldsymbol{k} \to 0$.
2. Two-dimensional stripes behave like noisy condensates of dimension $D = 1.5$, if one judges from the exponents of the noise spectra in the low-frequency limit. As discussed above (see also Fig. 14.5), the singularity of the spatial noise spectrum is strongly squeezed in the direction along the stripes. It is then plausible that the noise characteristics of this anisotropic system are between those of isotropic one- and two-dimensional systems.

3. Similarly, three-dimensional stripes (lamellae) behave like two-dimensional condensates. Both display power spectra with $\alpha = 1$.

14.2.2 Stochastic Drifts

Since the temporal power spectra for stripe patterns diverge as $1/\omega^{3/2}$, the stochastic drift of stripes should be subdiffusive, as follows from (14.15) and (14.17). We tested this prediction about stochastic drift of the stripe pattern by numerically solving the Swift–Hohenberg equation (14.21) in 1D. We calculated the displacement of the stripe pattern as a function of time. The displacement $x(t)$ of the stripe position for the SH equation is directly proportional to the phase of the order parameter $B(x,t)$ at the corresponding spatial location in the amplitude equation (14.22). Figure 14.7a shows the power spectrum of the displacement, which follows an $\omega^{-3/2}$ law, in accordance with the analytical predictions. Figure 14.7b shows the power spectrum of the variation (the temporal derivative $x(t) - x(t - \Delta t)$) of the displacement, which follows an $\omega^{1/2}$ law. The average square displacement of the stripe position $x(t)$, averaged over many realizations, is shown in Fig. 14.7c. The predicted slope of $1/2$ is clearly seen for times up to $t \approx 1000$. For very large times, the usual (Brownian) stochastic drift is obtained. This behavior for large times (corresponding to small frequencies) is, however, an artifact of the numerical space discretization. A subdiffusive stochastic drift of kinks (fronts) in 1D systems (for small times, however) was recently found in [12].

The above discussion of stochastic drifts concerns large times: the variance of the position of 1D stripes of the form $t^{1/2}$ is related to the $\omega^{-3/2}$ power spectrum at small frequencies. The $\omega^{-1.75}$ spectrum at large frequencies ($\omega \geq \omega_c \approx 4k_0^2$) predicts, equally, a $t^{3/4}$ law for the stochastic drift at small times. The results of numerical calculations in Fig. 14.7 do not, however, take account of small timescales ($t \leq 2\pi/\omega_c$), and thus the small-time drift law was not observed numerically.

The stochastic drift (although subdiffusive) of the order parameter means that for large times the fluctuations become, on average, of the order of magnitude of the order parameter itself. The long-range order eventually breaks up even for a small temperature. In general, for a $1/\omega^\alpha$ power spectrum with $\alpha > 1$, such finite perturbations occur for times $t \geq t_c \propto T^{-1/(\alpha-1)}$. We tested this dependence on 1D stripes, where the critical time is $t_c \propto T^{-2}$. For this purpose, we prepared numerically an off-resonance stripe pattern using the SH equation for 1D without a stochastic term. The off-resonance stripe was stable (it was within the Eckhaus stability range). We then switched on the stochastic term and waited until the fluctuations of the stripe pattern grew and destroyed it locally. We observed that after the stripe pattern was destroyed in some place, a resonant stripe appears there and invades the whole pattern in the form of propagating switching waves. The state of the system changes in this way from a local potential minimum (off-resonance stripe) to
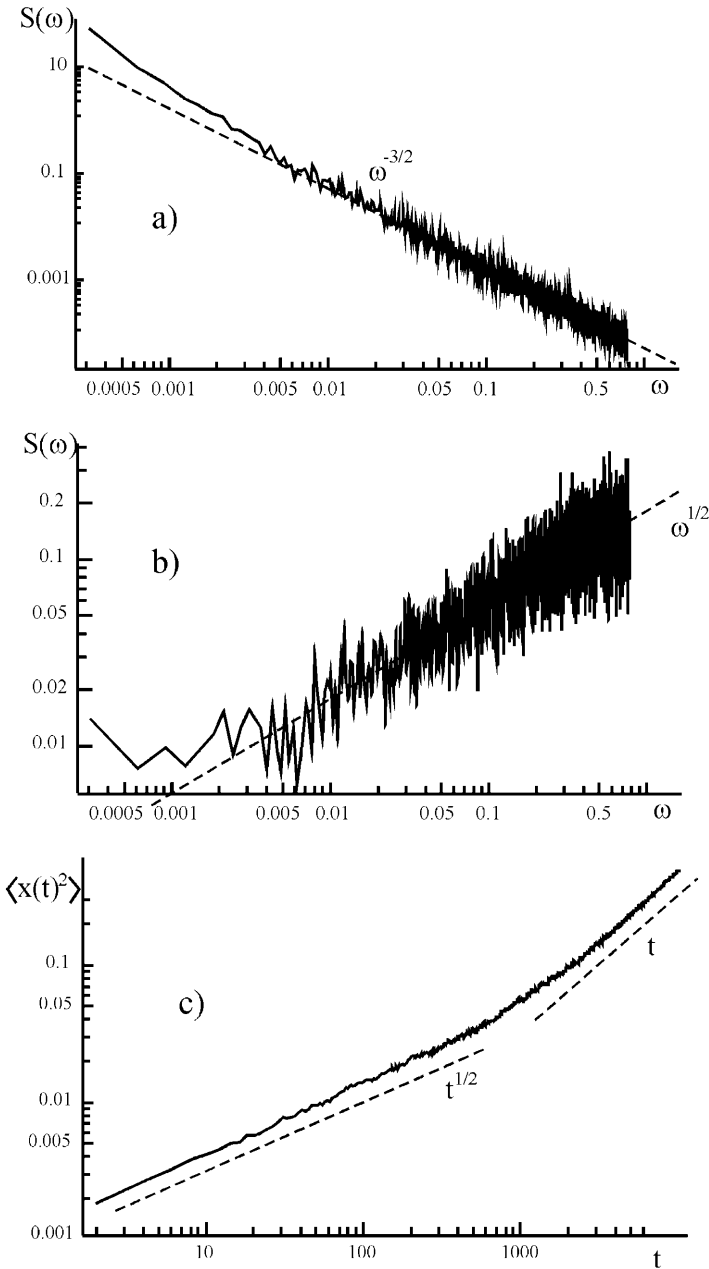
Fig. 14.7. Statistical properties of the position of a stripe pattern as obtained by numerical integration of the SH equation in 1D with $p = 1$ and $\Delta = 0.7$. (**a**) The power spectrum of the displacement $x(t)$. The *dashed line* with a slope corresponding to $\omega^{-3/2}$ serves to guide the eye. (**b**) The power spectrum of the variation of the displacement $x(t) - x(t - \Delta t)$. The *dashed line* with a slope corresponding to $\omega^{1/2}$ serves to guide the eye. (**c**) The average square displacement of the stripe position, as averaged over 1000 realizations

the global potential minimum (resonant stripe) as a result of triggering by a local perturbation.

In Fig. 14.8, the numerically calculated lifetime of the off-resonance stripe pattern is plotted as a function of the temperature of the stochastic force. Again, as predicted by analytic calculations, the dependence $t_c \propto T^{-2}$ is obtained. This shows that in spatially extended systems, the switching from a local potential minimum to a deeper global minimum does not depends exponentially on time as in zero-dimensional (compact) systems, but obeys a power law. In particular, for stripe patterns, the switching time is $t_s \propto T^{-2}$ in 1D.
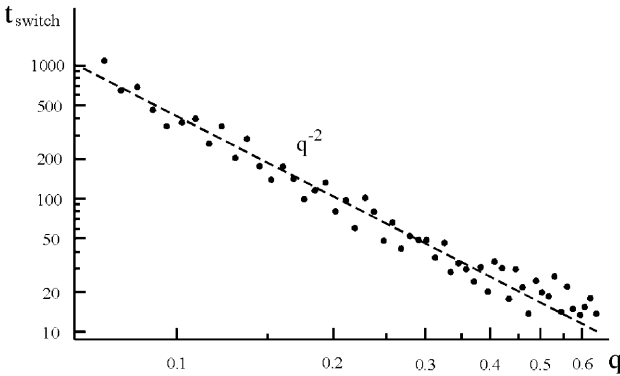

Fig. 14.8. Lifetime of an off-resonant stripe pattern as a function of the noise temperature T, as obtained by numerical integration of the SH equation in 1D with $p = 1$. A resonant stripe pattern with $k_0^2 = 1$ was excited for $\Delta = 1$. The detuning value was then reduced to 0.75, and the time was measured until the new resonant stripe pattern took over. Every point was obtained by averaging over 10 realizations

14.2.3 Consequences

To conclude, we recall that simple models for stripe patterns (the stochastic Swift–Hohenberg equation for the order parameter, and the stochastic Newell–Whitehead–Segel equation for the envelope of the stripes) allow one to calculate spatio-temporal noise power spectra, and to predict the following properties of stripe patterns in the presence of noise:

1. An anisotropic form of the singularities in the spatial power spectrum.
2. Stability conditions that depend on the number of spatial dimensions.
3. A $1/\omega^\alpha$ temporal power spectrum with an exponent that depends explicitly on the number of spatial dimensions.
4. Subdiffusive stochastic drift.

5. A power-law temperature dependence of the lifetime of a locally stable stripe pattern (corresponding to a local potential minimum).

References

1. J. Viñals, E. Hernandez-Garcia, M. San Miguel and R. Toral, Numerical study of the dynamical aspects of pattern selection in the stochastic Swift–Hohenberg equation in one dimension, Phys. Rev. A **44**, 1123 (1991); K.R. Elder, J. Viñals and M. Grant, Ordering dynamics in the two-dimensional stochastic Swift–Hohenberg equation, Phys. Rev. Lett. **68**, 3024 (1992). 205
2. R.J. Deissler, External noise and the origin and dynamics of structure in convectively unstable systems, J. Stat. Phys. **54**, 1459 (1989); J. García-Ojalvo, A. Hernández-Machado and J.M. Sancho, Effects of external noise on the Swift–Hohenberg equation, Phys. Rev. Lett. **71**, 1542 (1993); R. Mueller, K. Lippert, A. Kuehnel and U. Behn, First-order nonequilibrium phase transition in a spatially extended system, Phys. Rev. E **56**, 2658 (1997). 205
3. J. García-Ojalvo and J.M. Sancho, *Noise in Spatially Extended Systems* (Springer, New York, 1999). 205
4. J.B Swift and P.C. Hohenberg, Hydrodynamic fluctuations at the convective instability, Phys. Rev. A **15**, 319 (1977). 206, 216
5. A.C. Newell and J.A. Whitehead, Finite bandwidth, finite amplitude convection, J. Fluid Mech. **38**, 279 (1969); L.A. Segel, Distant side-walls cause slow amplitude modulation of cellular convection, J. Fluid Mech. **38**, 203 (1969). 206, 217
6. L.D. Landau and E.M. Lifshitz, *Course of Theoretical Physics*, vols. 6 and 9 (Pergamon, London, New York, 1959); R. Brout, *Phase Transitions* (Benjamin, New York, 1965). 207
7. P. Dutta and P.M. Horn, Low-frequency fluctuations in solids: $1/f$ noise, Rev. Mod. Phys. **53**, 497 (1981); Sh.M. Kogan, Low frequency current noise with $1/f$ spectrum in solids, Sov. Phys. Usp. **28**, 170 (1985); M.B. Weissman, $1/f$ noise and other slow, nonexponential kinetics in condensed matter, Rev. Mod. Phys. **60**, 537 (1988); G.P. Zhigal'skii, $1/f$ noise and nonlinear effects in thin metal films, Sov. Phys. Usp. **40**, 599 (1997). 214
8. F.K. du Pre, A suggestion regarding the spectral density of flicker noise, Phys. Rev. **78**, 615 (1950); A. Van der Tiel, On the noise spectra of semi-conductor noise and on flicker effect, Physica (Amsterdam) **16**, 359 (1950). 214
9. P. Bak, C. Tang and K. Wiesenfeld, Self-organized criticality: an explanation of the $1/f$ noise, Phys. Rev. Lett. **59**, 381 (1987); P. Bak, C. Tang and K. Wiesenfeld, Self-organized criticality, Phys. Rev. A **38**, 364 (1988). 215
10. J.M. Kosterlitz and D.J. Thouless, Ordering, metastability and phase transitions in two-dimensional systems, J. Phys. C **6**, 1181 (1973). 216
11. M.C. Cross and P.C. Hohenberg, Pattern formation outside of equilibrium, Rev. Mod. Phys. **65**, 851 (1993). 217
12. A. Rocco, U. Ebert and W. van Saarloos, Subdiffusive fluctuations of "pulled" fronts with multiplicative noise, Phys. Rev. E **62**, R13 (2000). 221